Combined Compression and Shear Structural Evaluation of Stiffened Panels Fabricated Using Electron Beam Freeform Fabrication

Erik Walter Nelson

A Thesis submitted to the Faculty of Virginia Polytechnic Institute and State University in partial fulfillment of the requirements for the degree of

Master of Science

in Aerospace Engineering

Rakesh K. Kapania, Committee Chair

Karen M. Taminger

Michael W. Hyer

Michael Philen

June 17, 2008

Blacksburg, Virginia

Keywords: Electron Beam Freeform Fabrication, finite element analysis, compression, shear, stiffened panels, stiffener, buckling

Acknowledgments

I would like to express a sincere thank you to Dr. Rakesh Kapania for his guidance through my degree. I would also like to thank Dr. Michael Hyer and Dr. Michael Philen for not only for their impeccable instruction, but also for serving on my committee. It was an honor and a pleasure to study and learn under all of you at Virginia Tech. I'd like to express my deepest gratitude to Karen Taminger for not only funding my program, but also her continued counsel throughout my stay at NASA. I'd also like to thank all the fine people at the NASA Langley Research Center especially those associated with the EBF^3 project for the polite and friendly nature in which they were always willing to help. I'd like to thank my mom, dad, brother, and sister for their continued support through not only this degree but in all the endeavors I've undertaken in my life. Lastly, I owe so much to my incredible girlfriend Katie, who had it not been for her encouragement, this degree would not have been.

This work was funded by NASA's Aeronautics program under grant number VT-03-01 through the National Institute of Aeronautics. The testing was conducted at NASA Langley Research Center.

Erik Walter Nelson

Virginia Polytechnic Institute and State University

June 2008

Combined Compression and Shear Structural Evaluation of Stiffened Panels Fabricated Using Electron Beam Freeform Fabrication

Erik Walter Nelson

Abstract

Unitized aircraft structures have the potential to be more efficient than current aircraft structures. The Electron Beam Freeform Fabrication (EBF^3) process can be used to manufacture unitized aircraft structures. The structural efficiency of blade stiffened panels made with EBF^3 was compared to panels made by integrally machining from thick plate. The panels were tested under two load cases in a combined compression-shear load test fixture. One load case tested the panels' responses to a higher compressive load than the shear load. The second load case tested the panels' responses to an equal compressive and shear load. Finite element analysis was performed to compare with the experimental results. The EBF^3 panels failed at a 18.5% lower buckling load than the machined panels when loaded mostly in compression but at an

almost two times higher buckling load than the machined panels when the shear matched the compressive load. The finite element analysis was in good agreement with the experimental results prior to buckling. The results demonstrate that the EBF^3 process has the capabilities of manufacturing stiffened panels that behave similarly to machined panels prior to buckling. Once the EBF^3 panels buckled, the buckled shape of the EBF^3 panels was different from the machined panels, generally buckling in the opposite direction of what was observed with the machined panels. This was also expected based on the finite element analysis. The different post-buckling response between the two manufacturing techniques was attributed to the residual stress and associated distortion induced during the EBF^3 manufacturing process.

Contents

Acknowledgments **ii**

Abstract **iv**

List of Figures **x**

List of Tables **xxvi**

Chapter 1 Introduction **1**

1.1 Unitized Structures 4

1.2 Solid Freeform Fabrication 7

1.3 Electron Beam Freeform Fabrication (EBF^3) Manufacturing Process 9

1.4 Previous EBF^3 Structural Panel Studies 12

1.5 Nonlinear Structural Response 14

1.5.1 Nonlinear Finite Element in NASTRAN 16

1.6 Goal 18

1.7 Organization of Thesis 18

Chapter 2 Experimental Setup **20**

2.1 Test Machine 20

2.2 Panel Design 23

2.2.1 Machined Panel 24

2.2.2 EBF^3 Panel 25

2.3 Data Acquisition 28

2.3.1 Strain Gages 28

2.3.2 Video Image Correlation 3-D Measurement System . . 29

2.3.3 Direct Current Displacement Transducer 30

2.4 Load Cases 32

Chapter 3 Results **34**

3.1 Load Case 1 Results 34

3.1.1 End-Shortening 34

3.1.2 Lateral Displacement 39

3.1.3 Out-Of-Plane Displacement 39

3.1.4 Strain in the Panels 49

3.1.5 Strain in the Stiffeners 50

3.1.6 Video Image Correlation 3-D Measurement System Results 59

3.2 Load Case 2 Results 70

3.2.1 End-Shortening 70

3.2.2 Lateral Displacement 75

3.2.3 Out-Of-Plane Displacement 79

3.2.4 Strain in the Panels 81

3.2.5 Strain in the Stiffeners 96
3.2.6 Video Image Correlation 3-D Measurement System Results 98

Chapter 4 Discussion of Results 112

4.1 Load Case 1 112
4.1.1 Irregular Hole Pattern and Load Platen Rotation . . . 112
4.1.2 Machined Panels' Responses 114
4.1.3 EBF^3 Panels' Responses 118
4.2 Load Case 2 124
4.2.1 Problems during the Tests 124
4.2.2 Machined Panels' Responses 125
4.2.3 EBF^3 Panels' Responses 128
4.3 Load Case 1 Compared to Load Case 2 132

Chapter 5 Finite Element Validation 134

5.1 Finite Element Model 134
5.2 Load Case 1 136
5.3 Load Case 2 158

Chapter 6 Concluding Remarks 179

Chapter 7 Future Work 184

Bibliography 186

Appendix A Supplementary Data For Load Case 1 193

Appendix B Supplementary Data For Load Case 2 **211**

Appendix C Supplementary Linear Finite Element Analysis For Machined and EBF^3 Panel 1 **221**

Appendix D Supplementary Linear Finite Element Analysis For Machined and EBF^3 Panel 3 **232**

Appendix E Additional Nonlinear Explanation **243**

E.1 Material nonlinearity 243

E.2 Geometric nonlinearity 246

E.3 Solving Nonlinear Equations 248

List of Figures

1.1 A) Non-unitized riveted structure, B) Non-unitized bonded structure, C) Unitized structure 4

1.2 Illustration of the EBF^3 Process 10

1.3 Inside View of the Large EBF^3 Machine[1][16] 11

2.1 Illustration of the Compression-Shear Combined Loads Test Fixture. P is the compressive load, S is the shear load [27]. . . 21

2.2 Specimen in Compression-Shear Frame[2] 22

2.3 Combined Loads Compression-Shear Test Fixture[3] 23

2.4 Design of Stiffened Panels 25

2.5 Example of Defects found on the EBF^3 Panel Stiffeners[4] . . . 26

2.6 Distortion in EBF^3 Panel 3 after bump-forming 27

2.7 Strain Gage Locations on the specimens. Gages marked as X(Y) mark back to back strain gages. 29

2.8 Illustration of the Video Image Correlation 3-D Measurement System 30

2.9 Locations of the six out-of-plane Direct Current Displacement Transducers (DCDTs) 31
2.10 Illustration of the Measured Lateral Displacement caused by the Shear Load 32
2.11 Diagram of the Angle of Rotation Alpha and Beta measured along the top of the panel 33

3.1 Illustration of Load Case 1: P was the compressive load to a maximum of 179.5 kips. S was the shear load at 40% of the compressive load up to a maximum of 71.8 kips. 35
3.2 Original Measured Experimental End-shortening Results for Load Case 1 37
3.3 Corrected Experimental End-shortening Results for Load Case 1 38
3.4 Angles of Rotation of the Load Platen for EBF^3 Panel 2 . . . 40
3.5 Original Measured Experimental Lateral Shear Displacements at the bottom of the Panels for Load Case 1 41
3.6 Corrected Experimental Lateral Shear Displacements at the bottom of the Panels for Load Case 1 42
3.7 Out-Of-Plane Displacement measured by DCDT 1, 2, and 3 for Machined Panels 1 and 2 45
3.8 Out-Of-Plane Displacement measured by DCDT 1, 2, and 3 for EBF^3 Panels 1 and 2 46
3.9 Out-Of-Plane Displacement measured by DCDT 4, 5, and 6 for Machined Panels 1 and 2 47

3.10 Out-Of-Plane Displacement measured by DCDT 4, 5, and 6 for EBF^3 Panels 1 and 2 48
3.11 Axial Strains measured from Strain Gages 1a-4a for Machined Panels 1 and 2 51
3.12 Axial Strains measured from Strain Gages 1a-4a for EBF^3 Panels 1 and 2 52
3.13 Axial Strains measured from Strain Gages 1b-4b for Machined Panels 1 and 2 53
3.14 Axial Strains measured from Strain Gages 1b-4b for EBF^3 Panels 1 and 2 54
3.15 Axial Strains measured from Strain Gages 5a-8a for Machined Panels 1 and 2 55
3.16 Axial Strains measured from Strain Gages 5a-8a for EBF^3 Panels 1 and 2 56
3.17 Lateral Strains measured from Strain Gages 5b-8b for Machined Panels 1 and 2 57
3.18 Lateral Strains measured from Strain Gages 5b-8b for EBF^3 Panels 1 and 2 58
3.19 Axial Strain in the stiffeners measured from Strain Gages 25a-28a for Machined Panels 1 and 2 60
3.20 Axial Strain in the stiffeners measured from Strain Gages 25a-28a for EBF^3 panels 1 and 2 61

3.21 Lateral Strain in the stiffeners measured from Strain Gages 25b-28b for Machined panels 1 and 2 62
3.22 Lateral Strain in the stiffeners measured from Strain Gages 25b-28b for EBF^3 panels 1 and 2 63
3.23 Out-of-plane Displacement measured in Machined Panel 2 from the VIC 3-D System in the lower half of the panel at A) 28.7 kips (pre-buckle) B) 45.5 kips (post-buckle) C) 138.7 (post-buckle) D) 179.5 (maximum load) E) 170.1 (post-failure). Load values expressed in terms of compressive load 65
3.24 Out-of-plane Displacement measured in EBF^3 Panel 1 from the VIC 3-D System in the lower half of the panel at A) 35.1 kips (pre-buckle) B) 83.5 kips (post-buckle) C) 135.1 (post-buckle) D) 179.1 (maximum load) E) 160.2 (post-failure). Load values expressed in terms of compressive load 66
3.25 Out-of-plane Displacement measured in EBF^3 Panel 2 from the VIC 3-D System in the lower half of the panel at A) 35.4 kips (pre-buckle) B) 85.7 kips (post-buckle) C) 134.2 (post-buckle) D) 179.5 (maximum load) E) 163.5 (post-failure). Load values expressed in terms of compressive load 67

3.26 Axial Strain measured in Machined Panel 2 from the VIC 3-D System in the lower half of the panel at A) 28.7 kips (pre-buckle) B) 45.5 kips (post-buckle) C) 138.7 (post-buckle) D) 179.5 (maximum load) E) 170.1 (post-failure). Load values expressed in terms of compressive load 68

3.27 Axial Strain measured in EBF^3 Panel 2 from the VIC 3-D System in the lower half of the panel at A) 35.4 kips (pre-buckle) B) 83.5 kips (post-buckle) C) 134.2 (post-buckle) D) 179.5 (maximum load) E) 163.5 (post-failure). Load values expressed in terms of compressive load 69

3.28 Illustration of Load Case 2: P was the compressive load to a maximum of 176.4 kips. S was the shear load at 100% of the compressive load up to a maximum of 100 kips. 71

3.29 Original Measured Experimental End-shortening Results for Load Case 2 72

3.30 Corrected Experimental End-shortening Results for Load Case 2 73

3.31 Angles of Rotation of the Load Platen for Load Case 2 76

3.32 Original Measured Experimental Lateral Shear Displacements from the bottom of the Panels for Load Case 2 77

3.33 Corrected Experimental Lateral Shear Displacements from the bottom of the Panels for Load Case 2 78

3.34 Out-Of-Plane Displacement measured by DCDT 1, 2, and 3 for Machined Panels 3 and 4 82

3.35 Out-Of-Plane Displacement measured by DCDT 1, 2, and 3 for EBF^3 Panel 3 83
3.36 Out-Of-Plane Displacement measured by DCDT 4, 5, and 6 for Machined Panel 3 84
3.37 Out-Of-Plane Displacement measured by DCDT 4, 5, and 6 for EBF^3 Panel 3 85
3.38 Axial Strains measured from Strain Gages 1a-4a for Machined Panels 3 and 4 88
3.39 Axial Strains measured from Strain Gages 1a-4a for EBF^3 Panel 3 89
3.40 Axial Strains measured from Strain Gages 1b-4b for Machined Panels 3 and 4 90
3.41 Axial Strains measured from Strain Gages 1b-4b for EBF^3 Panel 3 91
3.42 Axial Strains measured from Strain Gages 5a-8a for Machined Panels 3 and 4 92
3.43 Axial Strains measured from Strain Gages 5a-8a for EBF^3 Panel 3 93
3.44 Lateral Strains measured from Strain Gages 5b-8b for Machined Panels 3 and 4 94
3.45 Lateral Strains measured from Strain Gages 5b-8b for EBF^3 Panel 3 95

3.46 Axial Strain in the stiffeners measured from Strain Gages 25a-28a for Machined Panels 3 and 4 99
3.47 Axial Strain in the stiffeners measured from Strain Gages 25a-28a for EBF^3 Panel 3 100
3.48 Lateral Strain in the stiffeners measured from Strain Gages 25b-28b for Machined Panels 3 and 4 101
3.49 Lateral Strain in the stiffeners measured from Strain Gages 25b-28b for EBF^3 Panel 3 102
3.50 Out-of-plane Displacement measured in Machined Panel 3 from the VIC 3-D System in the lower half of the panel at A) 26.8 kips (pre-buckle) B) 61.5 kips (post-buckle) C) 110.2 (post-buckle) D) 152.7 (maximum load) E) 144.3 (post-failure). Load values expressed in terms of compressive load 104
3.51 Out-of-plane Displacement measured in Machined Panel 4 from the VIC 3-D System in the lower half of the panel at A) 28.5 kips (pre-buckle) B) 62.2 kips (post-buckle) C) 110.5 (post-buckle) D) 175.5 (maximum load) E) 167.6 (post-failure). Load values expressed in terms of compressive load 105
3.52 Out-of-plane Displacement measured in EBF^3 Panel 3 from the VIC 3-D System in the lower half of the panel at A) 39.3 kips (pre-buckle) B) 113.9 kips (post-buckle) C) 150.8 (post-buckle) D) 176.4 (maximum load) E) 170.7 (post-failure). Load values expressed in terms of compressive load 106

3.53 Out-of-plane Displacement measured in EBF^3 Panel 4 from the VIC 3-D System in the lower half of the panel at A) 42.1 kips (pre-buckle) B) 112.7 kips (post-buckle) C) 152.1 (post-buckle) D) 172.6 (maximum load) E) 169.9 (post-failure). Load values expressed in terms of compressive load 107

3.54 Axial Strain measured in Machined Panel 3 from the VIC 3-D System in the lower half of the panel at A) 26.8 kips (pre-buckle) B) 61.5 kips (post-buckle) C) 110.2 (post-buckle) D) 152.8 (maximum load) E) 144.3 (post-failure). Load values expressed in terms of compressive load 108

3.55 Axial Strain measured in Machined Panel 4 from the VIC 3-D System in the lower half of the panel at A) 28.5 kips (pre-buckle) B) 62.2 kips (post-buckle) C) 110.5 (post-buckle) D) 175.5 (maximum load) E) 167.6 (post-failure). Load values expressed in terms of compressive load 109

3.56 Axial Strain measured in EBF^3 Panel 3 from the VIC 3-D System in the lower half of the panel at A) 39.3 kips (pre-buckle) B) 113.9 kips (post-buckle) C) 150.8 (post-buckle) D) 176.4 (maximum load) E) 170.7 (post-failure). Load values expressed in terms of compressive load 110

3.57 Axial Strain measured in EBF^3 Panel 4 from the VIC 3-D System in the lower half of the panel at A) 42.1 kips (pre-buckle) B) 112.7 kips (post-buckle) C) 152.1 (post-buckle) D) 172.6 (maximum load) E) 169.9 (post-failure). Load values expressed in terms of compressive load 111

5.1 The Finite Element Model for the Machined Panels under Load Case 1 136

5.2 Isometric view of First Buckling Mode Shape from the Finite Element Analysis for the Machined Panels under Load Case 1 139

5.3 Top view of First Buckling Mode Shape from the Finite Element Analysis for the Machined Panels under Load Case 1 140

5.4 Isometric view of Second Buckling Mode Shape from the Finite Element Analysis for the Machined Panels under Load Case 1 141

5.5 Top view of Second Buckling Mode Shape from the Finite Element Analysis for the Machined Panels under Load Case 1 . . 142

5.6 Isometric view of First Buckling Mode Shape from the Finite Element Analysis for the EBF^3 Panels under Load Case 1 . . 143

5.7 Top view of First Buckling Mode Shape from the Finite Element Analysis for the EBF^3 Panels under Load Case 1 144

5.8 Isometric view of Second Buckling Mode Shape from the Finite Element Analysis for the EBF^3 Panels under Load Case 1 . . 145

5.9 Top view of Second Buckling Mode Shape from the Finite Element Analysis for the EBF^3 Panels under Load Case 1 146

5.10 Linear Finite Element Analysis Results and Experimental Results of Strain Gages 5b-8b for Machined Panel 1 148
5.11 Linear Finite Element Analysis Results and Experimental Results of Strain Gages 5b-8b for EBF^3 Panel 1 149
5.12 Linear Finite Element Analysis Results and Experimental Results of DCDTs 1, 2 and 3 for Machined Panel 1 150
5.13 Linear Finite Element Analysis Results and Experimental Results of DCDTs 1, 2 and 3 for EBF^3 Panel 1 151
5.14 Nonlinear Finite Element Analysis Results and Experimental Results of Strain Gages 3a-4a for Machined Panels 1 and 2 . . 153
5.15 Nonlinear Finite Element Analysis Results and Experimental Results of Strain Gages 3a-4a for EBF^3 Panels 1 and 2 154
5.16 Nonlinear Finite Element Analysis Results and Experimental Results of Strain Gages 3b-4b for Machined Panels 1 and 2 . . 155
5.17 Nonlinear Finite Element Analysis Results and Experimental Results of Strain Gages 3b-4b for EBF^3 Panels 1 and 2 156
5.18 Isometric view of First Buckling Mode Shape from the Finite Element Analysis for the Machined Panels under Load Case 2 160
5.19 Top view of First Buckling Mode Shape from the Finite Element Analysis for the Machined Panels under Load Case 2 161
5.20 Isometric view of Second Buckling Mode Shape from the Finite Element Analysis for the Machined Panels under Load Case 2 162

5.21 Top view of Second Buckling Mode Shape from the Finite Element Analysis for the Machined Panels under Load Case 2 . . 163
5.22 Isometric view of First Buckling Mode Shape from the Finite Element Analysis for the EBF^3 Panels under Load Case 2 . . 164
5.23 Top view of First Buckling Mode Shape from the Finite Element Analysis for the EBF^3 Panels under Load Case 2 165
5.24 Isometric view of Second Buckling Mode Shape from the Finite Element Analysis for the EBF^3 Panels under Load Case 2 . . 166
5.25 Top view of Second Buckling Mode Shape from the Finite Element Analysis for the EBF^3 Panels under Load Case 2 167
5.26 Linear Finite Element Analysis Results and Experimental Results of Strain Gages 5b-8b for Machined Panel 3 169
5.27 Linear Finite Element Analysis Results and Experimental Results of Strain Gages 5b-8b for EBF^3 Panel 3 170
5.28 Linear Finite Element Analysis Results and Experimental Results of DCDTs 1, 2 and 3 for Machined Panel 3 171
5.29 Linear Finite Element Analysis Results and Experimental Results of DCDTs 1, 2 and 3 for EBF^3 Panel 3 172
5.30 Nonlinear Finite Element Analysis Results and Experimental Results of Strain Gages 3a-4a for Machined Panels 3 and 4 . . 174
5.31 Nonlinear Finite Element Analysis Results and Experimental Results of Strain Gages 3a-4a for EBF^3 Panel 3 175

5.32 Nonlinear Finite Element Analysis Results and Experimental Results of Strain Gages 3b-4b for Machined Panels 3 and 4 . . 176
5.33 Nonlinear Finite Element Analysis Results and Experimental Results of Strain Gages 3b-4b for EBF^3 Panel 3 177

A.1 Strain measured from Strain Gages 1c-6c for Machined Panel 1 194
A.2 Axial Strain measured from Strain Gages 9a and 11a-15a for Machined Panel 1 195
A.3 Lateral Strain measured from Strain Gages 9b, 11b, 13b, and 15b for Machined Panel 1 196
A.4 Strain in the stiffeners measured from Strain Gages 17-24 for Machined Panel 1 197
A.5 Out-of-plane Displacement measured in Machined Panel 1 from the VIC 3-D System in the lower half of the panel at A) 28.6 kips (prebuckle) B) 46.2 kips (postbuckle) C) 80.6 (postbuckle) D) 150.8 (maximum load) E) 156.8 (post-failure). Load values expressed in terms of compressive load 198
A.6 Axial Strain measured in Machined Panel 1 from the VIC 3-D System in the lower half of the panel at A) 28.6 kips (prebuckle) B) 46.2 kips (postbuckle) C) 80.6 (postbuckle) D) 150.8 (maximum load) E) 156.8 (post-failure). Load values expressed in terms of compressive load 199
A.7 Strain measured from Strain Gages 1c-6c for Machined Panel 2 200

A.8 Axial Strain measured from Strain Gages 9a and 11a-15a for Machined Panel 2 201
A.9 Lateral Strain measured from Strain Gages 9b, 11b, 13b, and 15b for Machined Panel 2 202
A.10 Strain in the stiffeners measured from Strain Gages 17-24 for Machined Panel 2 203
A.11 Strain measured from Strain Gages 1c-6c for EBF3 Panel 1 . . 204
A.12 Strain measured from Strain Gages 9a-16a for EBF3 Panel 1 . 205
A.13 Lateral Strain measured from Strain Gages 9b-16b for EBF3 Panel 1 206
A.14 Axial Strain measured in EBF^3 Panel 1 from the VIC 3-D System in the lower half of the panel at A) 35.1 kips (prebuckle) B) 83.5 kips (postbuckle) C) 135.1 (postbuckle) D) 179.1 (maximum load) E) 160.2 (post-failure). Load values expressed in terms of compressive load 207
A.15 Strain measured from Strain Gages 1c-4c for EBF3 Panel 2 . . 208
A.16 Strain measured from Strain Gages 9a-16a for EBF3 Panel 2 . 209
A.17 Lateral Strain measured from Strain Gages 9b-16b for EBF3 Panel 2 210

B.1 Strain measured from Strain Gages 1c, 3c, and 4c for Machined Panel 3 212
B.2 Axial Strain measured from Strain Gages 9a and 11a-15a for Machined Panel 3 213

B.3 Lateral Strain measured from Strain Gages 9b and 11b-15b for Machined Panel 3 214
B.4 Strain measured from Strain Gages 1c-4c for Machined Panel 4 215
B.5 Axial Strain measured from Strain Gages 9a and 11a-15a for Machined Panel 4 216
B.6 Lateral Strain measured from Strain Gages 9b and 11b-15b for Machined Panel 4 217
B.7 Strain measured from Strain Gages 1c-4c for EBF3 Panel 3 . . 218
B.8 Strain measured from Strain Gages 9a-15a for EBF3 Panel 3 . 219
B.9 Lateral Strain measured from Strain Gages 9b-14b for EBF3 Panel 3 220

C.1 Linear Finite Element Analysis Results and Experimental Results of DCDTs 4, 5, and 6 for Machined Panel 1 222
C.2 Linear Finite Element Analysis Results and Experimental Results of DCDTs 5, 6, and 6 for EBF^3 Panel 1 223
C.3 Linear Finite Element Analysis Results and Experimental Results of Strain Gages 1a-4a for Machined Panel 1 224
C.4 Linear Finite Element Analysis Results and Experimental Results of Strain Gages 1a-4a for EBF^3 Panel 1 225
C.5 Linear Finite Element Analysis Results and Experimental Results of Strain Gages 1b-4b for Machined Panel 1 226
C.6 Linear Finite Element Analysis Results and Experimental Results of Strain Gages 1b-4b for EBF^3 Panel 1 227

C.7 Linear Finite Element Analysis Results and Experimental Results of Strain Gages 5a-8a for Machined Panel 1 228
C.8 Linear Finite Element Analysis Results and Experimental Results of Strain Gages 5a-8a for EBF^3 Panel 1 229
C.9 Linear Finite Element Analysis Results and Experimental Results of Strain Gages 25a-28a for Machined Panel 1 230
C.10 Linear Finite Element Analysis Results and Experimental Results of Strain Gages 25a-28a for EBF^3 Panel 1 231

D.1 Linear Finite Element Analysis Results and Experimental Results of DCDTs 4, 5, and 6 for Machined Panel 3 233
D.2 Linear Finite Element Analysis Results and Experimental Results of DCDTs 4, 5, and 6 for EBF^3 Panel 3 234
D.3 Linear Finite Element Analysis Results and Experimental Results of Strain Gages 1a-4a for Machined Panel 3 235
D.4 Linear Finite Element Analysis Results and Experimental Results of Strain Gages 1a-4a for EBF^3 Panel 3 236
D.5 Linear Finite Element Analysis Results and Experimental Results of Strain Gages 1b-4b for Machined Panel 3 237
D.6 Linear Finite Element Analysis Results and Experimental Results of Strain Gages 1b-4b for EBF^3 Panel 3 238
D.7 Linear Finite Element Analysis Results and Experimental Results of Strain Gages 5a-8a for Machined Panel 3 239

D.8 Linear Finite Element Analysis Results and Experimental Results of Strain Gages 5a-8a for EBF^3 Panel 3 240
D.9 Linear Finite Element Analysis Results and Experimental Results of Strain Gages 25a-28a for Machined Panel 3 241
D.10 Linear Finite Element Analysis Results and Experimental Results of Strain Gages 25a-28a for EBF^3 Panel 3 242

E.1 Full Newton-Raphson versus Modified Newton-Raphson[25] . . 250

List of Tables

3.1 End-shortening Results for Load Case 1 37
3.2 Lateral Displacement Results for Load Case 1 40
3.3 End-shortening Results for Load Case 2 74
3.4 Lateral Displacement Results for Load Case 2 75

5.1 Comparison of Finite Element Analysis (FEA) and Experimental Buckling Loads for Load Case 1 138
5.2 Comparison of Finite Element Analysis (FEA) and Experimental Buckling Results for Load Case 2 160

Chapter 1

Introduction

Aeronautical engineering comprises many areas; the dominant ones are: aerodynamics, propulsion, avionics, airframe such as hydraulics and electrical systems, and lastly aerostructures. All these areas have developed at their own rates for nearly a century, and with the subsequent addition of spacecraft, aeronautical engineering transformed into aerospace engineering. The field of aerostructures has grown tremendously from the days of the Wright brothers and wooden structures with wire bracing [1].

The function of aircraft structures is to conform to contour, shape, and clearance requirements while supporting aerodynamic loads. Normally, these loads consist of a normal pressure and bending (from wing or fuselage), leading to axial stresses and overall torsion which causes shear in the skin. The main goal of furthering the capabilities of aerostructures is to make the structure stiffer, stronger, and lighter. The material selection and the kind of structure including the shape and manufacturing method greatly influence the strength

and weight of an airframe [2].

There are many materials used in airframes. The metals predominantly used are steel, aluminum alloys, and titanium. Steel is very strong, however very heavy. As a result, steel is only used in sections where its high strength is needed, such as in the landing gear. Aluminum alloys, conversely, are one of the most widely used materials in aircraft structures. Aluminum alloys have a reasonable cost, an excellent strength-to-weight ratio, are easy to machine, and are lightweight, which contribute to their wide use. Titanium has a superior strength-to-weight ratio compared to aluminum alloys and also retains its strength at higher temperatures. However, it can be hard to machine and is more costly than aluminum alloys. Titanium is predominantly used in supersonic aircraft due to its ability to retain its strength in high temperatures, seen at speeds above Mach 2.4 and on high-performance aircraft where large loads are induced into the structure due to the plane's maneuvers [3].

Besides metals, composites have made a recent significant impact as an aircraft material. The definition of a "composite material" simple means two or more materials combined together on a macroscopic scale to make a more useful material. While any material could be used to make a composite structure, in reference to aircraft structures, graphite/epoxy composites are typically used [4]. Composites have the ability to carry higher loads with a reduction in weight when compared with metals. Composites do have limitations however. Composites have no real plastic range, thus, there is little warning before a composite structure fails. Also, composites are generally

orthotropic instead of metals which are isotropic. This could result in a composite structure failing at a low load if the structure is loaded in a direction it is not designed to receive load [3].

Aircrafts are comprised of mostly large panels. The fuselage consists of large curved panels and the wings contain a number of large semi-flat panels. To reduce the weight but increase the strength of a panel, a stiffener can be added to the structure. Stiffeners allow the combined structure to carry higher loads than just a column or a plate individually. The addition of a stiffener can be used to increase the buckling stress, sustain a part of the load, or a combination of both [2].

Common methods used for joining a stiffener to a skin are the use of fasteners and welding. Fasteners, such as rivets or bolts, have been one of the primary methods for building any metallic structure. Fasteners are relatively easy to design with and use and, for example, can be used to attach a stiffener to a plate which could offer the needed structural rigidity [1]. Welding can replace rivets or bolts with a weld. The extra parts (i.e., bolts and rivets) are eliminated, and consequently so are the corresponding holes that are stress concentration sites and can lead to crack initiation and growth [5].

Sometimes the advances in a field are related to the manufacturing techniques available. The combination of skin/stiffeners has been an established design element of both airframes and spacecraft. Attaching a stiffener to the skin of an aircraft via mechanical fasteners is easy and the technology has been developed, understood, and used since the 1940's. To reduce cost

or weight, a significant deviation from these conventional fastener practices is necessary. Methods like friction stir welding and mechanical fasteners have a limit in the reduction of weight due to the number of bolts or rivets and extra flange material needed for joining. In addition to the added weight, there is an extra cost for the material and labor in joining the pieces [6]. Developing unitized structures has increased the potential of skin/stiffener combination to be stronger, lighter, cheaper, and more beneficial to the manufacturers, and is a positive way to deviate from the conventional design practices [7].

1.1 Unitized Structures

Unitized structures refer to structures made of one solid piece, in the past they have been referred to as integrally stiffened structures. In a unitized stiffened structure, the stiffener is not fabricated separately and attached to the plate but rather fabricated as a single a piece with the plate. An example of two non-unitized structures joined by conventional methods and a unitized structure is shown in Figure 1.1.

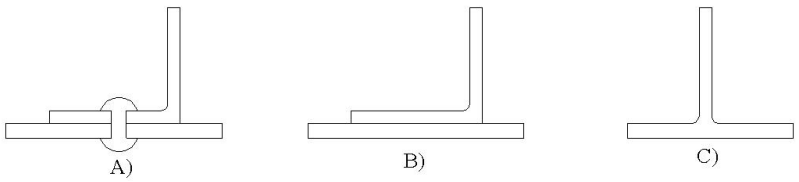

Figure 1.1: A) Non-unitized riveted structure, B) Non-unitized bonded structure, C) Unitized structure

With regards to aircraft manufacturing, unitized stiffened structures offer many advantages over traditional manufacturing techniques [8]:

- An improvement of performance and nonbuckling characteristics through smoother exterior surfaces of the skin caused by the reduced number of attachments
- A reduction in the amount of sealant needed in pressurized fuel tank structures
- A removal of possible locations that initiate corrosion
- A reduction in weight
- An elimination of holes

A group of researchers at Virginia Polytechnic Institute and State University are exploring the structural capabilities of unitized structures. A computer code has been developed that is capable of optimizing the placement of straight stiffeners on a panel. The first approach looked only at blade stiffeners. The end placements of the stiffeners were specified as discrete points along the border of the panel. The program then cycled through every possible placement of the stiffener to insure a global minimum was found. While this method is effective, it quickly becomes extremely computationally and time intensive as more stiffeners and end points are added [9]. A group of researchers from the University of Oslo in Norway have developed a semi-analytical postbuckling and strength analysis of arbitrarily stiffened plates like the panels

developed by Mulani, et al. This study reduced the computational time significantly by ignoring the nonlinear part of the Airy's stress function. This reduced the computation time significantly with little impact on the accuracy of the results [10].

Further work focused on how the placement of blade stiffeners can influence the weight of the panel. The weight of every panel was optimized to its lowest value with constraints on the Eigen-value buckling load, von-Mises stress, and geometric variables in the problem [11]. The research showed how the orientation of the stiffeners can drastically affect the design. Only blade stiffeners were considered because of the simplicity of the design. When the stiffeners were placed on the panel loaded in pure shear, the weight of the panel could be reduced in half. The effects of the stiffeners' spacing were also considered. It was shown that if the space between stiffeners is too large, the panel resembles an unstiffened panel, offering little structural advantage. Conversely, if the stiffener spacing is too small, the plate is equivalent to an unstiffened plate with an increased thickness. The effects of the location on the stiffener were also found to have an impact on the weight of the structure. Poor placement of the stiffeners results in added weight with little structural advantage [12, 11].

The previous methods used for optimizing a stiffened plate were extremely computationally and time intensive. For this reason Joshi, et al. [13] further developed the code to include surrogate modeling on blade stiffeners. Surrogate models are approximations to computationally expensive models.

The developed surrogate model optimizes the design to within 1% of the mass of the panel obtained by the previous finite element models but was not nearly as computationally expensive. As a result, the optimization for the placement of blade stiffeners could be feasible for use in industry [13].

1.2 Solid Freeform Fabrication

Techniques such as rapid prototyping or solid freeform fabrication (SFF) provide an opportunity for fabricating complex unitized structures. These techniques use additive manufacturing instead of subtractive or forming processes (additive manufacturing techniques allow the user to build structures layer by layer). As a result, complicated designs can be manufactured easily or structures that previously needed to be joined can be built as a single piece [14]. Because of the advantages of these processes, a new level of design flexibility and efficiency is achievable [7].

There are several SFF processes that have been developed in the past several years, one of which is Selective Laser Sintering. In this method, a high power laser is rastered over a layer of powder, melting it and creating a thin solid layer. A new layer of powder is spread on top and the process continually repeats, building the structure one layer at a time. Laser Additive Manufacturing, Laser Engineered Net Shaping, Direct Metal Deposition, and Direct Layer Powder Deposition are SFF methods that utilize a laser and material powders to create parts one layer at a time, however, the powder is fed directly into a molten pool created by the laser. The powder then solidifies

creating a layer of the structure [15].

Electron Beam Freeform Fabrication (EBF^3) is similar to direct layer powder deposition except an electron beam is used, and in the place of powder, a solid wire is fed into the molten pool [16]. There are many different SFF techniques and an overview can be found in papers by Cooper [14], Sears [15], and Buswell, et al [17].

The problem with some of the current SFF techniques is that they are not suitable for aircraft manufacturing. Many powder manufacturing techniques have very low deposition rates, on the order of 3-20 in^3/hr, and small build areas that are a cube on the order of approximately 8-12 inches per a side. A low deposition rate and small build envelope are not cost-effective or practical when building large aircraft panels. In addition, the majority of SFF techniques and their processable material selection may not be suitable for some aircraft manufacturing. Some of the laser SFF techniques are not compatible with aircraft grade alloys of titanium or aluminum. Lastly, the quality of the build varies for different SFF techniques. Some techniques are not capable of depositing metals at full density, which could significantly impact the strength of a structure and requires an additional consolidation step, which adds time and cost [15]. EBF^3 is examined because of its ability to deposit aircraft grad alloys at high deposition rates and at full density.

1.3 Electron Beam Freeform Fabrication (EBF^3) Manufacturing Process

EBF^3 is a new manufacturing process being develop at NASA Langley. While many SFF methods use lasers which are unsuccessful in processing with highly reflective metallic materials, the electron beam in EBF^3 allows it to process many materials used in the aerospace field such as aluminum and titanium. In addition, EBF^3 is capable of a large build area and deposition rate of 150 in^3/hr in bulk deposition. Finer detail can be achieved at lower deposition rates. The EBF^3 process also deposits at the full density of the material [18].

The EBF^3 technique uses a focused electron beam to generate a molten pool on a metallic substrate. A metal wire is fed into the molten pool while the beam translates with respect to the base plate, thus allowing the user to build structures in a layer-additive fashion. An electron beam can be controlled and deflected very easily, creating a precise melt pool. A few trace elements are added to the wire feedstock to account for volitization during the deposition process, thus the material characteristics of the metal after deposition are very similar to that of the original metal [16, 18, 19]. Besides these few trace elements, the process is nearly 100% efficient in feedstock consumption and approaches 95% efficiency in power usage. The diameter of the wire is the main controlling factor in determining the resolution of the build. For example, larger diameter wire may be used to increase the amount of material deposited, while smaller diameter wire may be used to increase resolution on the build

[18]. The EBF^3 process is illustrated in Figure 1.2.

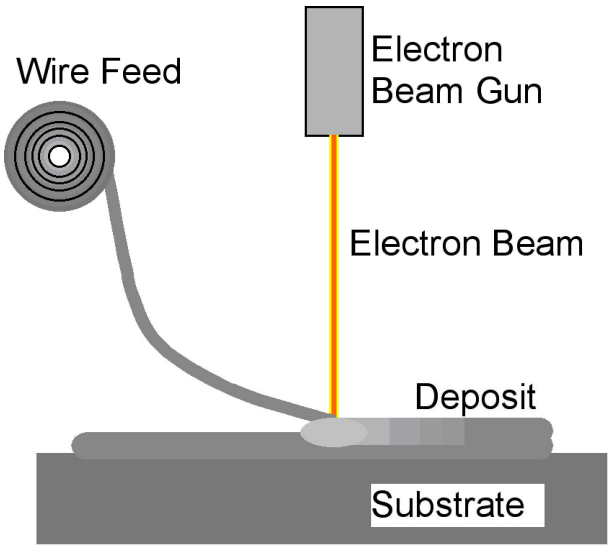

Figure 1.2: Illustration of the EBF^3 Process

Because of the electron beam, the process must take place in a vacuum on the order of 5×10^{-5} torr. If not, the beam would attenuate before reaching the base plate. Currently at NASA Langley Research Center, a steel chamber of 108 by 100 by 76 inches with a build envelope of 72 by 24 by 24 inches is used for manufacturing with EBF^3 [16]. The inside of the large EBF^3 machine and the different parts of the machine are shown in Figure 1.3. There is also a second smaller portable EBF^3 system with a chamber that is 38 inches^3 and a build envelope of 12 by 12 by 6 inches^3 [18].

While EBF^3 is a process for manufacturing unitized structures like stiffened panels on an airplane, it also has other uses. EBF^3 could be used

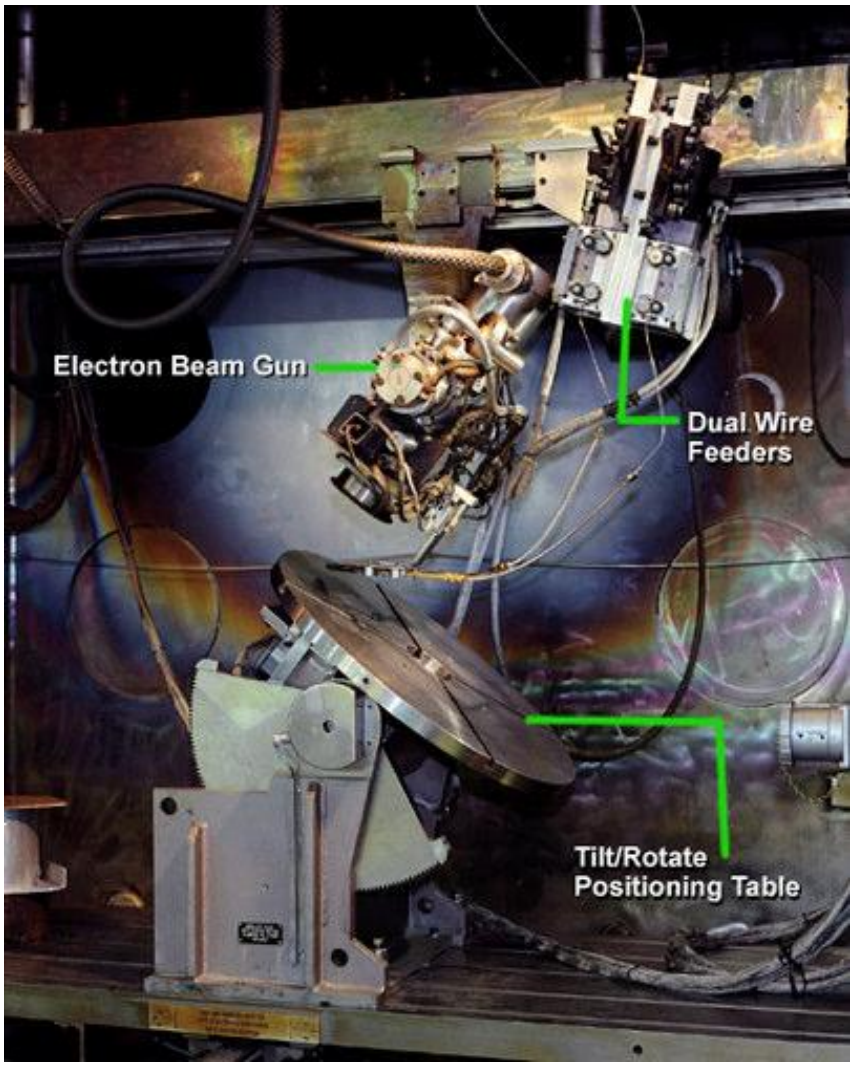

Figure 1.3: Inside View of the Large EBF^3 Machine[1][16]

as a way to manufacture in space, especially because of its ease of handling wire feedstock in zero-gravity, high feedstock consumption efficiency, and high power efficiency. It also could be used as a technique for repairing cracks or defects in metallic structures [16].

One challenge that has been identified with EBF^3 is the residual stress and distortion associated with the localized melting. The molten pool is at a very high temperature and the material around the molten pool is considerably cooler. This temperature gradient results in residual stresses in the component and an associated distortion [18].

1.4 Previous EBF^3 Structural Panel Studies

In reports by Brickler [20] and Nelson, et al. [21], single blade stiffened panels were made by four different manufacturing techniques. A panel with the stiffener made from EBF^3 was compared to panels with a stiffener integrally machined from a thick plate, riveted on to the base plate, or friction stir welded on to the base plate. All plates were loaded in uniaxial compression until failure. The panels were designed with a single blade stiffener because of its ease to manufacture and model. The plates were 24 by 10 inches with a thickness of 0.190 inches. The blade stiffeners were 0.75 by 0.15 inch running the length of the panel.

The integrally machined plate was machined from a 1 inch thick plate of aluminum 2219 in the T851 condition. The EBF^3 panels were fabricated using

[1]Used with permission from NASA Langley Research Center, Hampton, Virginia

aluminum 2219 in the T851 temper. Aluminum 2219 in the T851 condition was used for the base plate of the riveted and FSW panels. Aluminum 2024 in the T851 condition was used for the stiffener for both the riveted and FSW panels and aluminum 2117 in the T4 condition was used for the rivets in the riveted panels.

The study showed that the integrally machined panel performed the best. All machined panels withstood a higher load before exhibiting geometric or material nonlinear effects when compared to the other three manufacturing techniques. This was expected from the results, since the machined panel did not have any residual stress or distortion from welding like the friction stir welded or EBF^3 panels, nor did the machined panel have holes drilled in the panel for the placement of rivets. The integrally machined panel had minimal effects of distortion and residual stresses [20, 21].

The riveted and friction stir welded panels both had an extra flange on the stiffener that the machined and EBF^3 panels did not. The extra flange was required for these processes for the joining of the stiffener to the plate. As a result, the riveted and friction stir welded panels behaved similarly. Both riveted and friction stir welded panels showed nonlinear effects around the same load and also had similar strains for a given load [20, 21].

The EBF^3 panels on average had a 16% lower maximum load than the other manufacturing techniques. EBF^3 panels A and B exhibited nonlinear effects early on in the compression tests due to irregularities in their build and the distortion caused during fabrication. EBF^3 Panel A buckled in the

opposite direction of the other panels, due to larger residual distortion from the deposition process than the other EBF^3 panels. EBF^3 Panel B had a flaw in the stiffener from manufacturing, which contributed to its poor performance. EBF^3 Panel C was the only panel to behave similarly to those produced using the other techniques, however, it still exhibited nonlinear effects at a lower load than the other manufacturing techniques [20, 21].

Ultimately, it was shown that the EBF^3 technique produced promising results as a viable manufacturing procedure, however, the technique needs to be refined to produce fewer flaws in the builds. Also, the residual stress and initial distortion of the welding process in EBF^3 needs to be minimized as the residual stress and distortion had a significant impact on the structural performance [20, 21].

1.5 Nonlinear Structural Response

The distortion and residual stresses in the panels from previous EBF^3 studies supports the need for geometric and material nonlinear analysis. Linear analysis of a structure can be used to show a good initial correlation with experimental results, but is only accurate up to a certain load or deformation. Nonlinear analysis is useful in analyzing the structure after the material begins to yield or the structure begins to buckle. Also, nonlinear analysis can be useful for structures made from EBF^3 because of the initial distortion, which can result in nonlinear behavior at lower loads than structures without initial distortion [22].

Nonlinearities occur in many different forms in structural mechanics. The simplified Hooke's law for the stress-strain relation can be invalid if the material stress-strain relationship is nonlinear. A nonlinearity of this nature is referred to as material nonlinearity. Nonlinearity can also occur when a structure has large deformations. This is referred to as geometric nonlinearity. A combination of material and geometric nonlinearities is also possible in structures. Certain boundary conditions also require nonlinear analysis. Boundary conditions such as nonlinear springs or gaps in the structure are nonlinear [23]. Nonlinear boundary conditions are not a part of this research. A review of material and geometric nonlinearities can be found in Appendix E.

Besides being computationally expensive, nonlinear analysis has other consequences. The principle of superposition cannot be utilized. That is, the loads applied in a problem cannot be scaled, factored, and combined as with linear analysis. Only one nonlinear load case can be used in the calculations at a time. Also, the order of the applied loads can be important to the problem. For example, a structure loaded in compression with an applied external pressure is not the same as being loaded from an external pressure then in compression. Lastly, the initial stress of the structure could be important, depending on its location and magnitude. As a result, the effects from welding on a structure could influence the experiment and might need to be considered for nonlinear analysis [22].

1.5.1 Nonlinear Finite Element in NASTRAN

NASTRAN, a finite element computer program, assumes the same Newton-Raphson incremental/iterative approach discussed in Appendix E. NASTRAN allows the user to customize many different aspects of the nonlinear analysis depending on the problem. The three main areas to customize are: advancing forward on the equilibrium path, estimating the tangent stiffness matrix, and the convergence criteria [24].

There are three schemes to choose from in deciding how to advance on the equilibrium path. The easiest and simplest is to specify a constant load increment. Like in the Newton-Raphson method, each increment is specified by a change in load. Another advancing scheme on the equilibrium path is specifying the increase in displacement. The user must specify a change in displacement for certain degrees of freedom. In order to specify the displacement, a basic understanding of the problem is needed to avoid an inconsistent displacement increment. The value of the displacement is measured from the undeformed state. This method is more complicated than the load increment method and may require tighter tolerances than the default convergence criteria. The last method is the Arc Length Increment method. In this method, the increments are specified on the load-displacement curve in terms of an arc. This method has the ability to follow the equilibrium path in an unstable region where the load increments can be negative, such as in a snap-through problem. The Arc Length Increment method requires that its use occurs in combination with the load increment. This method has a significant number

of advantages and allows the user more options to customize the incremental method on the equilibrium curve. It is, however, more complicated to program and requires a greater understanding of the problem [24].

At every increment on the equilibrium path a calculation of the stiffness matrix needs to be performed. NASTRAN allows users to customize how the stiffness matrix is updated. The stiffness matrix can be updated after every iteration as seen in the full Newton-Raphson method [24]. This is the most robust method but also requires the most computation time [25]. The stiffness matrix could be updated every k-th iteration, where k is some specified number. This is similar to the modified Newton-Raphson method in that the stiffness matrix is not calculated at every iteration [24]. Again this saves on computational time but could cause the answer to diverge if large displacements are seen during the increment [25]. Lastly, a Quasi-Newton stiffness update can be utilized [24]. A Quasi-Newton method does not reform the stiffness matrix at every iteration, instead, the stiffness matrix is altered to approximate the true stiffness matrix [26].

Lastly, a convergence criteria needs to be specified. The convergence criteria should be dimensionless and independent of the structural characteristics. The convergence criteria should also be applicable to all load cases and have smooth transitions after the stiffness matrix update and loading changes. The three convergence criteria that can be specified are the load, work, and displacement. NASTRAN sets the displacement and load tolerances at 1×10^{-3} and the work tolerance at 1×10^{-7}. The tolerances should not be large enough

that the analysis causes inaccuracies, but also should not be small enough to waste computational time [24].

1.6 Goal

A paper by Pettit et al. [6] has shown that there is a benefit to unitized structures in aircraft manufacturing. The goal of this research is to look at the potential benefits of EBF^3 as a unitized structure manufacturing technique. EBF^3 was chosen because of the ability to build panels large enough for aircraft manufacturing with materials used in aircrafts today.

Integrally machined panels were chosen as a conventional manufacturing method as a baseline for comparison with EBF^3. Four integrally machined and four EBF^3 stiffened plates were manufactured and tested under combined compression and shear loading conditions at NASA Langley Research Center. Each set of panels were tested under two different load cases. A finite element eigenvalue buckling analysis, linear analysis, and nonlinear analysis were performed to compare with the experimental results.

1.7 Organization of Thesis

Chapter 2 explains the design of the panels, the test machine, and the equipment used to record the data. Chapter 3 presents the results from the experiments. Chapter 4 discusses the results from both load cases. For each load case, the machined panel response is discussed and then the EBF^3 panels are

compared to the machined panels' responses. Lastly, load case 1 and 2 are compared to each other. Chapter 5 explains the finite element model used. Chapter 5 then presents and discusses the finite element results compared to the experimental results. The remaining results collected but not discussed are found in Appendix A for load case 1 and Appendix B for load case 2. The remaining results from the finite element results that were not discussed are found in Appendix C for load case 1 and Appendix D for load case 2. Lastly, Appendix E contains a review of material and geometric nonlinearities and a brief overview of solving nonlinear equations.

Chapter 2

Experimental Setup

2.1 Test Machine

All tests were conducted in a compression-shear combined loads test fixture. The fixture was used in NASA Langley's 300 kip compression machine. An illustration of the fixture is found in Figure 2.1. The test fixture was capable of handling 24 by 28 inch test specimens. The compression loading was parallel to the 24 inch side. The test specimen was secured in an eight-piece test frame with pins in the corners to allow for rotation due to the shear loading. A panel in the test frame is shown in Figure 2.2. The test frame was bolted to two "L" brackets. The shear load was introduced by a hydraulic actuator through a self-reacting load mechanism acting on the "L" brackets. The top "L" bracket was bolted to the machine while the lower "L" bracket rested on rollers, allowing the shear load to be applied under compression. The shear load caused the frame to transform from a rectangle to a parallelogram,

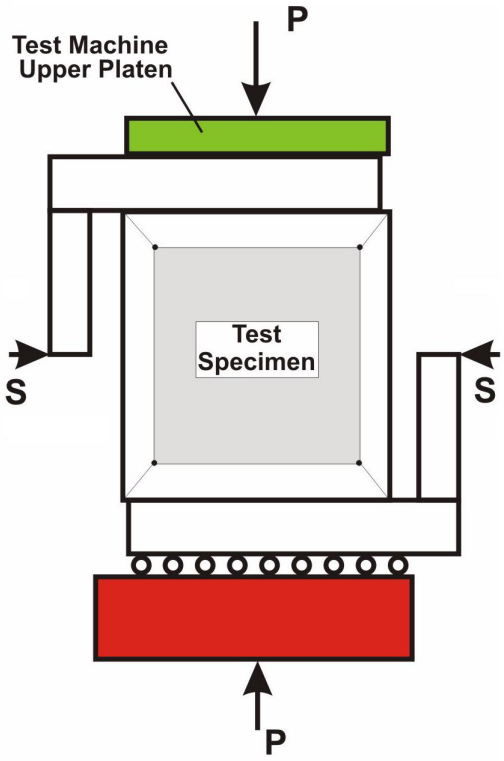

Figure 2.1: Illustration of the Compression-Shear Combined Loads Test Fixture. P is the compressive load, S is the shear load [27].

and thus introduced shear into the test specimen. The compressive load was controlled by the displacement of the load platen on the machine. The test frame was slotted in the direction of the compressive load to allow the load to transfer directly into the specimen and not the frame.

The frame was designed to test a specimen with a minimum or maximum thickness between 0.250 and 0.530 inches respectively. The load was introduced through the eighty bolts used to attach the frame to the specimen. The test frame was not manufactured to the specified tolerances. As a result, the eighty holes positioned around the test frame were not in the precise lo-

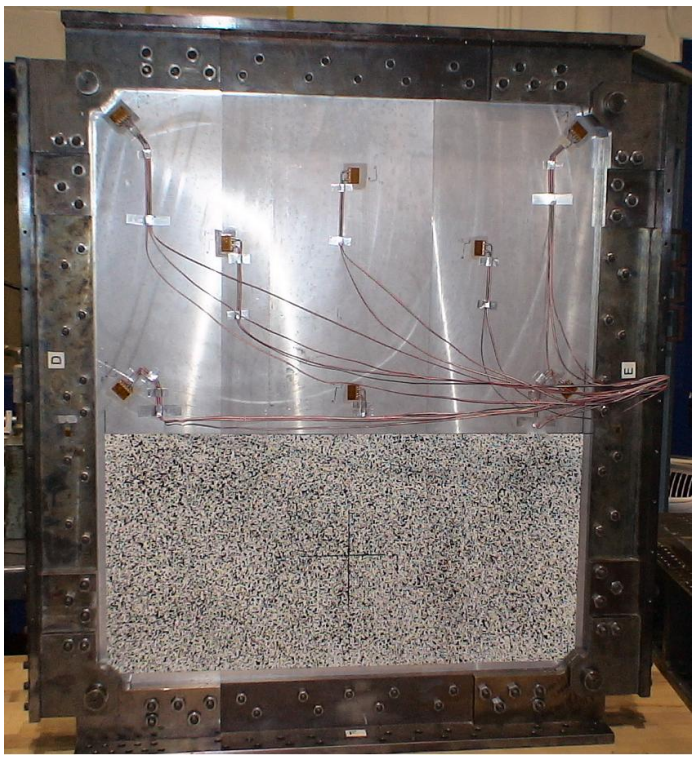

Figure 2.2: Specimen in Compression-Shear Frame[2]

cations in the design drawings. This created problems in manufacturing the panels. The fixture assembled with a specimen in place is shown in Figure 2.3 [27].

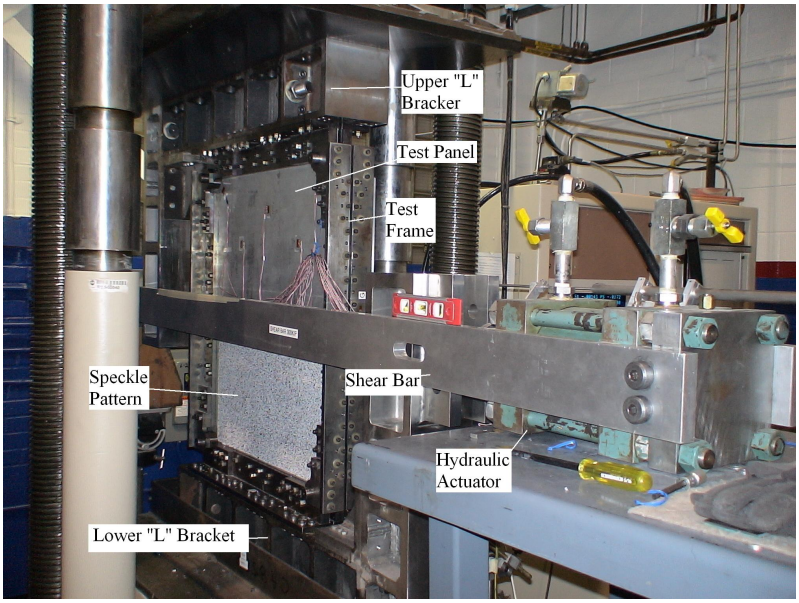

Figure 2.3: Combined Loads Compression-Shear Test Fixture[3]

2.2 Panel Design

The test panels were sized to meet the constraints of the test fixture. The panels had a thickness of 0.250 inches. This was based on the minimum thickness the test frame can support and the stock material available to manufacture the EBF^3 panels. Each panel had a 24 by 28 inch test section with two straight blade stiffeners spaced 8 inches apart. Blade stiffeners were chosen because of

[2]Property of the author, photographed May 2008
[3]Property of the author, photographed May 2008

their ease to manufacture and model. The stiffeners were 27 inches long with 30 degree run-outs at both ends. The stiffeners had to be shorter than the full length of the test section to avoid making contact with the test frame once the panels deformed from the compressive force. The stiffeners were 0.150 inches thick and 0.750 inches high. The stiffeners width was chosen based on previous EBF^3 studies. The stiffener height was chosen based on the 1 inch thick material available for the integrally machined panels and the 0.25 inch minimum thickness constraint for the test frame. The panels also had the necessary tabs on all sides of the test section to allow the panels to be attached to the test frame.

2.2.1 Machined Panel

The integrally machined panels were made from a 1 inch thick stock plate of aluminum 2219 in the T851 condition. The panels were machined to the specified dimensions shown in Figure 2.4. The stiffeners were built parallel to the rolling direction of the plate of aluminum.

The initial holes drilled in the machined panels did not line up with the location of the holes on the test frame. As a result, the eighty holes in the specimens had to have the diameter increased by an extra 0.03125 inches which allowed the bolts to attach the frame to the panels.

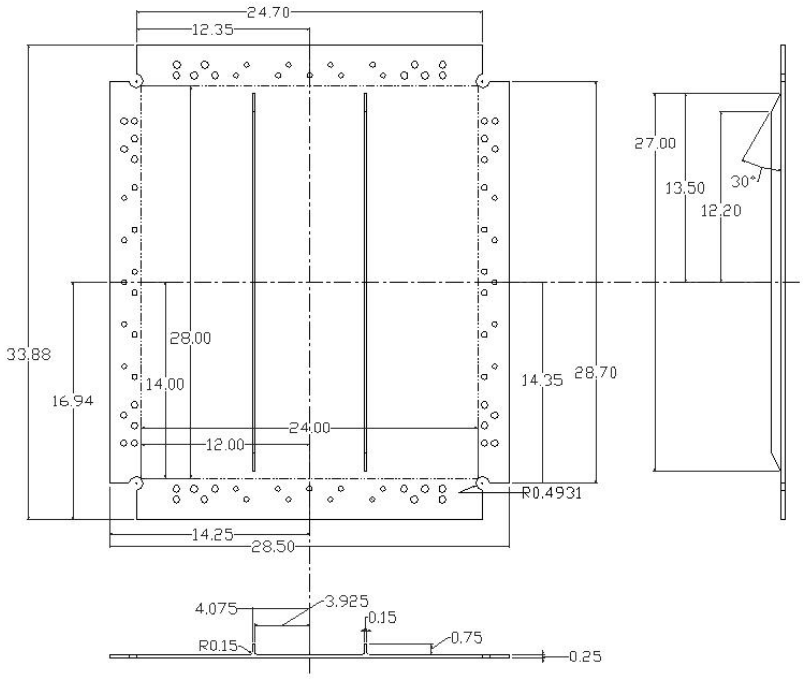

Figure 2.4: Design of Stiffened Panels

2.2.2 EBF^3 Panel

The EBF^3 panels were deposited on 0.250 inch thick aluminum 2219 in the T851 condition. The plates were water-jet cut to the panel shape for the base plate. The stiffeners were then deposited on the base plates.

The stiffeners were oversized in length when deposited which accounted for any errors in the starting and stopping of the deposition process.

This allowed for minor machining to be performed to the stiffeners to achieve final tolerances equivalent to those of the integrally machined panels. Unknown at the time of fabrication of the EBF^3 panels, the molten pool shifted mid-way through the deposition. The stiffeners made by the EBF^3

process were between 0.18 and 0.20 inches wide after deposition. However, the pool shifted approximately 0.04 inches off the centerline while cooling. As a result, the deposits did not attain the full 0.15 inch target width, which resulted in voids of material in the stiffeners after machining. An example of the defects found on the stiffeners is shown in Figure 2.5. The defects were typically less than 0.01 inches deep.

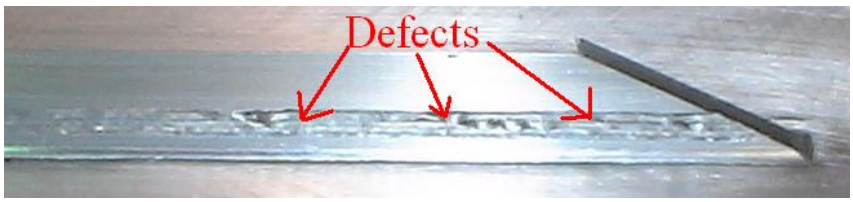

Figure 2.5: Example of Defects found on the EBF^3 Panel Stiffeners[4]

After deposition, the stiffeners were in the annealed condition. The stiffeners were built in the rolling direction of the plate of aluminum and then bump-formed in the direction of the stiffeners, thereby reducing some of the distortion from the deposition process. Bump-forming is the process of bending a plate via a hydraulic press to a more flat condition. The process can remove some of the initial distortion in the panels but not all. The panels could not be bump-formed in the direction perpendicular to the stiffeners without the hydraulic press crushing the stiffeners. The shape of EBF^3 Panel 3 after bump-forming as measured by a Coordinate Measurement Machine is shown in Figure 2.6 [28]. All EBF^3 panels had a similar shape to EBF^3 Panel 3. Even after the panels were bump-formed, a slight distortion of the panels was still observable. Once the panels were clamped into the test frame, the distortion

[4]Property of the author, photographed May 2008

around the edges was mechanically constrained flat, however the distortion in the middle of the panels remained.

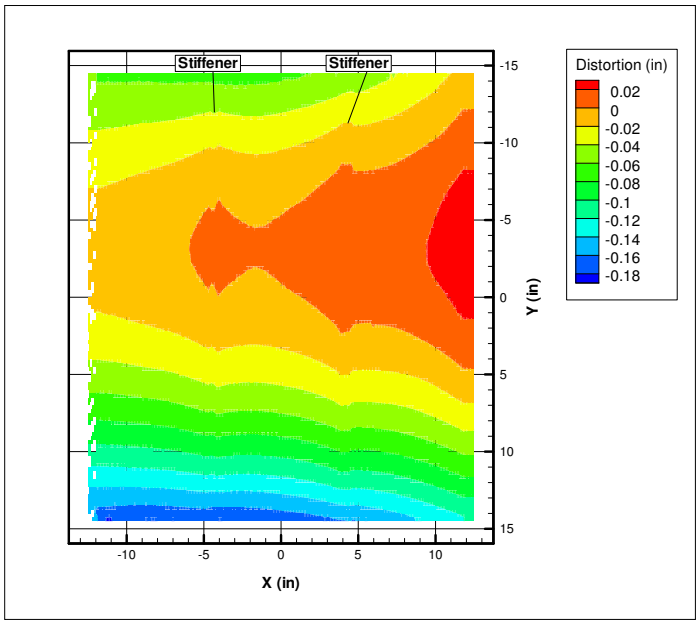

Figure 2.6: Distortion in EBF^3 Panel 3 after bump-forming

After bump-forming, the panels were heat treated at 375^0F for 36 hours and machined to the dimensions shown in Figure 2.4. In the as-deposited state of the panels, the stiffeners and base plates were at two different tempers. To try to bring the EBF^3 panels to a more uniform temper, the panels were heated at 375^0F for 36 hours. This brought the stiffeners to a heat treatment roughly equivalent to a T6 condition, and the base plates to an over-aged condition. However, the exact effect on the whole specimens was unknown. For modeling purposes, the specimens were assumed to be in the T6 condition [29].

The EBF^3 panels' holes were matched directly to the frame so no further widening of the holes was performed to allow the frame to be attached to the panels.

2.3 Data Acquisition

2.3.1 Strain Gages

A total of twenty-eight strain gages were used to measure strain around the specimen. The locations of the strain gages are shown in Figure 2.7. Eight three-element 45° rosettes were used on the base plates, labeled as strain gages 1-8 in Figure 2.7. Twelve two-element tee rosettes were used on the base plates and the stiffeners, labeled as strain gages 9-16 and 25-28 in Figure 2.7. Lastly, eight axial strain gages were used to measure the strain in the stiffener run-outs, labeled as strain gages 17-24 in Figure 2.7. When rosettes were used, a strain gage labeled with an "a" refers to axial strain, a strain gage labeled with a "b" refers to the lateral strain, and a strain gage labeled with a "c" refers to the strain in a 45° angle between the axial and lateral strains. The stiffener with strain gages 25 and 26 is referred to as stiffener A and the stiffener with strain gages 27 and 28 is referred to as stiffener B. The strain gages were accurate to within ±1.0%.

All strain gages were universal general-purpose gages with a thermal expansion coefficient suitable for aluminum alloys. The gages were 2.5 millimeters in length and had a resistance of 350 ohms.

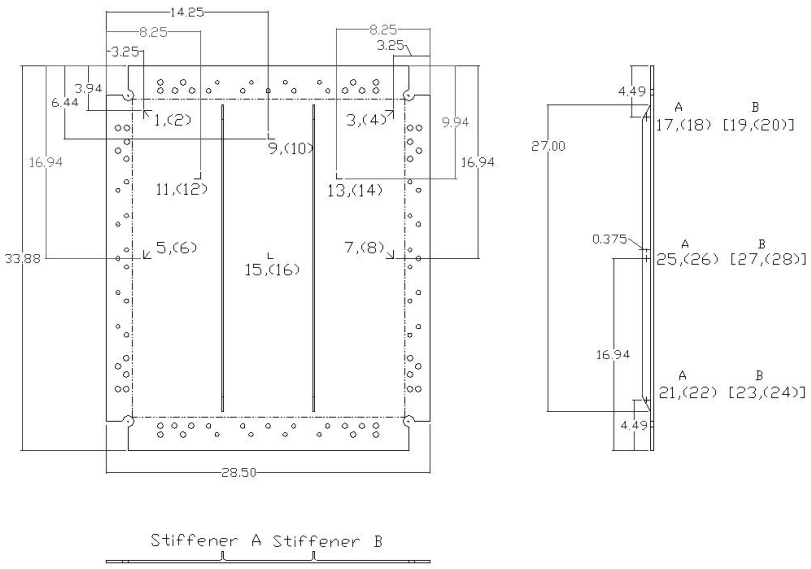

Figure 2.7: Strain Gage Locations on the specimens. Gages marked as X(Y) mark back to back strain gages.

2.3.2 Video Image Correlation 3-D Measurement System

The strain gages were only placed on the top half of the panels. A Video Image Correlation (VIC) 3-D measurement system was used to measure the strain and out-of-plane displacement in the lower half of the panel. The specimens were painted white with random black speckles in the area being analyzed by the VIC 3-D system. During the tests, a series of digital images were taken by two cameras, spaced a known distance apart. The software analyzed the pictures and compared the speckle pattern from the two cameras. As the tests progressed and the panels deformed, the VIC 3-D software was used to detect movement in the specimens through the changes in the speckle pattern and

then calculated the strain and displacement. The VIC 3-D system made it easy to measure strain and displacement in large sections and in three-dimensions [30, 31]. An illustration of the VIC 3-D system is shown in Figure 2.8. Because of the placement of the test machine console, the VIC 3-D system could only be used on the unstiffened side of the panels not facing the console. Also because of the shear loading bar, the VIC 3-D system was only used on the lower half of the test specimens.

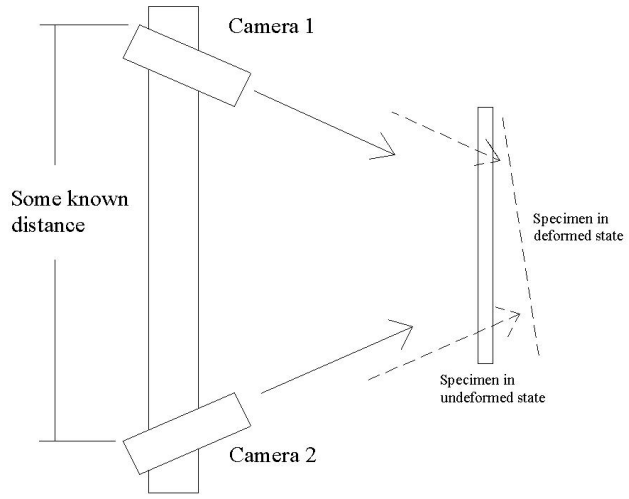

Figure 2.8: Illustration of the Video Image Correlation 3-D Measurement System

2.3.3 Direct Current Displacement Transducer

Direct Current Displacement Transducers (DCDTs) were used to measure out-of-plane, end-shortening, and lateral displacements during the experiments. The DCDTs were accurate to within ±0.5%. A total of six DCDTs were used

to measure the out-of-plane displacement of the panels. The locations of the six out-of-plane DCDTs are shown in Figure 2.9. Three DCDTs were used to measure the end-shortening of the panels. The three DCDTs were placed on three of the four corners of the load platen. As a result, any rotation of the load platen could also be measured in addition to measuring the end-shortening on the panels. Lastly, a DCDT was used to measure the lateral displacement at the bottom of the panels as a result of the shear load. An illustration of the measured lateral displacement is found in Figure 2.10.

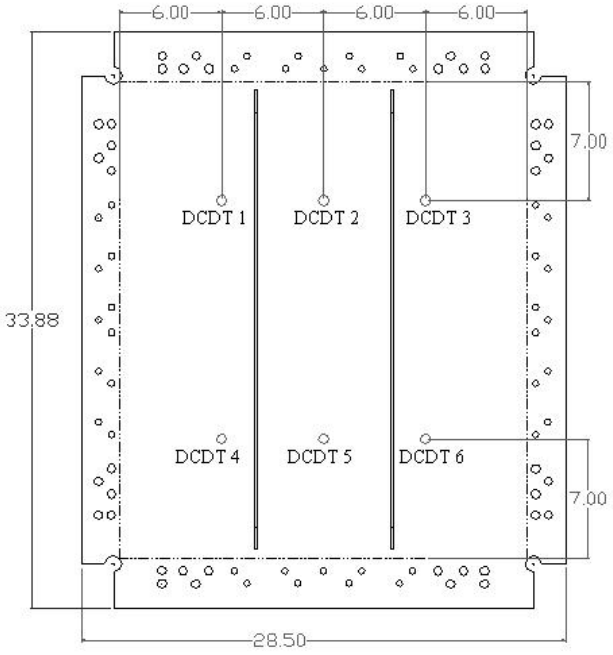

Figure 2.9: Locations of the six out-of-plane Direct Current Displacement Transducers (DCDTs)

When testing Machined Panels 1 and 2 and EBF^3 Panel 1, it was assumed that the load platen displaced evenly. For these tests only one end-

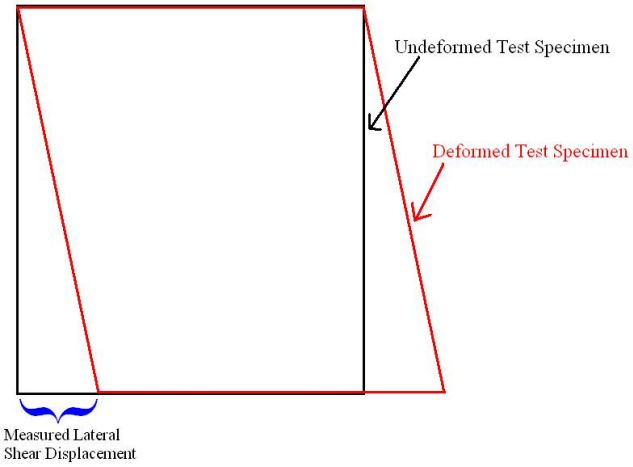

Figure 2.10: Illustration of the Measured Lateral Displacement caused by the Shear Load

shortening measurement was taken. For Machined Panels 3 and 4 and EBF^3 Panels 2, 3, and 4, three end-shortening measurements were taken from the three DCDTs placed on the corners of the load platen. The angle of rotation alpha refers to the rotation about the axis running parallel to the width of the panels and the angle of rotation beta refers to the rotation about the axis running parallel to the thickness of the panels as shown in Figure 2.11.

2.4 Load Cases

Two specimens of each manufacturing technique were tested under two load cases. Two load cases were chosen to obtain a better understanding of the effects of the combined compression-shear loads. Machined and EBF^3 Panels 1 and 2 were tested under the first load case with the shear load at 40% $\pm$0.1% of the compressive load. This was chosen to see the effect of a mostly

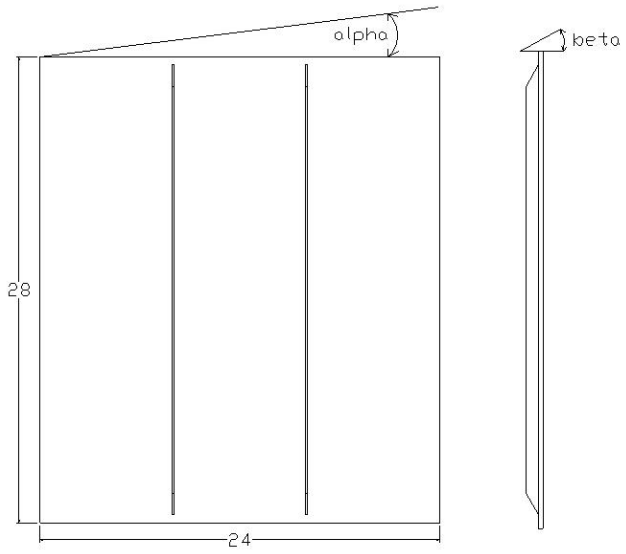

Figure 2.11: Diagram of the Angle of Rotation Alpha and Beta measured along the top of the panel

compressive load. Machined and EBF^3 Panels 3 and 4 were tested under the second load case where the shear force was 100% $\pm$0.1% of the compressive load. The load cell which measured the shear force applied was only capable of measuring a maximum shear force of 100 kips. As a result, in the second load case when the compression and shear loads reached 100 kips, the shear load was held constant at 100 kips while the compressive load continued to increase until global failure. Load case 2 was chosen to see the effects of matched shear and compressive loads on the panels.

Chapter 3

Results

3.1 Load Case 1 Results

The loads applied in load case 1, where the shear load was 40% of the compressive load, are depicted in Figure 3.1. Supplemental data for load case 1 which are not discussed are found in Appendix A.

3.1.1 End-Shortening

The compressive load applied along the top of the panels caused an end-shortening of the panels. The measured end-shortenings from Machined and EBF^3 Panels 1 and 2 are found in Figure 3.2. At the beginning of the tests, a small amount of load induced a large amount of measurable displacement as the panels were seated in the test fixture. Therefore, the end-shortening measurements have been adjusted so the measured data were zeroed from

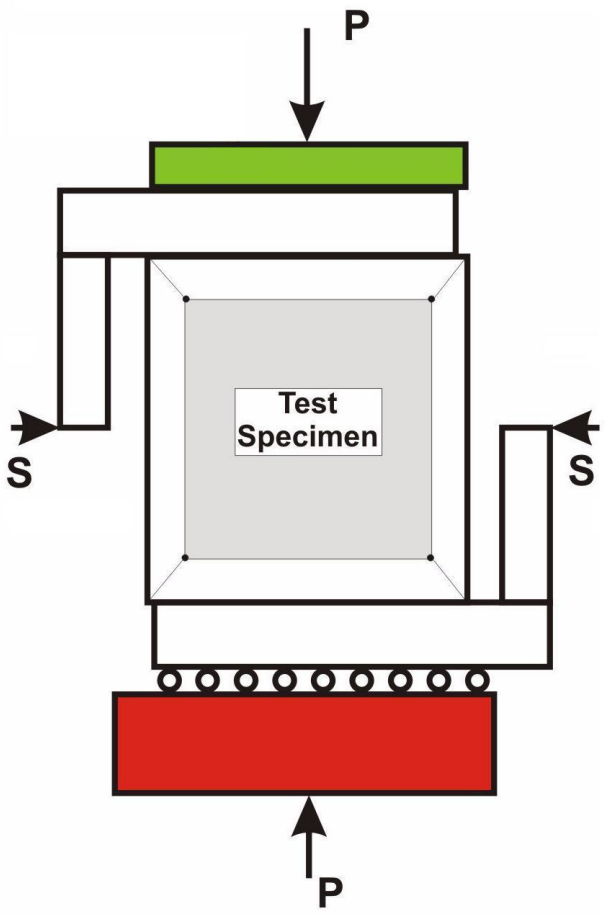

Figure 3.1: Illustration of Load Case 1: P was the compressive load to a maximum of 179.5 kips. S was the shear load at 40% of the compressive load up to a maximum of 71.8 kips.

the point the loads were established in the test panels. The corrected end-shortenings for Machined and EBF^3 Panels 1 and 2 as a function of the applied loads are shown in Figure 3.3. There was still a gradual transition at the beginning of the tests into the linear relationship between the applied loads and the end-shortening displacements after zeroing had been taken into account.

As seen in Figure 3.3, the two machined panels behaved similarly, but Machined Panel 2 had the largest end-shortening for a given load value. The EBF^3 panels behaved similarly, but had slightly steeper slopes than the machined panels. Machined Panel 2 and EBF^3 Panels 1 and 2 failed just below 180 kips compression and Machined Panel 1 failed at just over 160 kips compression, as shown in Figure 3.3.

The corrected end-shortenings at the maximum compressive loads for load case 1 are listed in Table 3.1. The machined panels had different results for maximum end-shortening and the maximum compressive load. Machined Panel 1 had a 15% lower end-shortening than Machined Panel 2. On average, the EBF^3 panels' end-shortening was 0.1105 inches, 13% and 33% lower than Machined Panels 1 and 2 respectively.

The rotations of the top platen from the DCDT data measured on EBF^3 Panel 2 are shown in Figure 3.4. The load platen was continually rotating throughout the entire test as shown by the angle of rotation alpha. The load platen only rotated initially during the beginning of the test and remained close to an angle of -0.03 degrees from a load of 50 kips compression

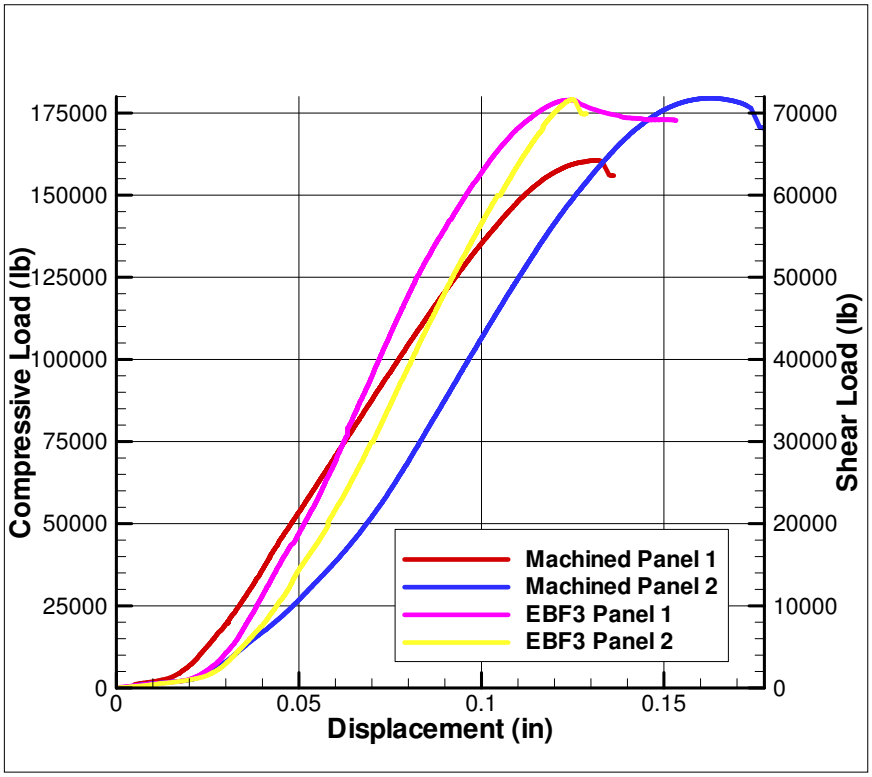

Figure 3.2: Original Measured Experimental End-shortening Results for Load Case 1

Table 3.1: End-shortening Results for Load Case 1

Panel	End-shortening (in)	Maximum Compressive Load (kips)
Machined Panel 1	0.1246	160.6
Machined Panel 2	0.1466	179.5
EBF^3 Panel 1	0.1110	179.0
EBF^3 Panel 2	0.1099	179.0

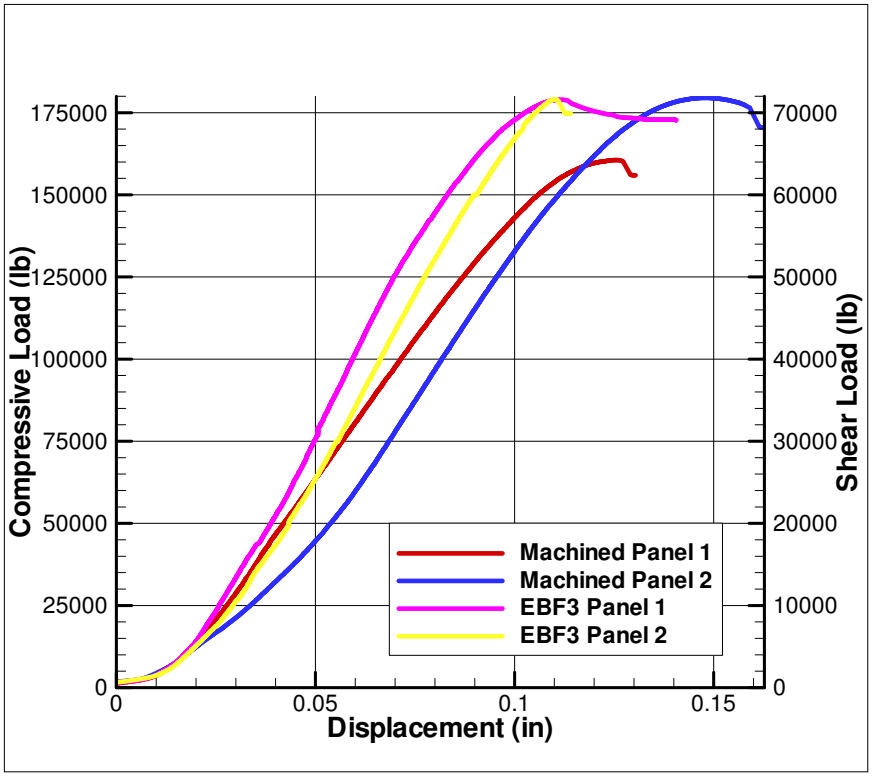

Figure 3.3: Corrected Experimental End-shortening Results for Load Case 1

onwards until failure as shown by the angle of rotation beta in Figure 3.4.

3.1.2 Lateral Displacement

The shear load applied at the bottom of the panels caused a lateral displacement. The measured lateral displacements as a function of the applied loads at the bottom of the panels for Machined and EBF^3 Panels 1 and 2 are shown in Figure 3.5. As with the DCDT data from the end-shortening measurements, the data of the lateral displacements required zeroing after the test fixture was seated at the beginning of the tests. The lateral displacements shown in Figure 3.6 are corrected for the initial movement from the seating of the test fixture. Machined Panels 1 and 2 and EBF^3 Panel 2 exhibited similar lateral displacements and applied shear load behavior, while EBF^3 Panel 1 exhibited a slightly larger lateral displacement.

The lateral displacements at the maximum shear loads for load case 1 are listed in Table 3.2. The maximum shear load occurred at the same time as the maximum compressive load. On average, the EBF^3 panels' lateral displacements were 10% higher than the machined panels. As with the compressive load, the maximum shear load for Machined Panel 1 was 11% lower than the other machined and EBF^3 panels.

3.1.3 Out-Of-Plane Displacement

The out-of-plane displacement was monitored to provide an indication of the onset of panel buckling. The out-of-plane displacements measured by Direct

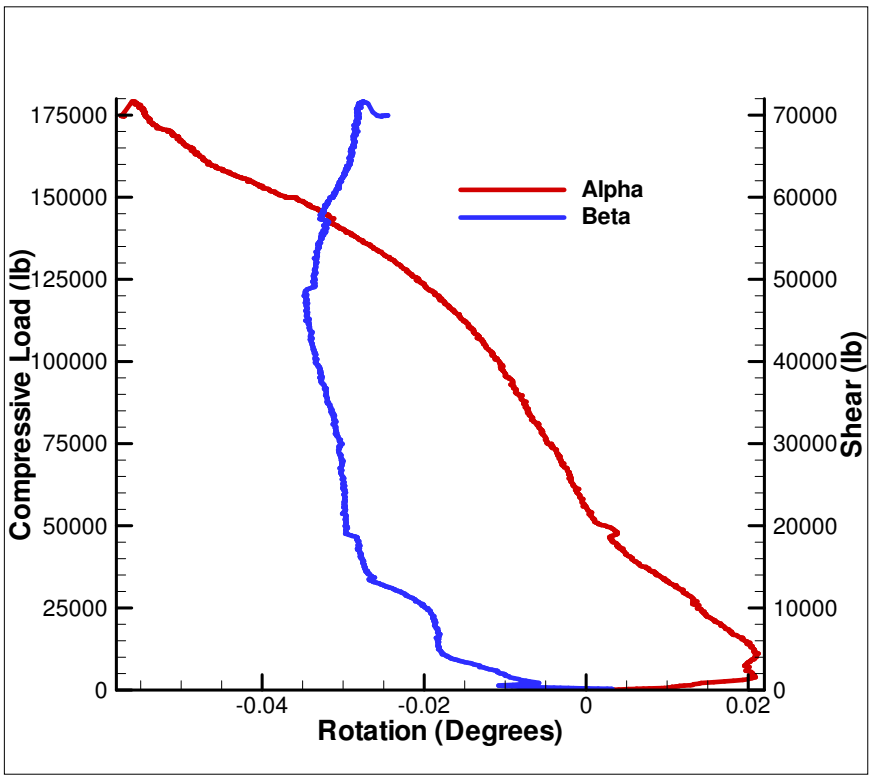

Figure 3.4: Angles of Rotation of the Load Platen for EBF^3 Panel 2

Table 3.2: Lateral Displacement Results for Load Case 1

Panel	Lateral Displacement (in)	Maximum Shear Load (kips)
Machined Panel 1	0.1228	64.2
Machined Panel 2	0.1333	71.8
EBF^3 Panel 1	0.1471	71.5
EBF^3 Panel 2	0.1338	71.7

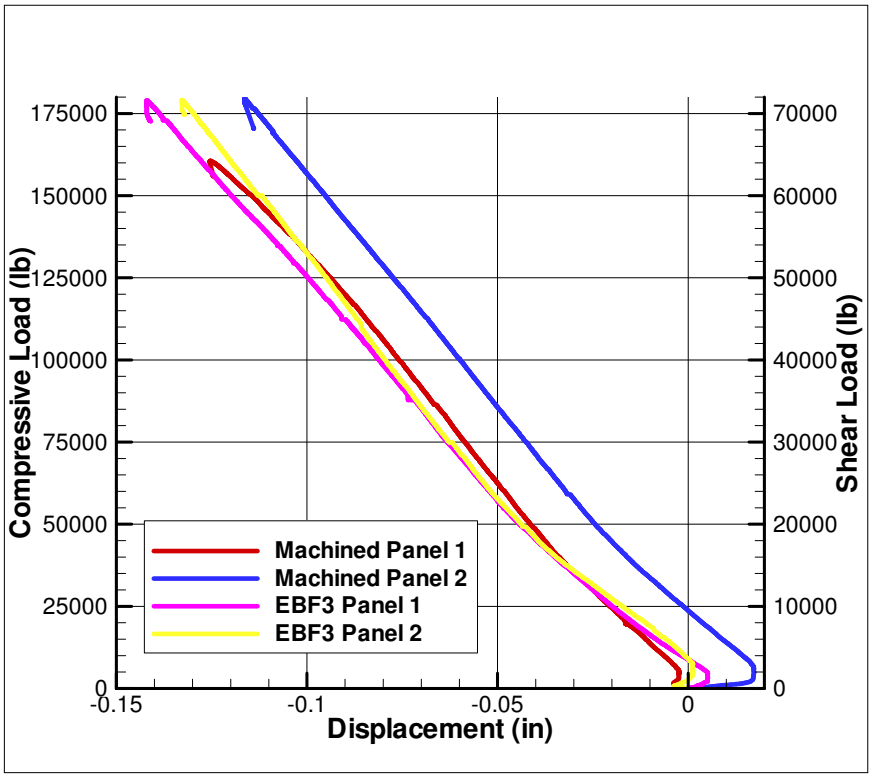

Figure 3.5: Original Measured Experimental Lateral Shear Displacements at the bottom of the Panels for Load Case 1

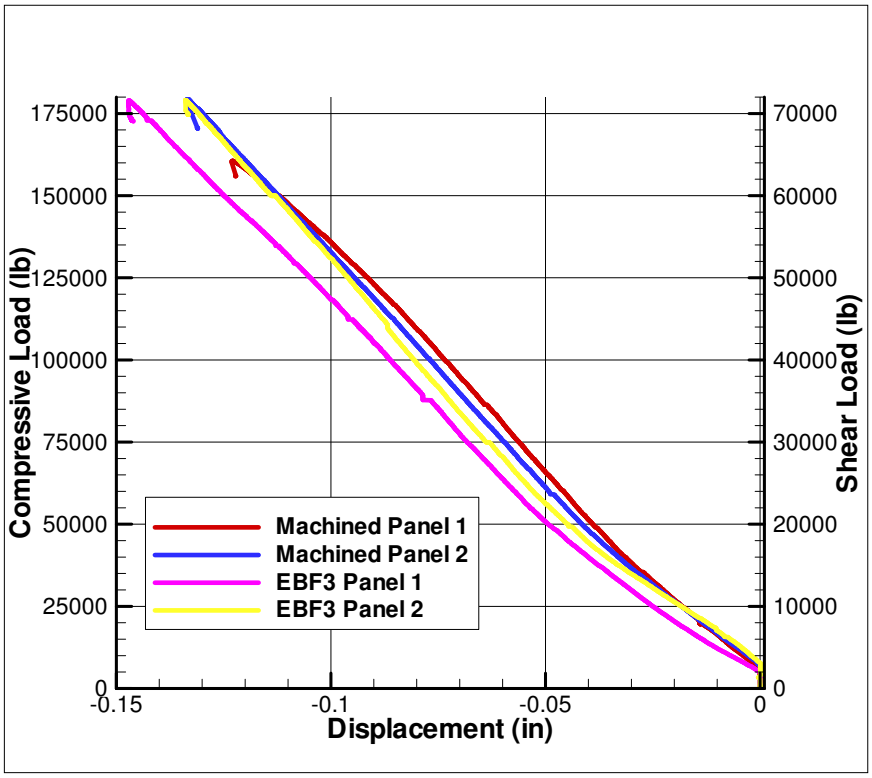

Figure 3.6: Corrected Experimental Lateral Shear Displacements at the bottom of the Panels for Load Case 1

Current Displacement Transducers (DCDTs) 1, 2, and 3 as a function of the applied loads are shown in Figures 3.7 and 3.8 for the machined and EBF^3 panels respectively. Refer to Figure 2.9 for the location of the DCDTs on the panels. The two machined panels had little out-of-plane displacement in the upper half of the panels when the compressive load was below 46 kips. The out-of-plane displacement increased dramatically as the load exceeded 46 kips compression. The change in slope at 46 kips compression was an inflection point. EBF^3 Panel 1 had drastically different results than the other panels and showed little out-of-plane displacement at loads below 100 kips compression and a small amount of negative out-of-plane displacement at loads between 40 and 100 kips compression. (Positive out-of-plane displacement was in the direction of the stiffeners, while negative out-of-plane displacement was in the opposite direction of the stiffeners) Above 100 kips compression, the out-of-plane displacement for EBF^3 Panel 1 increased nonlinearly for a small increase in load. EBF^3 Panel 2 also behaved differently from the machined panels, having almost zero out-of-plane displacement at loads below 35 kips compression and an inflection point occurred at a load of 35 kips compression.

Typically DCDT 2, located in the center of the panels, had the largest out-of-plane displacement for Machined Panels 1 and 2 and EBF^3 Panel 2 in the top half of the panels. For EBF^3 Panel 1, DCDTs 1 and 2 measured similar out-of-plane displacements. DCDT 3, on average, had the smallest out-of-plane displacement in the top half of the machined and EBF^3 panels. The machined panels had larger measured out-of-plane displacement at the

end of the tests than the EBF^3 panels.

The out-of-plane displacement measured by DCDTs 4, 5, and 6 as a function of the applied loads are shown in Figures 3.9 and 3.10 for the machined and EBF^3 panels respectively. DCDTs 4, 5, and 6 are located on the lower half of the panels. The machined panels had comparable results with DCDT 1, 2, and 3. In this situation, there was little out-of-plane displacement at loads below 46 kips compression and a significant increase in out-of-plane displacement occurred after the onset of buckling. Both EBF^3 panels showed smaller out-of-plane displacement compared to the machined panels. After a load of 100 kips compression for EBF^3 Panel 2 and 75 kips compression for EBF^3 Panel 2, there was a significant increase in out-of-plane displacement. All panels had a complete out-of-plane displacement reversal in the lower half of the panel at the end of the tests. This was seen by the sharp change from positive out-of-plane displacement to negative out-of-plane displacement measured by DCDTs 4, 5, and 6 at the maximum compressive load.

Similar to the top half, the bottom half of panels fabricated using both manufacturing techniques showed nonsymmetrical out-of-plane displacement. The largest measured out-of-plane displacement occurred at the location of DCDT 5 and the smallest out-of-plane displacement was measured by DCDT 4 in the lower half of the panels. The exception was EBF^3 Panel 1 where DCDT 6 measured the smallest out-of-plane displacement, which was measured at forces below 140 kips compression.

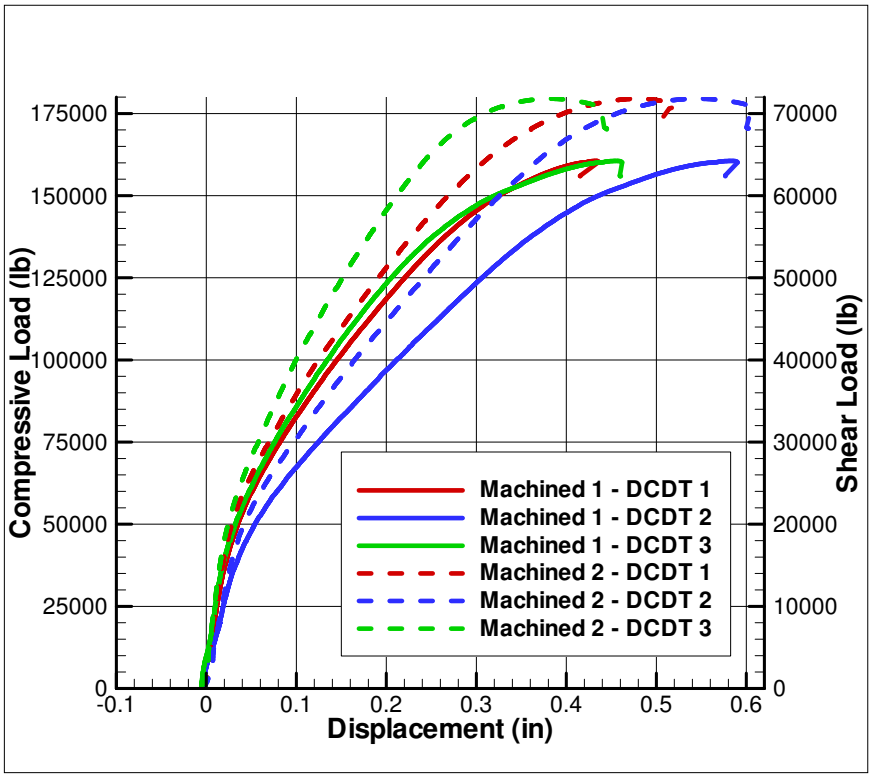

Figure 3.7: Out-Of-Plane Displacement measured by DCDT 1, 2, and 3 for Machined Panels 1 and 2

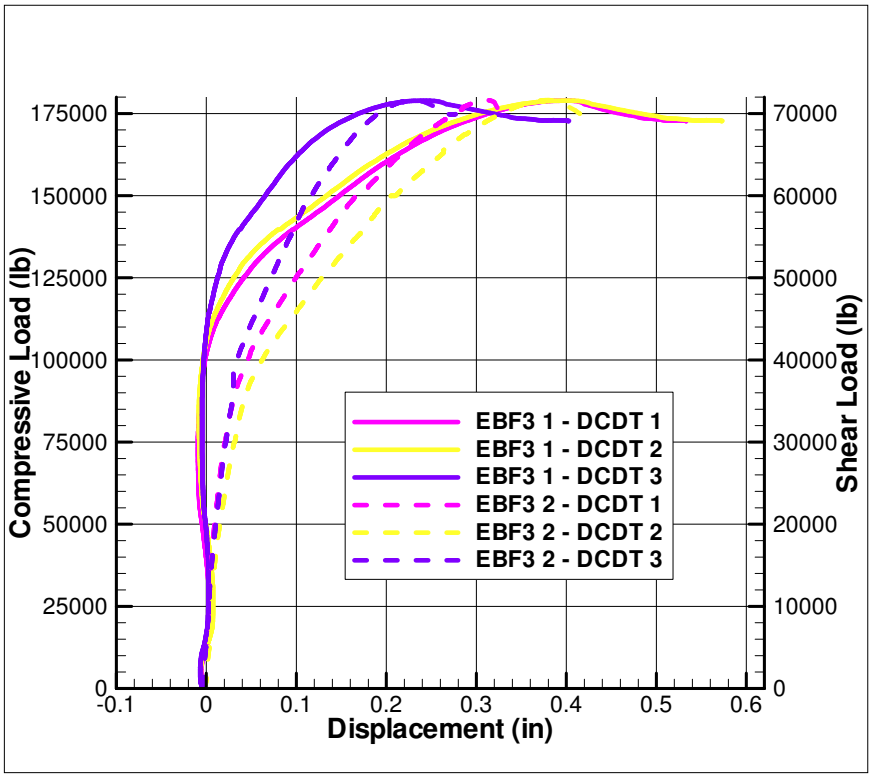

Figure 3.8: Out-Of-Plane Displacement measured by DCDT 1, 2, and 3 for EBF^3 Panels 1 and 2

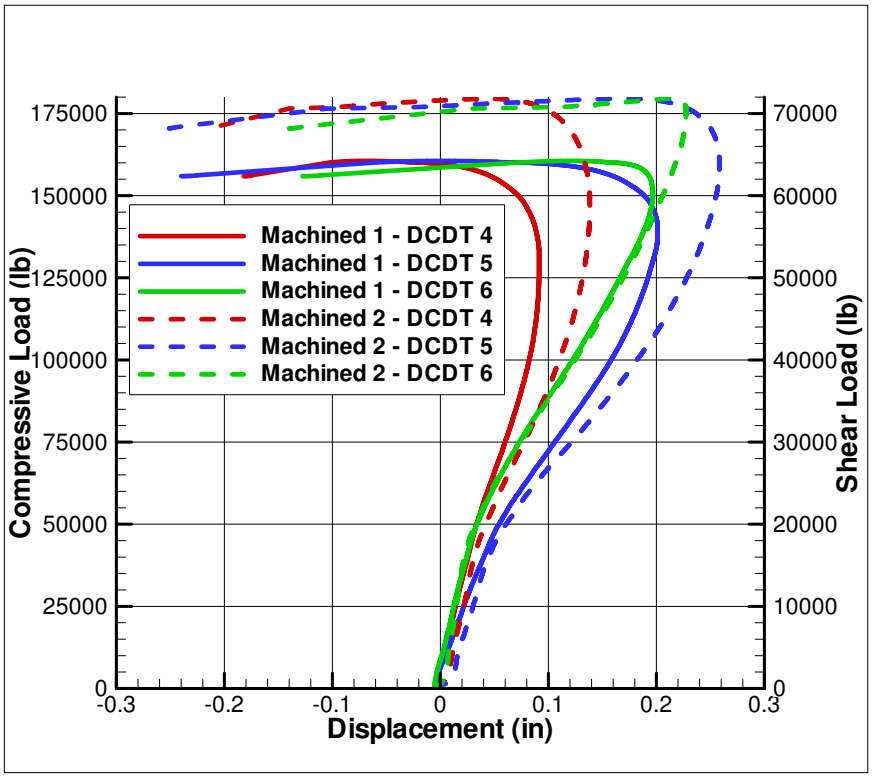

Figure 3.9: Out-Of-Plane Displacement measured by DCDT 4, 5, and 6 for Machined Panels 1 and 2

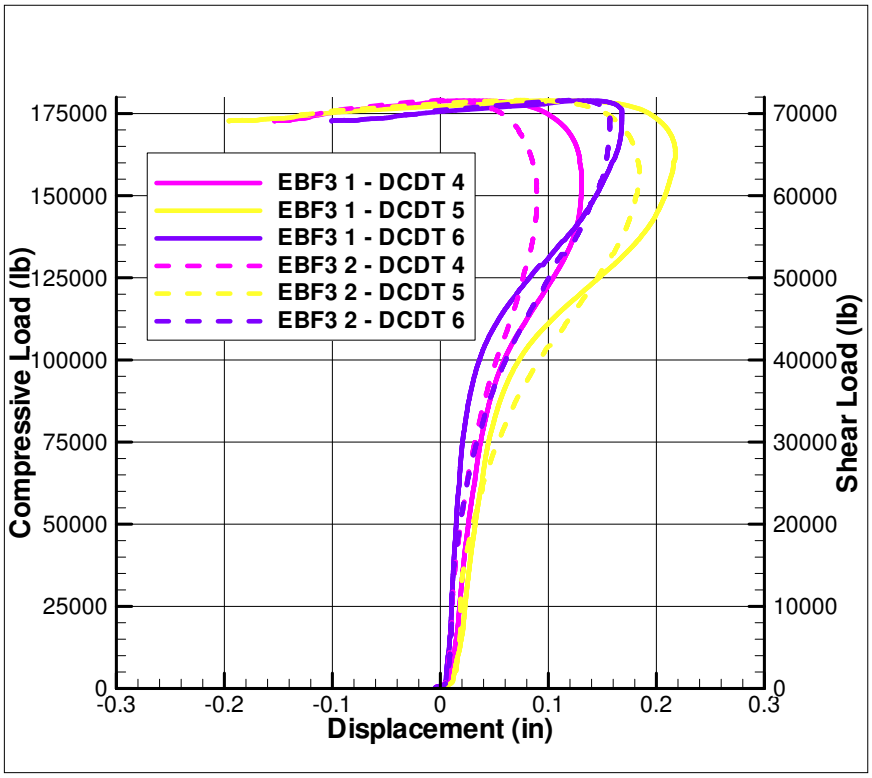

Figure 3.10: Out-Of-Plane Displacement measured by DCDT 4, 5, and 6 for EBF^3 Panels 1 and 2

3.1.4 Strain in the Panels

The strain gages provided information on localized strain. Strain gages 1a-4a were located at the top two corners of the panels. The axial strains measured from strain gages 1a-4a as a function of the applied loads are shown in Figures 3.11 and 3.12 for the machined and EBF^3 panels respectively. Both the machined and EBF^3 panels exhibited linear behavior until the panels started to yield.

The axial strains measured from strain gages 1b-4b as a function of the applied loads are shown in Figures 3.13 and 3.14 for the machined and EBF^3 panels respectively. Machined and EBF^3 Panels 1 and 2 had little lateral strains measured from strain gages 1b-4b. For the machined panels, a slight amount of nonlinear behavior was measured by strain gages 1b-4b starting at a load of 75 kips compression. Strain gages 1b and 2b for Machined Panel 1 showed a small increase in strain at a load of 110 kips compression. EBF^3 Panels 1 and 2 also had little lateral strain. Nonlinear behavior for the EBF^3 panels started just under a load of 50 kips compression.

The axial strain measured from strain gages 5a-8a as a function of the applied loads is shown in Figures 3.15 and 3.16 for the machined and EBF^3 panels respectively. Strain gages 5-8 were located in the middle of the panels 1 inch from the edge of the test frame. The strain in the machined panels exhibited some nonlinearity at loads below 75 kips compression, after which the load-strain relationship remained linear until failure. Conversely, the strain in the EBF^3 panels was linear until just below a load of 75 kips compression.

After this point, the strain in the panels showed a small amount of nonlinearity until failure.

The lateral strains measured from strain gages 5b-8b as a function of the applied loads are shown in Figures 3.17 and 3.18 for the machined and EBF^3 panels respectively. The lateral strain measurements for the machined panels were linear with respect to compressive loads at loads below 45 kips, then the results became nonlinear until failure. EBF^3 Panels 1 and 2 showed linear lateral strain at loads below approximately 75 kips compression, after which nonlinear behavior was observed until failure.

3.1.5 Strain in the Stiffeners

The axial strains in the stiffeners measured by strain gages 25a-28a as a function of the applied loads are shown in Figures 3.19 and 3.20 for the machined and EBF^3 panels respectively. The machined panels exhibited initial negative strains measured from strain gages 25a-28a; at a load of 46 kips compression the measured axial strains in the stiffeners reversed direction, becoming positive until the panels failed. The EBF^3 panels exhibited similar behavior to the machined panels, although the strain values and inflection points occurred at different load and strain values. The EBF^3 panels exhibited higher strains in EBF^3 Panel 1 than in EBF^3 Panel 2. Also higher strains were measured in stiffener B than in stiffener A for EBF^3 Panel 1. EBF^3 Panel 1 started to reverse strain values at a load of 87 kips compression while EBF^3 Panel 2 reversed strain at a load of 72 kips compression.

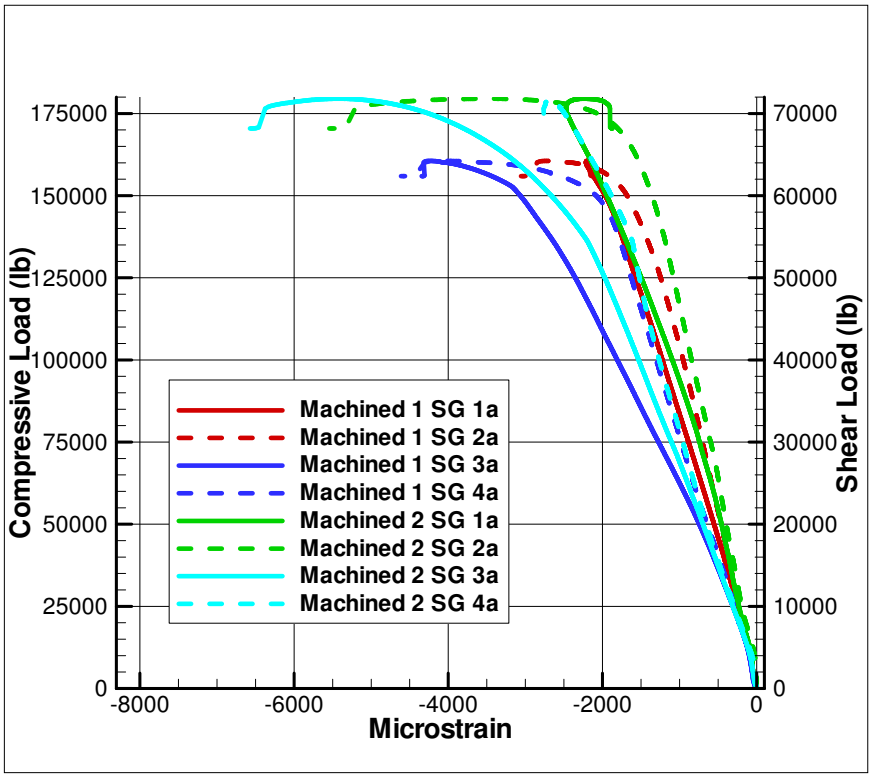

Figure 3.11: Axial Strains measured from Strain Gages 1a-4a for Machined Panels 1 and 2

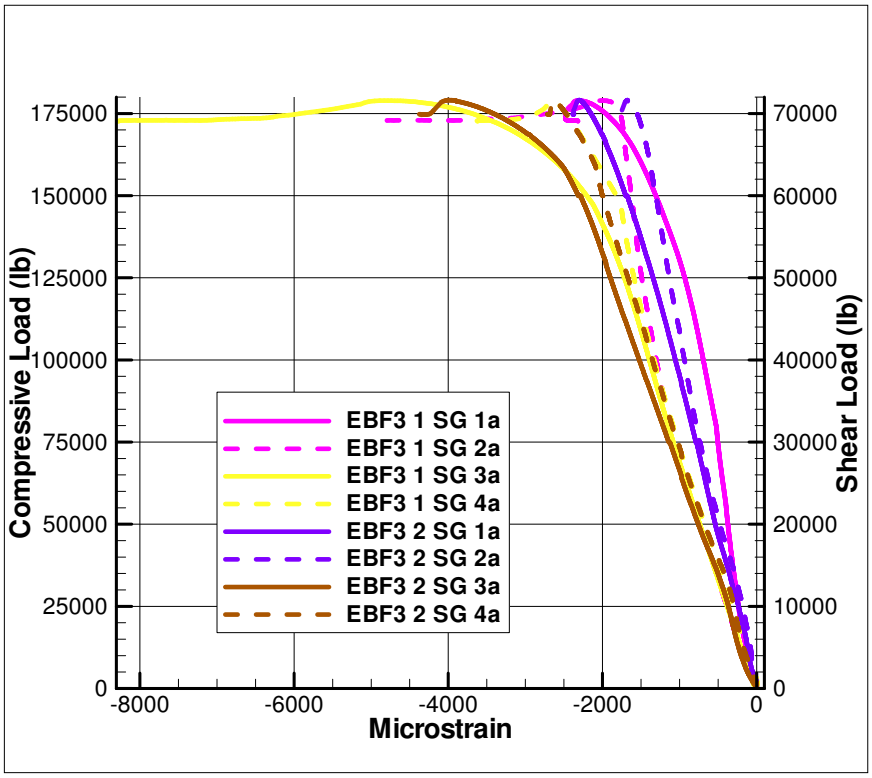

Figure 3.12: Axial Strains measured from Strain Gages 1a-4a for EBF^3 Panels 1 and 2

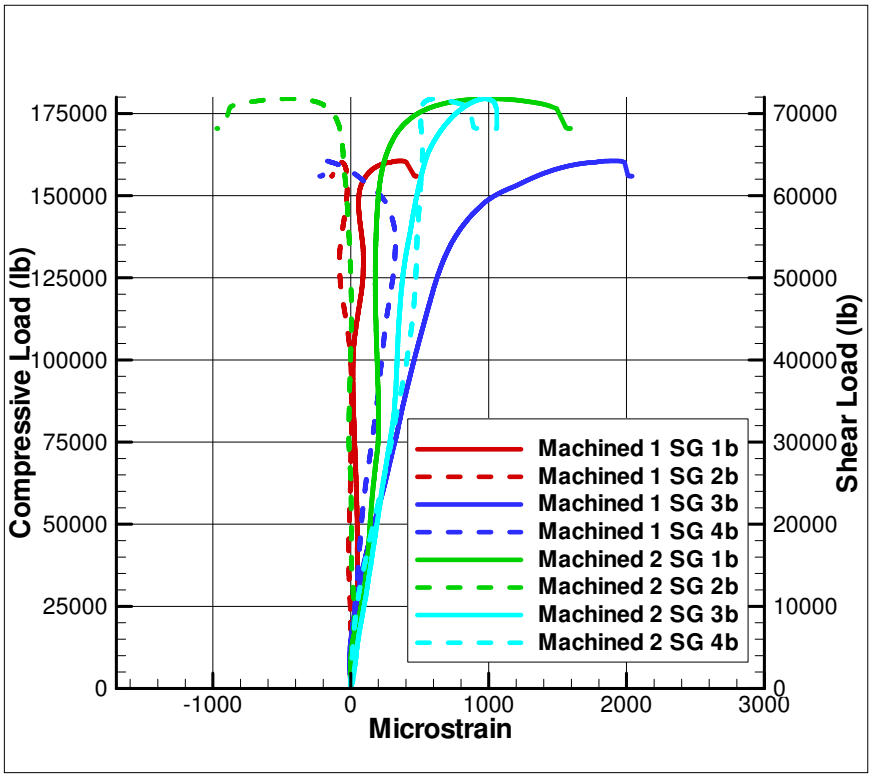

Figure 3.13: Axial Strains measured from Strain Gages 1b-4b for Machined Panels 1 and 2

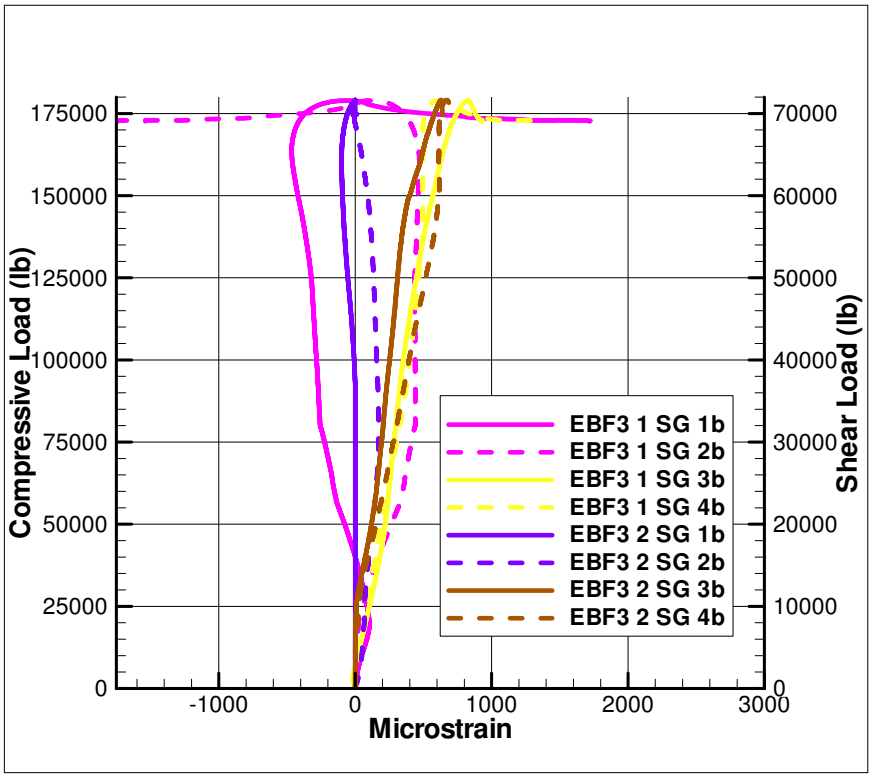

Figure 3.14: Axial Strains measured from Strain Gages 1b-4b for EBF^3 Panels 1 and 2

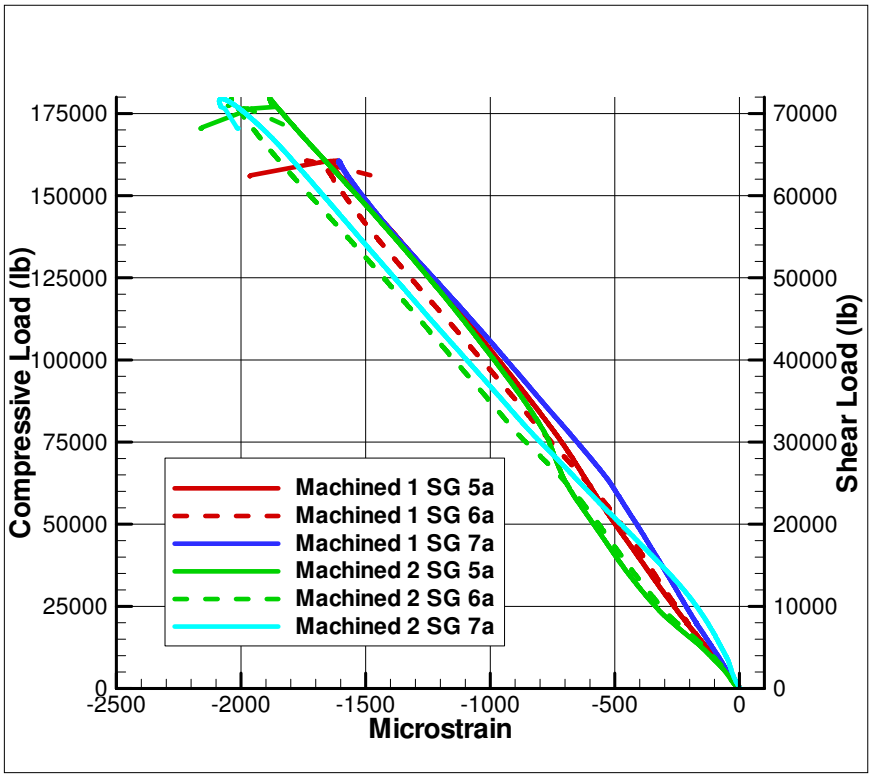

Figure 3.15: Axial Strains measured from Strain Gages 5a-8a for Machined Panels 1 and 2

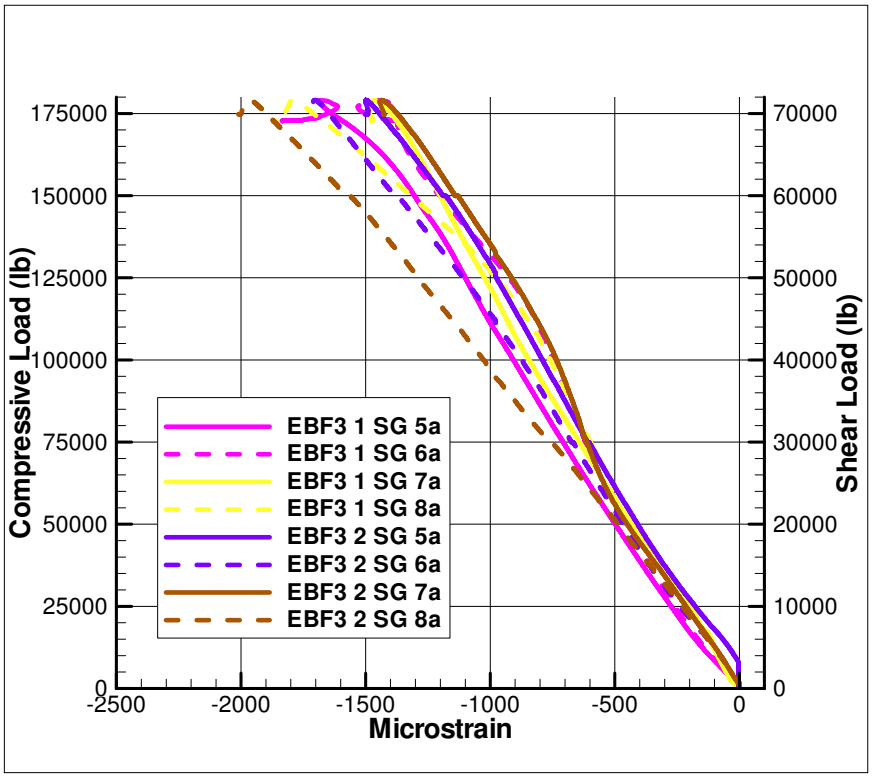

Figure 3.16: Axial Strains measured from Strain Gages 5a-8a for EBF^3 Panels 1 and 2

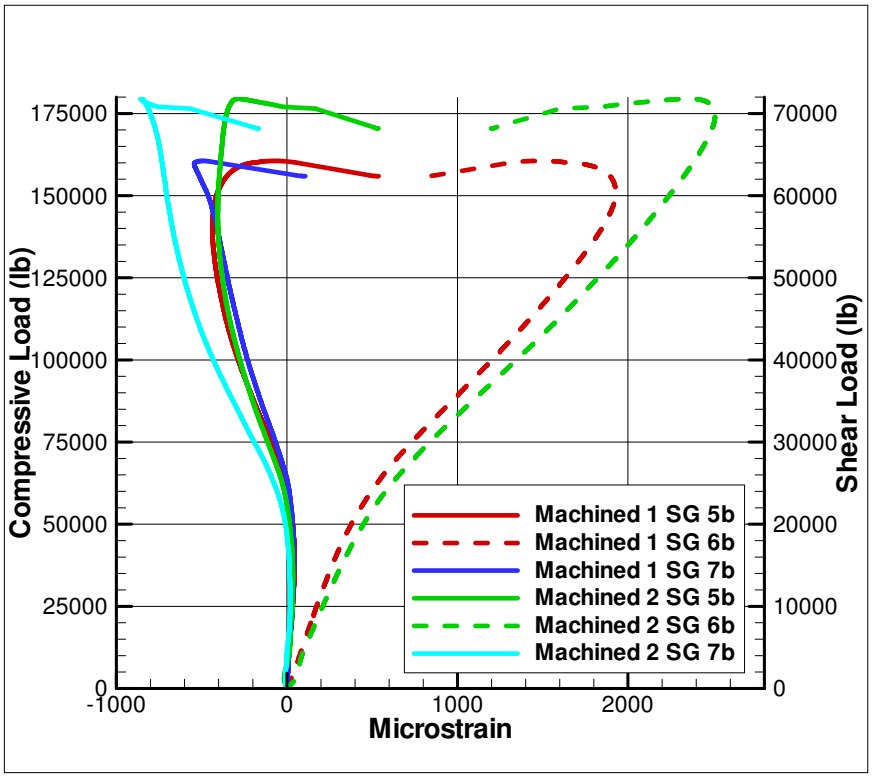

Figure 3.17: Lateral Strains measured from Strain Gages 5b-8b for Machined Panels 1 and 2

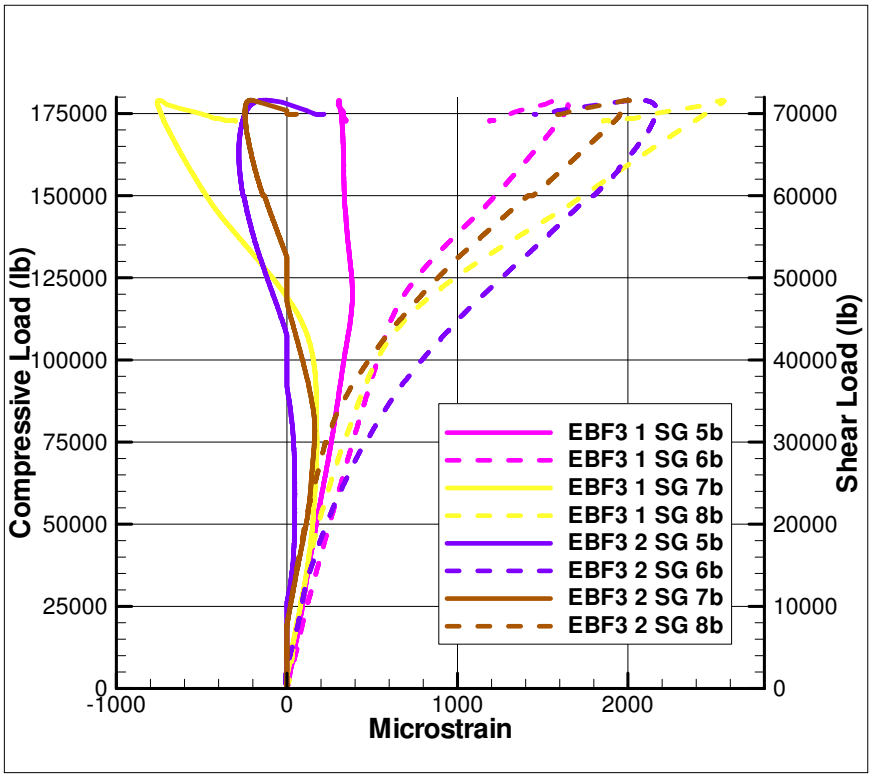

Figure 3.18: Lateral Strains measured from Strain Gages 5b-8b for EBF^3 Panels 1 and 2

The lateral strains in the stiffeners found in strain gages 25b-28b as a function of the applied loads are shown in Figures 3.21 and 3.22 for the machined and EBF^3 panels respectively. The machined panels had linear strain measurements with respect to the compressive loads up to loads of 46 kips compression, after which the strain reversed direction becoming negative. The EBF^3 panels' lateral strain measurements also showed a strain reversal in EBF^3 Panel 1 at a load of 87 kips compression and EBF^3 Panel 2 at a load of 72 kips compression.

3.1.6 Video Image Correlation 3-D Measurement System Results

The out-of-plane displacement measured in the lower half of the panel from the VIC 3-D system for Machined Panel 2 is shown in Figure 3.23. The out-of-plane displacement measured in the lower half of the panels from the VIC 3-D system is shown in Figures 3.24 and 3.25 for EBF^3 Panels 1 and 2 respectively. For each of the panels, a point prior to buckling, two points post-buckle, the point at maximum load, and a point post-failure were chosen to compare for the VIC 3-D data analysis. As with the DCDT measurements, positive out-of-plane displacement was in the direction of the stiffeners while negative out-of-plane displacement was in the opposite direction of the stiffeners. The panels exhibited positive out-of-plane displacement as shown by the green and red areas before failure, although EBF^3 Panel 1 showed more out-of-plane displacement on the left side of Figure 3.24(A,B). After failure, negative out-

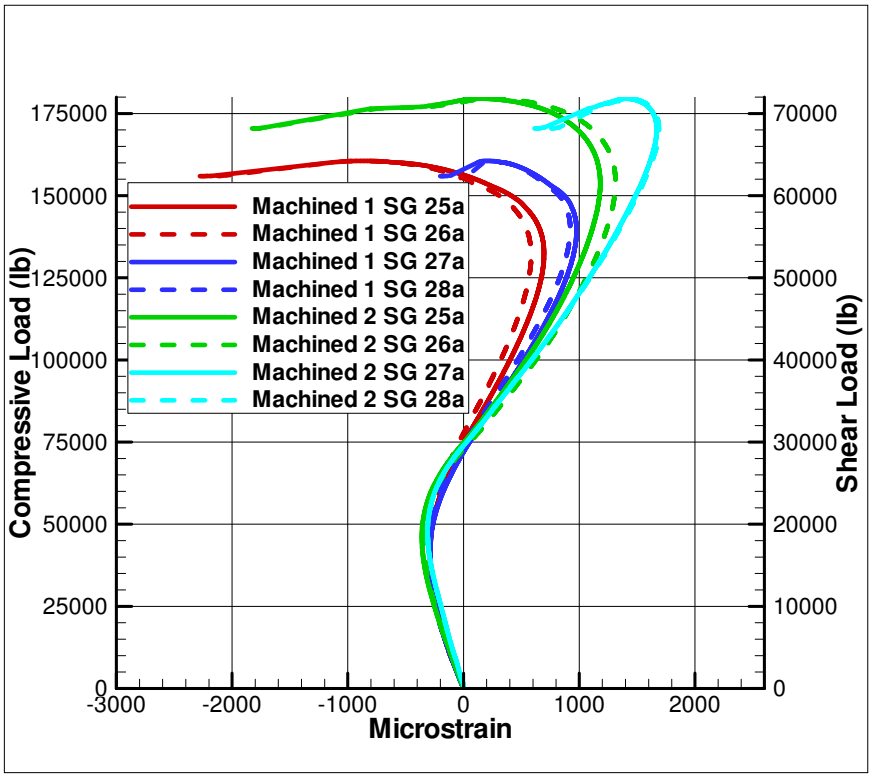

Figure 3.19: Axial Strain in the stiffeners measured from Strain Gages 25a-28a for Machined Panels 1 and 2

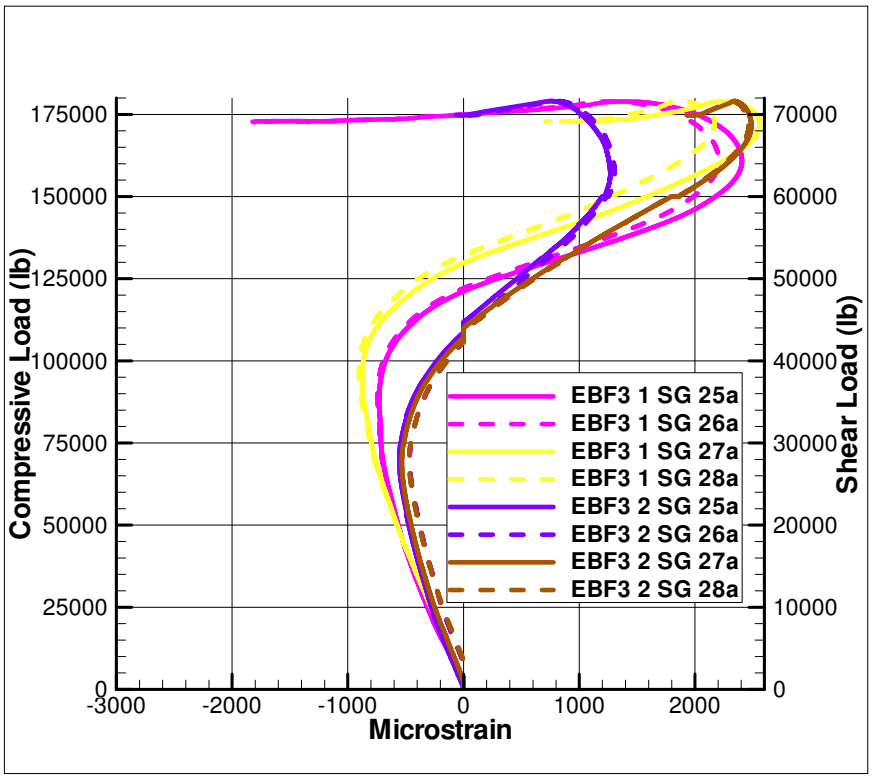

Figure 3.20: Axial Strain in the stiffeners measured from Strain Gages 25a-28a for EBF^3 panels 1 and 2

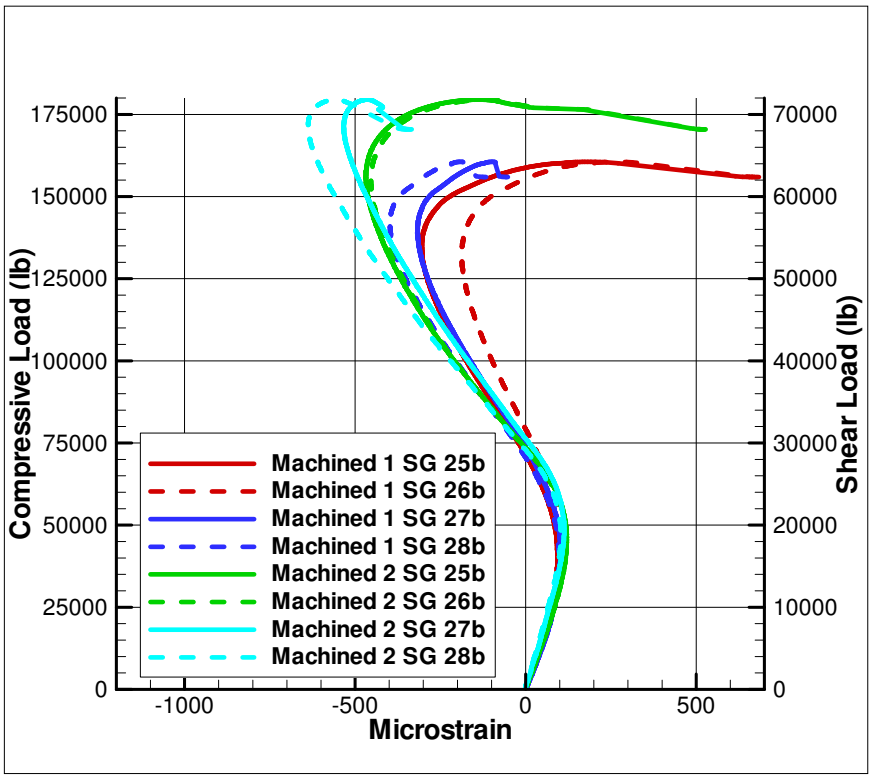

Figure 3.21: Lateral Strain in the stiffeners measured from Strain Gages 25b-28b for Machined panels 1 and 2

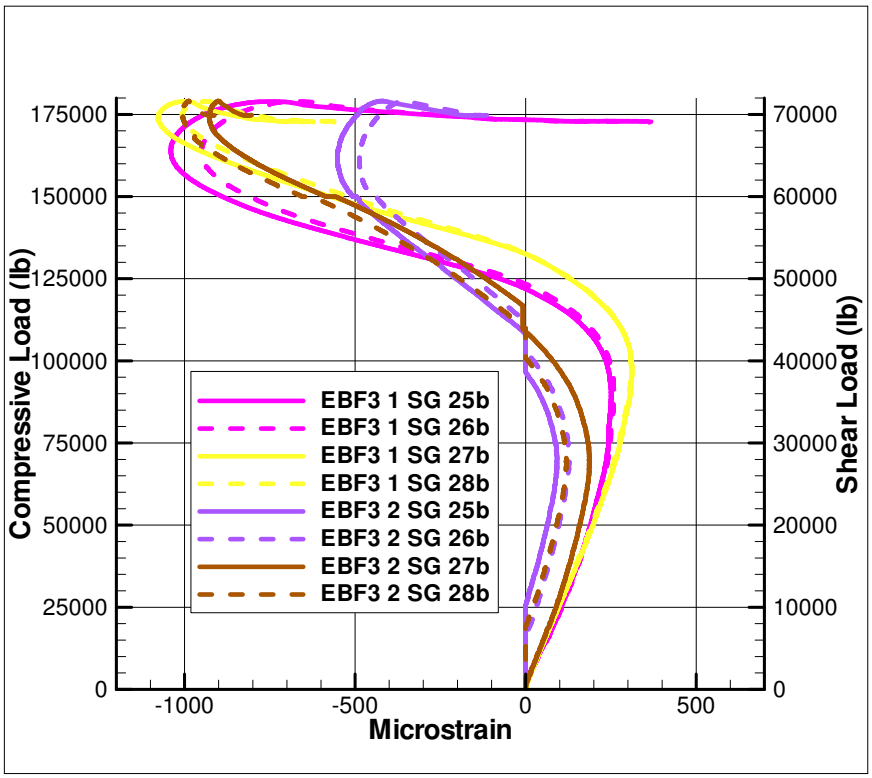

Figure 3.22: Lateral Strain in the stiffeners measured from Strain Gages 25b-28b for EBF^3 panels 1 and 2

of-plane displacement was evident as shown in blue. Supplemental data for the VIC 3-D out-of-plane displacement for Machined Panel 1 are shown in Appendix A.

The measured axial strain is shown in Figure 3.26 for Machined Panel 2 and Figure 3.27 for EBF^3 Panel 2, both measured in the lower half of the panel from the VIC 3-D system. Axial strain measurements are shown at the same load levels as was shown in Figure 3.23 and 3.25. Both panels experienced larger strain in the bottom left corner propagating to the top of the photos which corresponds to the middle of the panels. After failure of the panels, a large amount of positive strain was measured in the middle of the lower half of the panels. There was also an area of strain concentration at the bottom edge of the panels. Supplemental axial strain data from the VIC 3-D system for Machined Panel 1 and EBF^3 Panel 1 can be found in Appendix A.

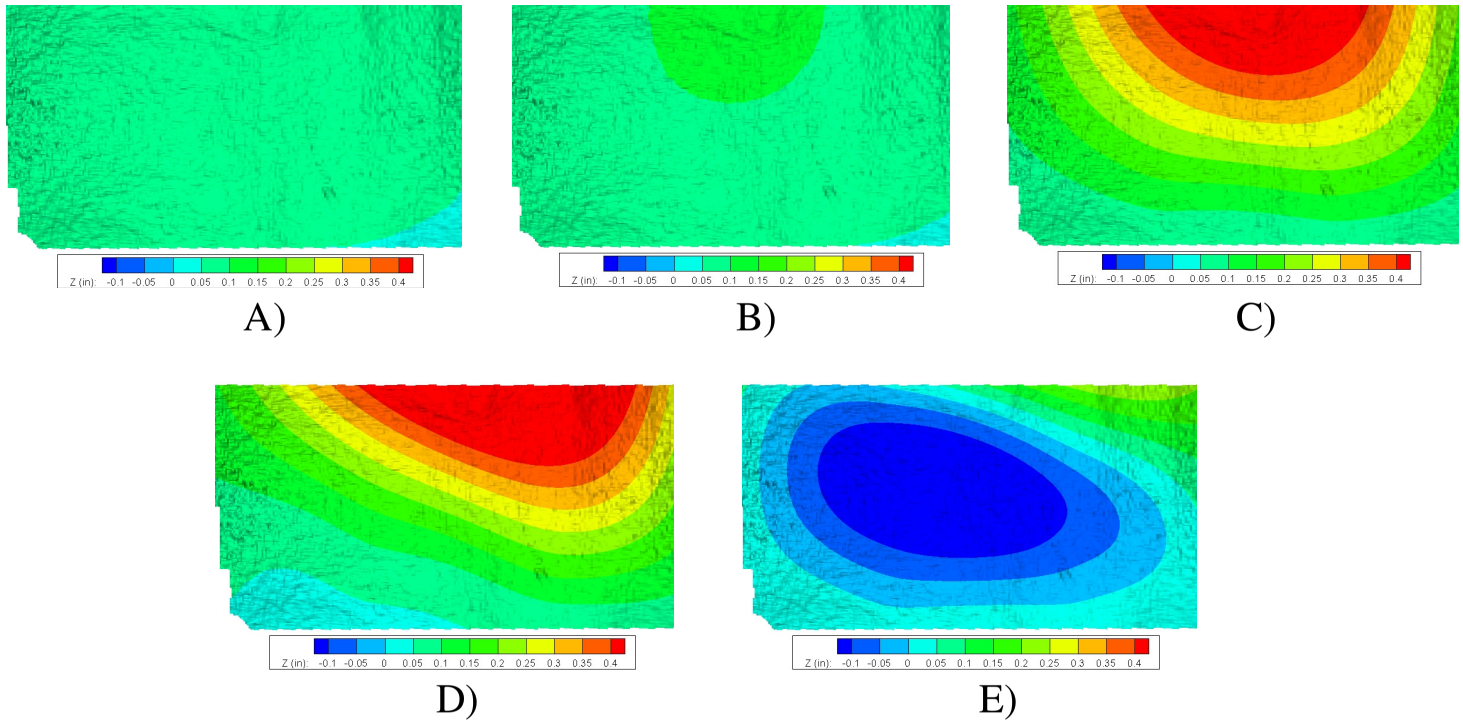

Figure 3.23: Out-of-plane Displacement measured in Machined Panel 2 from the VIC 3-D System in the lower half of the panel at A) 28.7 kips (pre-buckle) B) 45.5 kips (post-buckle) C) 138.7 (post-buckle) D) 179.5 (maximum load) E) 170.1 (post-failure). Load values expressed in terms of compressive load

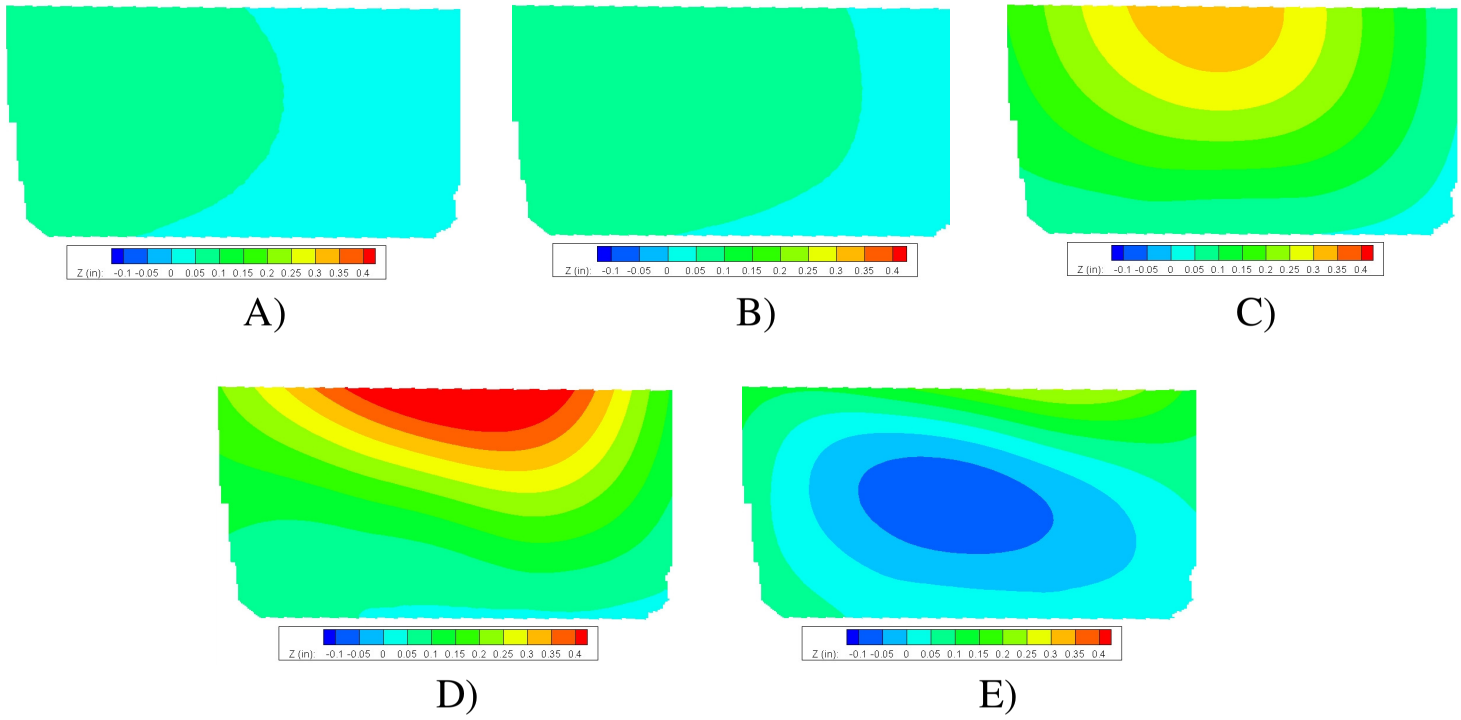

Figure 3.24: Out-of-plane Displacement measured in EBF^3 Panel 1 from the VIC 3-D System in the lower half of the panel at A) 35.1 kips (pre-buckle) B) 83.5 kips (post-buckle) C) 135.1 (post-buckle) D) 179.1 (maximum load) E) 160.2 (post-failure). Load values expressed in terms of compressive load

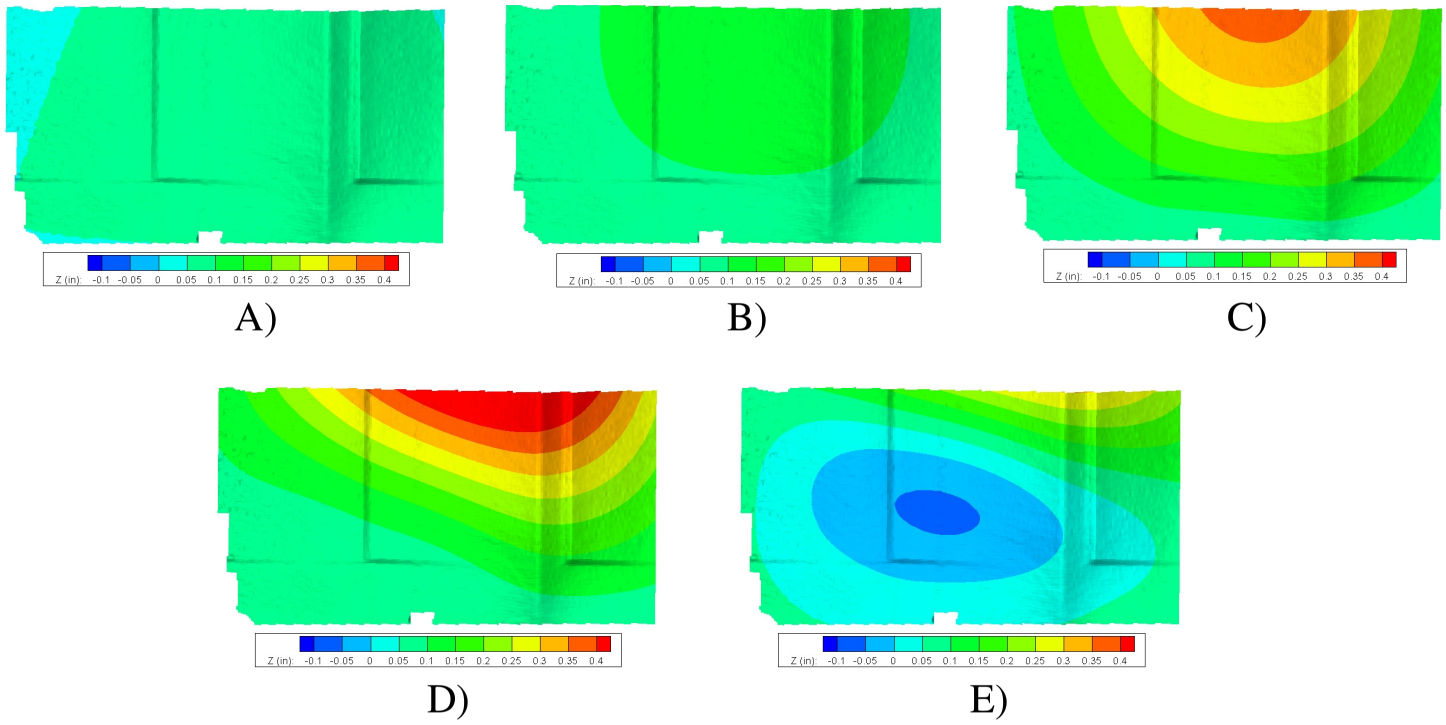

Figure 3.25: Out-of-plane Displacement measured in EBF^3 Panel 2 from the VIC 3-D System in the lower half of the panel at A) 35.4 kips (pre-buckle) B) 85.7 kips (post-buckle) C) 134.2 (post-buckle) D) 179.5 (maximum load) E) 163.5 (post-failure). Load values expressed in terms of compressive load

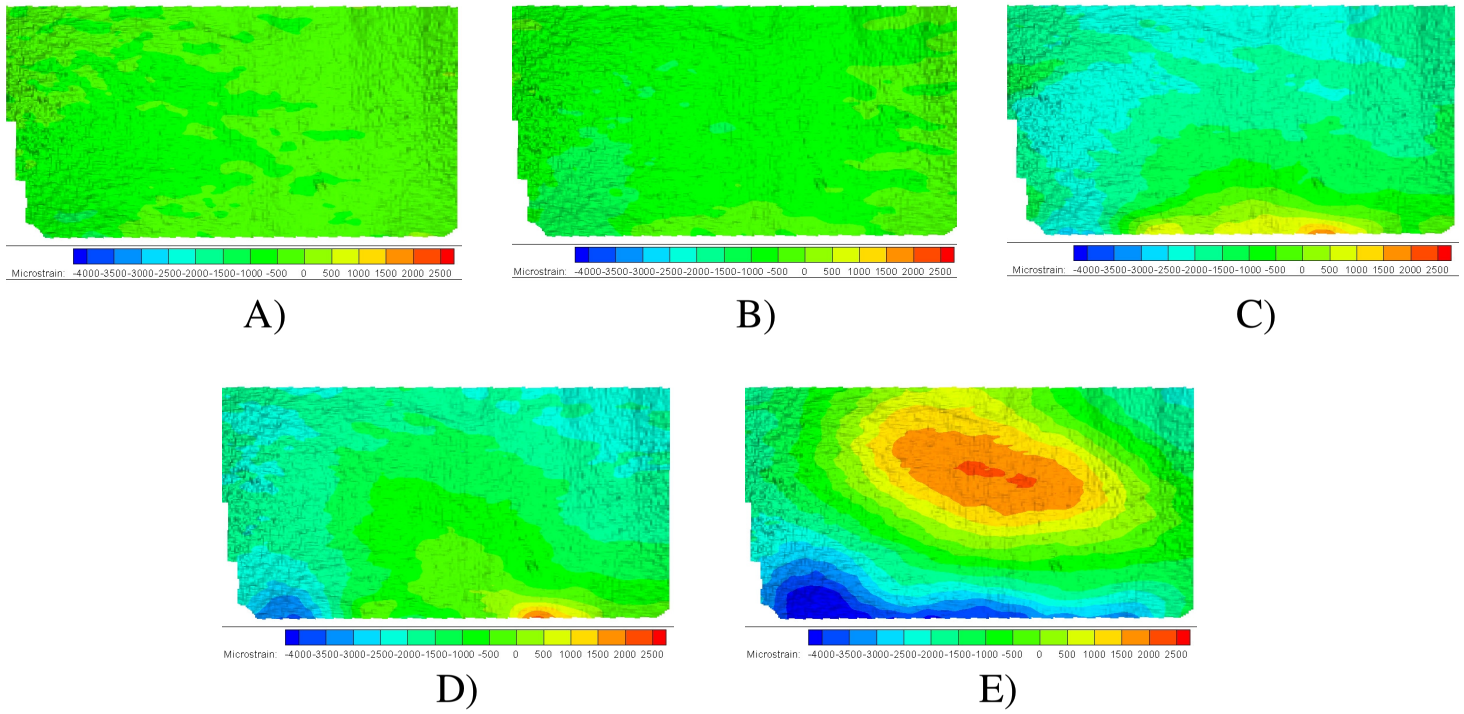

Figure 3.26: Axial Strain measured in Machined Panel 2 from the VIC 3-D System in the lower half of the panel at A) 28.7 kips (pre-buckle) B) 45.5 kips (post-buckle) C) 138.7 (post-buckle) D) 179.5 (maximum load) E) 170.1 (post-failure). Load values expressed in terms of compressive load

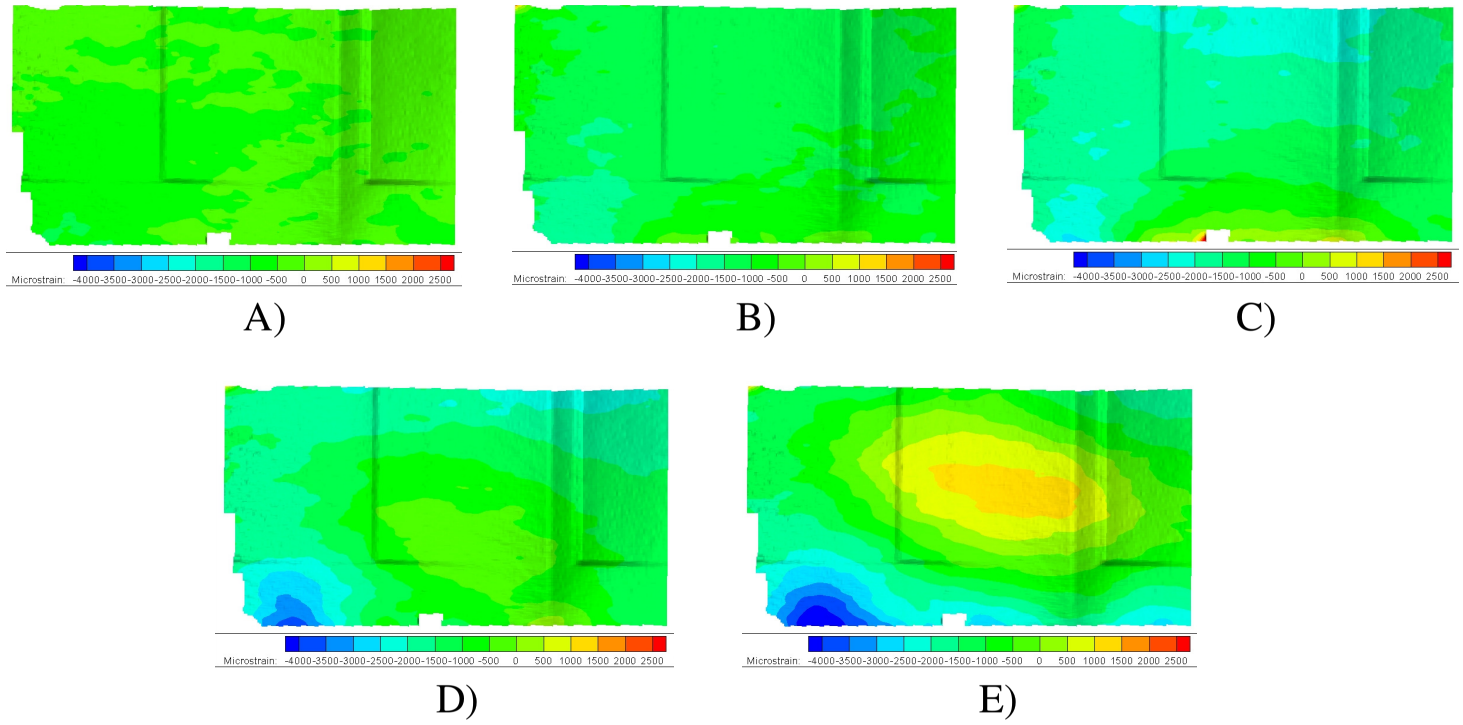

Figure 3.27: Axial Strain measured in EBF^3 Panel 2 from the VIC 3-D System in the lower half of the panel at A) 35.4 kips (pre-buckle) B) 83.5 kips (post-buckle) C) 134.2 (post-buckle) D) 179.5 (maximum load) E) 163.5 (post-failure). Load values expressed in terms of compressive load

3.2 Load Case 2 Results

The loads applied in load case 2 are depicted in Figure 3.28. Supplemental data for load case 2 which were not discussed are found in Appendix B. EBF^3 Panel 4 was tested but no strain gage nor DCDT data were recorded. The test results discussed for EBF^3 Panel 4 were based upon observations during the test.

3.2.1 End-Shortening

The measured end-shortenings from Machined Panels 3 and 4 and EBF^3 Panel 3 as a function of the applied loads are shown in Figure 3.29. The measured data were zeroed from when the loads were established in the test panels. The corrected end-shortenings for Machined Panels 3 and 4 and EBF^3 Panels 3 as a function of the applied loads are shown in Figure 3.30.

There was a gradual transition at the beginning of the tests into the linear relationship between the applied loads and the end-shortening, once zeroing was taken into account. Machined Panel 3 experienced a drop in load at 105 kips compression and can be seen in all of the DCDT and strain measurements for Machined Panel 3 including Figure 3.29. No DCDT or strain measurements were recorded from the start of the test until the load was at 18.3 kips for Machined Panel 4, as shown in Figure 3.29. EBF^3 Panel 3 also had a change in slope at 100 kips compression. Machined Panel 3 had the largest end-shortening for any load and EBF^3 Panel 3 had the smallest end-shortening after a load of 65 kips compression until failure. EBF^3 Panel 3

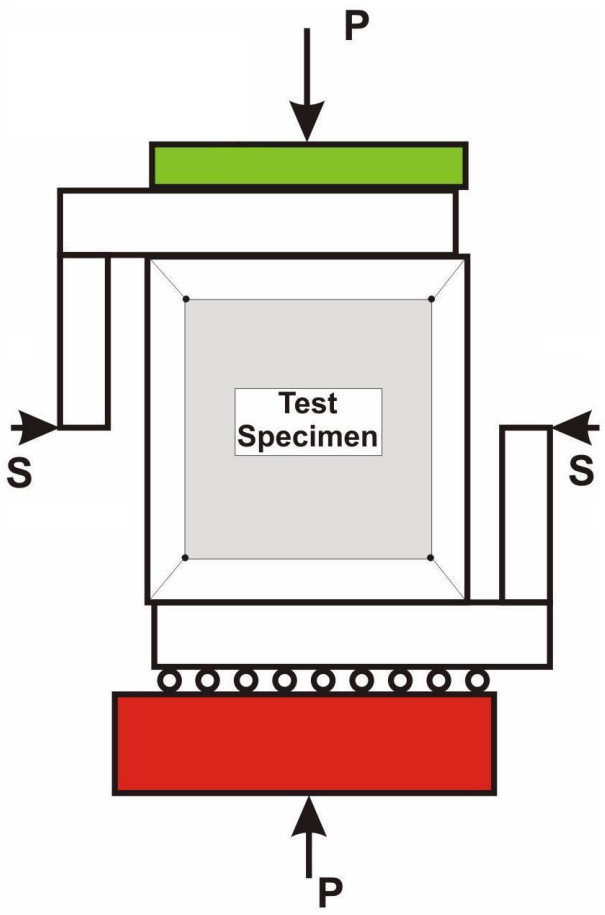

Figure 3.28: Illustration of Load Case 2: P was the compressive load to a maximum of 176.4 kips. S was the shear load at 100% of the compressive load up to a maximum of 100 kips.

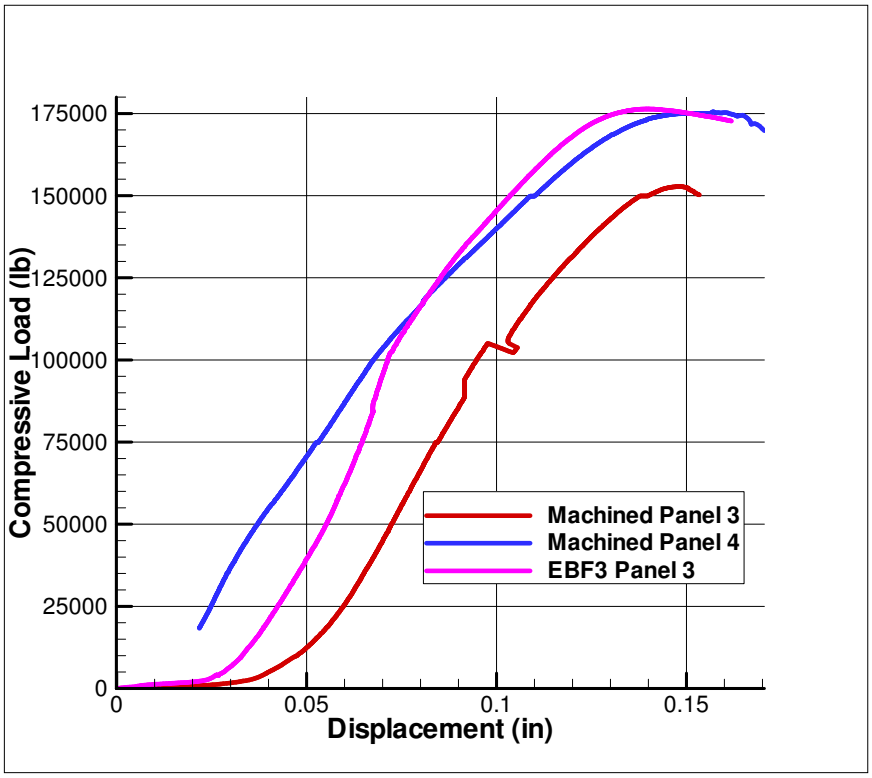

Figure 3.29: Original Measured Experimental End-shortening Results for Load Case 2

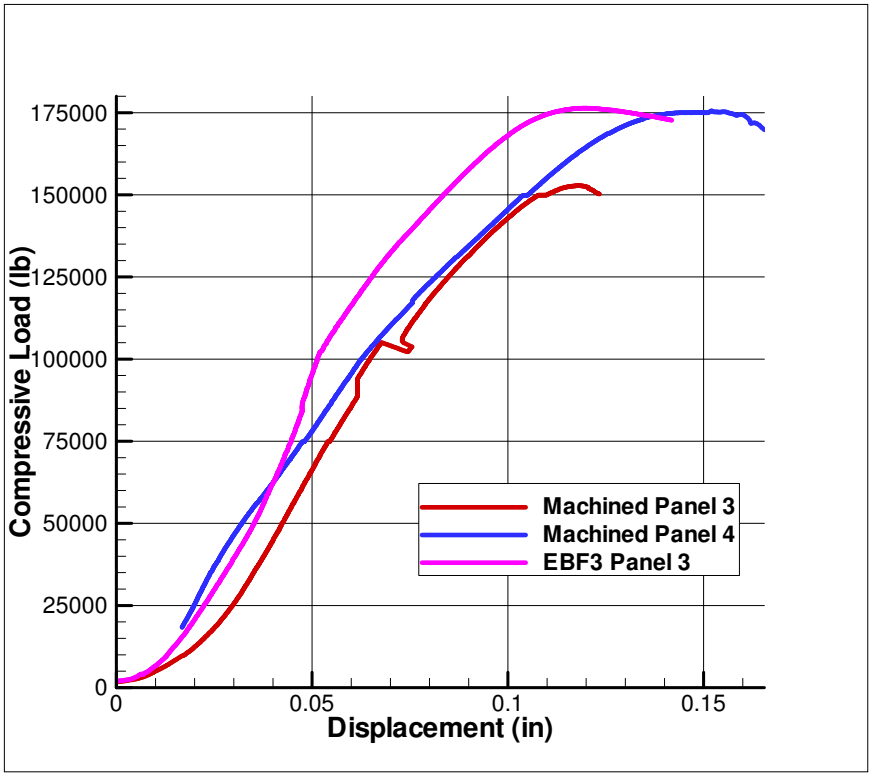

Figure 3.30: Corrected Experimental End-shortening Results for Load Case 2

had a steeper slope than Machined Panels 3 and 4 before loads of 100 kips compression. After a load of 100 kips compression, Machined Panels 3 and 4 and EBF^3 Panel 3 exhibited similar slopes.

The corrected end-shortenings at the maximum compressive loads for load case 2 are listed in Table 3.3. EBF^3 Panel 4's maximum compressive load was recorded but the maximum end-shortening was not. On average, Machined Panel 4 and EBF^3 Panels 3 and 4 had a maximum load within 2% of each other and 14% higher than Machined Panel 3. EBF^3 Panel 3 had 12% lower end-shortening than the average machined panels' end-shortening.

Table 3.3: End-shortening Results for Load Case 2

Panel	End-shortening (in)	Maximum Compressive Load (kips)
Machined Panel 3	0.1171	152.7
Machined Panel 4	0.1519	175.5
EBF^3 Panel 3	0.1187	176.4
EBF^3 Panel 4	Not Recorded	172.6

The rotations of the top platen from DCDT data measured on Machined Panels 3 and 4 and EBF^3 Panel 3 as a function of the applied loads are shown in Figure 3.31. The load platen continually rotated through the all tests across the width of the panels as shown by the angle of rotation alpha. The load platen only rotated initially across the thickness of the panels during the beginning of the tests as shown by the angle of rotation beta.

Machined Panel 3 had the largest angle of rotation alpha and beta values. Machined Panels 3 and 4 and EBF^3 Panel 3 had a large amount of

rotation with only a small amount of load initially. The panels then maintained steady rotation until the failure of the panels.

3.2.2 Lateral Displacement

The shear load applied at the bottom of the panels caused a lateral displacement. The measured lateral displacements from the bottom of the panels as a function of the applied loads are shown in Figure 3.32 for Machined Panels 3 and 4 and EBF^3 Panel 3. The corrected lateral displacements as a function of the applied loads are shown in Figure 3.33 for Machined Panels 3 and 4 and EBF^3 Panel 3.

Machined Panels 3 and 4 and EBF^3 Panel 3 had similar lateral displacements. The maximum lateral displacements for load case 2 are listed in Table 3.4. The maximum shear load for all panels tested in load case 2 was 100 kips. EBF^3 Panel 4's maximum shear displacement was not recorded. EBF^3 Panel 3's maximum shear displacement was 9% lower than Machined Panel 3 and nearly identical to Machined Panel 4.

Table 3.4: Lateral Displacement Results for Load Case 2

Panel	Lateral Displacement (in)
Machined Panel 3	0.2726
Machined Panel 4	0.2466
EBF^3 Panel 3	0.2483
EBF^3 Panel 4	Not Recorded

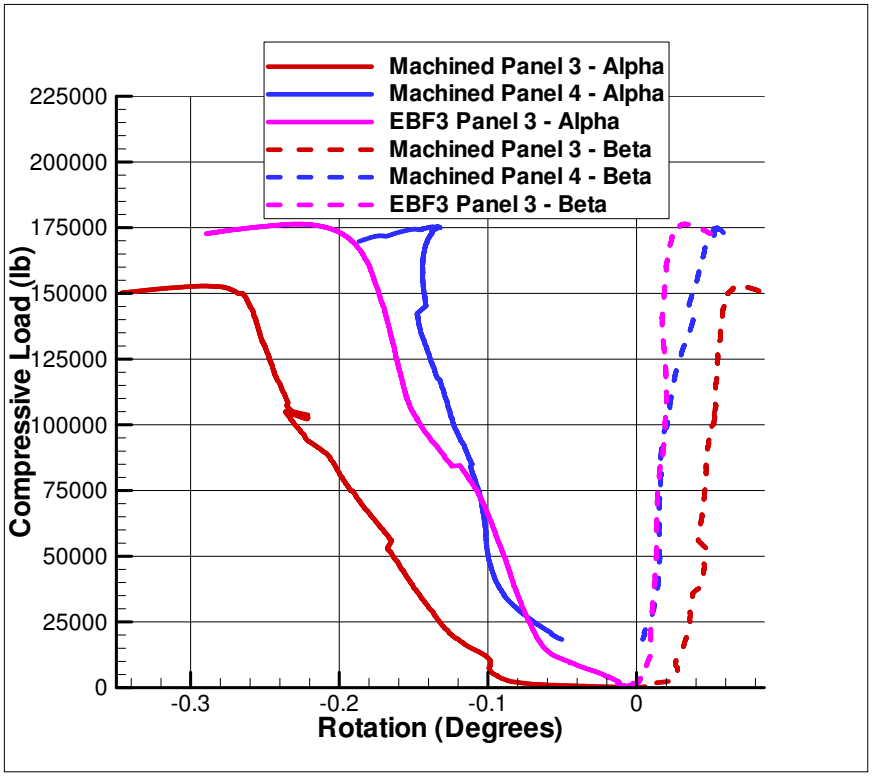

Figure 3.31: Angles of Rotation of the Load Platen for Load Case 2

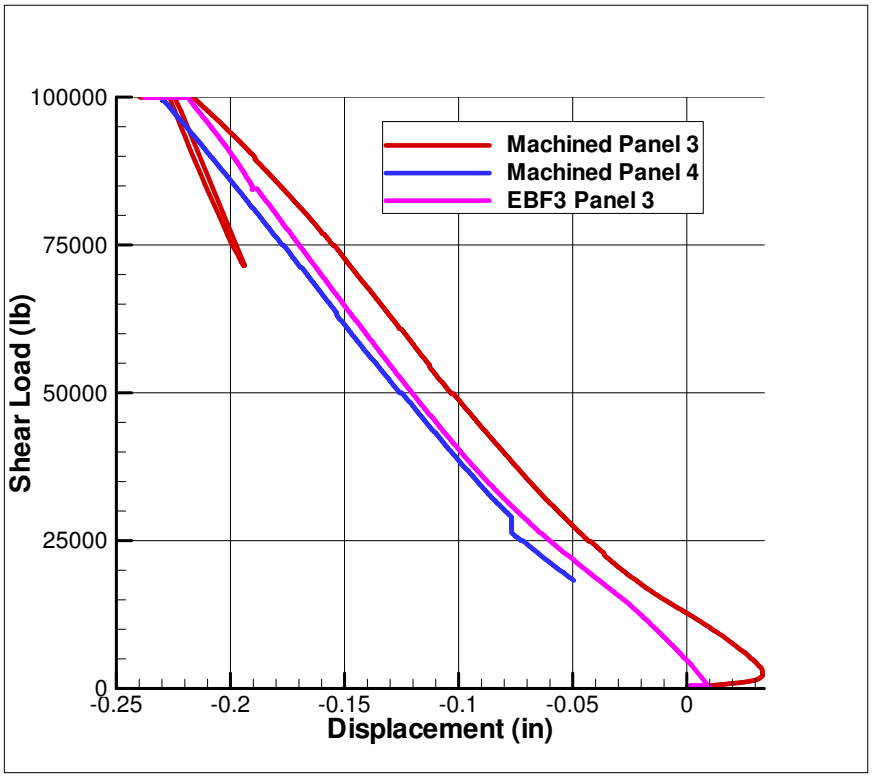

Figure 3.32: Original Measured Experimental Lateral Shear Displacements from the bottom of the Panels for Load Case 2

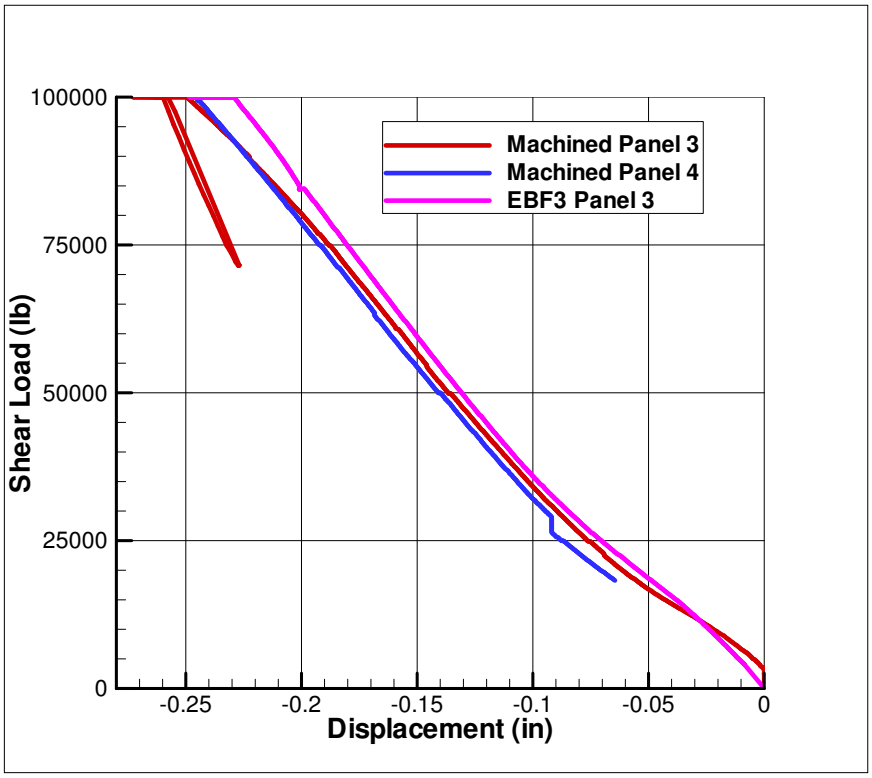

Figure 3.33: Corrected Experimental Lateral Shear Displacements from the bottom of the Panels for Load Case 2

3.2.3 Out-Of-Plane Displacement

The out-of-plane displacements measured by Direct Current Displacement Transducers (DCDTs) 1, 2, and 3 as a function of the applied loads are shown in Figure 3.34 for Machined Panels 3 and 4 and Figure 3.35 for EBF^3 Panel 3. Machined Panels 3 and 4 had a small amount of out-of-plane displacement in the upper half of the panels when the compressive load was below 35 kips. Machined Panel 3 showed an inflection point at a load of 33 kips compression and Machined Panel 4 showed an inflection point at a load of 37 kips compression. At a load of 100 kips compression, the slopes of the out-of-plane displacement curves decreased for the machined panels again.

The EBF^3 panels showed completely different results than the machined panels. EBF^3 Panel 3 had almost zero out-of-plane displacement at loads below 100 kips compression. At a load of 100 kips compression, EBF^3 Panel 3 showed a clear inflection point by the significant change in the out-of-plane displacement. The out-of-plane displacement in the upper half of the panel quickly decreased approximately -0.05 inches. EBF^3 Panel 3 had negative displacement for the remainder of the test.

Typically, DCDT 2 measured the largest out-of-plane displacement for Machined Panels 3 and 4 and EBF^3 Panel 3 in the top half of the panels. DCDT 1 measured higher out-of-plane displacement than DCDT 3 for Machined Panel 3 and the opposite happened for Machine Panel 4. The EBF^3 panels had a very similar magnitude of out-of-plane displacements between DCDT 1 and 3.

The out-of-plane displacements measured by DCDTs 4, 5, and 6 as a function of the applied loads are shown in Figures 3.36 and 3.37 for Machined Panel 3 and EBF^3 Panel 3 respectively. Machined Panel 3 had an inflection point at a load of 33 kips compression. Machined Panel 3 had an out-of-plane displacement reversal as measured by DCDTs 4, 5, and 6 at the end of the test.

EBF^3 Panel 3 showed similar results in the lower half of the panel compared to the upper half at loads below 100 kips compression. There was a very small amount of positive out-of-plane displacement at loads below 100 kips compression, less than 0.05 inches. All three DCDTs measured an immediate decrease in out-of-plane displacement as shown by the "C" shaped curve of the measured out-of-plane displacement between loads of 100 and 140 kips compression.

Machined Panel 3 had the largest out-of-plane displacement measured from DCDT 5 at loads below 85 kips compression, after which DCDT 6 measured the largest out-of-plane displacement. DCDT 5 measured the largest out-of-plane displacement at loads below 100 kips compression for EBF^3 Panel 3. Between loads of 100 kips and 135 kips compression, DCDT 4 had the largest out-of-plane displacement for EBF^3 Panel 3. After a load of 135 kips compression, DCDT 5 measured the largest out-of-plane displacement until the end of the test for EBF^3 Panel 3. Furthermore, the out-of-plane displacement in the lower half was significantly lower than in the upper half of the panel. The upper half of the panels showed a maximum out-of-plane displace-

ment for Machined Panels 3 and 4 and EBF^3 Panel 3 at approximately 0.5 inches, as where the lower half of the panel showed a maximum out-of-plane displacement near 0.3 inches.

3.2.4 Strain in the Panels

The axial strains measured from strain gages 1a-4a as a function of the applied loads are shown in Figure 3.38 for Machined Panels 3 and 4 and Figure 3.39 for EBF^3 Panel 3. Machined Panel 3 had linear results at loads below 69 kips compression. At a load of 69 kips compression, strain gages 3a and 4a showed a sharp change in slope and the results remained linear but at a shallower slope. Machined Panel 4 showed a change in slope at a load of 34 kips compression in strain gages 3a and 4a but also remained linear. After a load of 100 kips compression, Machined Panels 3 and 4 started to show nonlinear behavior in strain gages 1a-4a. Machined Panels 3 and 4 showed larger strains in strain gages 3a and 4a than in strain gages 1a and 2a.

EBF^3 Panel 3 showed linear results at loads below 100 kips compression, and conversely at loads after 100 kips compression, nonlinear results were seen. EBF^3 Panel 3 also exhibited larger strains in strain gages 3a and 4a than in strain gages 1a and 2a. Strain gages 3a for Machined Panels 3 and 4 and strain gage 4a for EBF^3 Panel 3 measured strains that surpassed the capabilities of the test machine collection system of $\pm$15,000 microstrain. Once the strains were larger than $\pm$15,000 microstrain, no more data were collected. In order to see data from the other strain gages in Figure 3.38 and 3.39, the

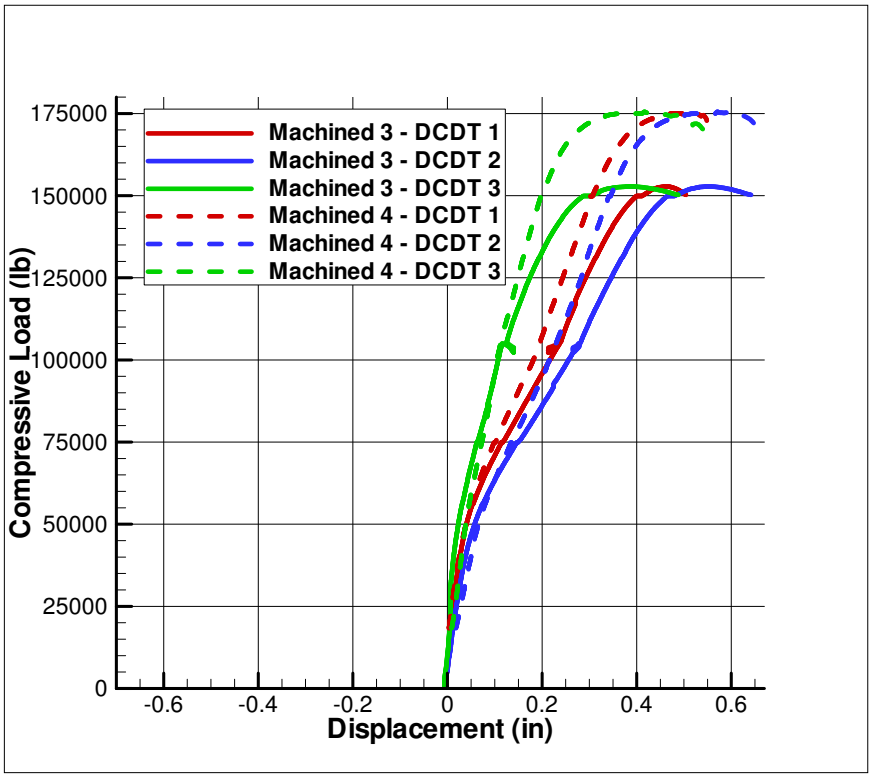

Figure 3.34: Out-Of-Plane Displacement measured by DCDT 1, 2, and 3 for Machined Panels 3 and 4

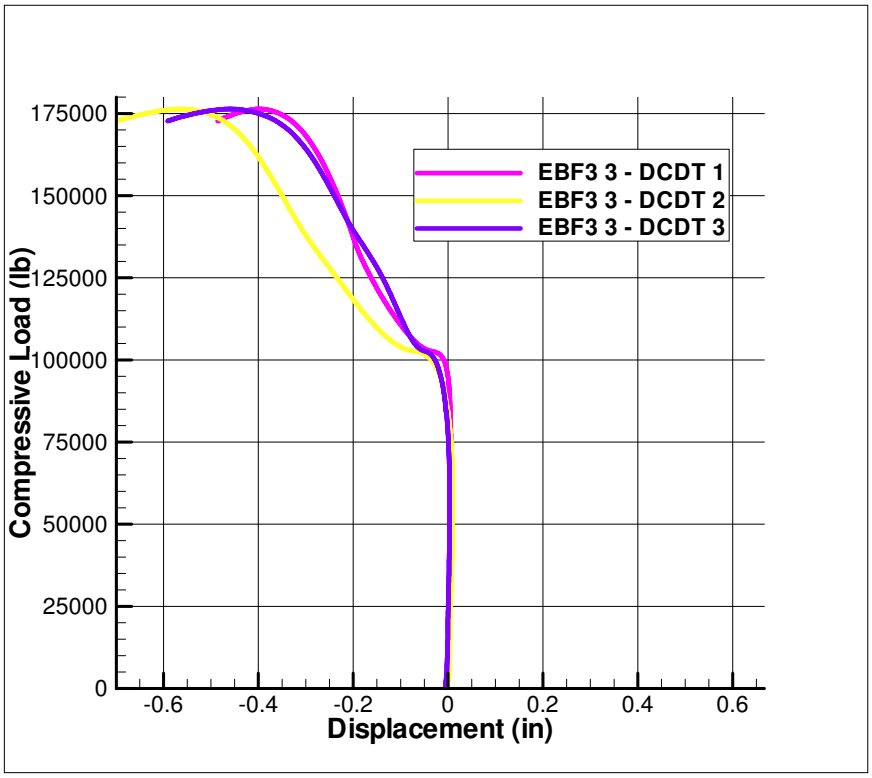

Figure 3.35: Out-Of-Plane Displacement measured by DCDT 1, 2, and 3 for EBF^3 Panel 3

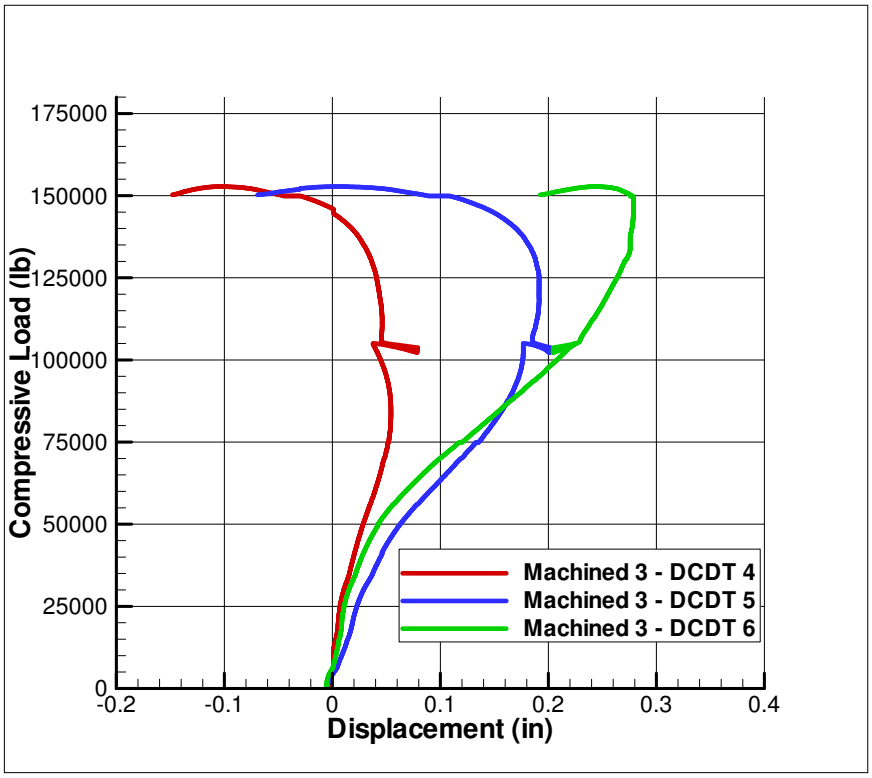

Figure 3.36: Out-Of-Plane Displacement measured by DCDT 4, 5, and 6 for Machined Panel 3

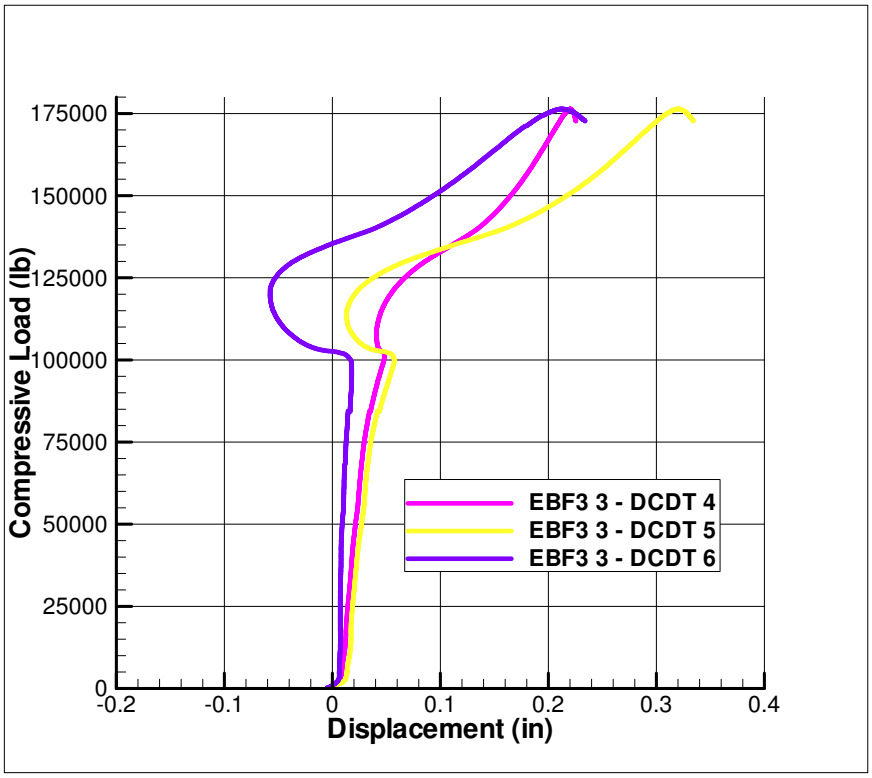

Figure 3.37: Out-Of-Plane Displacement measured by DCDT 4, 5, and 6 for EBF^3 Panel 3

data larger than -8000 microstrain were not shown. Strain gage 3a for Machined Panel 3 reached -15,000 microstrain at a load of 152.6 kips compression, strain gage 3a for Machined Panel 4 reached -15,000 microstrain at a load of 175.3 kips compression, and strain gage 4a for EBF^3 Panel 3 reached -15,000 microstrain at a load of 176.3 kips compression.

The axial strains measured from strain gages 1b-4b as a function of the applied loads are shown in Figure 3.40 for Machined Panels 3 and 4 and Figure 3.41 for EBF^3 Panel 3. There were little lateral strains measured in strain gages 1b and 2b for most of the tests. Strain gages 3b and 4b measured less than 1000 microstrain from Machined Panels 3 and 4 and EBF^3 Panel 3 prior to failure. Strain gages 3b and 4b started to measure a small amount of strain at approximately a load of 50 kips compression for the machined panels and a load of 20 kips compression for the EBF^3 panels. At the end of the tests, strain gages 3b and 4b measured almost an instantaneous increase in strain for all panels.

The axial strains measured from strain gages 5a-8a as a function of the applied loads are shown in Figure 3.42 for Machined Panels 3 and 4 and Figure 3.43 for EBF^3 Panel 3. The strain results for Machined Panels 3 and 4 in strain gages 5a-8a were linear at loads below approximately 55 kips compression. After a load of 55 kips compression, the results became nonlinear until failure. Strain gages 7a and 8a showed the largest change in strain after a load of 50 kips.

EBF^3 Panel 3 remained linear at loads below 100 kips compression.

After which, a "C" shaped curve in the measured axial strains between loads of 100 kips and 140 kips compression for strain gages 5a and 6a can be seen. Strain gages 7a and 8a measured a small amount of nonlinear axial strain after a load of 100 kips compression. EBF^3 Panel 3, in general, showed slightly lower strain results than Machined Panels 3 and 4.

The lateral strains measured from strain gages 5b-8b as a function of the applied loads are shown in Figures 3.44 and 3.45 for Machined Panels 3 and 4 and EBF^3 Panel 3 respectively. The lateral strain measurements for the machined panels were linear at loads below approximately 55 kips compression, after which the results became nonlinear until failure.

EBF^3 Panel 3 showed linear results at loads below 100 kips compression. At loads between 100 kips and 140 kips compression, an increase was measured by the strain gages located on the top of the panel while a decrease in strain was seen by strain gages located on the bottom of the panel. Also, EBF^3 Panel 3 showed drastically different lateral strains in strain gages 5b-8b than Machined Panels 3 and 4. Machined Panels 3 and 4 exhibited negative strains in strain gages 5b and 7b and exhibited strains larger than 2000 microstrain in strain gages 6b and 8b. EBF^3 Panel 3 exhibited small positive strains below 1000 microstrain from strain gages 5b-8b and exhibited no negative strain.

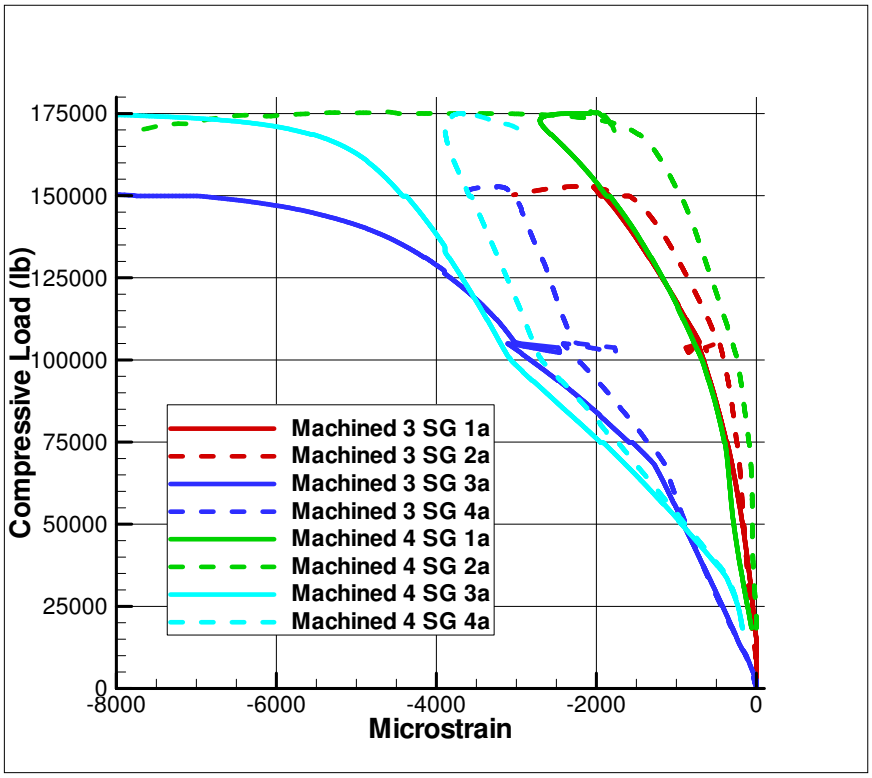

Figure 3.38: Axial Strains measured from Strain Gages 1a-4a for Machined Panels 3 and 4

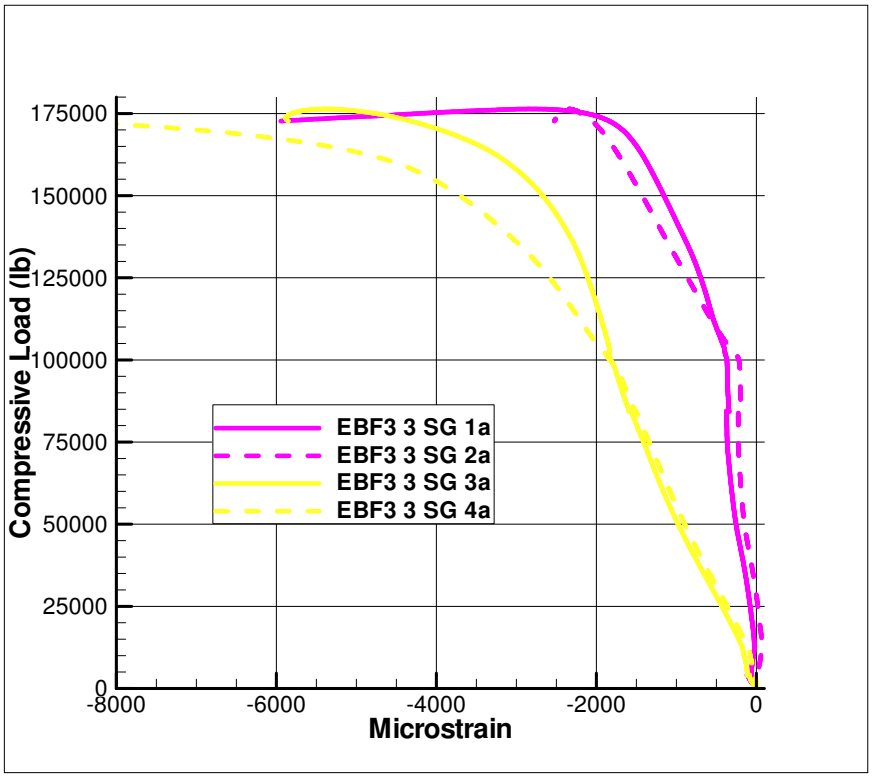

Figure 3.39: Axial Strains measured from Strain Gages 1a-4a for EBF^3 Panel 3

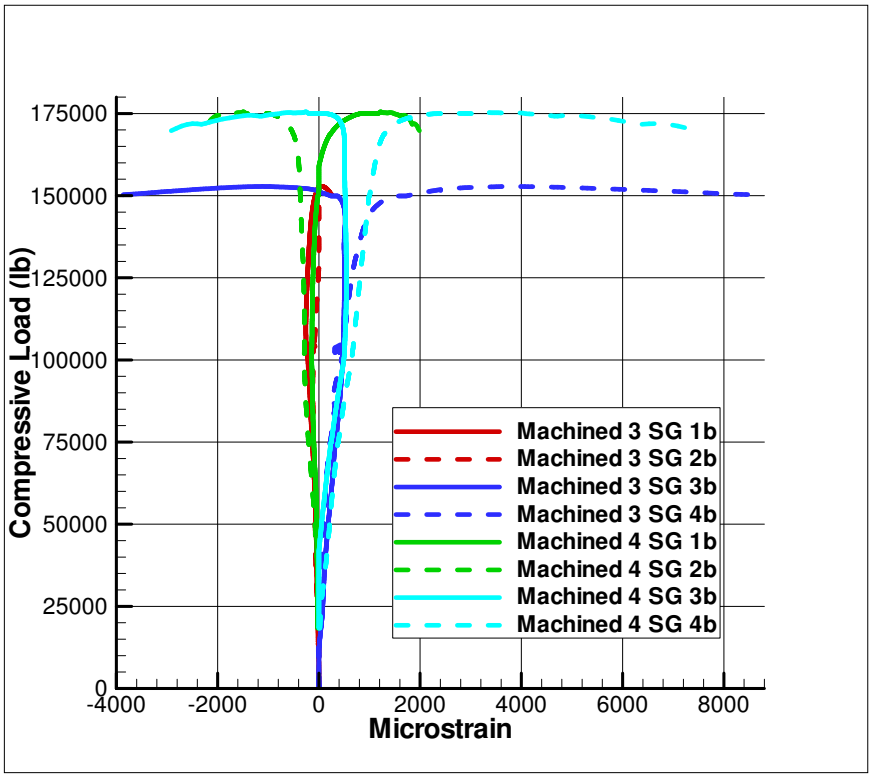

Figure 3.40: Axial Strains measured from Strain Gages 1b-4b for Machined Panels 3 and 4

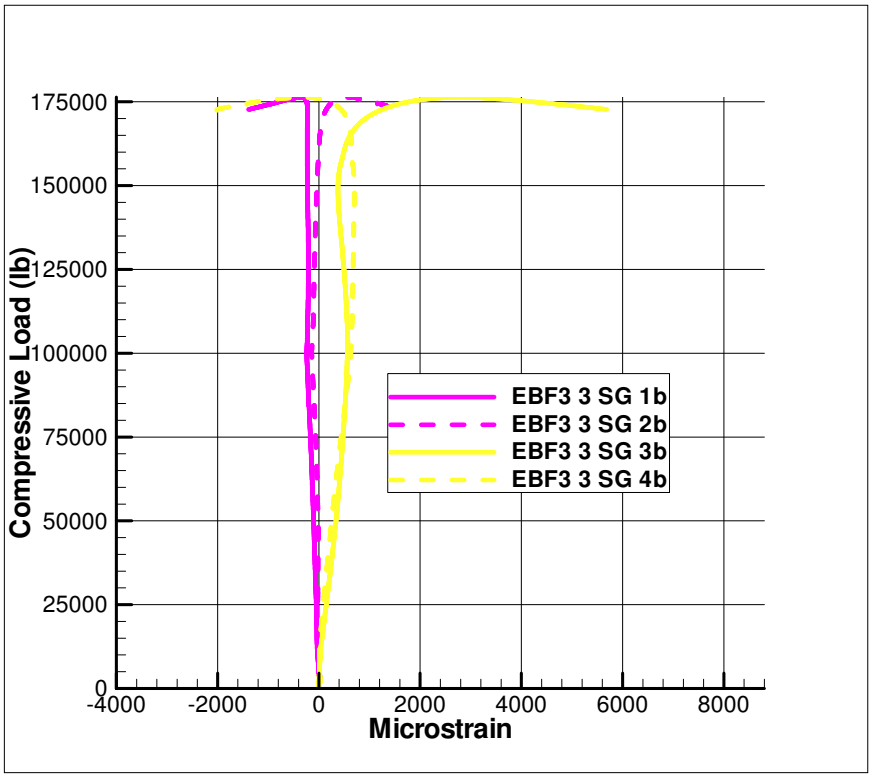

Figure 3.41: Axial Strains measured from Strain Gages 1b-4b for EBF^3 Panel 3

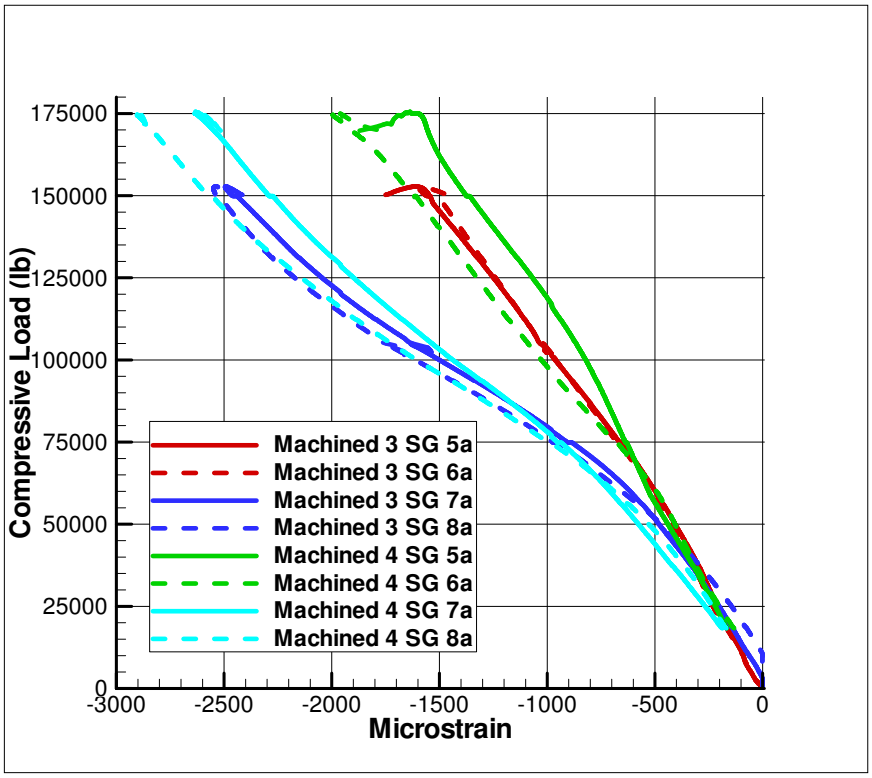

Figure 3.42: Axial Strains measured from Strain Gages 5a-8a for Machined Panels 3 and 4

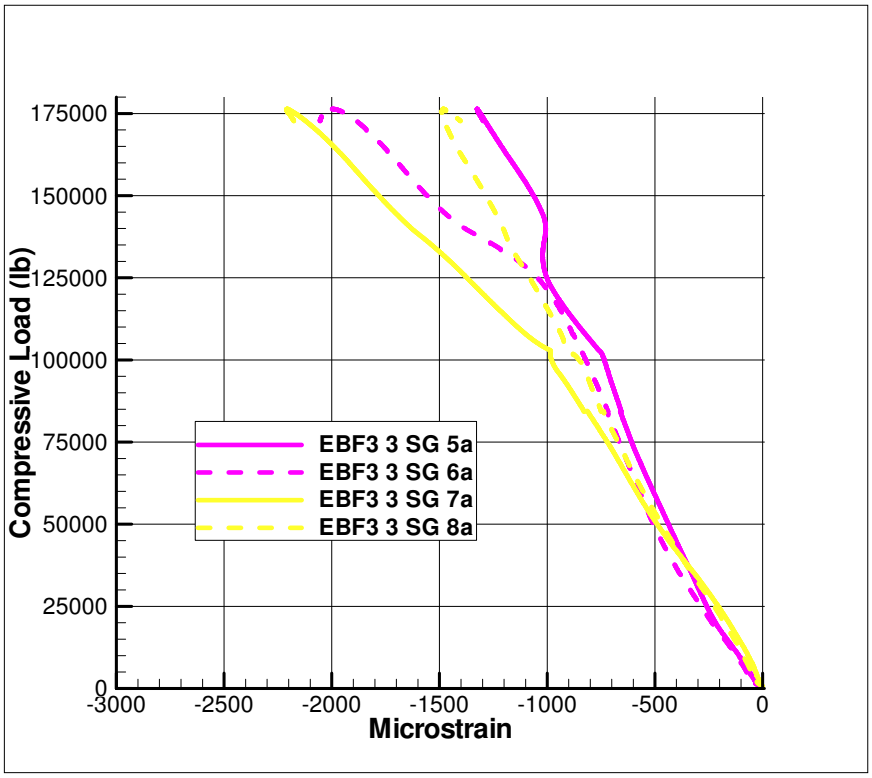

Figure 3.43: Axial Strains measured from Strain Gages 5a-8a for EBF^3 Panel 3

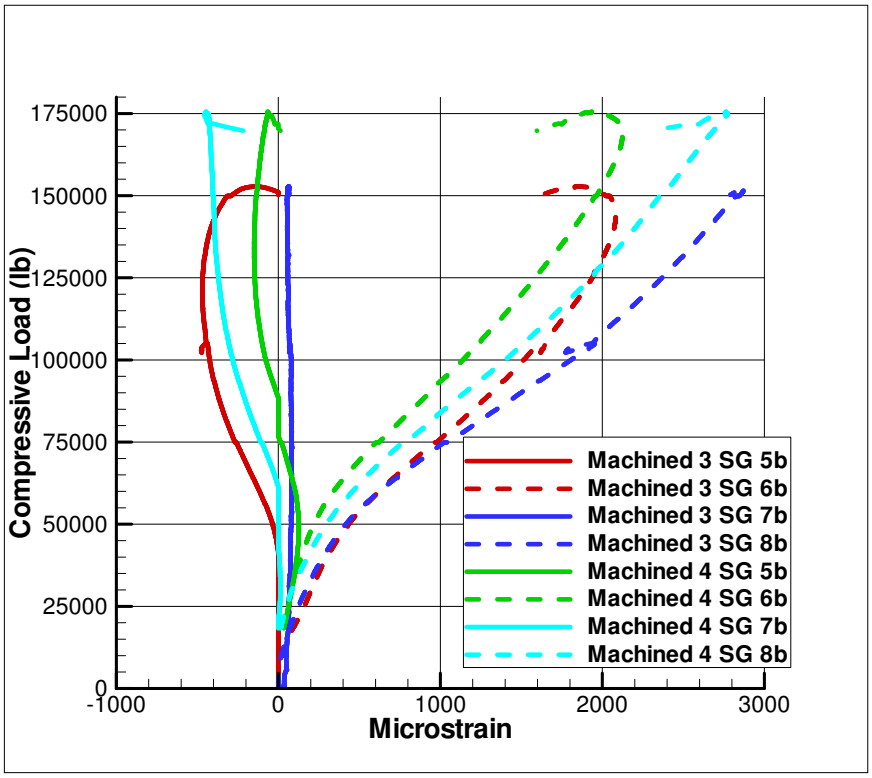

Figure 3.44: Lateral Strains measured from Strain Gages 5b-8b for Machined Panels 3 and 4

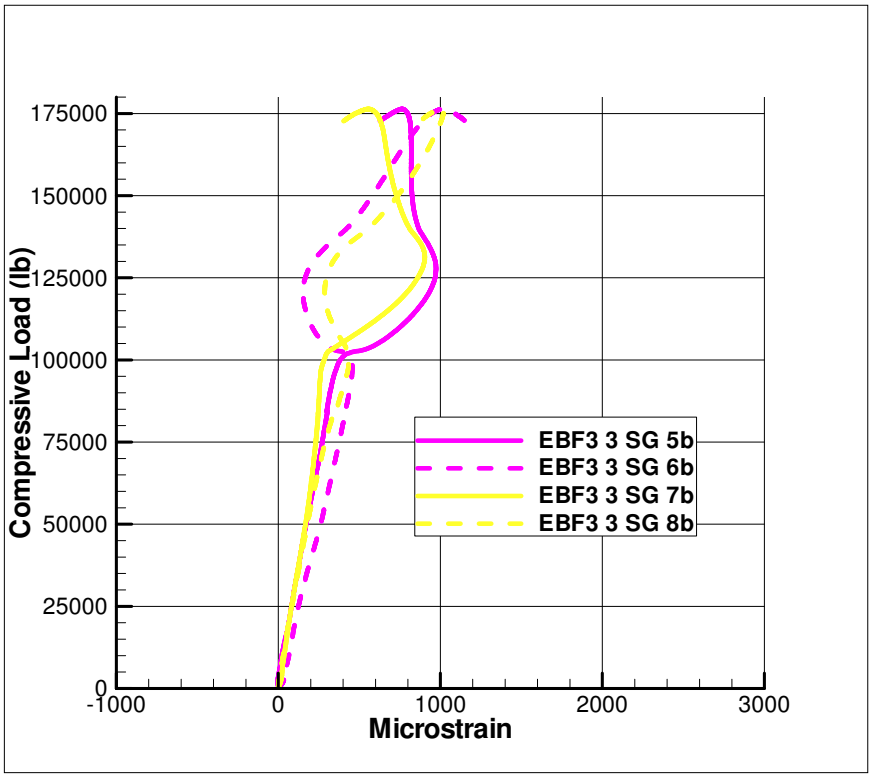

Figure 3.45: Lateral Strains measured from Strain Gages 5b-8b for EBF^3 Panel 3

3.2.5 Strain in the Stiffeners

The axial strains in the stiffeners measured by strain gages 25a-28a as a function of the applied loads are shown in Figure 3.46 for Machined Panels 3 and 4 and Figure 3.47 for EBF^3 Panel 3. The machined panels exhibited a small amount of negative strain when the load was introduced. At a load of 33 kips compression for Machined Panel 3 and 37 kips compression for Machined Panel 4, the strain started to reverse direction becoming positive.

After crossing the y-axis at load of approximately 60 kips, the strain remained positive until failure of the panels. Strain gages 25a-28a measured a linear relationship between the measured axial strains and the applied loads at loads between 55 kips and 100 kips compression in the machined panels. After a load of 100 kips compression the strain variation became nonlinear until failure.

EBF^3 Panel 3 showed radically different results than the machined panels in strain gages 25a-28a. The relationships between the axial strains and applied loads were linear until a load of 100 kips compression. After which, EBF^3 Panel 3 had nonlinear behavior with a "C" shaped curve in the measured axial strain, at loads between approximately 100 kips and 140 kips compression.

The lateral strains in the stiffeners measured by strain gages 25b, 27b, and 28b as a function of the applied loads for Machined Panel 3 and strain gages 25b-28b for Machined Panel 4 are shown in Figure 3.48. The lateral strains in the stiffeners measured by strain gages 25b-28b as a function of the

applied loads for EBF^3 Panel 3 are shown in Figure 3.49. The lateral strain measurements are the opposite of the axial strain measurements in strain gages 25a-28a for Machined Panels 3 and 4 and EBF^3 Panel 3. There was no measured strain in all of the stiffener strain gages at loads below 55 kips compression except in strain gages 27b and 28b for Machined Panel 4. Strain gages 27b and 28b for Machined Panel 4 measured little positive lateral strains at loads below 60 kips compression. All strain gages had positive linear strain measurements at loads between 55 and 100 kips compression with the exception of strain gages 27b and 28b for Machined Panel 4. After a load of 100 kips compression, Machined Panels 3 and 4 showed nonlinear behavior from the lateral strain measured in the stiffeners.

EBF^3 Panel 3 exhibited radically different results in strain gage 25a-28a than the machined panels. The relationships between the axial strains and applied loads were linear until a load of 100 kips compression, after which the panel exhibited nonlinear behavior as seen by the reversed "C" shaped curve in the lateral strain at loads between approximately 100 kips and 140 kips compression.

Strain gages 27a, 27b, 28a, and 28b measured larger strain in magnitude than in strain gages 25a, 25b, 26a, and 26b at failure as shown in Figures 3.46, 3.47, 3.48, and 3.49. Again, EBF^3 Panel 3 behaved significantly different than the machined panels. For nearly the entirety of the test, EBF^3 Panel 3 exhibited the opposite sign of measured strain than in the machined panels. EBF^3 Panel 3 had linear results until a higher load and showed drastically

different nonlinear results than the machined panels.

3.2.6 Video Image Correlation 3-D Measurement System Results

The out-of-plane displacement measured from the VIC 3-D system is shown in Figures 3.50 and 3.51 for Machined Panels 3 and 4 respectively, and Figures 3.52 and 3.53 for EBF^3 Panels 3 and 4 respectively. For both panels, a point before buckling, two points post-buckle, the point at maximum load, and a point post-failure were chosen to compare for VIC 3-D data analysis. The machined panels exhibit positive out-of-plane displacement as shown by the green and red areas before failure. After failure, negative out-of-plane displacement was evident, shown by the blue area. EBF^3 Panel 3 showed little out-of-plane displacement initially and negative out-of-plane displacement after buckling. After buckling, positive out-of-plane displacement was measured as shown in Figures 3.52(C,D,E) and 3.53(C,D,E). EBF^3 Panel 4 showed little out-of-plane displacement before buckling and positive out-of-plane displacement afterwards. EBF^3 Panel 4 had only positive out-of-plane displacement in the lower half of the panel and larger out-of-plane displacement than EBF^3 Panel 3 after buckling.

The axial strain measured in the lower half of the panel from the VIC 3-D system is shown in Figures 3.54 and 3.55 for Machined Panels 3 and 4 respectively. Axial strain measurements are shown at the same load levels as was shown in Figure 3.50 and 3.51. Both machined panels experienced larger

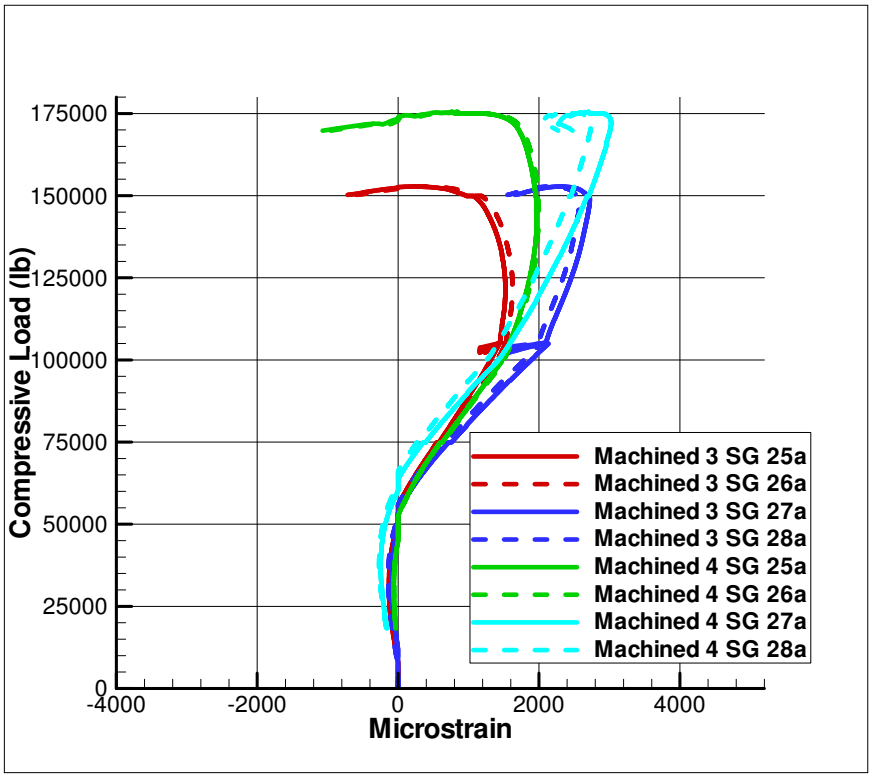

Figure 3.46: Axial Strain in the stiffeners measured from Strain Gages 25a-28a for Machined Panels 3 and 4

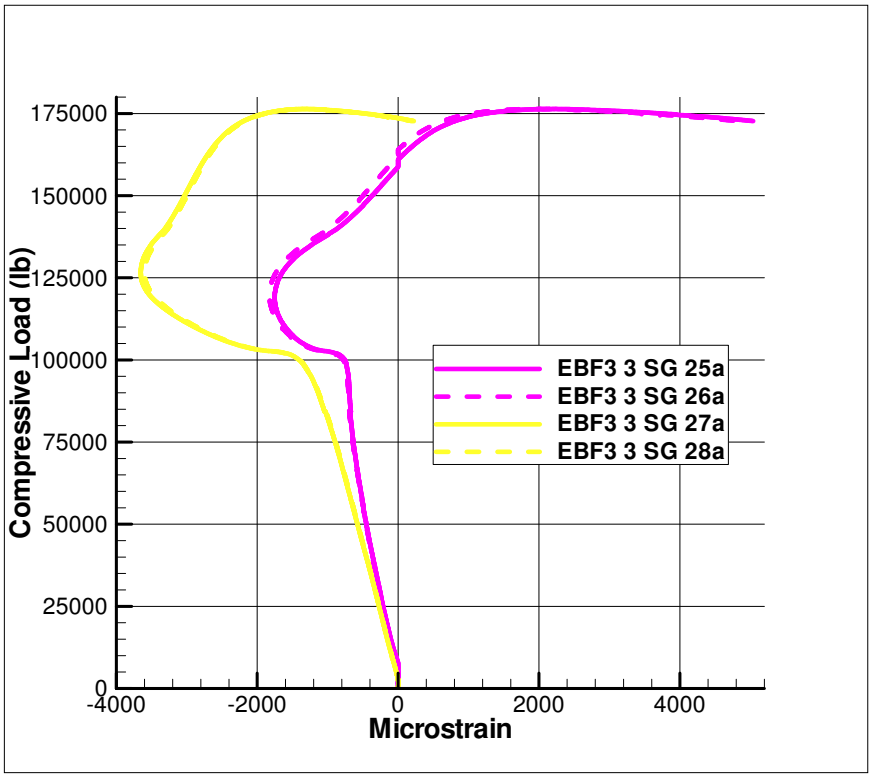

Figure 3.47: Axial Strain in the stiffeners measured from Strain Gages 25a-28a for EBF^3 Panel 3

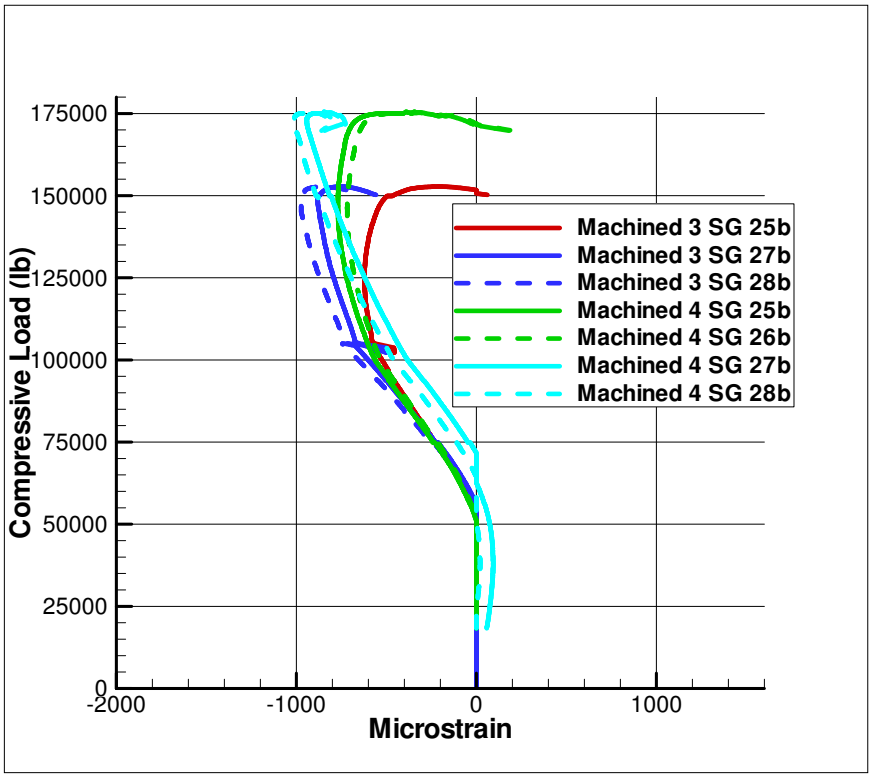

Figure 3.48: Lateral Strain in the stiffeners measured from Strain Gages 25b-28b for Machined Panels 3 and 4

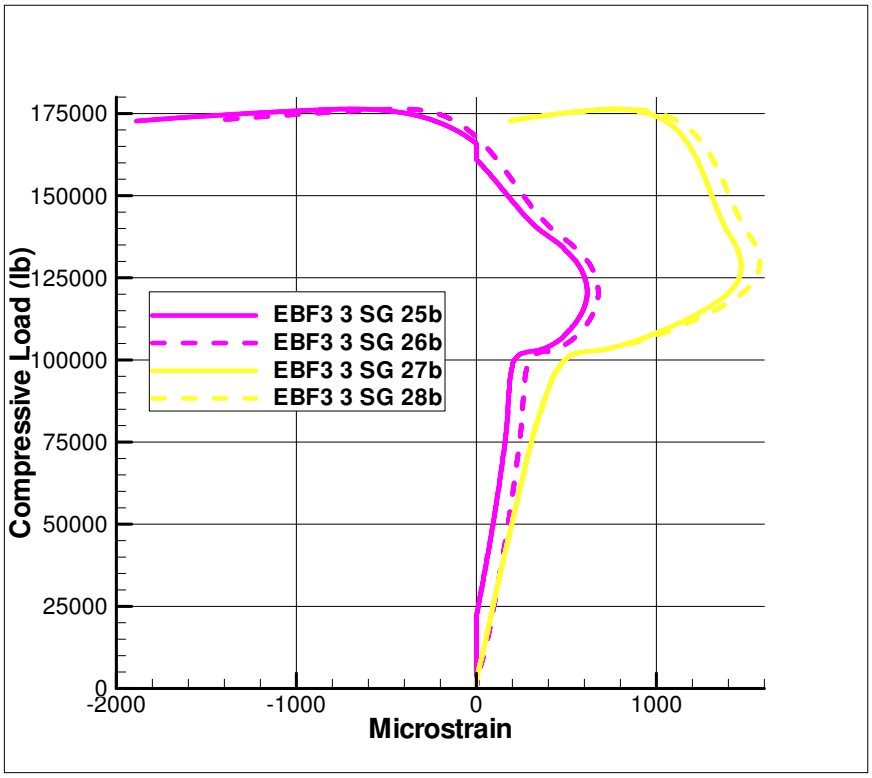

Figure 3.49: Lateral Strain in the stiffeners measured from Strain Gages 25b-28b for EBF^3 Panel 3

strain in the bottom left corner, than in the rest of the panels, propagating to the top of the pictures, corresponding to the middle of the panels. After failure of the panels, a large amount of positive strain was measured in the middle of the lower half of the panels. There was also an area of strain concentration at the bottom edge of the panels as shown in Figures 3.54(C,D,E) and 3.55(C,D,E).

The axial strain measured in the lower half of the panels from the VIC 3-D system is shown in Figures 3.56 and 3.57 for EBF^3 Panels 3 and 4 respectively. Axial strain measurements are shown at the same load levels as was shown in Figure 3.52 and 3.53. Both EBF^3 panels experienced larger strain in the bottom left corner, than in the rest of the panels, propagating to the middle of the picture which correlated with the lower part of the panels. EBF^3 Panel 4 had larger strain than EBF^3 Panel 3. Lastly, there was an area of strain concentration at the bottom edge of the panels as shown in Figures 3.56(C,D,E) and 3.57(C,D,E).

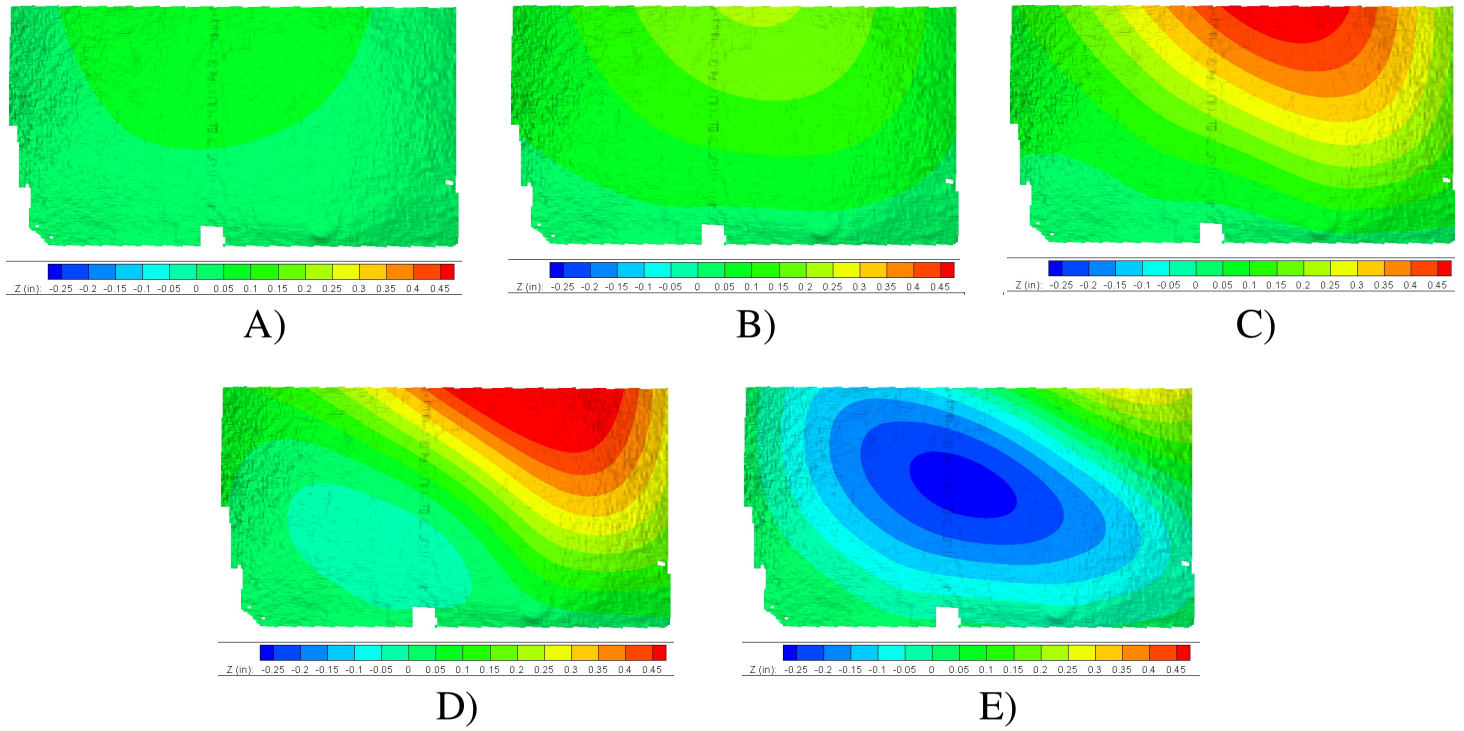

Figure 3.50: Out-of-plane Displacement measured in Machined Panel 3 from the VIC 3-D System in the lower half of the panel at A) 26.8 kips (pre-buckle) B) 61.5 kips (post-buckle) C) 110.2 (post-buckle) D) 152.7 (maximum load) E) 144.3 (post-failure). Load values expressed in terms of compressive load

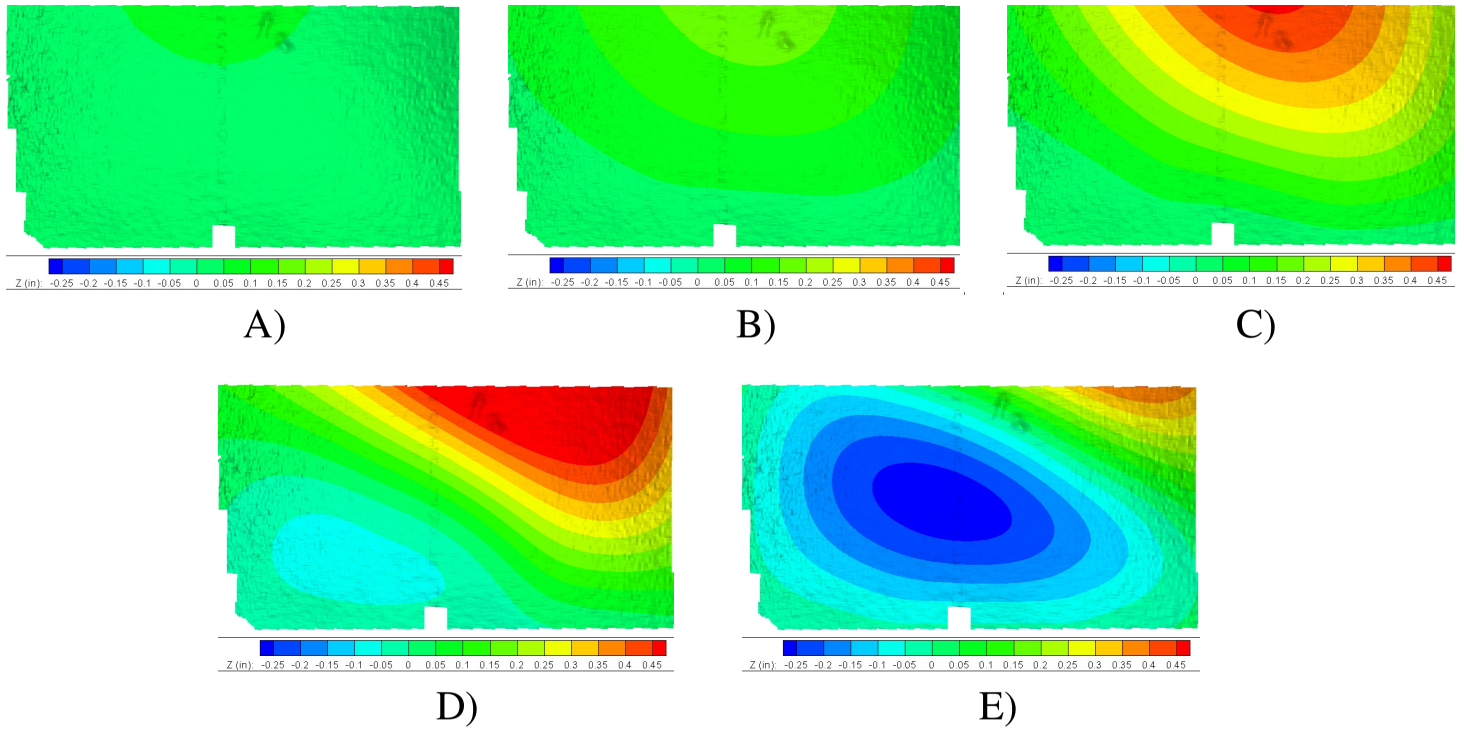

Figure 3.51: Out-of-plane Displacement measured in Machined Panel 4 from the VIC 3-D System in the lower half of the panel at A) 28.5 kips (pre-buckle) B) 62.2 kips (post-buckle) C) 110.5 (post-buckle) D) 175.5 (maximum load) E) 167.6 (post-failure). Load values expressed in terms of compressive load

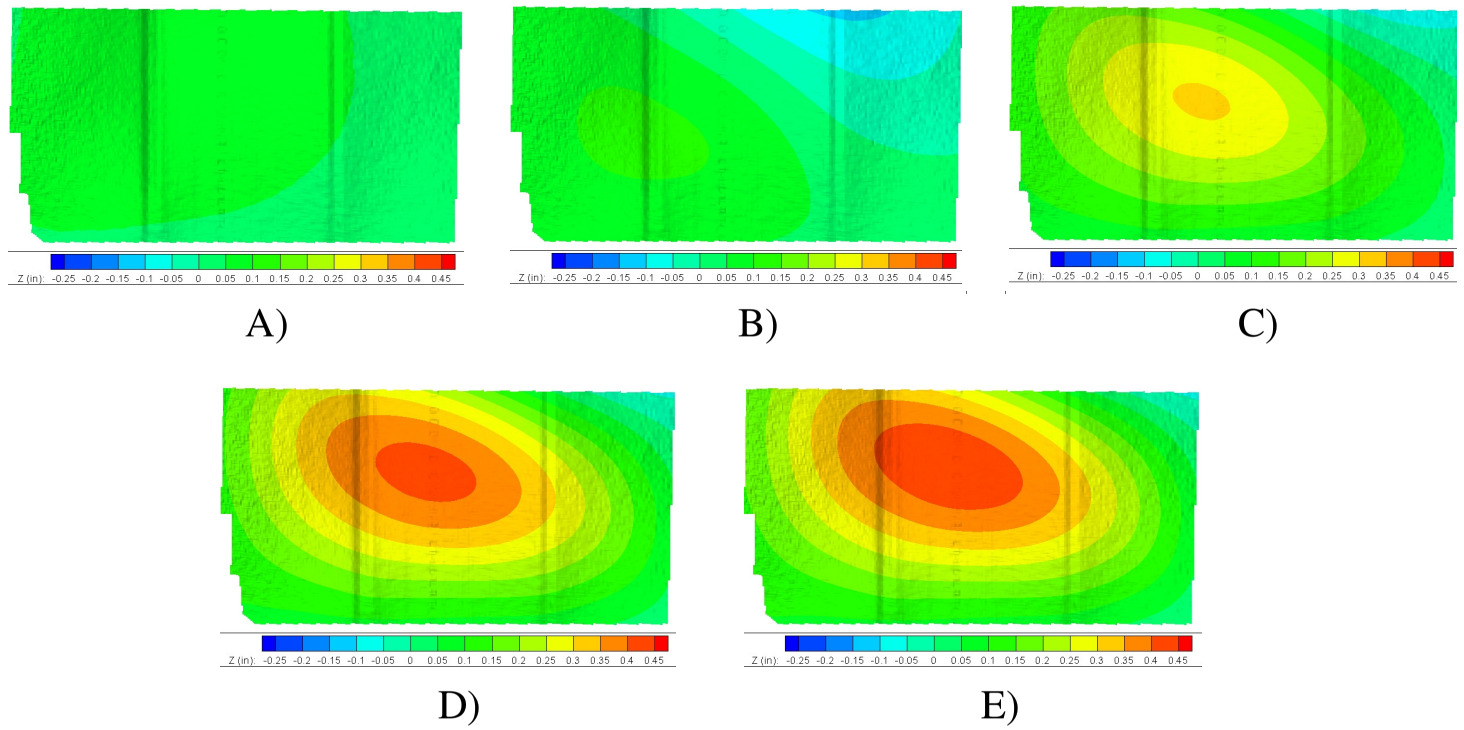

Figure 3.52: Out-of-plane Displacement measured in EBF^3 Panel 3 from the VIC 3-D System in the lower half of the panel at A) 39.3 kips (pre-buckle) B) 113.9 kips (post-buckle) C) 150.8 (post-buckle) D) 176.4 (maximum load) E) 170.7 (post-failure). Load values expressed in terms of compressive load

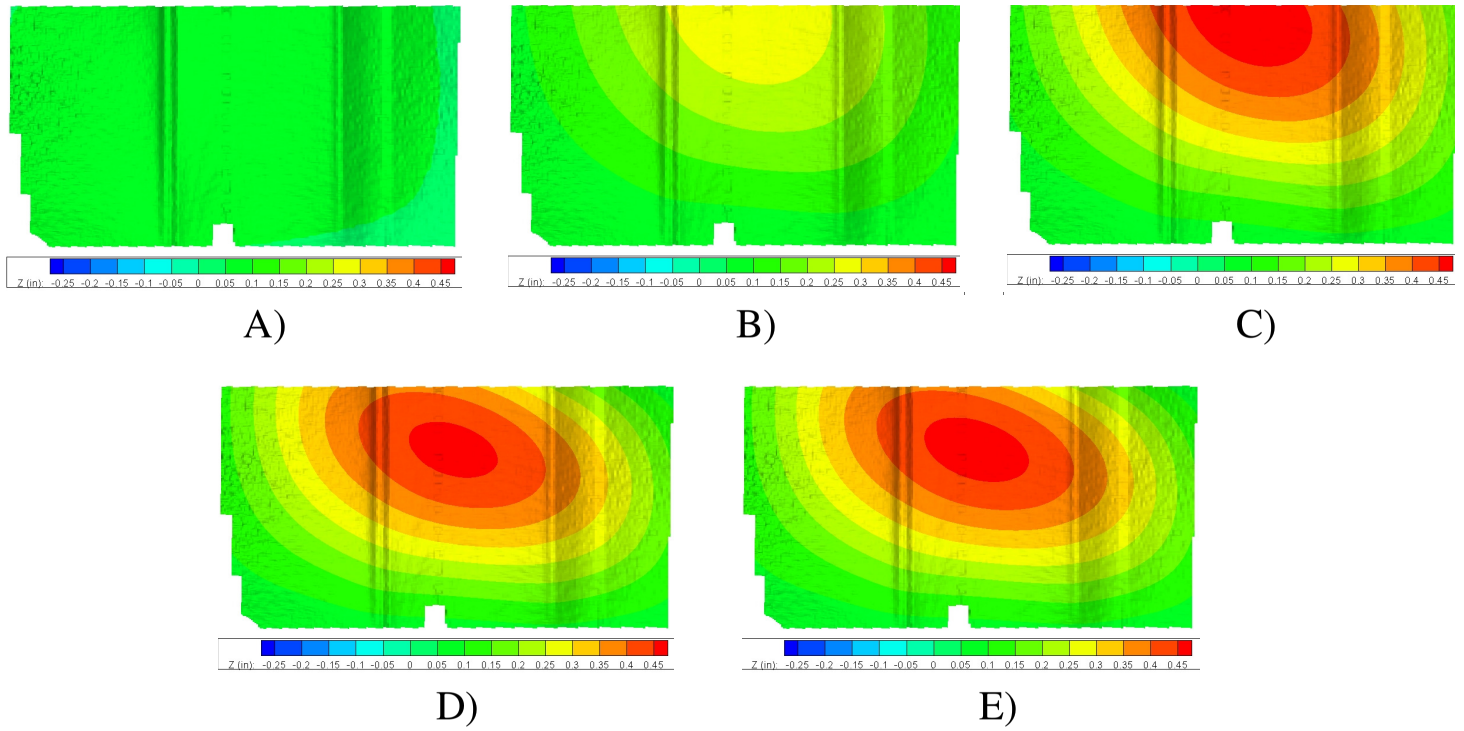

Figure 3.53: Out-of-plane Displacement measured in EBF^3 Panel 4 from the VIC 3-D System in the lower half of the panel at A) 42.1 kips (pre-buckle) B) 112.7 kips (post-buckle) C) 152.1 (post-buckle) D) 172.6 (maximum load) E) 169.9 (post-failure). Load values expressed in terms of compressive load

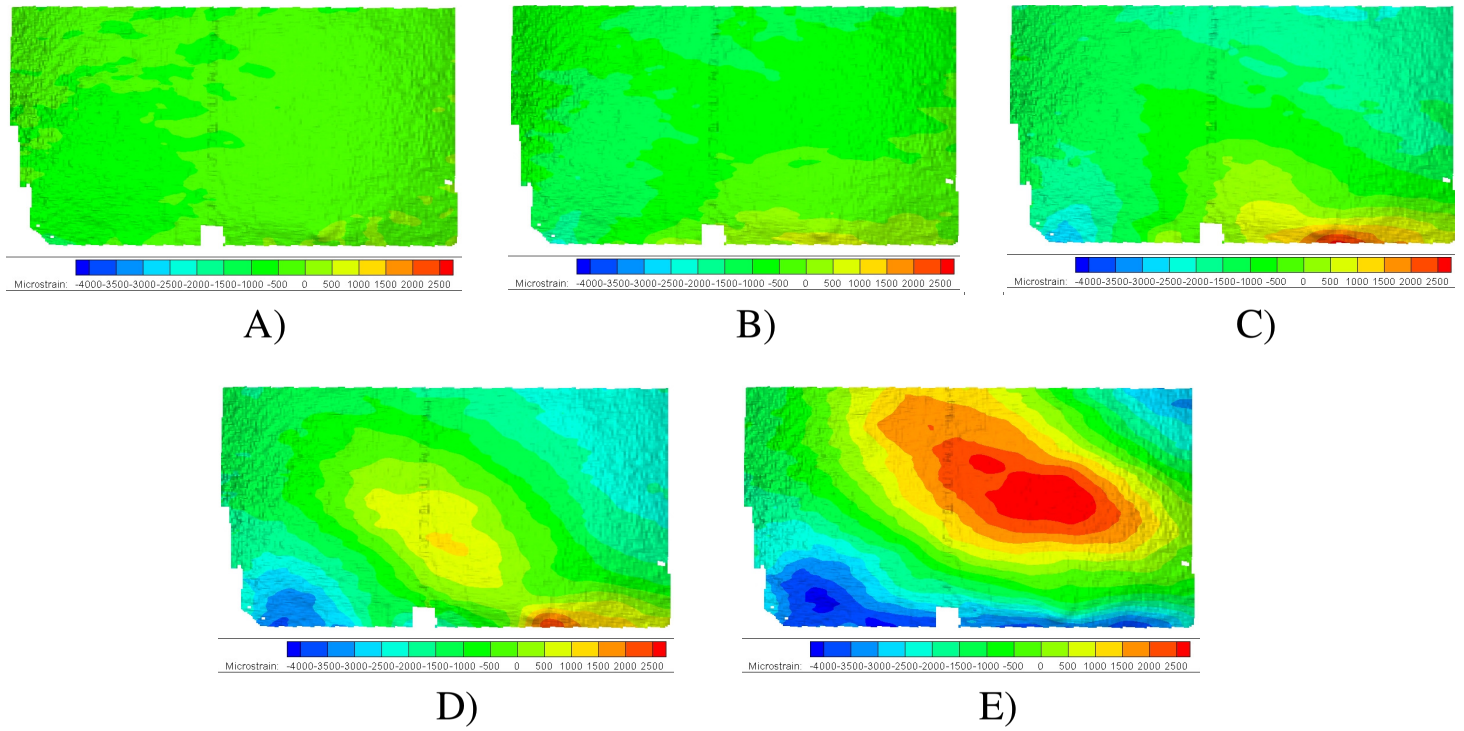

Figure 3.54: Axial Strain measured in Machined Panel 3 from the VIC 3-D System in the lower half of the panel at A) 26.8 kips (pre-buckle) B) 61.5 kips (post-buckle) C) 110.2 (post-buckle) D) 152.8 (maximum load) E) 144.3 (post-failure). Load values expressed in terms of compressive load

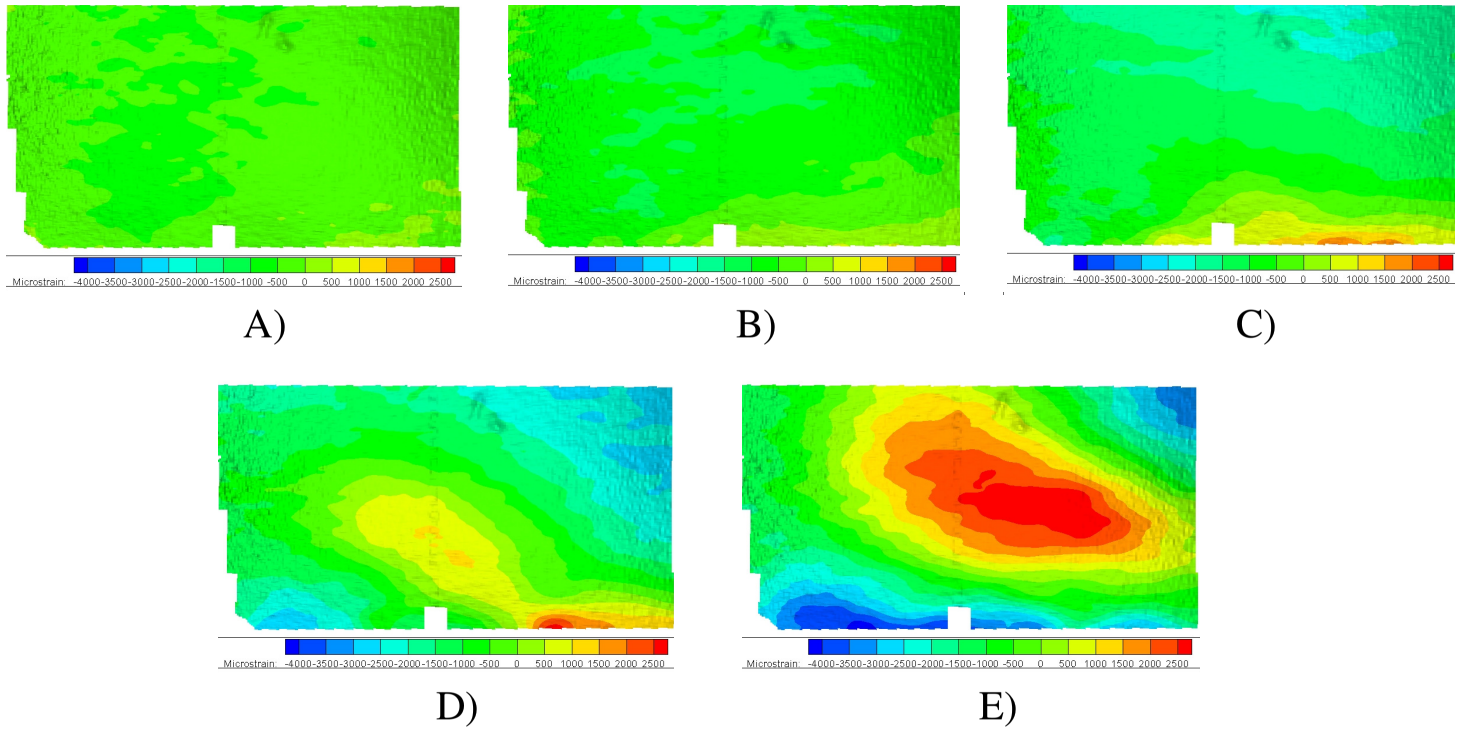

Figure 3.55: Axial Strain measured in Machined Panel 4 from the VIC 3-D System in the lower half of the panel at A) 28.5 kips (pre-buckle) B) 62.2 kips (post-buckle) C) 110.5 (post-buckle) D) 175.5 (maximum load) E) 167.6 (post-failure). Load values expressed in terms of compressive load

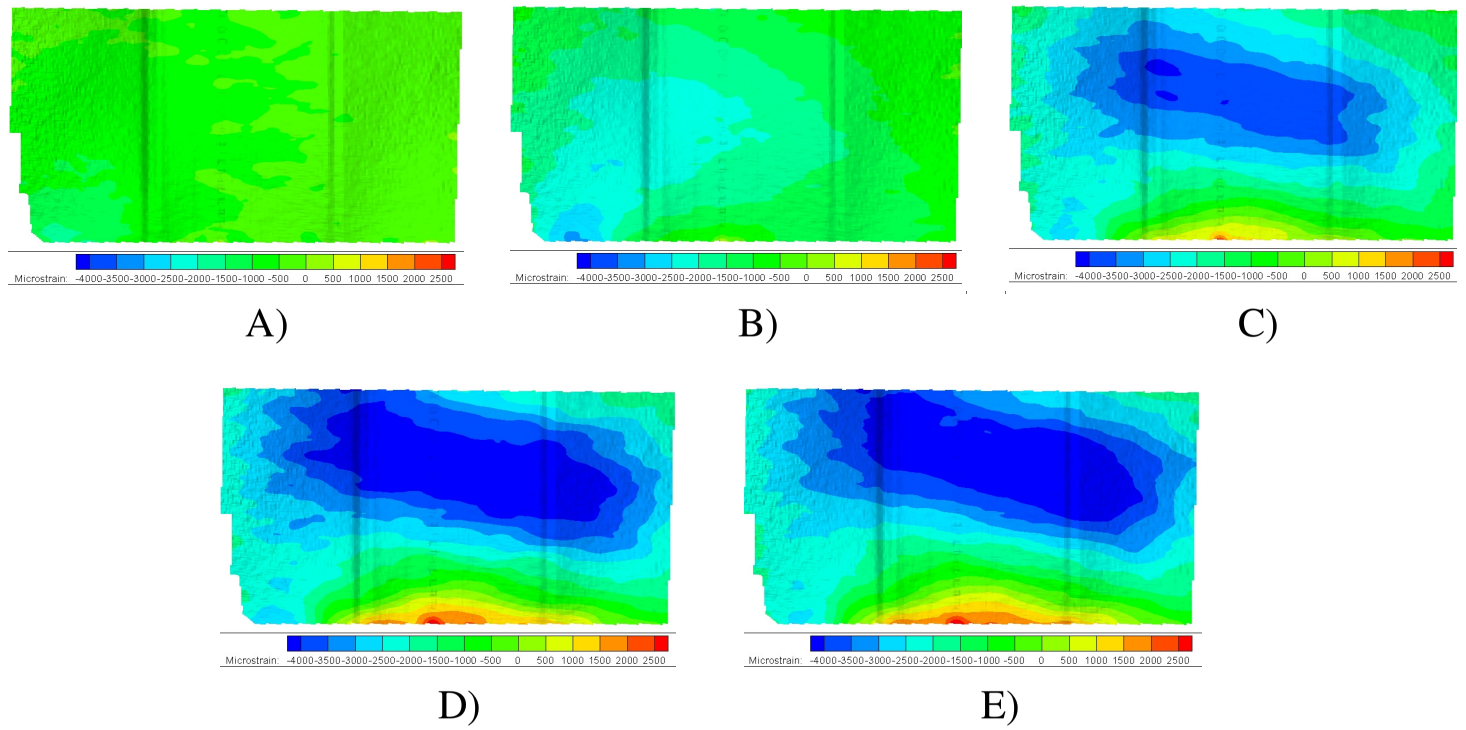

Figure 3.56: Axial Strain measured in EBF^3 Panel 3 from the VIC 3-D System in the lower half of the panel at A) 39.3 kips (pre-buckle) B) 113.9 kips (post-buckle) C) 150.8 (post-buckle) D) 176.4 (maximum load) E) 170.7 (post-failure). Load values expressed in terms of compressive load

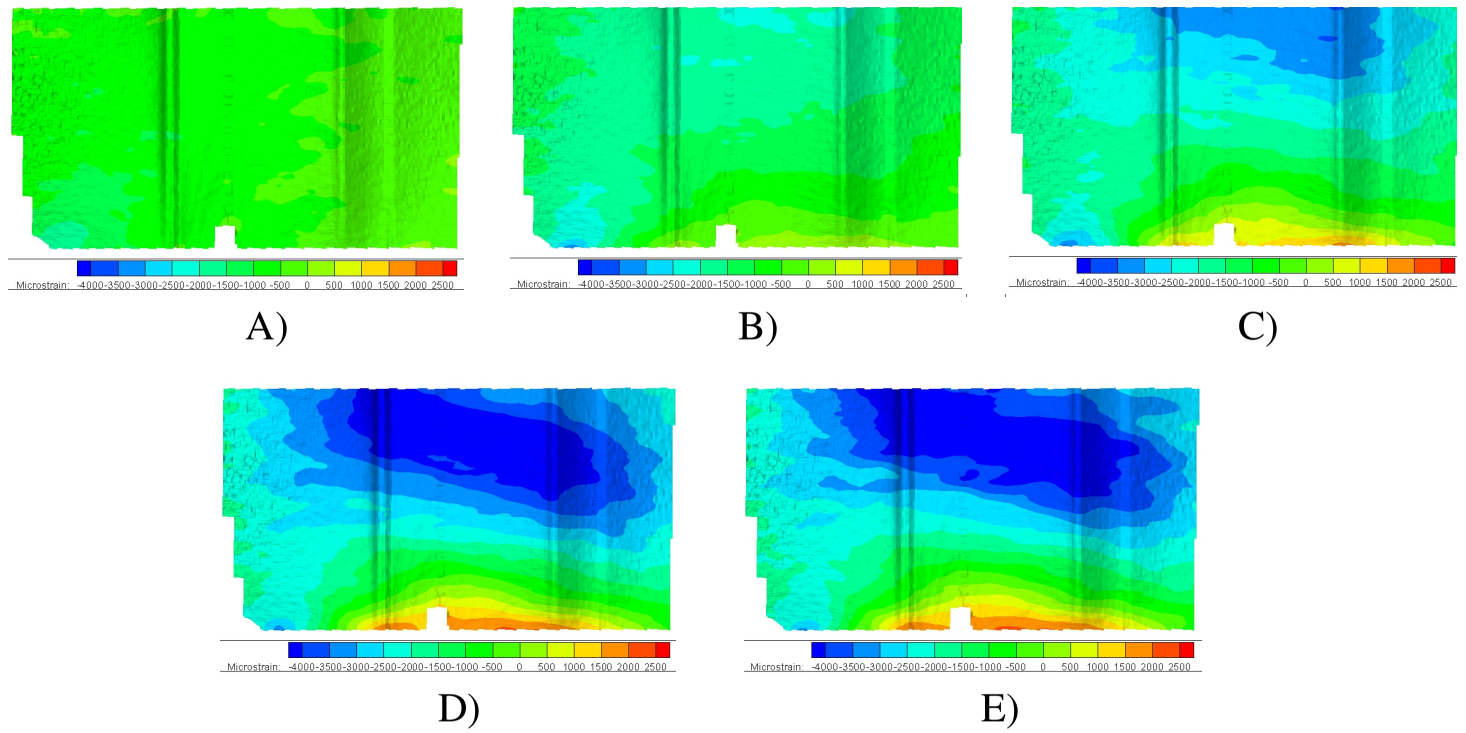

Figure 3.57: Axial Strain measured in EBF^3 Panel 4 from the VIC 3-D System in the lower half of the panel at A) 42.1 kips (pre-buckle) B) 112.7 kips (post-buckle) C) 152.1 (post-buckle) D) 172.6 (maximum load) E) 169.9 (post-failure). Load values expressed in terms of compressive load

Chapter 4

Discussion of Results

4.1 Load Case 1

This section discusses the results from machined and EBF^3 Panels 1 and 2 under load case 1, where the shear load was 40% of the compressive load.

4.1.1 Irregular Hole Pattern and Load Platen Rotation

The initial measured movements prior to the specimens taking up load in the end-shortening and lateral displacement (Figures 3.2 and 3.5) are blamed on the oversized hole pattern in the test panels. Because the frame and the test specimen did not line up exactly, the frame shifted slightly upon loading of the panels. The most significant initial movement was seen by the machined panels where the diameter of the bolt holes was widened by 0.03125 inches. Because material had to be removed from the bolt holes, there was more permissible

room for the frame to shift. No load was actually transferred into the panels, therefore it was valid to zero the data at the point the loads were introduced.

Even though the data resulting from the shift in the frame was removed, a noticeable gradual transition into the linear relationships between the applied loads and the displacements in Figures 3.3 and 3.6 can be seen. This behavior was typically observed at the beginning of the tests as the panels supported the load platen and as excess slack was taken out of the test set-up. Also, because of the aforementioned irregular bolt pattern, some bolts may have been loaded before others, causing an initial nonuniform load introduction into the panels.

In addition to the oversized holes in the machined panels, the rotation of the load platen measured from EBF^3 Panel 2 showed that there was a nonuniform loading. The rotation of the head was not measured for Machined Panels 1 and 2 and EBF^3 Panel 1, however, because the panels are of similar geometry and strength, it was assumed that the load platen rotated an amount similar to that measured in EBF^3 Panel 2 during their respective tests.

The oversized holes in the machined panels and the rotation of the load platen resulted in a nonuniform load being applied to the panels. The nonuniform load distribution could have had a negative effect on the panels' performances and could explain the lower failure load of Machined Panel 1 as well as explain some of the marginally different strain results between the panels [32].

4.1.2 Machined Panels' Responses

The loads at the strain reversal in the stiffeners in Machined Panels 1 and 2 in Figures 3.19 and 3.21 were used to calculate the buckling load for the machined panels. The initial strain measured at the beginning of the tests in the stiffeners was a result of the compressive load. As the panels started to buckle and deform outwards, the strain in the stiffeners caused by the compressive force started to be released [33]. However, the panels' displacements in the outwards direction kept on increasing and the out-of-plane displacements more than likely created strain in the stiffeners, thus explaining the strain reversal seen in both the axial and lateral strain measurements in the stiffeners [34].

The strain reversal technique can be imprecise when calculating the buckling load. Therefore, the inflection point from the out-of-plane displacement in Figures 3.7 and 3.9 was used to provide a more precise method for calculating the buckling loads [34]. The strain reversal technique and the inflection point technique both indicated a buckling load at 46 kips compression for Machined Panels 1 and 2.

It was unclear what caused Machined Panel 1 to fail at a significantly lower load than the other machined and EBF^3 panels tested under load case 1. The test for Machined Panel 1 was interrupted due to problems with the hydraulic lines. Machined Panel 1 was loaded approximately 30 kips in compression and 12 kips in shear when the test was aborted. The test specimen was unloaded and the test was restarted after the problem was addressed. The interruption during the test of Machined Panel 1 could have caused mi-

nor plasticity in the stiffeners and panel, resulting a lower failure load [33].

A rectangular plate subjected to pure shear results in tension and compression stresses of equal magnitude acting on the plate at a 45° angle with respect to the direction of the induced shear force. The compressive stresses cause a destabilization of the panel while the tensile stresses in the perpendicular direction partially resists the destabilizing nature of the compressive stresses. This would result in a buckling mode of several waveforms in the direction of the 45° compressive stresses [34]. With the addition of the compressive force on the top of the panels, the panels would not have buckled into the wave forms but rather have a skewed half-sine wave shape [35].

The out-of-plane displacements from DCDTs 1-6 showed the asymmetrical deformation of the panels during the tests (Figures 3.7 and 3.9). DCDTs 2 and 5, located along the centerline of the panels, had the largest positive out-of-plane displacements which indicated the panels had a half-sine wave shape along the length of the panel. This was the typical deformation shape expected in pure compression tests [36].

The second highest out-of-plane displacements (Figures 3.7 and 3.9) for Machined Panels 1 and 2 was measured by DCDT 1, located in the top half of the panels, and by DCDT 6, located in the lower half of the panels. Lastly, the least amount of out-of-plane displacements from Machined Panels 1 and 2 was measured by DCDT 3, located in the top half of the panels, and by DCDT 4, located in the lower half of the panels. This was consistent with the out-of-plane distortion data and predicted panel shape of an asymmetric

half-sine wave [35].

The VIC 3-D data supported the data measured by DCDTs 4, 5, and 6 (Figure 3.9). Machined Panel 2 had almost no out-of-plane displacement in Figure 3.23(A) before the panel buckled, consistent with the measurements from DCDTs 4, 5, and 6. The panel just after buckling is shown in Figure 3.23(B). The larger out-of-plane displacement shown at the top (the middle of the panel) of Figure 3.23(B) was expected for a panel loaded in compression and shear as described in a paper by Nemeth [35]. The out-of-plane displacement continued to increase as seen in Figure 3.23(C) as the load increased. Larger out-of-plane displacement on the right side of the panel is shown in Figure 3.23(D) for Machined Panel 2, supporting the asymmetrical shape measured by DCDTs 4, 5, and 6. Also, the effects of the stiffeners on the panels was not seen in the VIC 3-D data. The panels shape after buckling was typical for a panel without stiffeners. This could have been a result of the stiffeners having a smaller thickness of 0.15 inches while the panels had a thickness of 0.25 inches. This could have resulted in the panels supporting most of the load and not the stiffeners. Machined Panel 1 showed similar results to Machined Panel 2.

The strain in the stiffeners (Figures 3.19 and 3.21) also supported the skewed half-sine wave deformation of the panels during the tests. Before the panels buckled, the amount of shear load was insufficient to induce skewed strains into the stiffeners. After the panels buckled, stiffener B had higher strains than stiffener A in the center of the stiffeners. Because of the asym-

metric deformation of the panel under the combined loads, stiffener B developed larger out-of-plane displacement in the center of the stiffener resulting in higher strains [35, 33].

When the panels failed globally, out-of-plane displacements measured from DCDTs 1, 2, and 3 (Figure 3.7) increased and remained positive. Conversely, the out-of-plane displacements measured from DCDTs 4, 5, and 6 (Figure 3.9) reversed directions. This indicated the panels buckled into the second buckling mode at the conclusion of the tests. VIC 3-D data also illustrated the negative out-of-plane displacement in the lower half of the panels. A large region of the lower half of the panels had negative out-of-plane displacement after failure of the panels as shown in Figure 3.23(E). Machined Panel 1 showed similar results to Machined Panel 2.

The strain measurements on the panels and stiffeners demonstrated the progression of failure in Machined Panels 1 and 2. Failure initiation was first measured in the stiffeners (Figures 3.19 and 3.21) at the onset of large out-of-plane displacement. After the stiffeners failed, global failure in the panels was expected to be evident in the lateral strain measurements in the middle of the panels (Figure 3.17), since the failure of a panel loaded in combined compression and shear will occur due to the large lateral displacements [2]. Lateral strains as measured by strain gages 5b-8b in Machined Panels 1 and 2 showed nonlinear behavior after the panels buckled. Failure was also seen in the top of the panels from strain gages 1a-4a and 1b-4b (Figures 3.11 and 3.13). A small amount of nonlinearity occurred in strain gages 1a-4a and 1b-4b

prior to the panels' global failures.

The axial strain distribution across the lower half of the panels can seen in the VIC 3-D data. Larger negative strain was seen in the bottom left of the panels and a smaller amount of strain was seen in the middle of the panels, as shown in Figure 3.26(A). The shear portion of the combined loading increased the strains in the lower left and the upper right corners [34]. The addition of the compressive load increased the strain and stress seen in those corners of the panels, thus explaining the higher strains in the lower left corner of the panels in Figure 3.26 and in the upper corner containing strain gages 3 and 4 in Figures 3.38 and 3.40 [34, 33].

Lastly, all panels had a large area of significant positive strain in the area corresponding to the negative out-of-plane displacement in Figure 3.26(E). This was expected due to the large movement of the panels as the panels buckled into their second mode causing an increase in strain [33].

The effect of translating the load from the picture frame to the test panels resulted in an increase of stress and strain along the edges of the panels, accounting for the strain concentration along the bottom edge of the panels as seen in Figure 3.26(C,D,E) [37].

4.1.3 EBF^3 Panels' Responses

The EBF^3 panels did not behave as an ideal flat plate, so the onset of buckling could not be determined using the same methodology as was used with the machined panels. The negative out-of-plane displacement in EBF^3 Panel 1

shown in Figure 3.8 indicated that EBF^3 Panel 1 buckled at a load of 40 kips compression. The inflection point in EBF^3 Panel 2 shown in Figure 3.8 indicated that the EBF^3 Panel 2 buckled at a load of 35 kips compression [34].

On average, the EBF^3 panels had an 18.5% lower buckling load than the machined panels. The EBF^3 panels had flaws in the stiffeners which may have resulted in stress concentrations on the stiffeners that could have induced premature failure [38]. Also, the EBF^3 panels and stiffeners were at different tempers than the machined panels, resulting in slightly lower material properties than the machined panels [29]. Lastly, the EBF^3 panels had initial distortion and residual stress from the manufacturing technique, which biased the panels' shapes and thus influenced the buckling behavior and caused the panels to buckle at lower loads [39].

The EBF^3 panels had smaller end-shortening at maximum load than both of the machined panels (Figure 3.3). Despite having a lower end-shortening and buckling load than the machined panels, the EBF^3 panels had a steeper slope and thus a stiffer structure [34].

Despite the machined and EBF^3 panels having identical designs, EBF^3 Panel 1 showed drastically different out-of-plane displacement than the machined panels (Figures 3.7, 3.8, 3.9, and 3.10). The buckling shape of a flat panel with stiffeners on one side of the panel with no external pressure would be expected to buckle in the direction of the stiffeners, like that seen with Machined Panels 1 and 2 [36]. EBF^3 Panel 1 did not buckle into the same

half-sine wave shape as the machined panels did. EBF^3 Panel 1 had a small amount of negative out-of-plane displacement after buckling. The negative out-of-plane displacement in the top of the panel and the positive out-of-plane displacement in the bottom of the panel, suggests that EBF^3 Panel 1 buckled into an "S" like shape. Only after a load of 100 kips compression did EBF^3 Panel 1 deform into the same half-sine wave shape that was observed in Machined Panel 1 and 2 and EBF^3 Panel 2.

The VIC 3-D data supported the out-of-plane displacements measured by DCDTs 4, 5, and 6 on EBF^3 Panel 1. The VIC 3-D data from the out-of-plane displacement measured in EBF^3 Panel 1 increased from the left side of the panel as shown in Figure 3.24, unlike the other panels in load case 1. As the load increased beyond 100 kips compression in EBF^3 Panel 1, the panel deformed into the skewed half-sine wave shape seen in Machined Panels 1 and 2, shown in Figure 3.24(C,D). As with the machined panels, the added strength of the stiffeners on the EBF^3 panels was not seen in the VIC 3-D data.

EBF^3 Panel 2 buckled into a similar shape as the machined panels shown by Figure 3.25. EBF^3 Panel 2 had the same skewed half-sine wave shape as the machined panels although the total out-of-plane displacement was lower than the machined panels.

Both machined panels showed little deformation at loads below 46 kips compression and then showed a steady increase in out-of-plane displacement until failure. The EBF^3 panels' out-of-plane displacement results, however,

were unpredictable. The initial shape of the panel has been shown to have a significant impact on the buckling shape of a panel. The EBF^3 panels had some initial distortion even after bump-forming, shown in Figure 2.6. The negative out-of-plane displacement in EBF^3 Panel 1 was directly attributed to the initial distortion of the panels. In a paper by Nelson et al., an EBF^3 panel in pure compression buckled in the opposite direction than expected. The initial distortion in the panel was concluded to be the most plausible cause [21].

Even though the EBF^3 panels had less out-of-plane displacement than the machined panels, the negative out-of-plane displacement in EBF^3 Panel 1 could be problematic for manufacturing aircraft parts made by the EBF^3 process. As mentioned previously, the function of aircraft structure is to conform to contour, shape, and clearance requirements while enduring different loads. The shape of the aircraft influences the lift and drag during the flight, therefore any out-of-plane displacement could be detrimental to the aerodynamics. Almost no out-of-plane displacement is desired in aircrafts in order to maintain the shape of the airfoil and fuselage [40]. If the buckling shape of a structure was known, the aircraft could be designed to incorporate the buckling shape into the aerodynamics [41]. However, a greater understanding of the effects of the initial distortion and residual stresses created during the EBF^3 process on the performance of the structure would be required if the EBF^3 process was to be used to manufacture unitized stiffened skin panels for aircrafts.

The strain results for the EBF^3 panels showed the same path of failure as the machined panels, even though the individual strain results were different. The EBF^3 panels did not show out-of-plane displacement in the stiffeners until approximately a load of 87 kips compression for EBF^3 Panel 1 and 72 kips compression for EBF^3 Panel 2. This was almost double the loads for failure measured in the machined panels' stiffeners. The failure in the stiffeners corresponded with the large out-of-plane displacement in the panels. Since both EBF^3 panels had less out-of-plane displacement at a higher load, a higher failure load in the stiffeners was expected.

The strains measured in the panels from strain gages 1a-4a (Figures 3.11 and 3.12) was linear for a large portion of the tests for both the machined and EBF^3 panels. The slight change in the strain observed in these strain gages corresponded to the occurrence of buckling. The strains measured in the panels from strain gages 5a-8a (Figures 3.15 and 3.16) were similar to the strains measured from strain gages 1a-4a for both the machined and EBF^3 panels (Figures 3.11 and 3.12). Since the machined and EBF^3 panels had similar strains, this suggested that the initial stress from the EBF^3 manufacturing process had little effect on the axial strain in the panel in areas away from the build zone.

The lateral strains in strain gages 1b-4b (Figures 3.13 and 3.14) were also consistent between the machined and EBF^3 panels. However, the lateral strains in strain gages 5b-8b (Figures 3.17 and 3.18) were more inconsistent for the EBF^3 panels. The EBF^3 panels showed smaller amounts of strain than

the machined panels and the strain-load relationships in the EBF^3 panels were not as smooth as that for the machined panels, as shown in Figure 3.18. The smoothness of the data was a result of the sampling rate of the test machine and the speed at which the strains were changing. The jagged results of the EBF^3 panels suggest that the strains in the EBF^3 panels were changing faster than the data sampling rate. The initial residual stress in the EBF^3 panels may have resulted in greater flexibility in the skins and stiffeners, which could have resulted in more dynamic changes in strains for an increase in load [39].

The machined panels also showed more uniform results in the stiffeners than in the EBF^3 panels (Figures 3.19, 3.20, 3.19, and 3.20). The machined panels behaved similar to each other with stiffener A showing smaller strain than stiffener B. The EBF^3 panels showed more variance, especially in the post-buckled region. The strains measured by strain gages 25a, 26a, 25b, and 26b on stiffener A for EBF^3 Panel 2 showed strains in the stiffeners on a similar magnitude to that of the machined panels, while the other strain gages on the stiffeners of EBF^3 Panels 1 and 2 measured higher strains than Machined Panels 1 and 2.

The variances between the EBF^3 panels and the machined panels were attributed to the manufacturing methods. The initial stress in the EBF^3 panels was greatest at the base of the stiffener and, as a result, has the greatest influence on the performance of the stiffeners. In addition, the heat treatment used to increase the strength of the EBF^3 stiffeners after deposition, may have been ineffective at bringing the strength of the stiffeners to the full strength

of the base plate [42].

4.2 Load Case 2

This section discusses the results from machined and EBF^3 Panels 3 and 4 under load case 2, where the shear load was 100% of the compressive load below 100 kips. The shear load was held constant at 100 kips for all loads where the compressive load exceeded 100 kips.

4.2.1 Problems during the Tests

The test experienced on Machined Panel 3 had a small drop in load at approximately 100 kips compression and this can be seen in the strain gage and DCDT results. As mentioned in Chapter 2, when the loads reached 100 kips in compression and shear, the shear load was stopped while the compressive load continued to increase. Problems occurred when the shear load was stopped and accidentally caused a decrease of 2 kips in the compressive load and a decrease of 29 kips in the shear. The drop in compressive load can easily be seen in Figure 3.30 and the drop in shear load can be seen as the large spike in Figure 3.33. The load was then immediately returned to where it had been prior to the loss of load. This may have affected the results for Machined Panel 3, potentially contributing to the lower failure load of the panel compared to the failure loads of the other panels under load case 2.

The data collection for Machined Panel 4 started at 18.3 kips compres-

sion. Also, the data for DCDTs 4, 5, and 6 for Machined Panel 3 were not presented because the DCDTs were placed in the wrong location on the panel. In addition, strain gage 26b for Machined Panel 3, had faulty wiring and no data were collected.

The data for the strain gages and the DCDTs for EBF^3 Panel 4 were not collected due to a technical error. Thus, only the VIC 3-D data and the maximum load at failure were collected.

4.2.2 Machined Panels' Responses

The buckling loads for Machined Panels 3 and 4 were predicted the same way as Machined Panels 1 and 2. The strain reversal in the stiffeners (Figures 3.46 and 3.48) and the inflection point in DCDTs 1-6 (Figures 3.34 and 3.36) indicated that Machined Panel 3 buckled at a compressive load of 33 kips and Machined Panel 4 buckled at a compressive load of 37 kips [34].

The out-of-plane distortions measured by the 6 DCDTs document the progression of the asymmetric shape of the machined panels during the test (Figures 3.34 and 3.36). Like load case 1, the machined panels buckled into a half-sine wave shape, which resulted in DCDTs 1-6 measuring positive out-of-plane displacements. The larger out-of-plane displacements seen in DCDT 1 and 6 than in DCDT 3 and 4 suggests that Machined Panels 3 and 4 buckled into the skewed half-sine wave shape as expected for a panel loaded in compression and shear [35]. Finally, at the end of the test, Machined Panel 3 exhibited negative out-of-plane displacement from DCDTs 4 and 5 (Figure

3.36), suggesting that the panel distorted into the second buckling mode with a partial "S" shape at failure.

The VIC 3-D data supported the data collected by DCDTS 4, 5 and 6. Before the panels buckled, as shown in Figures 3.50(A) and 3.51(A), there was almost no out-of-plane displacement. After the panels buckled, as shown in Figures 3.50(B) and 3.51(B), there was a small amount of out-of-plane displacement towards the center of the panels. In the post-buckled region, as shown in Figures 3.50(C,D) and 3.51(C,D), there was a large amount of positive out-of-plane displacement, the largest of which lied on the right side of the panels. This was the same region where DCDT 6 was located, which further supported that the panels had an asymmetrical deformed shape. After failure of the panels, as shown in Figures 3.50(E) and 3.51(E), there was some negative out-of-plane displacement shown in the lower half of the panels, however not in the area where DCDT 6 was located due to the skewed buckling shape of the panels. This supported that DCDTs 4 and 5 measured negative out-of-plane displacement while DCDT 6 (Figure 3.36) measured positive out-of-plane displacement.

Although there was no out-of-plane displacement measurements for Machined Panel 4 in the lower half of the panel, the VIC 3-D data showed similar results between Machined Panels 3 and 4, thus, supporting that Machined Panel 4 buckled into the same asymmetrical shape as Machined Panel 3 (Figures 3.50 and 3.51).

After the machined panels buckled, strains measured by the strain gages

located on the panels (Figures 3.38, 3.40, 3.42, and 3.44) became nonlinear with respect to the compressive load, at approximately a load of 50 kips compression. However, strain gages 3a and 4a for Machined Panels 3 and 4 measured nonlinear data at lower loads than the other strain gages on the panels. As with load case 1, the lower left corner and the upper right corner of the panels, which contained strain gages 3 and 4, were loaded in compression inclined at 45° with respect to the panel edges as a result of the shear load. When combined with the compressive load applied to the top of the panels, this increased the strain and stress in those corners [34, 33]. The higher stress in the corner containing strain gages 3a and 4a could explain the data becoming nonlinear in the panel at a lower load.

After a load of 100 kips compression, when the shear load was held constant at 100 kips, there was a reduction in the slopes in the strain-load behaviors for the machined panels. Once the shear load stopped increasing, the strain measured from all the strain gages continues to increase, but at a slower rate since the compressive load was the only load increasing [33].

The progression of the strain across the lower half of the panels can be shown by the VIC 3-D data. Before buckling, larger negative strain was present in the bottom left of the panels than in the rest of the lower half of the panels, as shown in Figures 3.54(A) and 3.55(A). Once the panels buckled, there was an increase in axial strain in the middle of the panels. As the load increased, larger strain was measured in the middle and the bottom left corner of the panels than in the rest of the panels, especially in Machined Panel 3 as

shown in Figures 3.54(C) and 3.55(C). This correlated with the higher strain measured in the top right corner of the panels from strain gages 3 and 4, since both corners were under high stresses due to the combined compression-shear loads [34, 33]. At the end of the tests, a large area of the machined panels had large positive strain in the same area as the negative out-of-plane displacement in Figures 3.54(E) and 3.55(E). The large movement of the panel caused the increase in strain [33].

There was also an increase in strain along the bottom edge of the panels, as shown in Figures 3.54 and 3.55. Similar to load case 1, the effect of transferring the load from the test frame into the panels resulted in an increase of stress and strain along the edge of the panels [37].

4.2.3 EBF^3 Panels' Responses

EBF^3 Panel 3 had nearly zero out-of-plane displacement in the upper half of the panel and a very small amount of out-of-plane displacement in the lower half of the panel until a compressive load of 100 kips. The inflection point in the displacement-load curve in Figure 3.35 indicated that the panel buckled at a load of 100 kips when the shear load stopped increasing [34]. EBF^3 Panel 4 also buckled at a load of 100 kips when the shear load stopped increasing.

The out-of-plane displacement suggested that the shear load prevented the EBF^3 panels from buckling, and thus when the shear load stopped increasing, the EBF^3 panels buckled immediately. Also, the upper half and part of the lower half of EBF^3 Panel 3 buckled in the opposite direction of

the stiffeners, shown by the negative out-of-plane displacement in Figures 3.35 and 3.37.

The VIC 3-D data were used to understand the movement of both EBF^3 panels. Almost no out-of-plane displacement was measured for EBF^3 Panel 3 in the pre-buckled condition as shown in Figure 3.52(A). This was comparable with the out-of-plane data from DCDTs 4, 5, and 6 (Figure 3.37). EBF^3 Panel 4 had little out-of-plane displacement initially, as shown in Figure 3.53(A). This was similar to EBF^3 Panel 3. There was negative out-of-plane displacement in the same region of the panel where DCDT 6 was located as shown in Figure 3.52(B). This supported the negative out-of-plane displacement from DCDT 6 in Figure 3.37. EBF^3 Panel 4 did not show any negative out-of-plane displacement in the lower half of the panel from the VIC 3-D data, suggesting that EBF^3 Panel 4 buckled into a slightly different shape than EBF^3 Panel 3. Although no data were recorded, it was observed during the test that EBF^3 Panel 4 had negative out-of-plane displacement in the upper half of the panel after buckling. The difference in the out-of-plane displacements between EBF^3 Panels 3 and 4 suggested that EBF^3 Panel 4 may have had less initial distortion in the lower half of the panel than was present in EBF^3 Panel 3.

EBF^3 Panels 3 and 4 buckled 185% higher than the average buckling load for Machined Panels 3 and 4. EBF^3 Panels 3 and 4 also had a different buckling shape from each other as well as from Machined Panels 3 and 4. This may be due to the effects of initial imperfections and distortion on the

panels, influencing both the buckling mode shapes and the loads of the panels in both theoretical and experimental analysis [43, 34]. Initial distortion has been shown to cause EBF^3 panels to buckle in an opposite direction than expected [21]. This was also seen in EBF^3 Panel 1 in load case 1. The higher buckling load of the EBF^3 panels was not associated with the EBF^3 panels being stiffer or stronger, but rather was likely associated with initial distortion having a drastic impact on the buckling loads of the EBF^3 panels.

The different buckling shapes in the EBF^3 panels than the machined panels resulted in different strain measurements in the stiffeners and middle of the panels (Figures 3.47 and 3.49). The "C" shaped strain-load curves for the strains in the stiffeners occurred during the same loads as the negative out-of-plane displacement in the lower half of EBF^3 Panel 3. The strains measured from EBF^3 Panel 3 from strain gages 5a-8a and 5b-8b (Figures 3.43 and 3.45) also had the same "C" shaped strain-load curves at the same loads as the negative out-of-plane displacement.

The immediate deformation of EBF^3 Panel 3 at the buckling load which coincided with the point when the shear load stopped was assumed to be the cause of the "C" shaped strain-load curves. Since strain was associated with the displacement of the panel, the large deformation of the panel was assumed to have caused the "C" shaped strain-load curves seen from strain gages 5a-8a, 5b-8b, 25a-28a, and 25b-28b [34, 33].

The strains measured from strain gages 1a-4a and 1b-4b (Figure 3.38, 3.39, 3.40, and 3.41) can be compared for Machined Panels 3 and 4 and EBF^3

Panel 3 because the dissimilar buckling shape of the EBF^3 Panel 3 had little effect at the corners of the test sections. The test section corners were clamped by the fixture on two sides, therefore preventing large displacement of the panels at the corners.

Machined Panels 3 and 4 generally measured larger strains from the strain gages located on same side of the panels as the stiffeners while EBF^3 Panel 3 measured larger strains in the strain gages located on the opposite side of the panels as the stiffeners. EBF^3 Panel 3 buckled in the opposite direction of the machined panels which could be the reason for why the strain gages on the opposite side of the panels measured larger strains.

EBF^3 Panel 3 had similar lateral displacement (Figure 3.33) to the machined panels, suggesting that the initial distortion of the EBF^3 panels and the negative out-of-plane displacement had little effect on the lateral displacement of the panels. EBF^3 Panel 3 also had higher strains from strain gages 3a, 3b, 4a, and 4b than in strain gages 1a, 1b, 2a, and 2b (Figures 3.39 and 3.41) like Machined Panels 3 and 4. The VIC 3-D data also measured larger strains in the bottom left corner of the panel in Figures 3.56 and 3.57. The larger strains from strain gages 3a, 3b, 4a, and 4b in EBF^3 Panel 3 and the bottom left corner of EBF^3 Panels 3 and 4 was attributed to the interaction between the shear and compressive loads also seen in Machined Panels 3 and 4.

There was also an increase in strain along the bottom edge of the panel, as shown in Figures 3.56 and 3.57. Similar to Machined Panels 1-4 and EBF^3

Panels 1 and 2, the effect of transferring the load from the picture frame to the test panels resulted in an increase of stress and strain along the edges of the panels [37].

4.3 Load Case 1 Compared to Load Case 2

The machined panels behaved similarly to each other for the two loads. All four machined panels showed higher strains in the bottom left corner, upper right corner, and the middle of the panels. All four machined panels showed an asymmetrical buckling shape and, at failure, buckled into a two half-sine wave shape. Machined Panels 3 and 4 were more asymmetrical after buckling than Machined Panels 1 and 2, shown by the VIC 3-D data in Figure 3.23 for Machined Panel 2 and Figures 3.50 and 3.51 for Machined Panels 3 and 4.

On average, Machined Panels 3 and 4 had a 24% lower buckling load than Machined Panels 1 and 2. This was expected since Machined Panels 3 and 4 had a higher shear load than Machined Panels 1 and 2, thus resulting in lower buckling loads [36]. Machined Panels 3 and 4 also had a 103% higher maximum lateral displacement than Machined Panels 1 and 2. Since Machined Panels 3 and 4 had a higher applied shear load, it was expected to see a higher lateral displacement in Machined Panels 3 and 4 [37]. The close results between all four machined panels showed that the higher shear load of load case 2 played an important role in the lateral displacements and the buckling loads of the panels.

The EBF^3 panels behaved differently between the two load cases. The

higher applied shear load had a drastically different effect on the EBF^3 panels than the machined panels, and resulted in EBF^3 Panels 3 and 4 showing different results when compared to EBF^3 Panels 1 and 2. On average, EBF^3 Panel 3 had a 70% higher maximum lateral displacement than EBF^3 Panels 1 and 2. Like the machined panels, EBF^3 Panel 3 was expected to have larger lateral displacement due to the higher shear load being applied [37].

Contrary to the machined panels, EBF^3 Panel 3 and 4 had a 167% higher buckling load than EBF^3 Panels 1 and 2. This was the opposite of what was expected from EBF^3 Panel 3 since it had a higher applied shear load. The negative out-of-plane displacement seen by EBF^3 Panel 3 was larger than the small amount of negative out-of-plane displacement seen by EBF^3 Panel 1. All four EBF^3 panels had similar initial distortion which affected the out-of-plane displacement. However, the larger permanent out-of-plane displacement was only seen by EBF^3 Panels 3 and 4. The difference between the two load cases for the EBF^3 panels suggested that the initial distortion of a panels played a more important role in the buckling of the panels when the higher shear load was present.

Chapter 5

Finite Element Validation

This chapter compares the finite element analysis (FEA) with the experimental results. The model was created in PATRAN and the analysis was performed in NASTRAN. The linear results were only compared with the first panel from each load case of the experimental results which allowed for easy interpretation of the results in the graphs.

5.1 Finite Element Model

A finite element model was created separately for the machined and EBF^3 panels. The finite element model for the machined panels containing the displacement constraints, the loads from load case 1 as a distributed load and the labels for the top, bottom and sides of the panel is shown in Figure 5.1. The machined base plate and stiffeners were modeled as flat 2-D plates using shell elements and had a total of 13254 nodes. The EBF^3 panel was also modeled

as a 2-D plate using shell elements and had 12949 nodes. The EBF^3 model was modeled using the warped shape of the panels after being manufactured, as shown in Figure 2.6. It was later realized that when the EBF^3 panels were placed into the test frame the shape of the panels may have been altered due to the constraint imposed by the test fixture. Thus, the shape of the panels during the test was not exactly what the model portrayed. For both manufacturing techniques, only the 24 by 28 inch test section was modeled. The bottom of the panels had no movement in the X, Y, and Z direction, while the other three sides had movement constrained only in the Z direction. Also, the rotation in the Y direction was prevented on all sides of the panels.

The shear load was applied on the three sides only constrained in the Z direction, thereby mimicking the effect of the test frame. Because the sides of the test frame are different lengths, two different distributed shear loads were needed to create the same shear load on all sides of the panels. The shear load applied across the top of the panel was 1250 lbs/in for load case 1 and 3125 lbs/in for load case 2. The shear load applied along the sides of the panel was 1071.4 lbs/in for load case 1 and 2678.6 lbs/in for load case 2. The compressive load was applied on the edge opposite of the side constrained in the X, Y, and Z direction. The compressive load applied across the top of the panel was 3125 lbs/in for both load cases. The finite element model assumed uniform compression and shear being applied throughout the whole test.

Both panels were modeled with a Young's Modulus of 10.6×10^6 psi and a Poisson's ratio of 0.33. Both panels were meshed with triangular elements,

0.25 inches in length. The triangle elements were chosen due to the angle created by the stiffener run-outs.

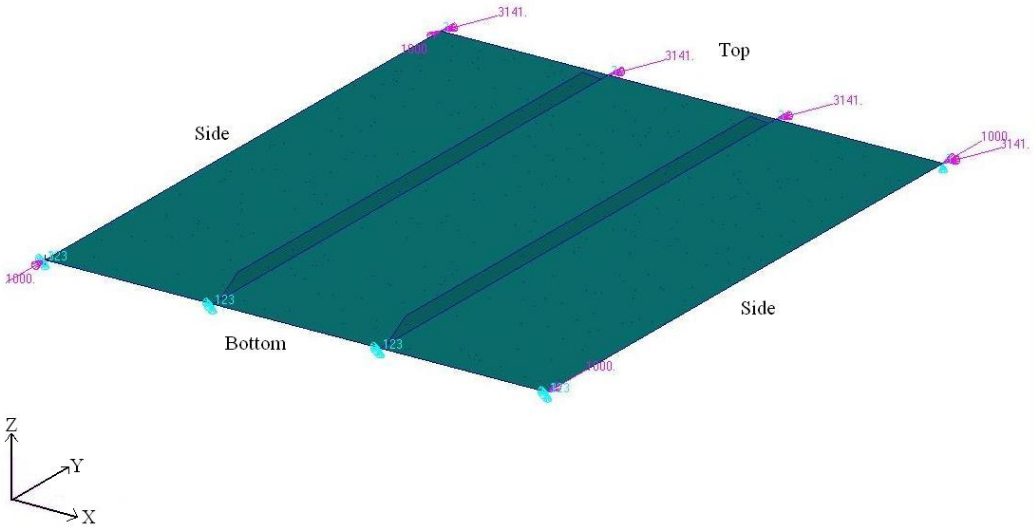

Figure 5.1: The Finite Element Model for the Machined Panels under Load Case 1

An eigenvalue buckling analysis was used to predict the buckling load and buckling shape. A linear analysis was performed to understand how the load was introduced into the panel before buckling and a nonlinear analysis was used to compare the panels in the post-buckled region.

5.2 Load Case 1

The average buckling loads from the experimental data and the FEA's prediction of the buckling load for load case 1 is listed in Table 5.1. The FEA predicted a buckling load of almost 13% higher than what was seen experimentally

for the machined panels and 20% higher than what was seen experimentally for the EBF^3 panels. The FEA's predicted buckling load was similar to the experimental buckling load for the machined panels. There could have been a slight amount of initial distortion in the machined panels once they were placed in the test fixture which could have affected the experimental buckling load and would yield a different FEA buckling load if that distortion were to be modeled. Since the EBF^3 panels were not modeled exactly like they were set-up in the test fixture, it was expected to have imprecise results for the FEA of the EBF^3 panels.

The first buckling mode shape from an isometric view is shown in Figure 5.2 and the first buckling mode shape from a top view is shown in Figure 5.3 for the machined panels under load case 1. The FEA predicated a buckling shape of a half-sine wave thus supporting the data from the experimental tests. The second buckling mode from an isometric view is shown in Figure 5.4 and the second buckling mode from a top view is shown in Figure 5.5 for the machined panels under load case 1. The FEA predicted the second buckling mode to be "S" shaped. This was the final shape of the panels at the end of the experimental tests.

The first buckling mode shape from an isometric view is shown in Figure 5.6 and the first buckling mode shape from a top view is shown in Figure 5.7 for the EBF^3 panels under load case 1. The FEA predicted the panel buckled into a half-sine wave shape in the opposite direction of the stiffener. A small amount of negative out-of-plane displacement was measured in EBF^3 Panel

1 but not the complete half-sine wave shape seen from the FEA. EBF^3 Panel 2 had no negative out-of-plane displacement until the end of the test. The second buckling mode shape from an isometric view is shown in Figure 5.8 and the second buckling mode shape from a top view is shown in Figure 5.9 for the EBF^3 panels under load case 1. The second buckling mode shape of the EBF^3 panels matched the "S" shape of EBF^3 Panels 1 and 2 at the end of the experimental tests.

The FEA predicted buckling shapes matched the experimental shapes with the exception of the first buckling mode of the EBF^3 panels. The difference in the FEA buckling shape and the experimental buckling shape for the EBF^3 panels was attributed to the distortion included in the FEA model being different from the actual shape of the EBF^3 panel due to constraints from the test fixture.

Table 5.1: Comparison of Finite Element Analysis (FEA) and Experimental Buckling Loads for Load Case 1

Panel	Average Buckling Load(kips)
Machined Panels 1 and 2	46
FEA for Machined Panels	52
EBF^3 Panels 1 and 2	37.5
FEA for EBF^3 Panels	45

The linear FEA lateral strains from strain gages 5b-8b are shown in Figures 5.10 and 5.11 for the machined and EBF^3 panels respectively. Although the FEA predicted a lower buckling load for the machined panels, the linear FEA correlated with the experimental strain results in the linear region.

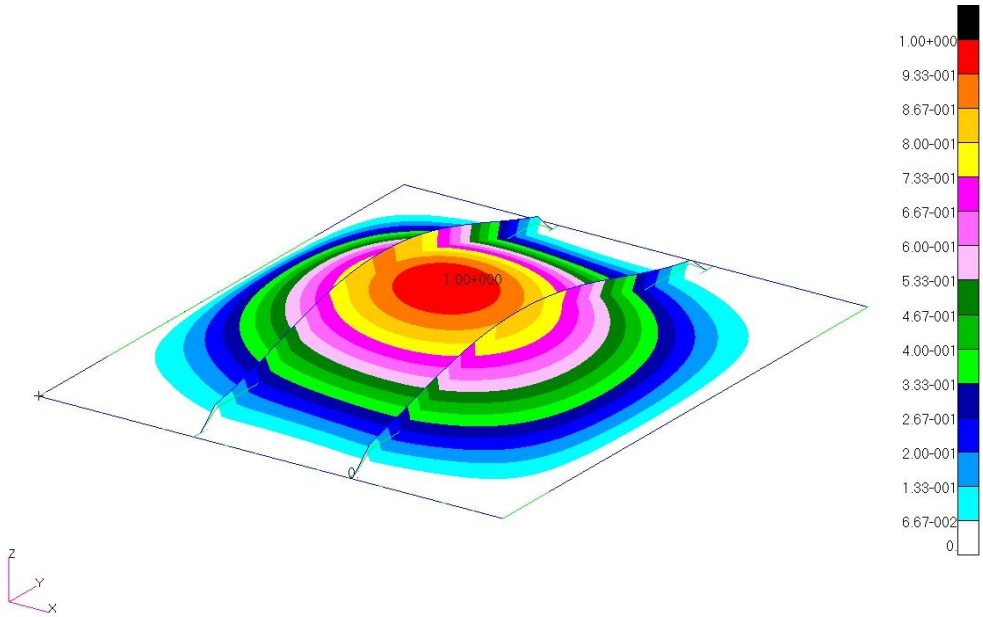

Figure 5.2: Isometric view of First Buckling Mode Shape from the Finite Element Analysis for the Machined Panels under Load Case 1

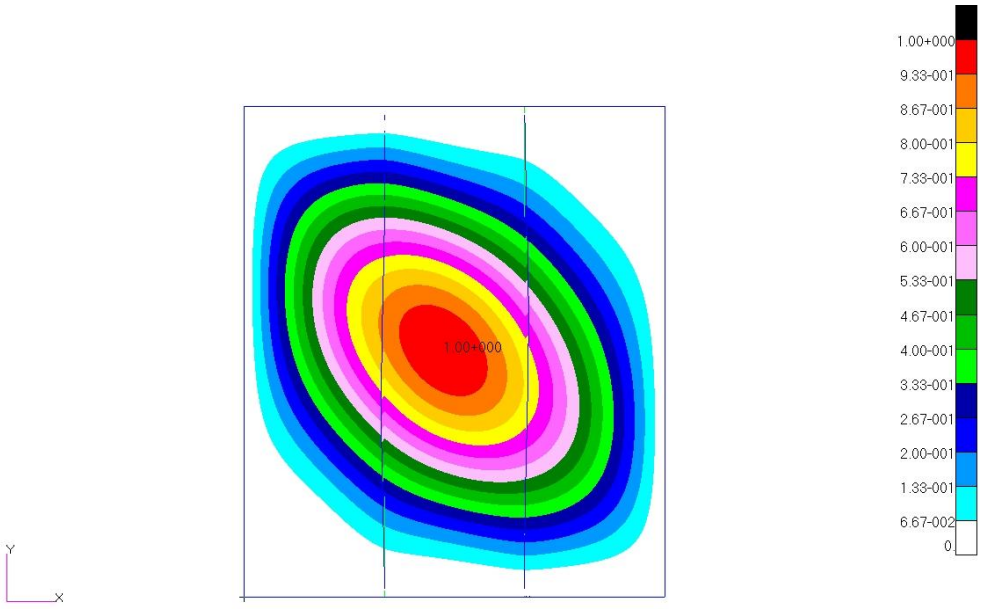

Figure 5.3: Top view of First Buckling Mode Shape from the Finite Element Analysis for the Machined Panels under Load Case 1

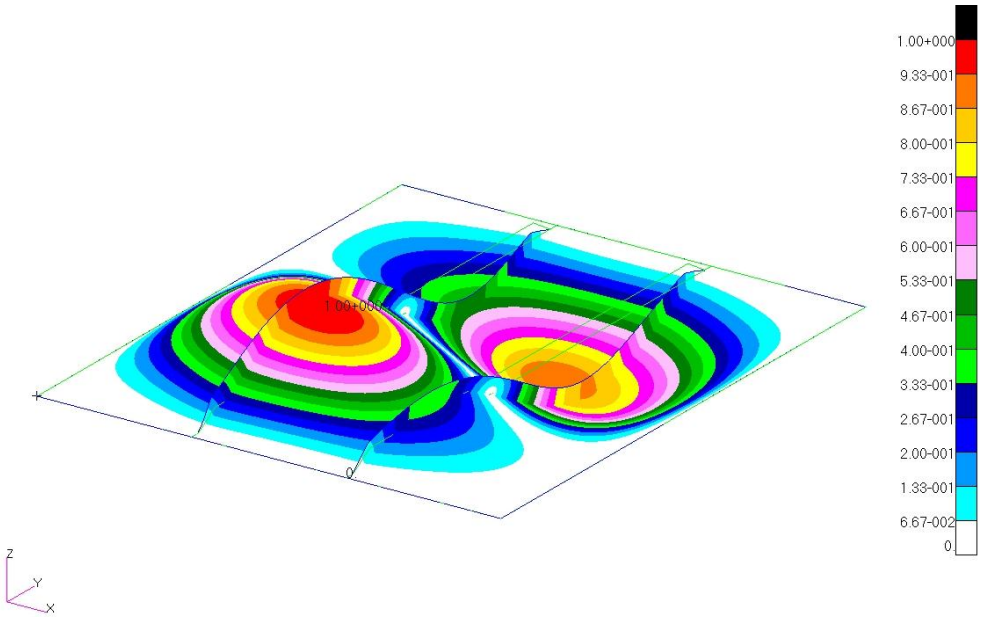

Figure 5.4: Isometric view of Second Buckling Mode Shape from the Finite Element Analysis for the Machined Panels under Load Case 1

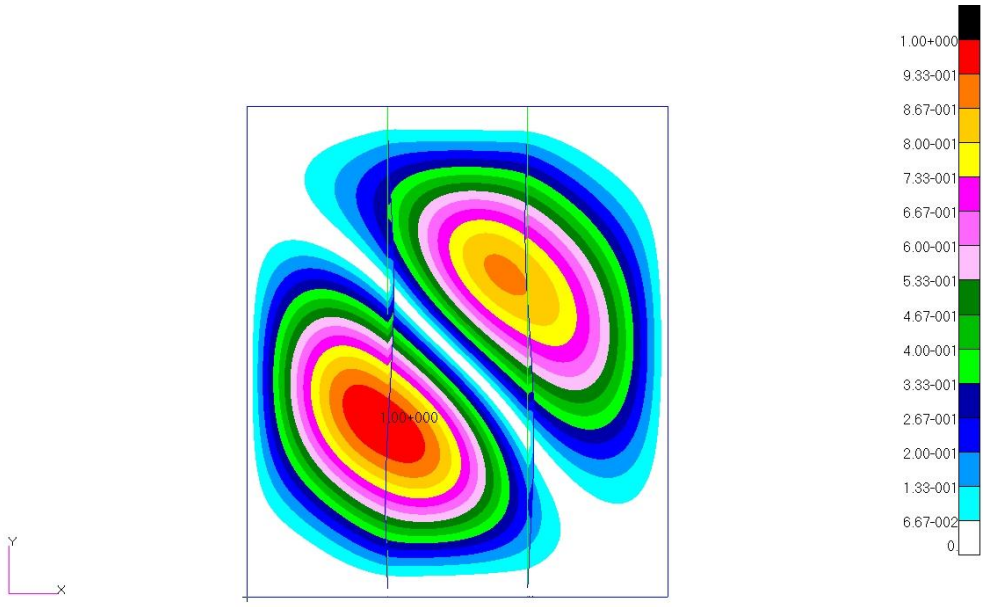

Figure 5.5: Top view of Second Buckling Mode Shape from the Finite Element Analysis for the Machined Panels under Load Case 1

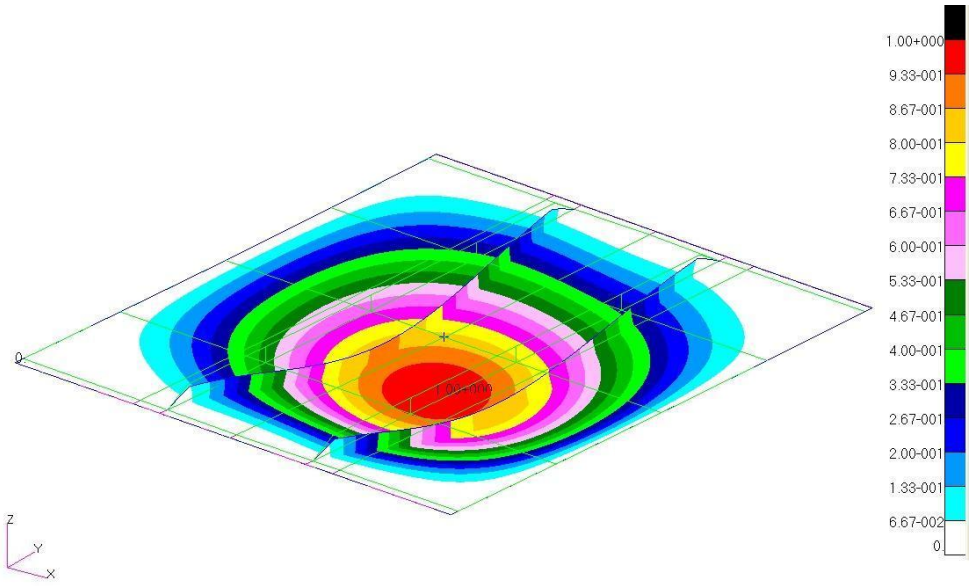

Figure 5.6: Isometric view of First Buckling Mode Shape from the Finite Element Analysis for the EBF^3 Panels under Load Case 1

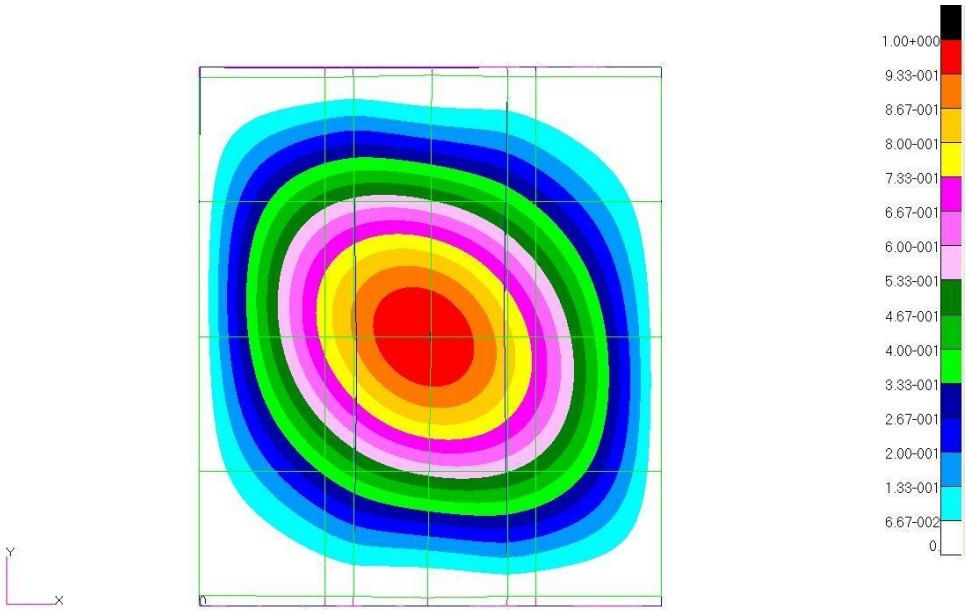

Figure 5.7: Top view of First Buckling Mode Shape from the Finite Element Analysis for the EBF^3 Panels under Load Case 1

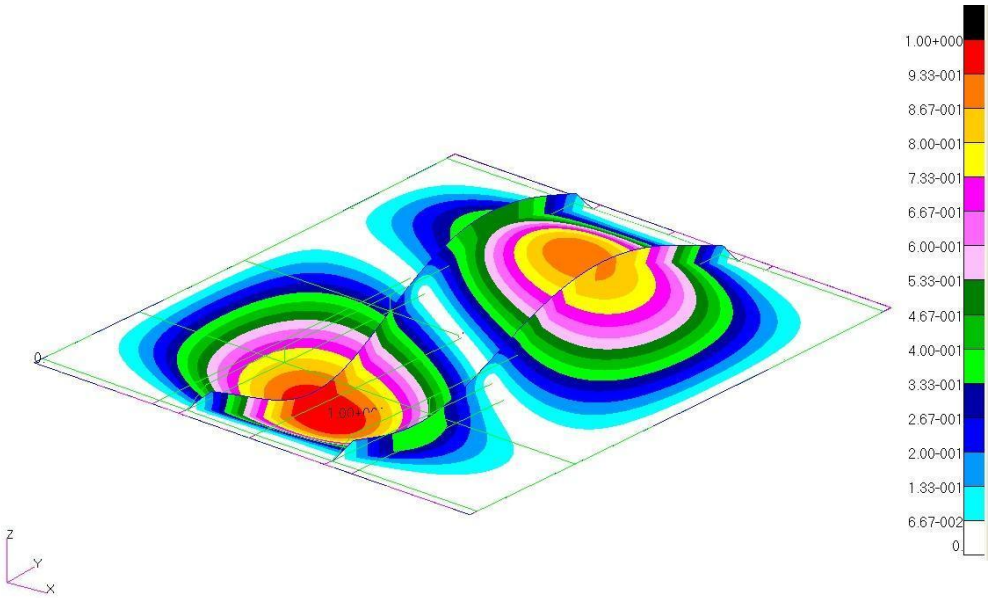

Figure 5.8: Isometric view of Second Buckling Mode Shape from the Finite Element Analysis for the EBF^3 Panels under Load Case 1

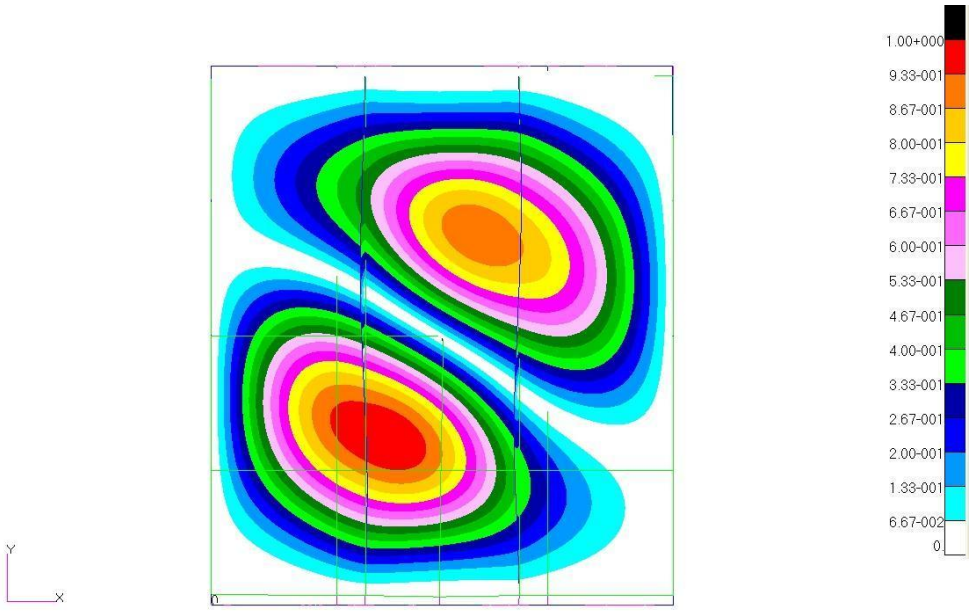

Figure 5.9: Top view of Second Buckling Mode Shape from the Finite Element Analysis for the EBF^3 Panels under Load Case 1

This suggested that before nonlinear behavior occurred, the loads were being introduced into the panels as modeled.

The linear FEA out-of-plane displacements compared against the experimental out-of-plane displacements measured from DCDTs 1, 2, and 3 are shown in Figures 5.12 and 5.13 for the machined and EBF^3 panels respectively. The linear FEA for the machined panels correlated with the linear behavior measured from DCDTs 1, 2, and 3. Once the panels buckled and the out-of-plane displacement became large, the linear FEA did not accurately predict the out-of-plane displacement for the panels. This was expected due to the capabilities of linear analysis [22]. The linear FEA for the EBF^3 panels predicted negative out-of-plane displacement. Negative out-of-plane displacement was seen in the experimental EBF^3 panels, but at a much smaller magnitude than was predicted with the linear FEA. This was attributed to the EBF^3 linear finite element model not being modeled after the exact distortion seen in the EBF^3 panels once the panels were bolted into the test fixture.

The remaining figures in Appendix C compare the linear FEA to the experimental data. The results are similar for all of load case 1. The linear FEA data was fairly accurate in the linear range of the experiment, however, once nonlinear behavior started in the experiments, the linear FEA analysis did not correlate well to the experimental results.

The nonlinear FEA axial strains and the experimental axial strains for strain gages 3a and 4a are shown in Figures 5.14 and 5.15 for the machined and EBF^3 panels respectively. The nonlinear FEA lateral strains and the

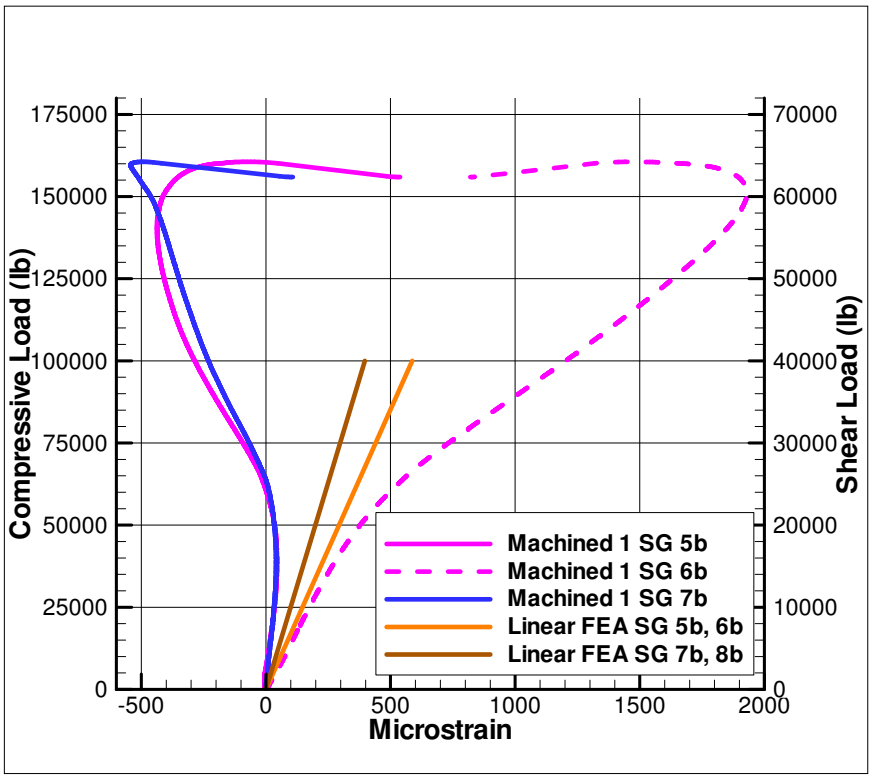

Figure 5.10: Linear Finite Element Analysis Results and Experimental Results of Strain Gages 5b-8b for Machined Panel 1

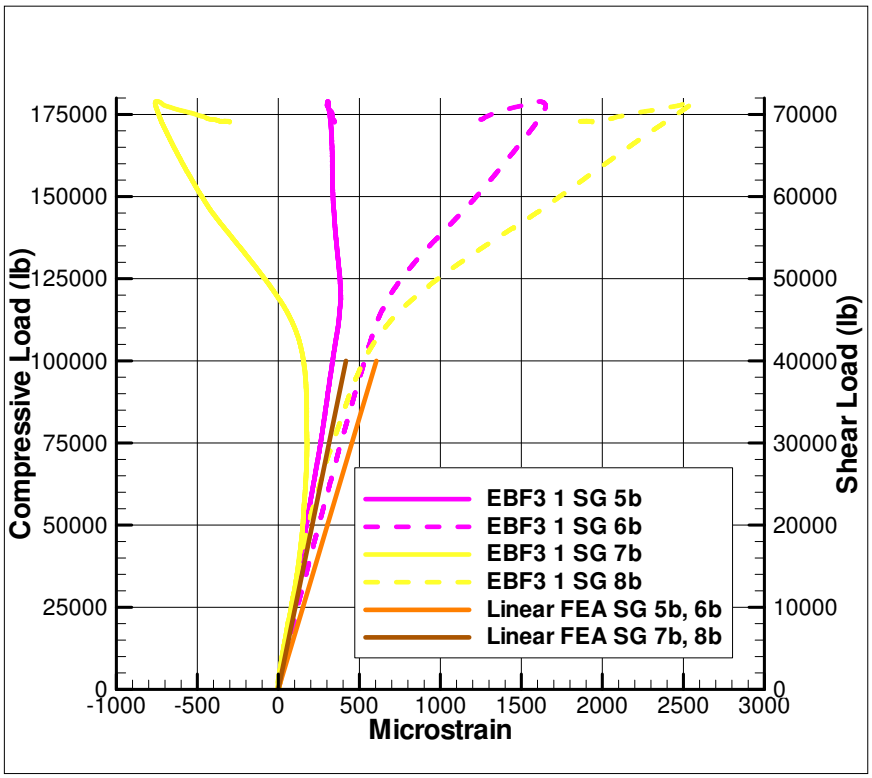

Figure 5.11: Linear Finite Element Analysis Results and Experimental Results of Strain Gages 5b-8b for EBF^3 Panel 1

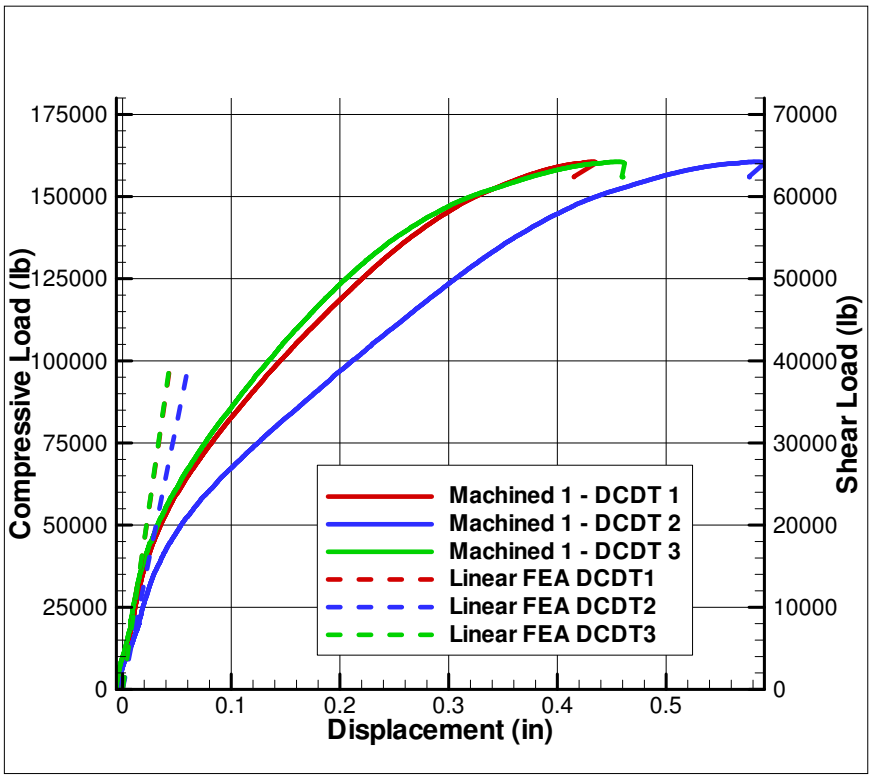

Figure 5.12: Linear Finite Element Analysis Results and Experimental Results of DCDTs 1, 2 and 3 for Machined Panel 1

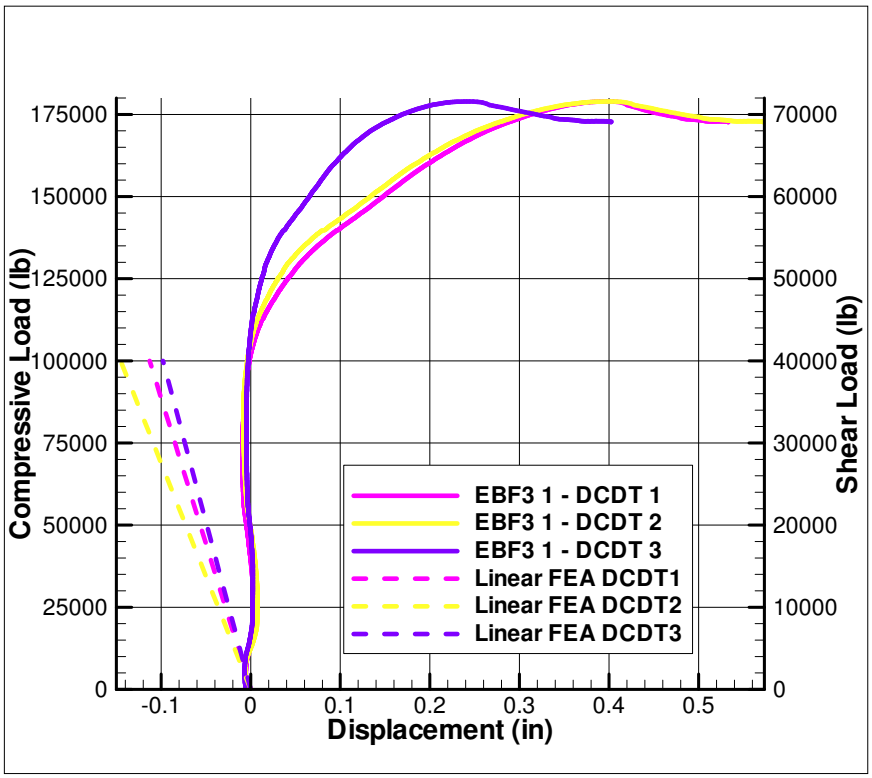

Figure 5.13: Linear Finite Element Analysis Results and Experimental Results of DCDTs 1, 2 and 3 for EBF^3 Panel 1

experimental lateral strains for strain gages 3b and 4b are shown in Figures 5.16 and 5.17 for the machined and EBF^3 panels respectively. Strain gages 3 and 4 were chosen to compare with the experimental results because the nonlinear FEA results from strain gages 3 and 4 were the most comparable with the experimental data. The machined panels' nonlinear FEA strain results showed a good correlation in the linear region. After the panels buckled, the strain from the nonlinear FEA became larger as the panels deformed more. This was similar to what occurred in the experimental strain results, except the nonlinear FEA strain results showed more nonlinearity at lower loads than the experimental strain results. The EBF^3 panels' nonlinear analysis was almost completely linear. This was contrary to the experimental strain results. The experimental strain results showed nonlinear behavior from the panels once buckling occurred. The FEA nonlinear data stopped at approximately at load of 70 kips compression for the machined panels and 65 kips compression for the EBF^3 panels because the stiffness matrix became singular and no more results could be obtained [24].

The discrepancy in the nonlinear FEA results was attributed to the difference between the problems with the test fixture and perfect conditions modeled in the finite element model. The boundary conditions acting on a panel play a significant role when determining the buckling load and shape of a panel. The boundary conditions could also have changed in the post-buckled region of the panels which could account for some of the discrepancies since the finite element model assumed uniform compression and shear throughout

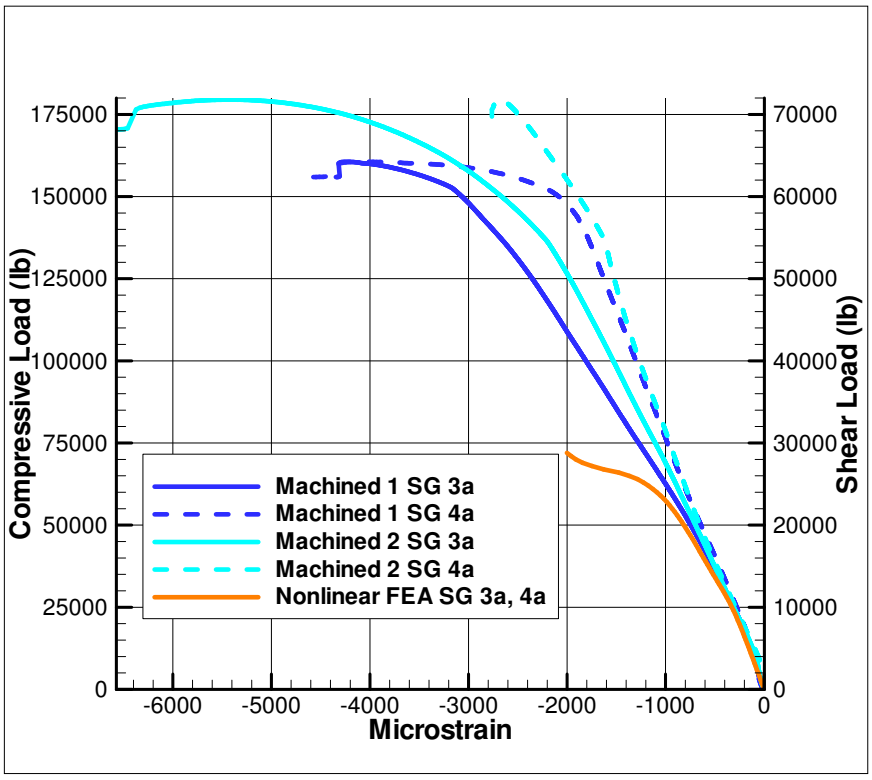

Figure 5.14: Nonlinear Finite Element Analysis Results and Experimental Results of Strain Gages 3a-4a for Machined Panels 1 and 2

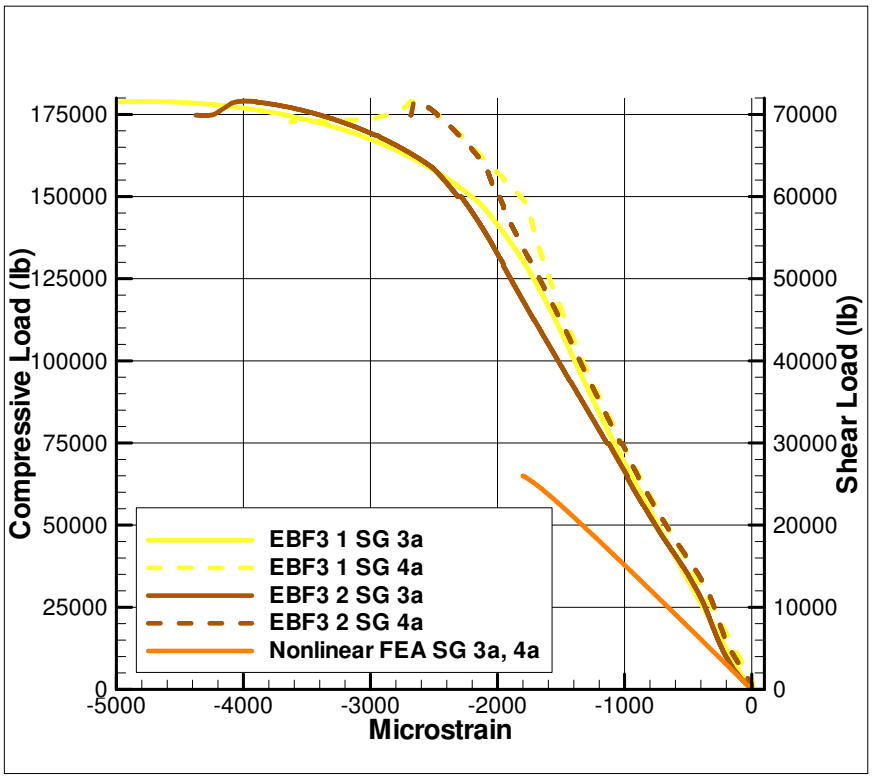

Figure 5.15: Nonlinear Finite Element Analysis Results and Experimental Results of Strain Gages 3a-4a for EBF^3 Panels 1 and 2

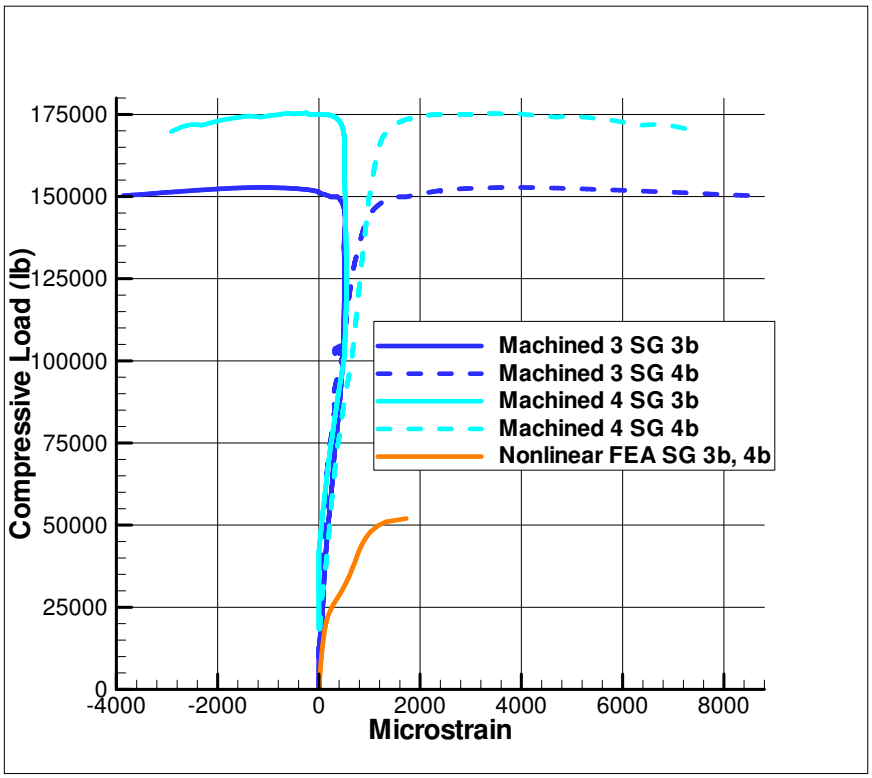

Figure 5.16: Nonlinear Finite Element Analysis Results and Experimental Results of Strain Gages 3b-4b for Machined Panels 1 and 2

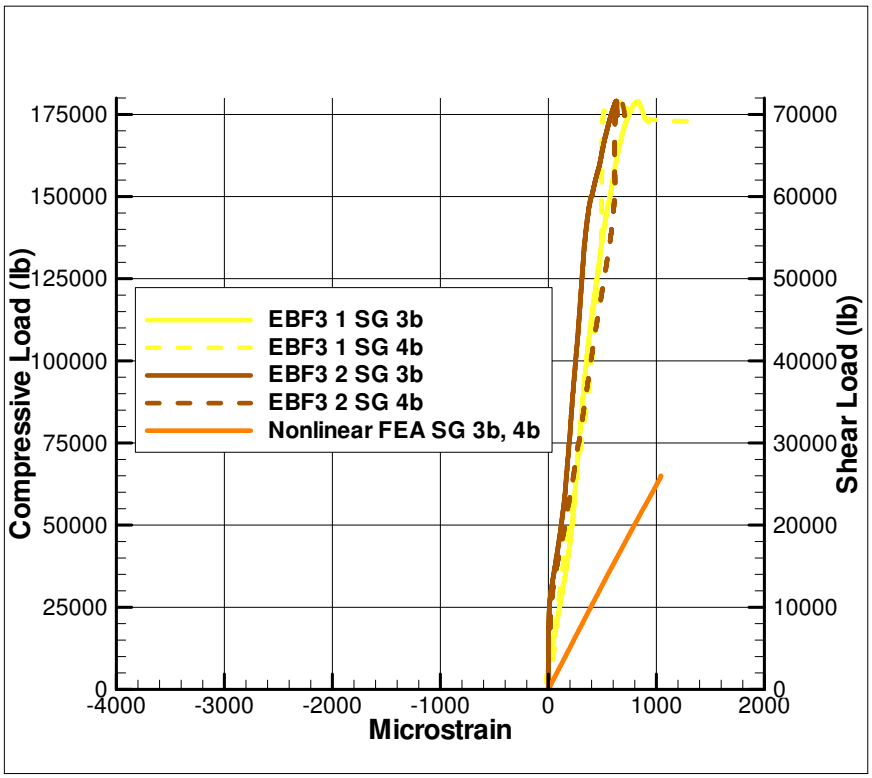

Figure 5.17: Nonlinear Finite Element Analysis Results and Experimental Results of Strain Gages 3b-4b for EBF^3 Panels 1 and 2

the whole test [44]. This predicted the buckling load, buckling shape, and the linear results of the panel that were comparable to the experimental results. However, after the panels buckled, the assumed perfect boundary conditions may not have been satisfactory in the post-buckled region of the experiment. The rotation of the load platen seen in Figures 3.4 as well as the irregular hole pattern caused a nonuniform load in the test specimens. Also, alignment problems and curvature of the panels, such as that seen with the EBF^3 panels, could have also caused the load to not be ideally introduced into the test specimen [45]. This could have caused some discrepancies between the finite element analysis and the experimental data. Lastly, the load capacity of the test fixture was unknown and it was possible that the tests were approaching the limits of the test fixture, potentially causing a nonuniform load to be introduced into the test specimens [44].

The initial distortion of the panels also contributed heavily to the nonlinear analysis [23]. The machined panels had a small amount of linear data from the nonlinear FEA from strain gages 3a and 4a that corroborated with the experimental strain results. However, the EBF^3 panels' nonlinear analysis was linear for all the FEA results. As stated earlier, if the machined panels had been modeled to depict the initial distortions that were present in the panels, the nonlinear FEA results may have been more consistent. Also, since EBF^3 panels were modeled in their free standing state instead of in the test fixture, the initial distortion was not entirely accurate for the nonlinear analysis thus causing more discrepancies in the data. Also the EBF^3 panels had

some residual stressed, especially in the area of the stiffeners. This could have caused a difference between the FEA results and the experimental results since the residual stresses were not modeled. Lastly, the problems with modeling the boundary conditions and conditions of the plate could also explain some of the discrepancies with the linear FEA.

5.3 Load Case 2

The average experimental buckling loads and the FEA's predication of the buckling loads for load case 2 are listed in Table 5.2. The FEA predicted a buckling load 14% higher than what was seen experimentally for the machined panels and 62% lower than what was seen experimentally for the EBF^3 panels. Again the variance in the FEA buckling could have occurred due to the machined panels' FEA model being modeled as a perfectly flat panel. However, there could have been some distortion which would have influenced the FEA of the machined panels. The FEA results were closer for the machined panels than the EBF^3 panels in load case 2 because the EBF^3 panels had a large buckling load in the experimental results.

An isometric view of the first buckling mode shape is shown in Figure 5.2 and a top view of the first buckling mode shape is shown in Figure 5.19 for the machined panels under load case 2. An isometric view of the second buckling mode shape is shown in Figure 5.4 and a top view of the second buckling mode shape is shown in Figure 5.21 for the machined panels under load case 2. Like with load case 1, the FEA predicted a first buckling mode

shape of a half-sine wave and an "S" shape for the second buckling mode. This supported the buckled shape of the panel from the experimental tests.

An isometric view of the first buckling mode shape is shown in Figure 5.6 and a top view of the first buckling mode shape is shown in Figure 5.23 for the EBF^3 panels under load case 2. An isometric view of the second buckling mode shape is shown in Figure 5.8 and a top view of the second buckling mode shape is shown in Figure 5.25 for the EBF^3 panels under load case 2. The FEA predicted the panels buckled into a negative half-sine wave shape for the first buckling mode, which was supported by the experimental buckling shape. The FEA accurately predicted the panels buckling into the "S" shape for the second buckling mode.

The FEA's predicted buckling shapes matched the experimental buckling shapes for load case 2. The buckling shapes predicated for load case 2 were similar to the predicted shapes for load case 1. However, it can be seen in the top views of the FEA predicted buckling shapes that the buckling shapes were more skewed in load case 2 than in load case 1. The experimental buckling shape also showed the skewed buckling shape and it was expected due to the higher shear load applied in load case 2 than in load case 1.

The linear FEA strain results and experimental strain results for strain gages 5b-8b are shown in Figures 5.26 and 5.27 for the machined and EBF^3 panels respectively. Like with load case 1, the linear FEA for load case 2 correlated with the experimental results in the linear region.

The linear FEA predicted out-of-plane displacements and experimental

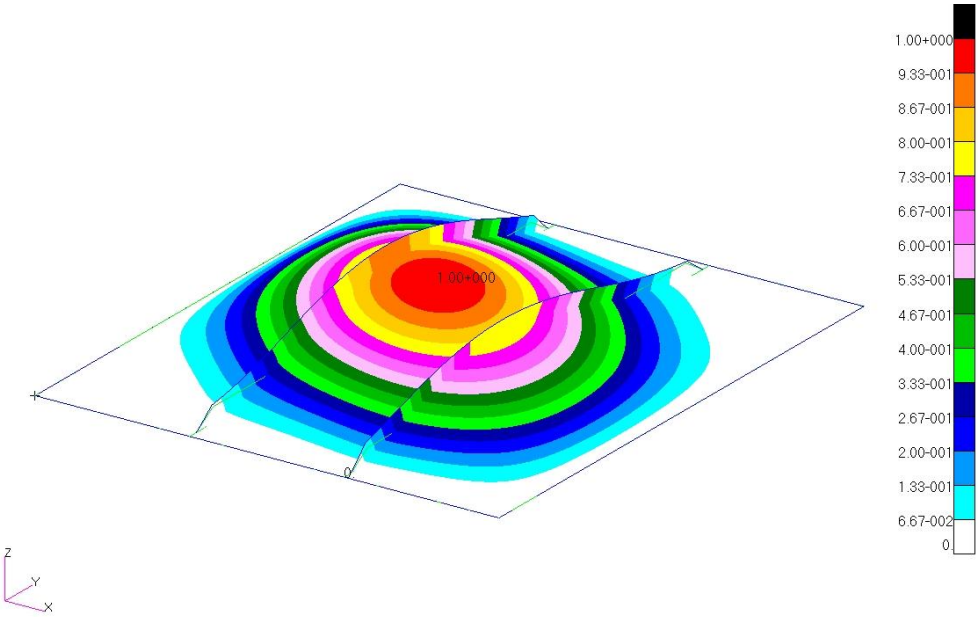

Figure 5.18: Isometric view of First Buckling Mode Shape from the Finite Element Analysis for the Machined Panels under Load Case 2

Table 5.2: Comparison of Finite Element Analysis (FEA) and Experimental Buckling Results for Load Case 2

Panel	Average Buckling Load(kips)
Machined Panels 3 and 4	35
FEA for Machined Panels	40
EBF^3 Panels 3 and 4	100
FEA for EBF^3 Panels	37.5

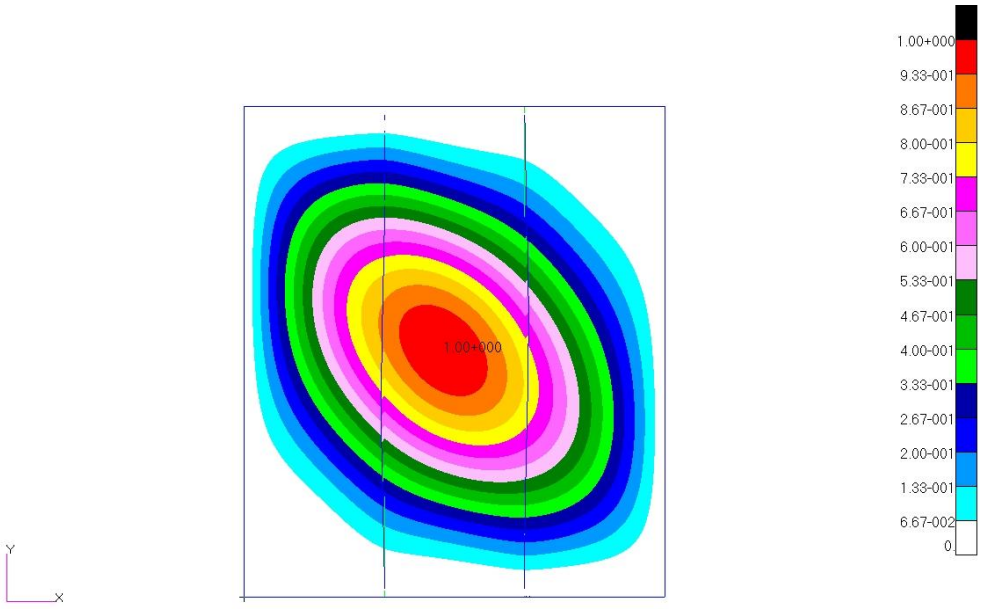

Figure 5.19: Top view of First Buckling Mode Shape from the Finite Element Analysis for the Machined Panels under Load Case 2

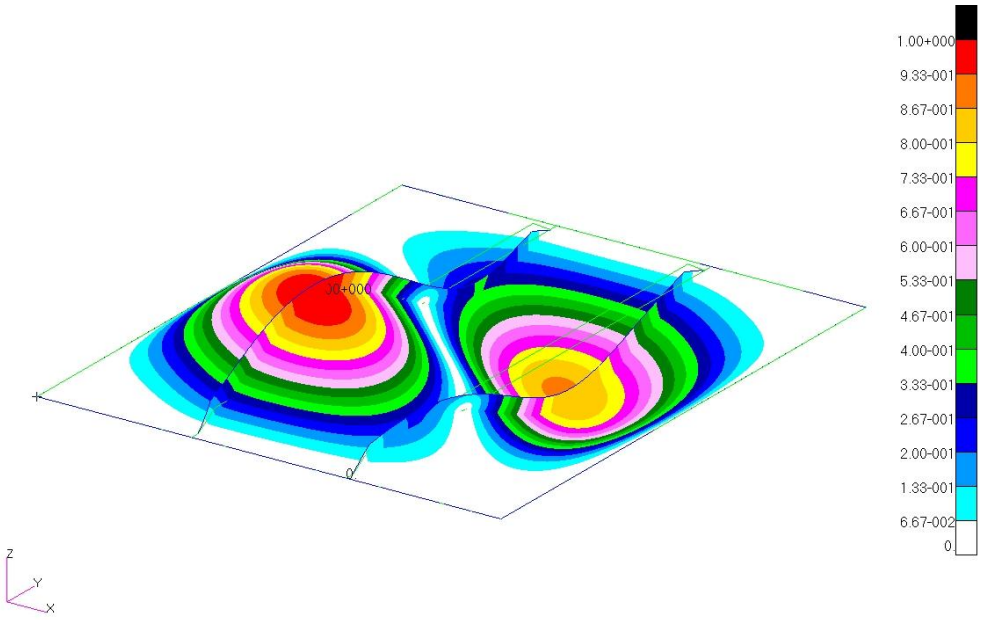

Figure 5.20: Isometric view of Second Buckling Mode Shape from the Finite Element Analysis for the Machined Panels under Load Case 2

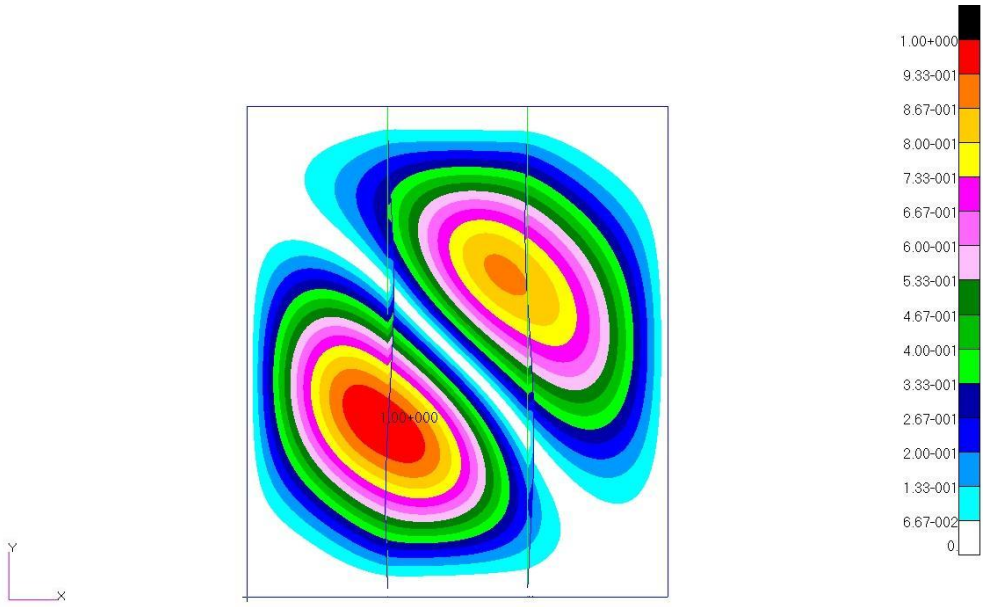

Figure 5.21: Top view of Second Buckling Mode Shape from the Finite Element Analysis for the Machined Panels under Load Case 2

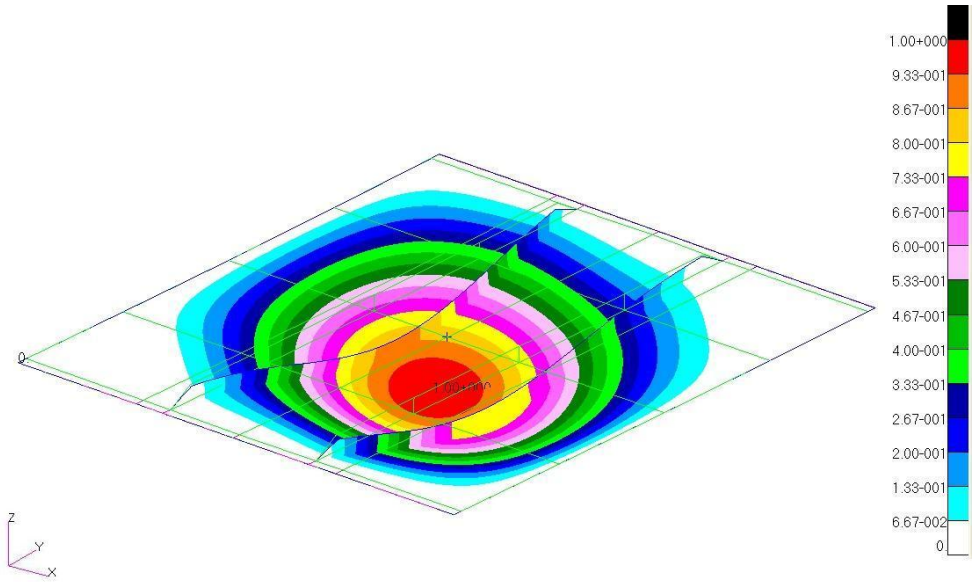

Figure 5.22: Isometric view of First Buckling Mode Shape from the Finite Element Analysis for the EBF^3 Panels under Load Case 2

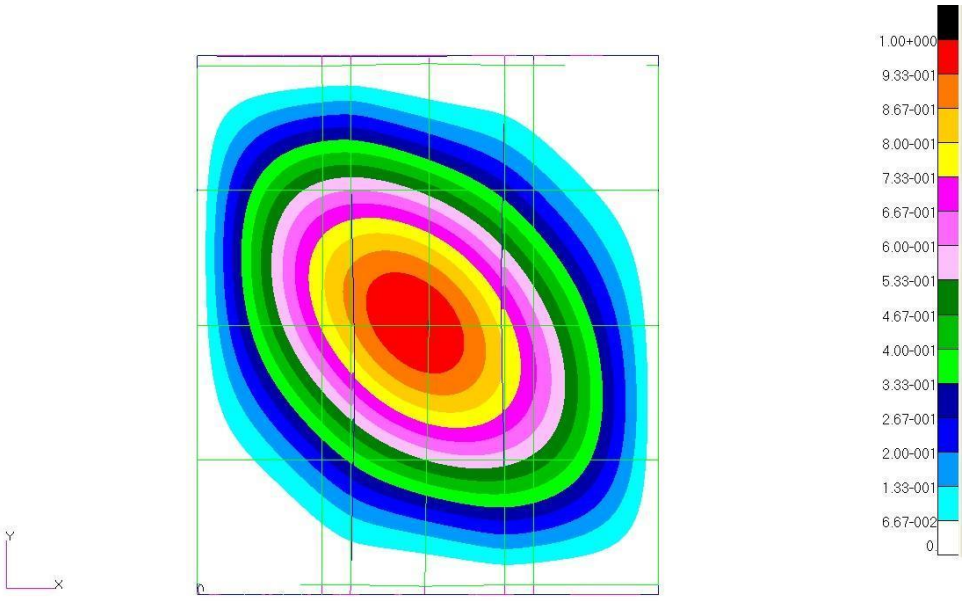

Figure 5.23: Top view of First Buckling Mode Shape from the Finite Element Analysis for the EBF^3 Panels under Load Case 2

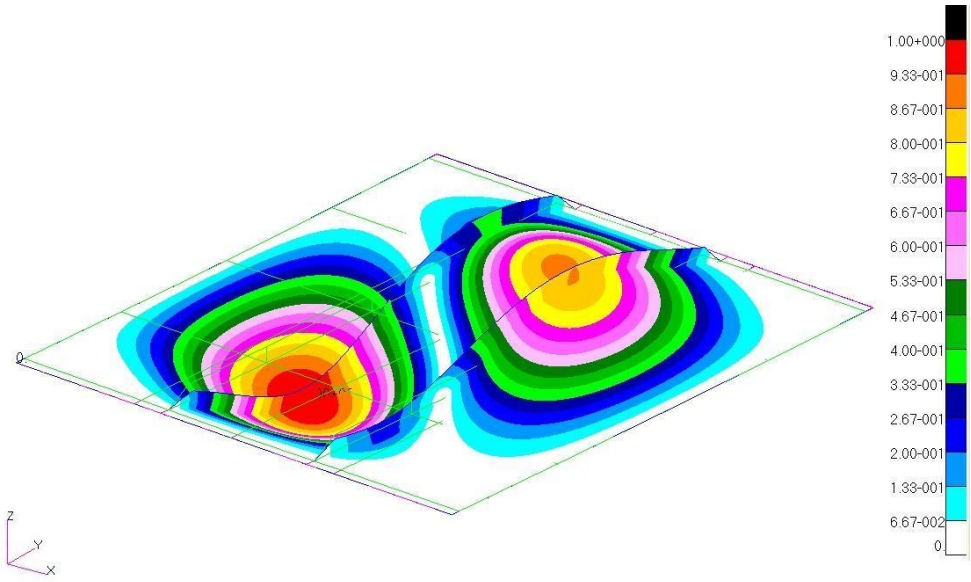

Figure 5.24: Isometric view of Second Buckling Mode Shape from the Finite Element Analysis for the EBF^3 Panels under Load Case 2

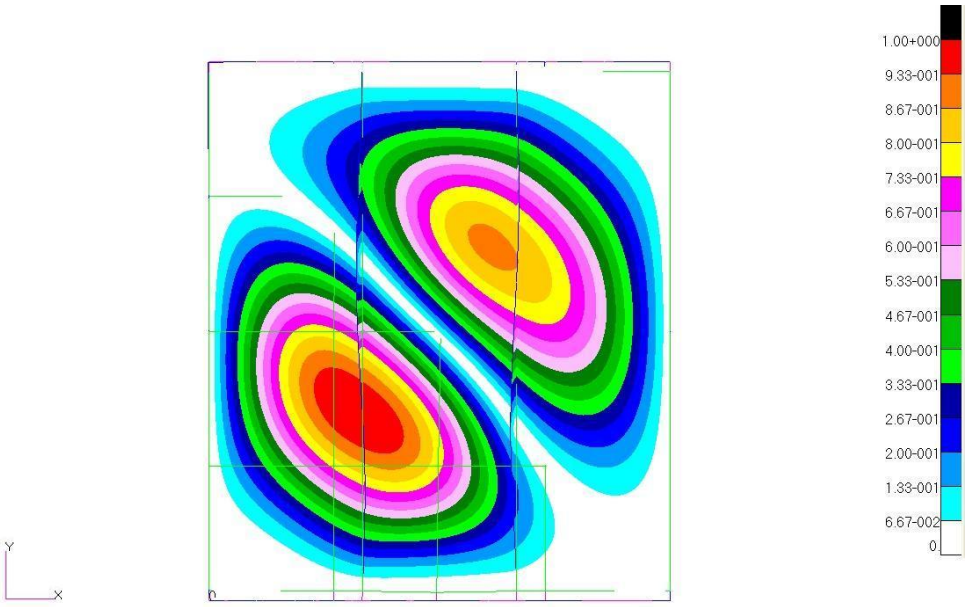

Figure 5.25: Top view of Second Buckling Mode Shape from the Finite Element Analysis for the EBF^3 Panels under Load Case 2

measured out-of-plane displacement for DCDTs 1, 2, and 3 are shown in Figures 5.28 and 5.29 for the machined and EBF^3 panels respectively. As with load case 1, the linear FEA for load case 2 for the machined panels predicted a good correlation in the linear region of the data measured from DCDTs 1, 2, and 3. However, once the panels buckled and the out-of-plane displacement became large, the linear FEA did not accurately predict the out-of-plane displacement of the panels. The linear FEA out-of-plane displacement did not predict the asymmetrical shape of the panel. This was expected because prior to the panels buckling, the displacements measured from DCDTs 1, 2, and 3 was similar to each other. The asymmetric shape of the panels was not seen until the panels buckled in the experiments.

The linear FEA for load case 2 for the EBF^3 panels also predicted negative out-of-plane displacement like load case 1. The linear FEA predicted a steady increase in the negative out-of-plane displacement while the experimental results measured a sudden increase in out-of-plane displacement at a load of 100 kips compression. As with load case 1, this was attributed to the EBF^3 finite element model not modeling the exact distortion as was seen in the panels once they were bolted into the test fixture.

The remaining figures in Appendix D compare the linear FEA data to the experimental data and predicted similar results for all of load case 2. The data was fairly accurate in the linear range of the experiment and once experimental nonlinear results began, the linear FEA did not correlate well with the experimental results.

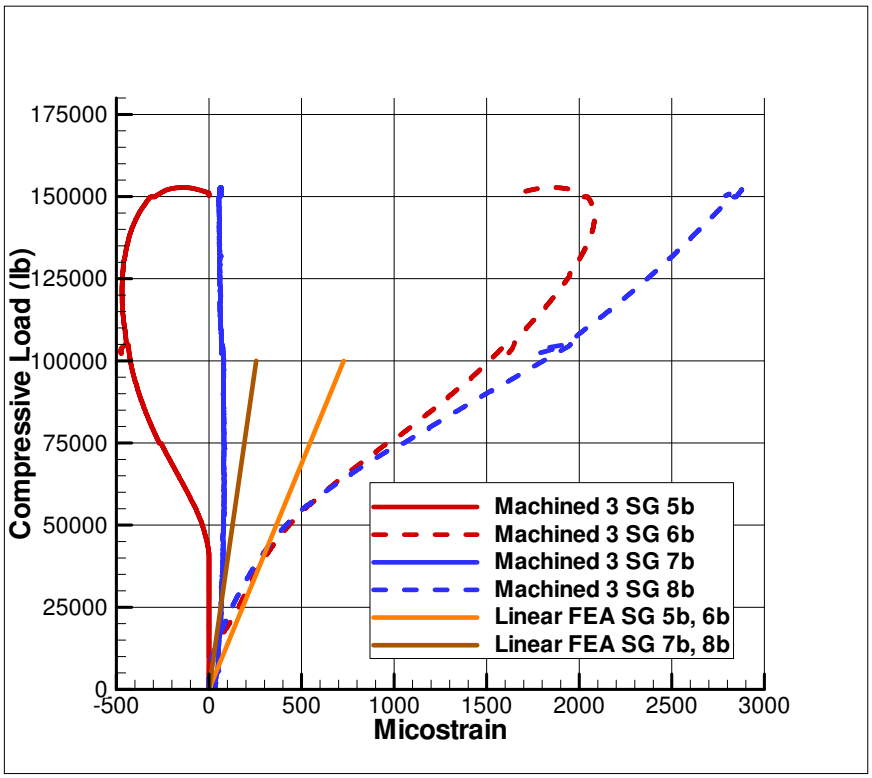

Figure 5.26: Linear Finite Element Analysis Results and Experimental Results of Strain Gages 5b-8b for Machined Panel 3

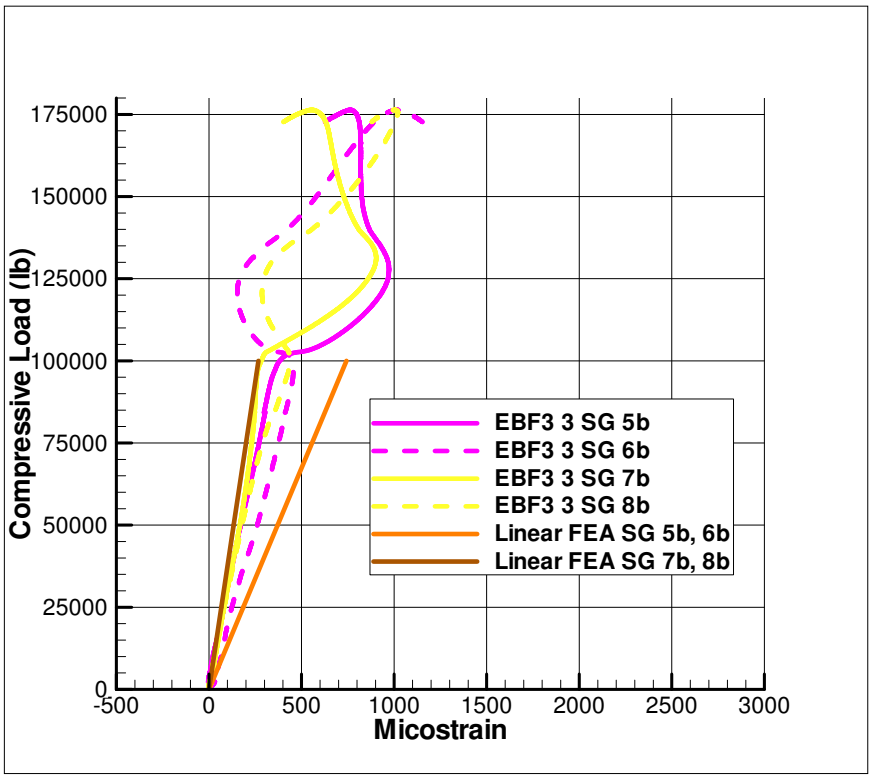

Figure 5.27: Linear Finite Element Analysis Results and Experimental Results of Strain Gages 5b-8b for EBF^3 Panel 3

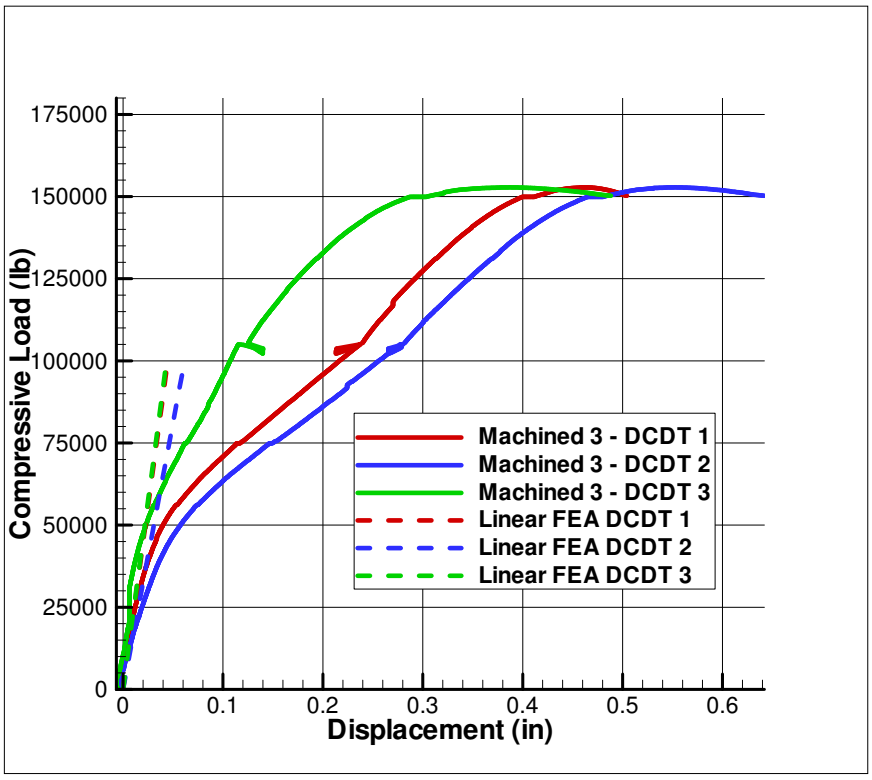

Figure 5.28: Linear Finite Element Analysis Results and Experimental Results of DCDTs 1, 2 and 3 for Machined Panel 3

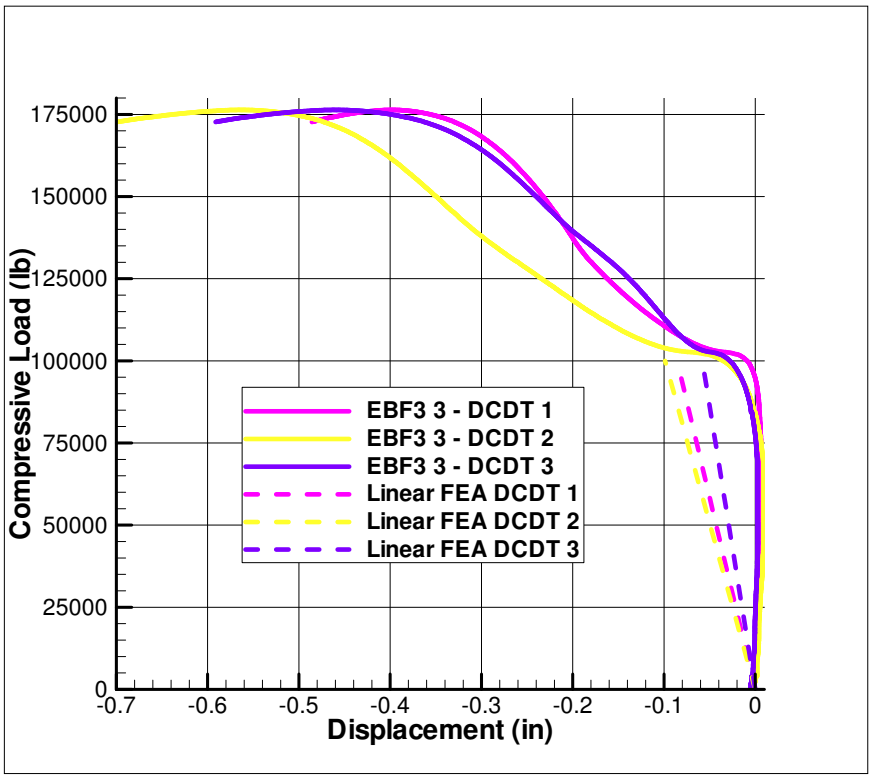

Figure 5.29: Linear Finite Element Analysis Results and Experimental Results of DCDTs 1, 2 and 3 for EBF^3 Panel 3

The nonlinear FEA strain results and the experimental strain results for strain gages 3a and 4a are shown in Figures 5.14 and 5.15 for the machined and EBF^3 panels respectively. The nonlinear FEA strain results and experimental strain results for strain gages 3b and 4b are shown in Figures 5.16 and 5.17 for the machined and EBF^3 panels respectively. Strain gages 3 and 4 were chosen to compare with the experimental results because the nonlinear FEA strain results from strain gages 3 and 4 were the most comparable with the experimental data.

As with load case 1, the machined panels' FEA nonlinear strain results are comparable to the experimental strain results in the linear region. After the panels buckled, the nonlinear FEA predicted nonlinear strain. Nonlinear behavior was seen in the machined panels during the tests, albeit larger strain was seen in the FEA strain results than in the experimental strain results. Similarly to load case 1, the FEA nonlinear data stopped at approximately a load of 53 kips compression for the machined panels because the stiffness matrix became singular.

The EBF^3 panels' FEA nonlinear strain results were almost completely linear like the experimental strain results, although the FEA strain results were generally larger in magnitude than the experimental strain results. Nonlinear behavior was not measured in the EBF^3 panels until after the shear load stopped increasing at 100 kips. The FEA had a maximum load of 51 kips compression for the EBF^3 panels in load case 2 because the stiffness matrix became singular like with load case 1.

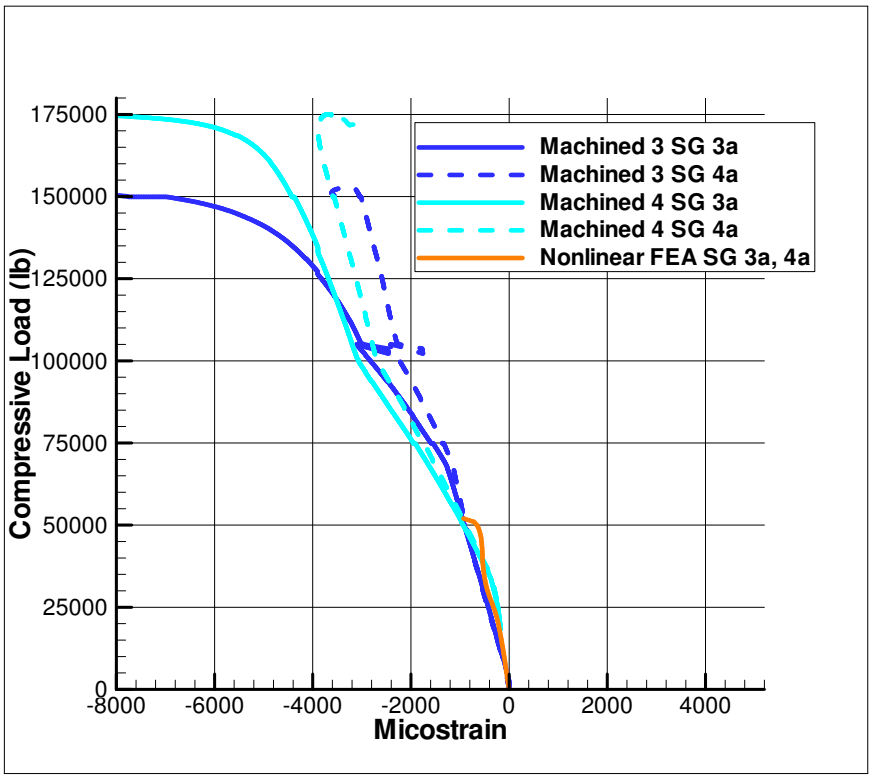

Figure 5.30: Nonlinear Finite Element Analysis Results and Experimental Results of Strain Gages 3a-4a for Machined Panels 3 and 4

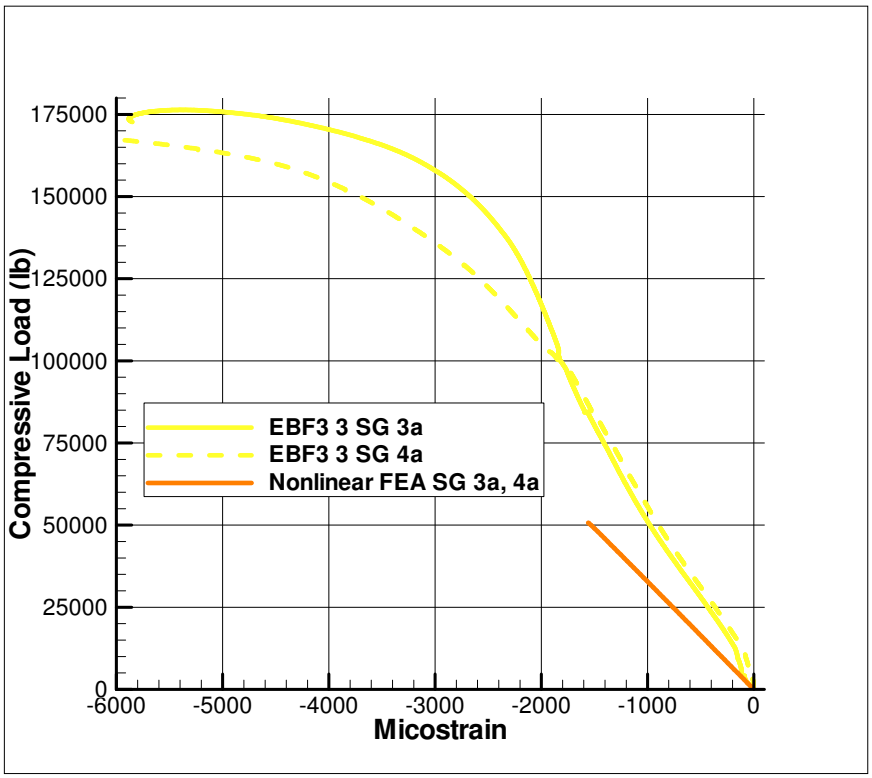

Figure 5.31: Nonlinear Finite Element Analysis Results and Experimental Results of Strain Gages 3a-4a for EBF^3 Panel 3

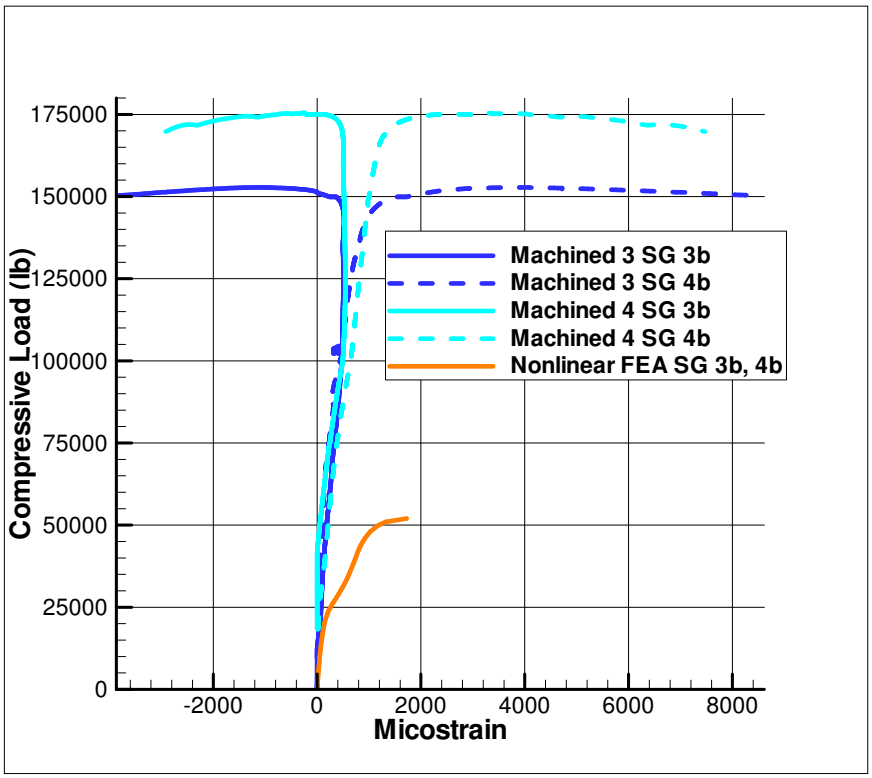

Figure 5.32: Nonlinear Finite Element Analysis Results and Experimental Results of Strain Gages 3b-4b for Machined Panels 3 and 4

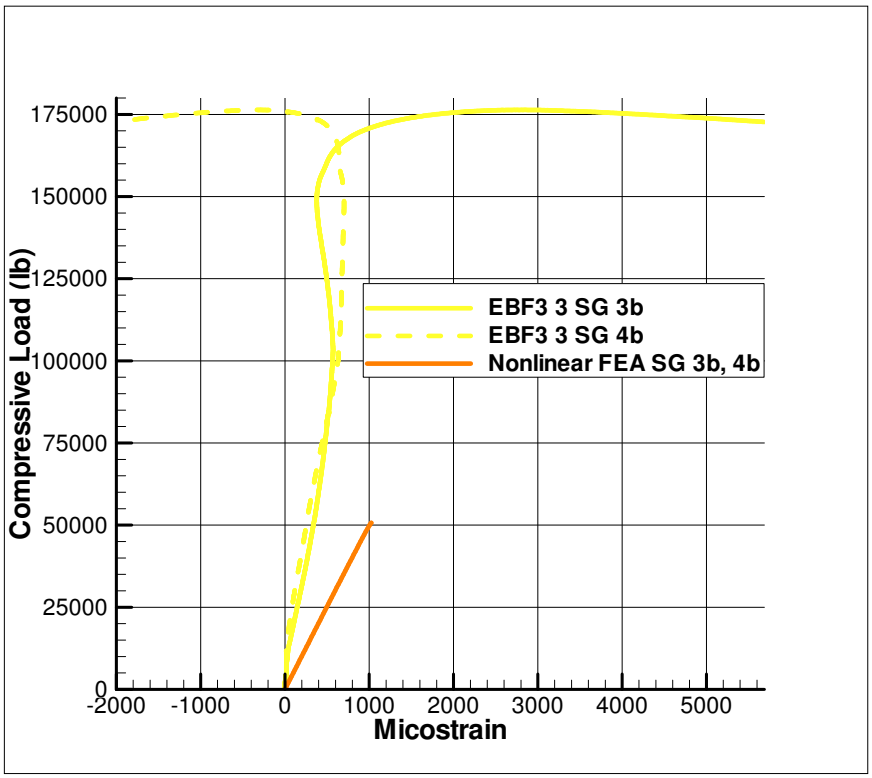

Figure 5.33: Nonlinear Finite Element Analysis Results and Experimental Results of Strain Gages 3b-4b for EBF^3 Panel 3

As with load case 1, the discrepancy between the nonlinear FEA results and experimental results from load case 2 was attributed to the problems with the test fixture and perfect conditions modeled in the finite element model as well as the initial distortion of the panels. Since the FEA had the shear and compressive load perfectly transferred into the panels, the FEA showed higher strain. Also because the true initial distortion of the panels was not modeled, the FEA results were different from the experimental results.

Chapter 6

Concluding Remarks

The structural capabilities of panels fabricated by the EBF^3 process were compared to panels fabricated by integrally machining under two different load cases. When the panels were loaded mostly in compression, the EBF^3 panels behaved similarly to the machined panels prior to buckling. The EBF^3 panels had a slightly lower buckling load than the machined panels. After buckling, EBF^3 Panel 2 buckled similarly to the machined panels, however EBF^3 Panel 1 buckled into the opposite direction as the machined panels for a portion of the test. The lower buckling load and different buckling shape of the EBF^3 panels was attributed to the flaws in the stiffeners, the residual stresses, and the initial distortion in the panels caused by the EBF^3 manufacturing process.

When the panels were loaded so that the shear load matched the compressive load up to 100 kips, the EBF^3 panels behaved quite differently than the machined panels. The EBF^3 panels had a significantly higher buckling load. The machined panels buckled at a slightly lower load for load case 2

than in load case 1. The EBF^3 panels in load case 2 did not buckle until the shear load stopped increasing, thus giving the EBF^3 panels a significantly higher buckling load than the machined panels from both load cases as well as the EBF^3 panels from load case 1. While the machined panels for load case 2 buckled into the same skewed half-sine wave shape from the machined panels in load case 1, the EBF^3 panels in load case 2 had large permanent negative out-of-plane displacement in the top half of the panels. The radically different buckling shape and load of the EBF^3 panels in load case 2 was attributed to the initial distortion of the plate. Since all of the EBF^3 panels had similar initial distortion, the results of load case 2 suggests that the buckling load and shape of the EBF^3 panels was heavily affected by the higher shear load present in load case 2. As previously mentioned, a shear load creates a compressive and tension force at 90° to each other. Due to the distortion in the EBF^3 panels, the tension force, as a stabilizing force, could have prevented the EBF^3 panels from buckling. However, once the shear force stopped increasing, the compressive load from the test machine could have caused the EBF^3 panels to buckle, possibly explaining the higher buckling load from the EBF^3 panels in load case 2. This could also explain why a higher buckling load was not seen from the machined panels or from the EBF^3 panels in load case 1, since the machined panels had smaller distortions and the EBF^3 panels in load case 1 had a smaller shear load and thus a smaller tension load.

Finite element analysis was performed to predict the buckling modes, buckling loads, and to identify the initiation of buckling. The finite element

analysis accurately predicted the buckling shape for the machined panels in both load cases. The predicted first mode buckling shape was a skewed half-sine wave shape buckling towards the stiffener for the machined panels. The EBF^3 panels reacted similarly, however the buckling shape was in the opposite direction of the prediction (buckled away from the stiffener). The finite element analysis (FEA) predicted a second buckling mode shape in an "S" shape as was seen in the experimental results. The FEA also showed the more skewed buckling shape in load case 2, because of the higher shear load in load case 2 than in load case 1.

The FEA predicted a negative buckling shape for the EBF^3 panels in load case 1. While EBF^3 Panel 1 showed a small amount of negative out-of-plane displacement after buckling much like the FEA, EBF^3 Panel 2 showed no negative out-of-plane displacement until the panel buckled into its second buckling mode shape. Thus, the FEA partially predicted the correct buckling mode shape for the EBF^3 panels in load case 1. The difference was attributed to the EBF^3 finite element model not matching the exact shape of the EBF^3 panels once bolted into the test frame.

The FEA predicted a higher buckling load for the machined panels in both load cases than what was seen in the experimental results. This was expected since the finite element model did not contain any of the small flaws or defects inherit in any experimental test which could lower the buckling load of a panel.

Also the FEA's predicted buckling load for the EBF^3 panels in load case

2 was higher than in the experimental results. It was noticed that the higher shear load in load case 2 had a more significant impact on the experimental response from the EBF^3 panels, however the FEA did not accurately show that effect.

The linear results from the FEA predicted the panels' responses fairly well before the panels buckled in the experiments. The close results of the buckling analysis and the linear analysis suggests that the compression-shear combined loads test fixture initiated the load as expected into the test specimen prior to the panels buckling.

The nonlinear results showed some correlation with the experimental results, albeit not as closely as anticipated. The initial distortion and residual stresses of the panels was not accurately modeled which affected the nonlinear FEA results for the EBF^3 panels. Modeling the correct initial distortion and residual stresses could result in more accurate nonlinear FEA results. Also, the boundary conditions and load introduction paths from the test fixture were unknown at higher loads and should be studied in the future to better understand how the fixture behaves at higher loads.

Even though the EBF^3 panels had different buckling shapes than the machined panels, the EBF^3 manufacturing technique was capable of creating panels that behave similarly to machined panels before buckling. The results suggest that a unitized structure could be designed and built using the EBF^3 manufacturing technique as long as the structure was not permitted to buckle. However, more consideration would be required to create a structure using the

EBF^3 manufacturing process that entered the post-buckled region. A greater understanding of the effects of the initial distortion and residual stresses created during the EBF^3 process on the performance of the structure would be required. Also, the effects of the initial distortion and residual stresses on the buckling shape of the structure would also need to be considered if the structure was to incorporate the buckling shape into the aerodynamics of the structure.

Chapter 7

Future Work

Methods to reduce the initial distortion and residual stresses during the EBF^3 process should be considered. This could help the EBF^3 process produce improved unitized structures. Also the effects of the initial distortion and residual stresses should be better understood and incorporated into the finite element model to yield better results from the nonlinear analysis, so that structures made from EBF^3 could be better modeled in the post-buckled region. The correlation between the initial distortion and higher shear load affecting the response of a stiffened panel made from EBF^3 should also be studied further. In addition, the capabilities of the combined compression-shear load fixture should be studied to better understand the limits of the test fixture. Once reaction of the test fixture is better understood at the loads tested here, the effects of the test fixture could be better modeled, thus resulting in improved nonlinear finite element analysis.

Lastly, code has been developed to suggest that unitized structures

with curvilinear stiffeners have the capabilities to outperform straight stiffened unitized structures under certain loads such as combined compression and shear. Further work is underway to study curvilinear stiffened panels. Panels with curvilinear stiffeners are being manufactured by EBF^3 and integrally machining. The panels are being tested in the same combined loads fixture under the same load conditions studied here. The results are to be compared against each other as well as the straight stiffened panels' results.

Bibliography

[1] J. Cutler. *Understanding Aircraft Structures*. Blackwell Science, 1999.

[2] R. M. Rivello. *Theory and Analysis of Flight Structures*. McGraw-Hill Book Company, 1969.

[3] J. D. Anderson. *Introduction to Flight*. McGraw Hill, 2000.

[4] R. M. Jones. *Mechanics of Composite Materials*. Taylor and Francis, Inc., 1999.

[5] E. K. Hoffman, R. A. Hafley, J. A. Wagner, D. C. Jegley, R. W. Pecquet, C. M Blum, et al. Compression buckling behavior of large-scale friction stir welded and riveted 2090-t83 al-li alloy skin-stiffener panels. Technical Report NASA/TM-2002-211770, NASA, 2002.

[6] R. G. Pettit, J. J. Wang, and C. Toh. Validated feasibility study of integrally stiffened metallic fuselage panels for reducing manufacturing costs. Technical Report NASA/CR-2000-209342, NASA, May 2000.

[7] J. Renton, D. Olcott, B. Roesler, R. Batzer, B. Baron, and A. Velicki.

Future of flight vehicle structures (2002-2023). *Journal of Aircraft*, 41(5):986–998, 2004.

[8] M. C. Y. Niu. *Airframe Structural Design: Practical Design Information and Data on Aircraft Structures*. Hong Kong Conmilit Press LTD., second edition.

[9] S. B. Mulani, J. Li, P. Joshi, and R. K. Kapania. Optimization of stiffened electron beam freeform fabrication panels using response surface approaches. In *AIAA-2007-1901, 48th AIAA/ASME/ASCE/AHS/ASC Structures, Structural Dynamics and Materials Conference*, 2007. Honolulu, Hawaii.

[10] L. Brubak and J. Hellesland. Semi-anylytical postbuckling and stength analysis of arbitrarily stiffened plates in local and global bending. *Thin-Walled Structures*, 45(6):620–633, 2007.

[11] J. Li. *Inverse Problems in Structural Mechanics*. PhD thesis, Virginia Polytechnic Institute and State University, 2005. Chapter 4: Optimal Design of Unitized Panels with Curvilinear Stiffeners.

[12] R. K. Kapania, J. Li, and H. Kapoor. Optimal design of unitized panels with curvilinear stiffeners. In *AIAA 5th Aviation, Technology, Integration, and Operations Conference/16th Lighter-than-Air and Balloon Systems Conference*, 2005. Arlington, Virginia.

[13] P. Joshi, S. B. Mulani, R. K. Kapania, and Y. S. Shin. Optimal de-

sign of unitized structures with curvilinear stiffeners using response surface methodology. In *49th AIAA/ASME/ASCE/AHS/ASC, Structures, Structural Dynamics and Materials Conference*, 2008. Chicago, Illinois.

[14] K. Cooper. Free form fabrication in space. Technical Report AIAA 2004-1207, AIAA, 2004.

[15] J. W. Sears. Direct laser powder depoition - state of the art. Technical Report KAPL-P-000311, KAPL, 1999.

[16] K. M. B. Taminger and R. A. Hafley. Characterization of 2219 aluminum produced by electron beam freeform fabrication. In *Proceedings of the 13th SFF Symposium*, pages 482–489, 2002.

[17] R. A. Buswell, R. C. Soar, A. G. F. Gibb, and A. Thorpe. Freeform construction: Mega-scale rapid manufacturing for construction. *Automation in Construction*, 16:224–231, 2007.

[18] K. M. B. Taminger and R. A. Hafley. Electron beam freeform fabrication for cost effective near-net shape manufacturing. Technical Report NASA/TM-2006-214284, NASA, 2006.

[19] K. M. B. Taminger, R. A. Hafley, and M. S. Domack. Evolution and control of 2219 aluminum microstructural features through electron beam freeform fabrication. Technical Report NASA/TM-2006-000000, NASA, 2006.

[20] A. Brickler. Structural evaluation of electron beam freeform fabrication of stiffened panels. Master's thesis, University of Maryland, Baltimore, MD, 2006.

[21] E. W. Nelson, A. Brickler, E. Hoffman, R. K. Kapania, and Karen M. Taminger. Nonlinear structural evaluation of electron beam freeform fabrication of stiffened panels. NASA, in preperation, 2008.

[22] E. Hinton. *NAFEMS: Introduction to Nonlinear Finite Element Analysis*. NAFEMS, 1992.

[23] M. Sathyamoorthy. *Nonlinear Analysis of Structures*. CRC Press, 1997.

[24] MacNeal-Schwendler Corporation. *MSC/NASTRAN Nonlinear Analysis Seminar Notes*, May 1994.

[25] J. F. Doyle. *Nonlinear Analysis of Thin-Walled Structures*. Springer, 2001.

[26] M. A. Crisfield. *Non-linear Finite Element Analysis of Solids and Structures: Volume 1: Essentials*. John Wiley and Sons, 1991.

[27] D. J. Baker. Combined load test fixture. Technical Report ARL-TR-3726, U.S. Army Research Laboratory, 2006.

[28] R. P. Thornburgh. Imperfections and thickness measurements of panels using a coordinate measurement machine. Technical Report NASA/TM-2006-213954, NASA, 2006.

[29] Anonymous. Aerospace structural metals handbook. Technical report, Purdue Research Foundation, 1999. Code 3205.

[30] http://www.correlatedsolutions.com/index.php?option=com_content&task=view&id=16&Itemid=27.

[31] M. W. Hilburger and M. P. Nemeth. Application of video image correlation techniques to the space shuttle external tank foam materials. Technical Report NASA/TM-2005-213944, NASA, 2005.

[32] Jr. J. H. Starnes, M. W. Hilburger, and M. P. Nemeth. The effects of initial imperfections on the buckling of composite cylindrical shells. In *Composite Structures: Theory and Practice*, ASTM STP 1383, West Conshohocken, PA, 2000. American Society for Testing and Materials, P. Grant and C. Q. Rousseau, Eds.

[33] F. P. Beer, E. R. Johnston, and J. T. DeWolf. *Mechanics of Materials*. McGraw Hill, 2002.

[34] J. Singer, J. Arbocz, and T. Weller. *Buckling Experiments: Experimental Methods in Buckling of Thin-Walled Structures Volume 1*. John Wiley and Sons, 1998.

[35] M. P. Nemeth. Buckling behavoir of long ansiotropic plates subjected to combined loads. Technical Report NASA/TP-3568, NASA, 1995.

[36] P. S. Bulson. *The Stability of Flat Plates*. American Elsevier Publishing Company, INC., 1969.

[37] G. L. Farley and D. J. Baker. In-plane shear test of thin panels. *Experimental Mechanics*, 23(1):81–88, 1983.

[38] J.A. Collins. *Mechanical Design of Machine Elements and Machines*. John Wiley and Sons, 2003.

[39] A. Murphy, W. McCune, D. Quinn, and M. Price. The characteristics of friction stir welding process effects on stiffened panel buckling performance. *Thin-Walled Structures*, 45:339–351, 2007.

[40] B. W. McCormick. *Aerodynamics, Aeronautics and Flight Mechanics*. John Wiley and Sons, 1995.

[41] N. M. Ursache, A. J. Keane, and N. W. Bressloff. Design of postbuckled spinal structures for airfoil camber and shape control. *AIAA Journal*, 44(12):3115–3123, 2007.

[42] D. Deng, H. Murakawa, and W. Liang. Numerical simulation of welding distortion in large structures. *Computer Methods in Applied Mechanics and Engineering*, 196:4613–4627, 2007.

[43] D.O. Brush and B.O. Almroth. *Buckling of Bars, Plates, and Shells*. McGraw-Hill, 1975.

[44] J. Singer, J. Arbocz, and T. Weller. *Buckling Experiments: Experimental Methods in Buckling of Thin-Walled Structures Volume 2*. John Wiley and Sons, 2002.

[45] M. W. Hyer and D. O. Douglas. A comparison between experimental and theory for a borsic-aluminum picture frame shear test. Technical Report NASA/CR-148931, NASA, 1976.

[46] MacNeal-Schwendler Corporation. *MSC/NASTRAN Reference Manual Volume 2*, 68 edition, 1994.

[47] W. Ramberg and W. Osgood. Description of stress-strain curves by three parameters. Technical Report NACA-TN-902, NASA, 1943.

[48] J. A. Stricklin, W. E. Haisler, and W. A. Von Riesemann. Evaluation of solution procedures for material and/or geometric nonlinear structural analysis by the direct stiffness method. Technical Report 72-353, AIAA, 1972.

[49] J. A. Stricklin, W. E. Haisler, and W. W. Von Riesemann. Formulation, computation, and solution procedures for material and/or geometric nonlinear structural analysis by the finite element method. Technical Report SC-CR-72 3102, Sandia Laboratories, 1972.

[50] W. E. Haisler, J. A. Stricklin, and F. J. Stebbins. Development and evaluation of solution procedures for geometric nonlinear structural analysis by the direct stiffness method. Technical Report 71-356, AIAA, 1971.

[51] H. Armen, H. Levine, A. Pifko, and A. Levy. Nonlinear analysis of structures. Technical Report NASA CR-2351, NASA, 1974.

Appendix A

Supplementary Data For Load Case 1

This section contains all the remaining experimental results not discussed for Load Case 1. If the results for a strain gages are not presented in the paper or in this section, the data was not recorded.

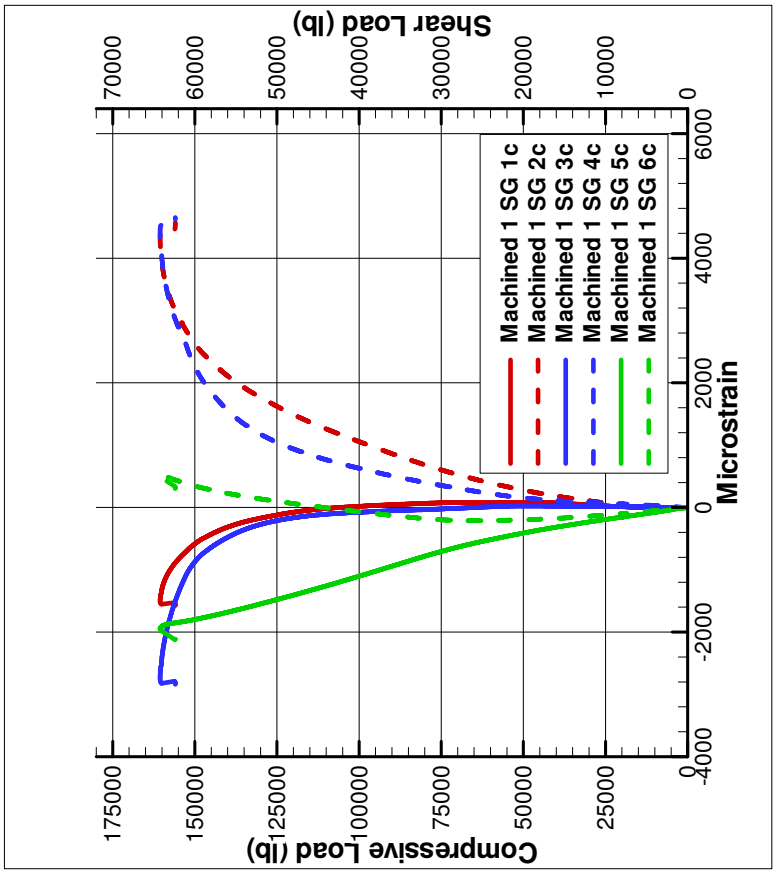

Figure A.1: Strain measured from Strain Gages 1c-6c for Machined Panel 1

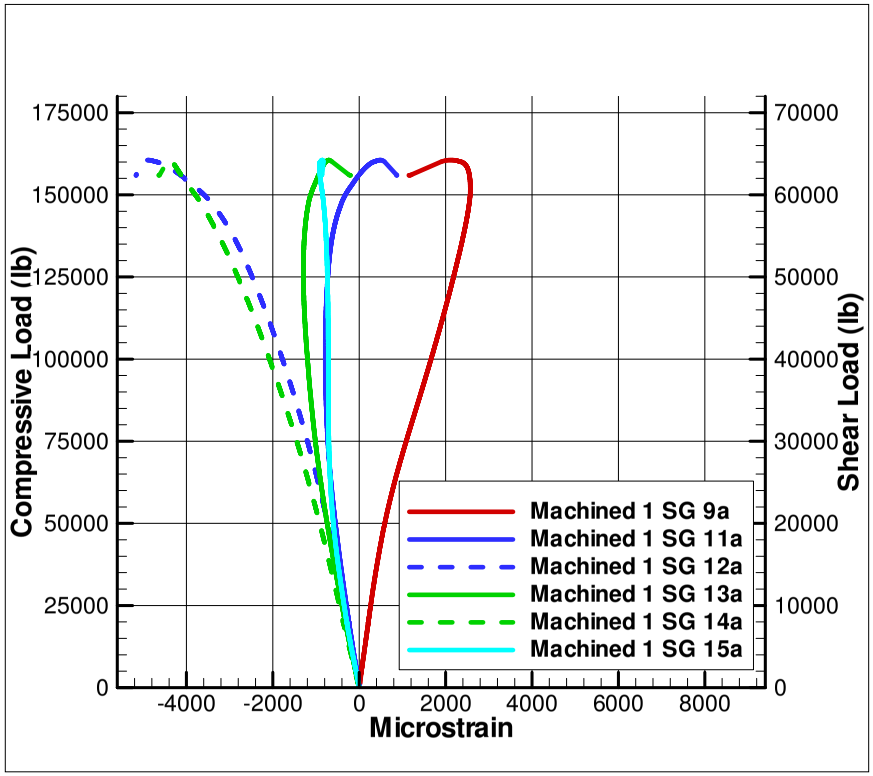

Figure A.2: Axial Strain measured from Strain Gages 9a and 11a-15a for Machined Panel 1

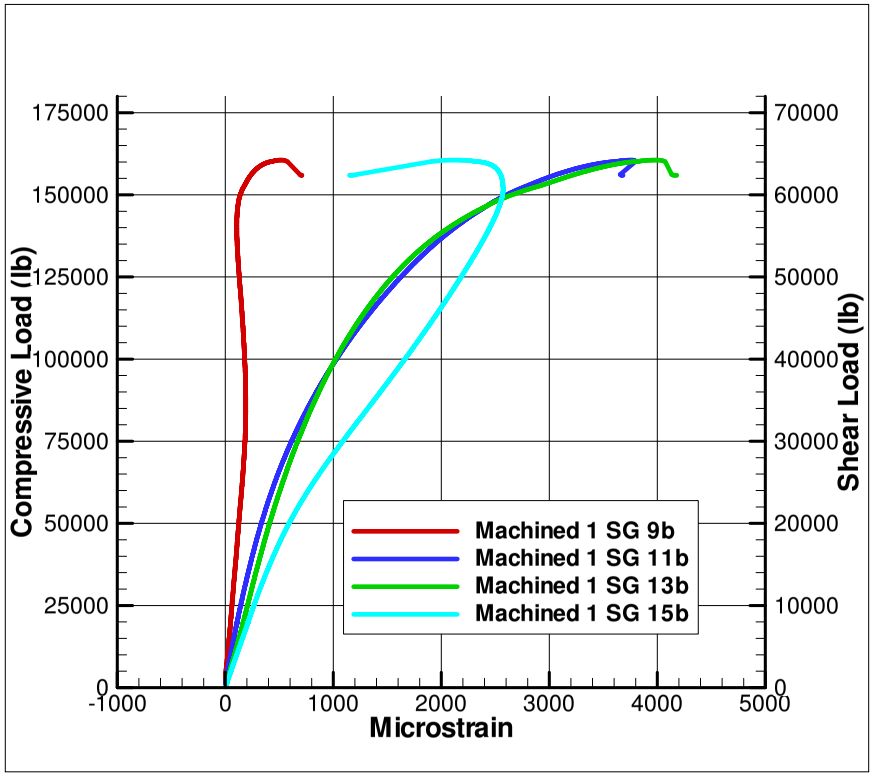

Figure A.3: Lateral Strain measured from Strain Gages 9b, 11b, 13b, and 15b for Machined Panel 1

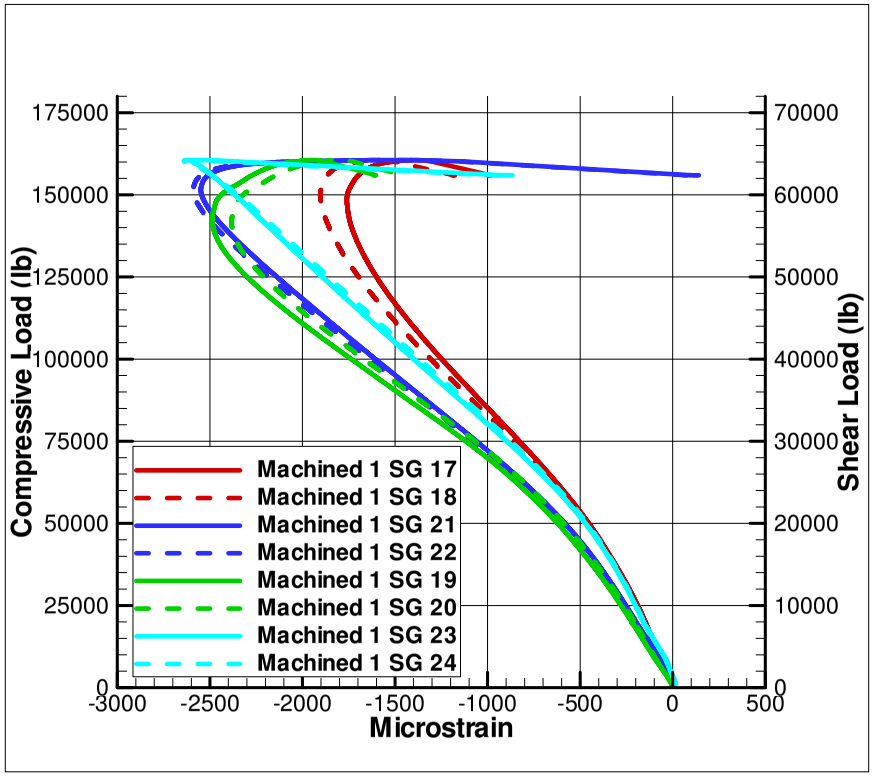

Figure A.4: Strain in the stiffeners measured from Strain Gages 17-24 for Machined Panel 1

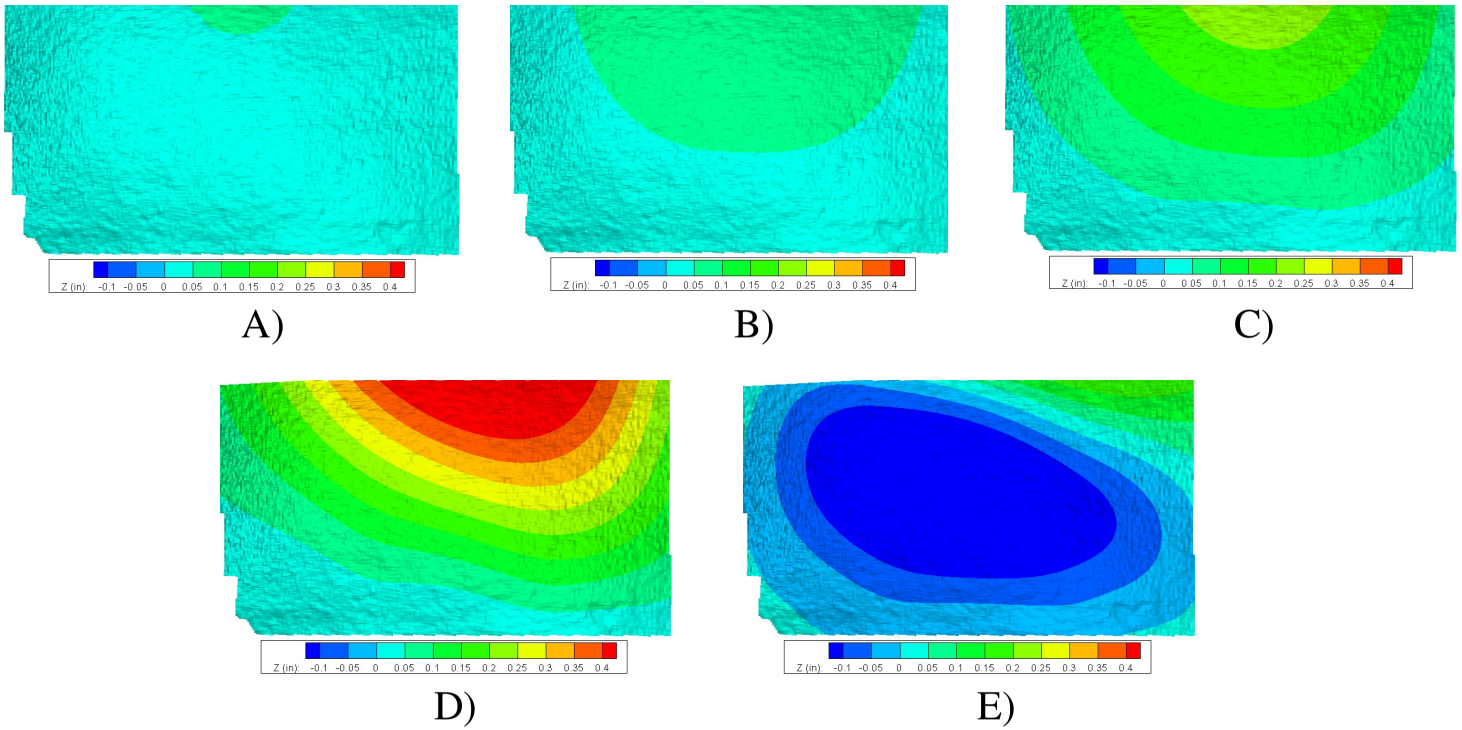

Figure A.5: Out-of-plane Displacement measured in Machined Panel 1 from the VIC 3-D System in the lower half of the panel at A) 28.6 kips (prebuckle) B) 46.2 kips (postbuckle) C) 80.6 (postbuckle) D) 150.8 (maximum load) E) 156.8 (post-failure). Load values expressed in terms of compressive load

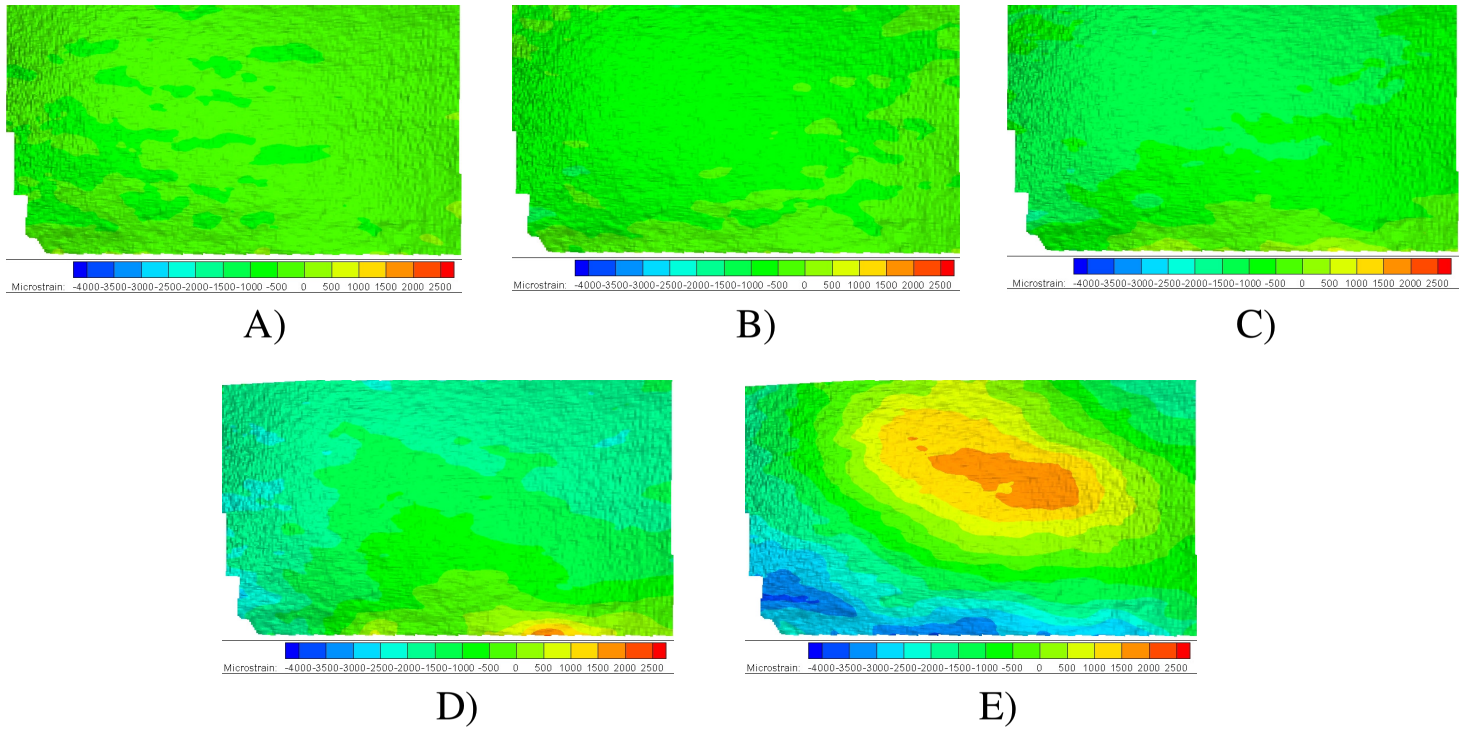

Figure A.6: Axial Strain measured in Machined Panel 1 from the VIC 3-D System in the lower half of the panel at A) 28.6 kips (prebuckle) B) 46.2 kips (postbuckle) C) 80.6 (postbuckle) D) 150.8 (maximum load) E) 156.8 (post-failure). Load values expressed in terms of compressive load

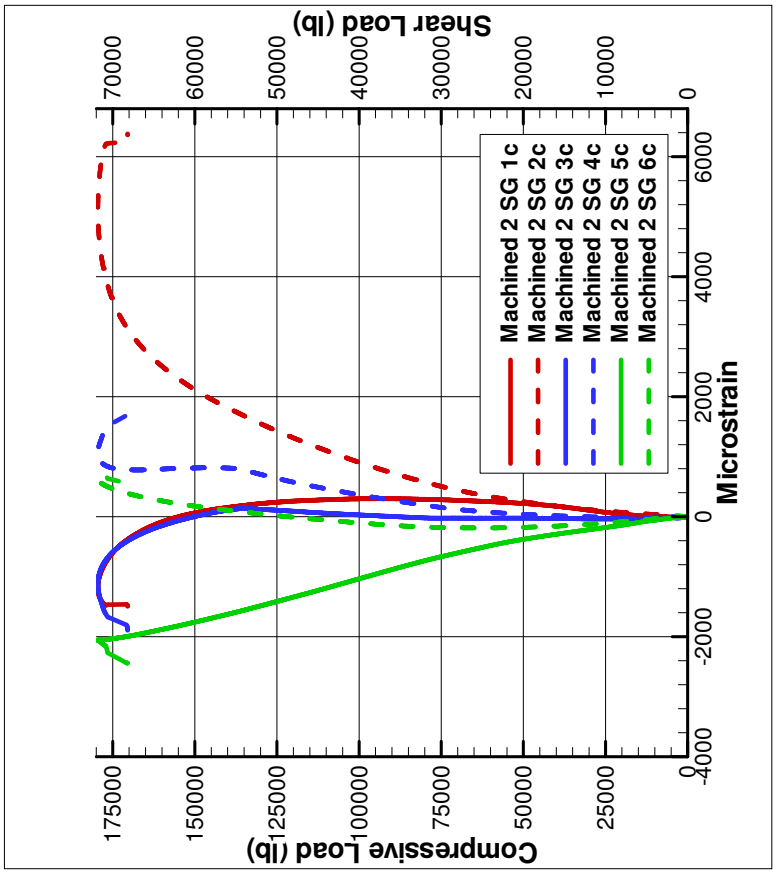

Figure A.7: Strain measured from Strain Gages 1c-6c for Machined Panel 2

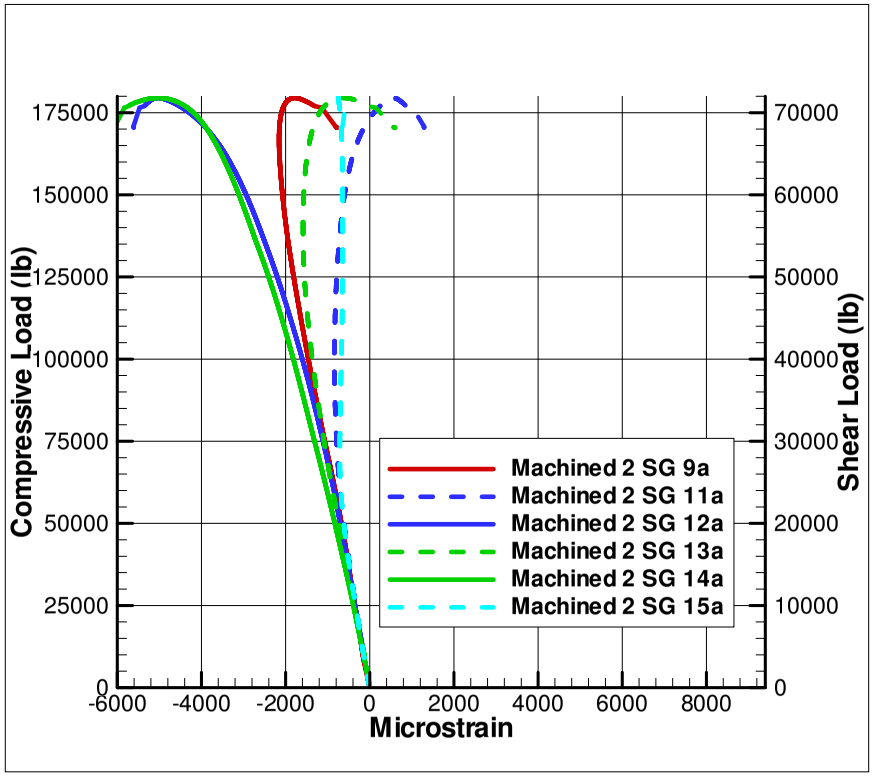

Figure A.8: Axial Strain measured from Strain Gages 9a and 11a-15a for Machined Panel 2

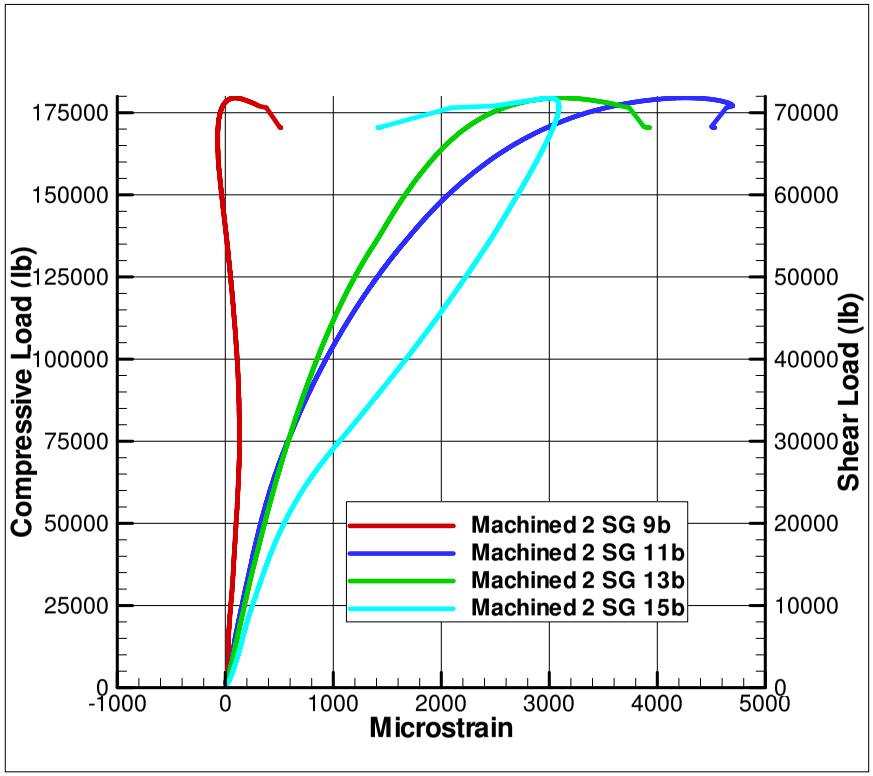

Figure A.9: Lateral Strain measured from Strain Gages 9b, 11b, 13b, and 15b for Machined Panel 2

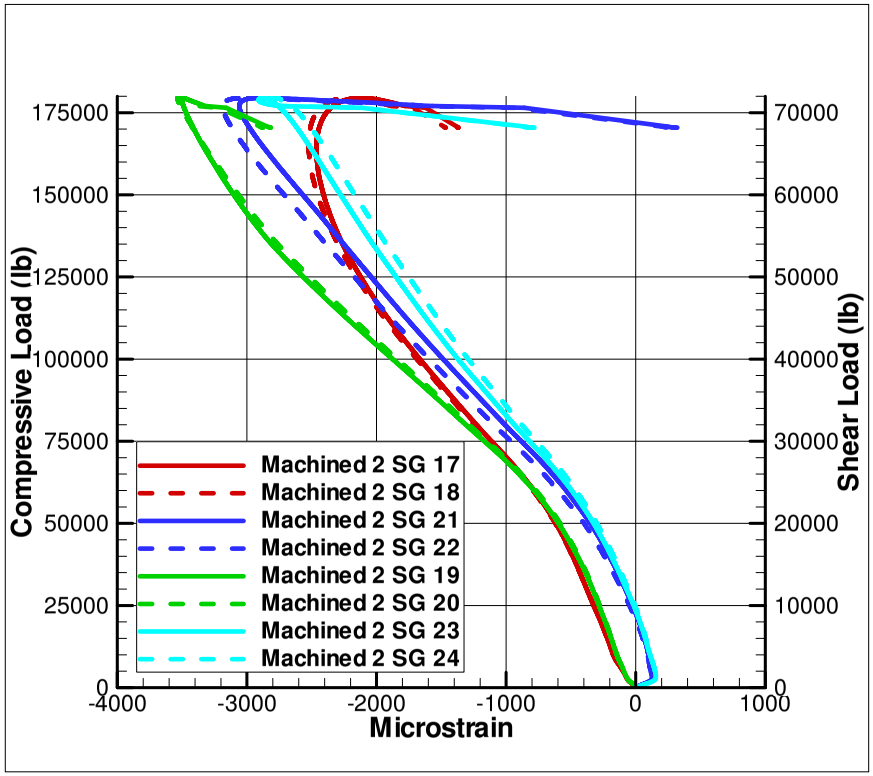

Figure A.10: Strain in the stiffeners measured from Strain Gages 17-24 for Machined Panel 2

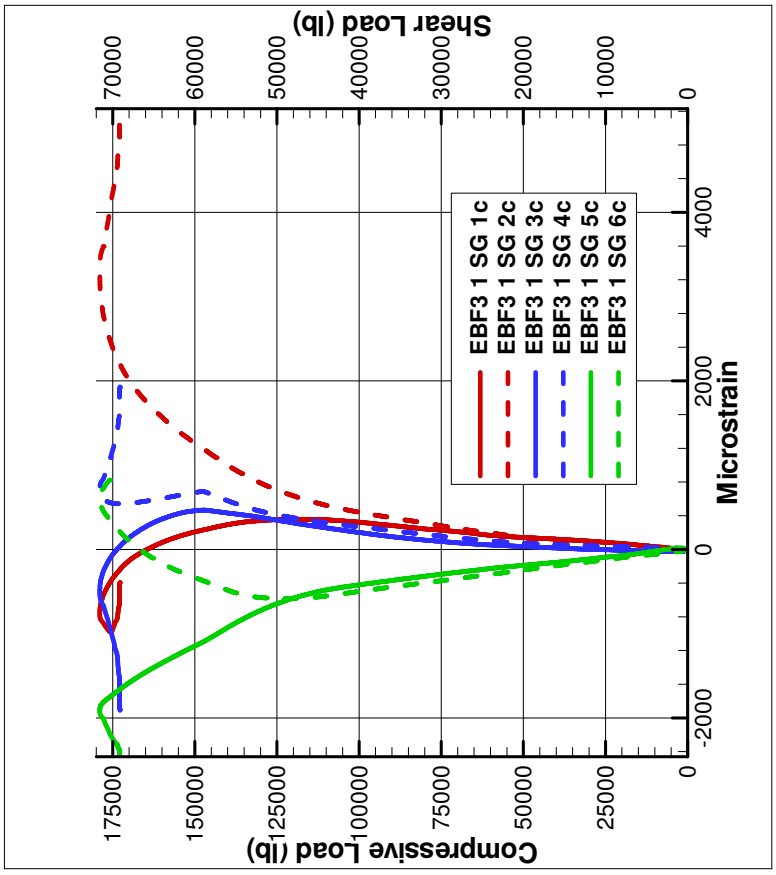

Figure A.11: Strain measured from Strain Gages 1c-6c for EBF3 Panel 1

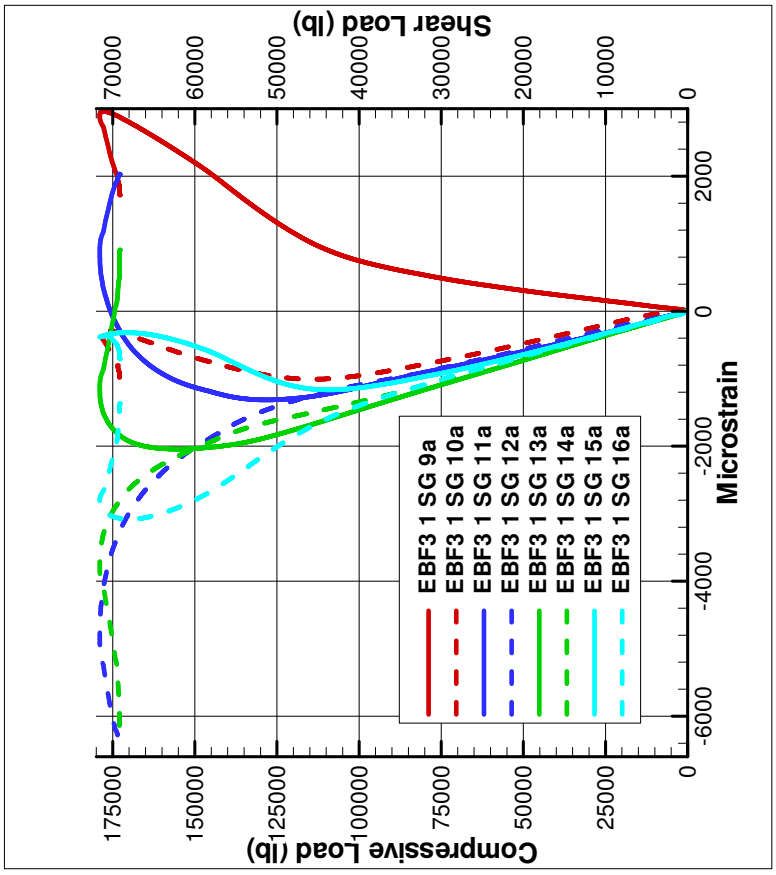

Figure A.12: Strain measured from Strain Gages 9a-16a for EBF3 Panel 1

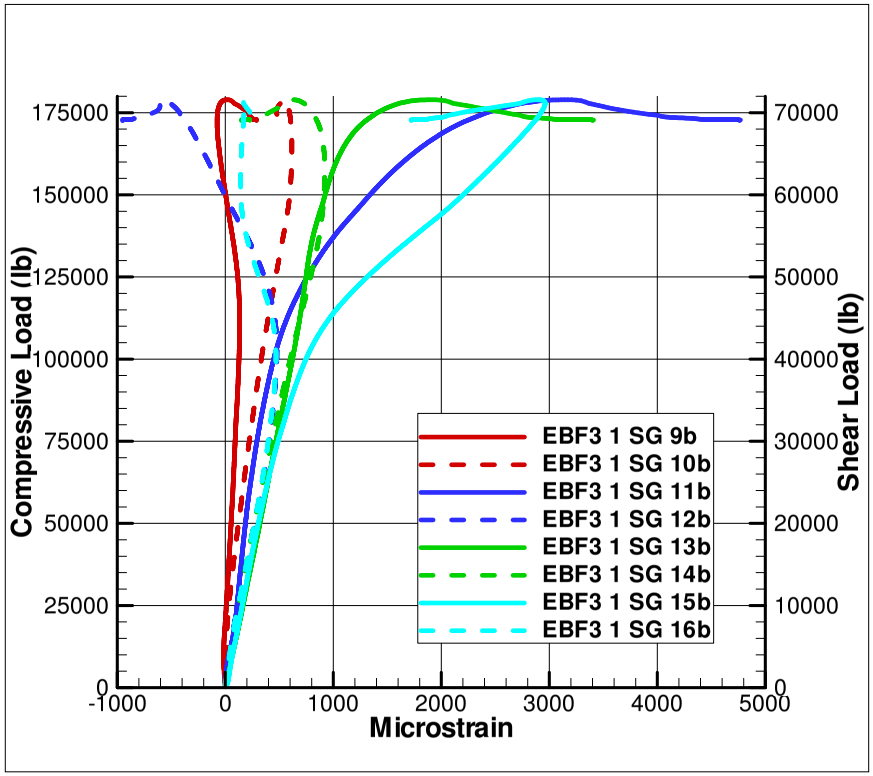

Figure A.13: Lateral Strain measured from Strain Gages 9b-16b for EBF3 Panel 1

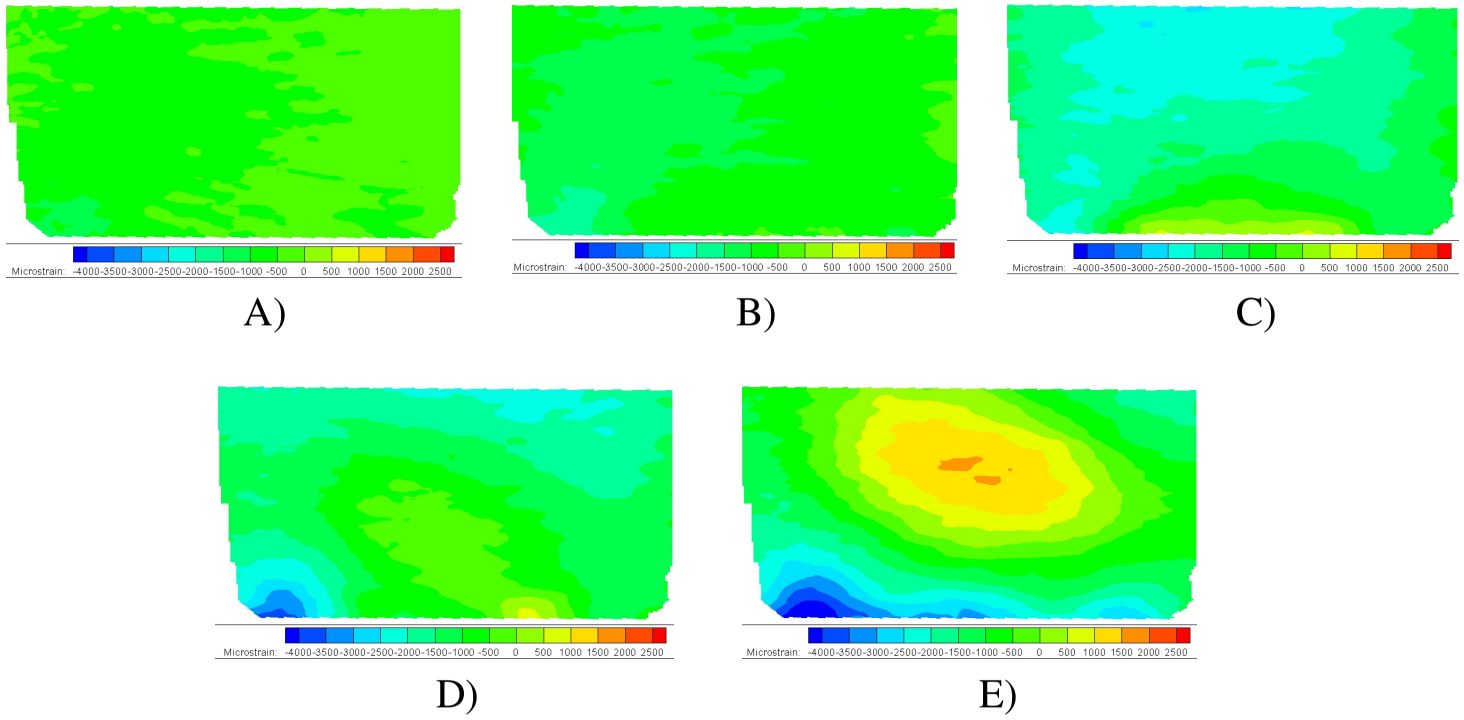

Figure A.14: Axial Strain measured in EBF^3 Panel 1 from the VIC 3-D System in the lower half of the panel at A) 35.1 kips (prebuckle) B) 83.5 kips (postbuckle) C) 135.1 (postbuckle) D) 179.1 (maximum load) E) 160.2 (post-failure). Load values expressed in terms of compressive load

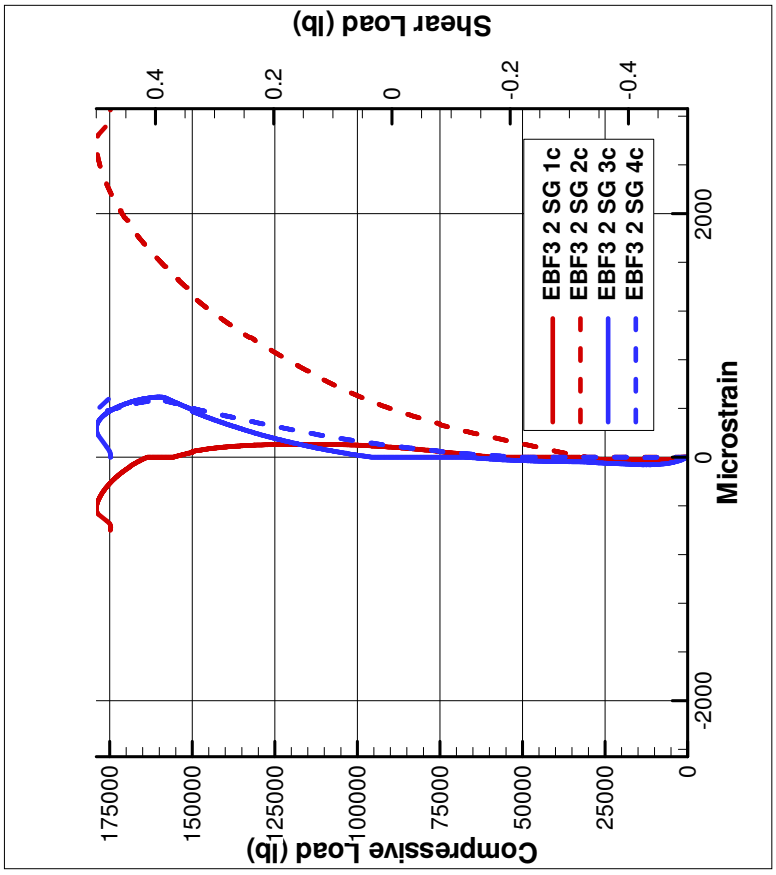

Figure A.15: Strain measured from Strain Gages 1c-4c for EBF3 Panel 2

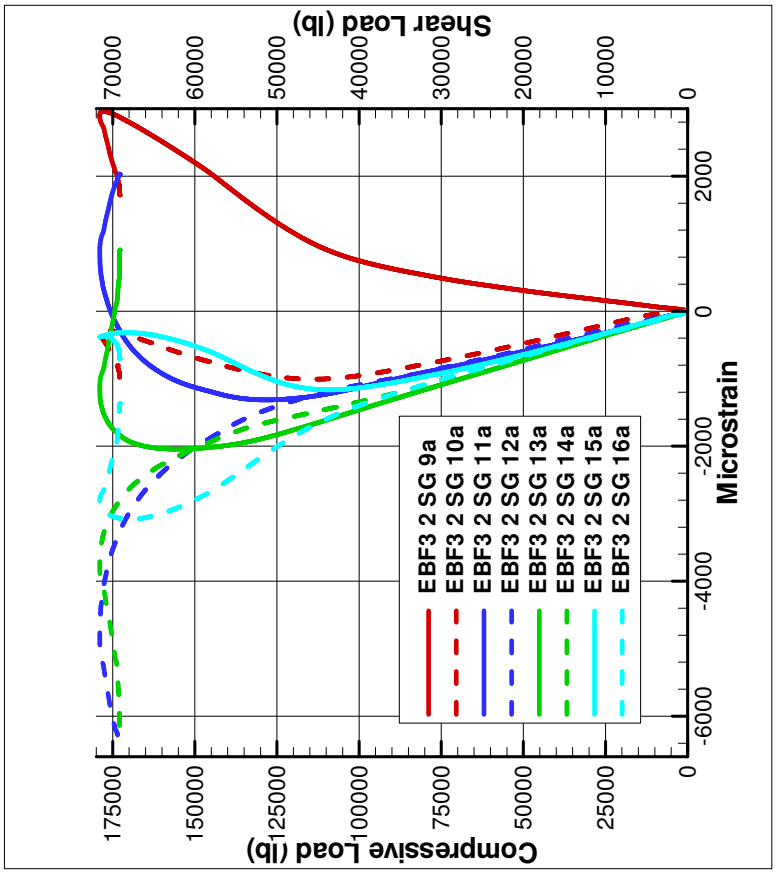

Figure A.16: Strain measured from Strain Gages 9a-16a for EBF3 Panel 2

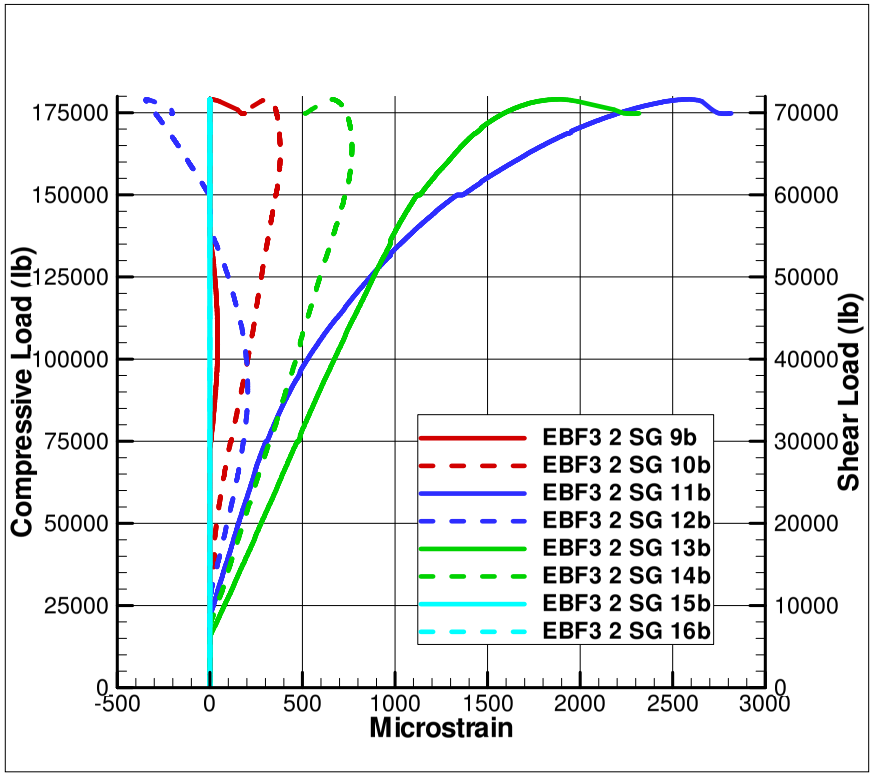

Figure A.17: Lateral Strain measured from Strain Gages 9b-16b for EBF3 Panel 2

Appendix B

Supplementary Data For Load Case 2

This section contains all the remaining experimental results not discussed for Load Case 2. If the results for a strain gages are not presented in the paper or in this section, the data was not recorded.

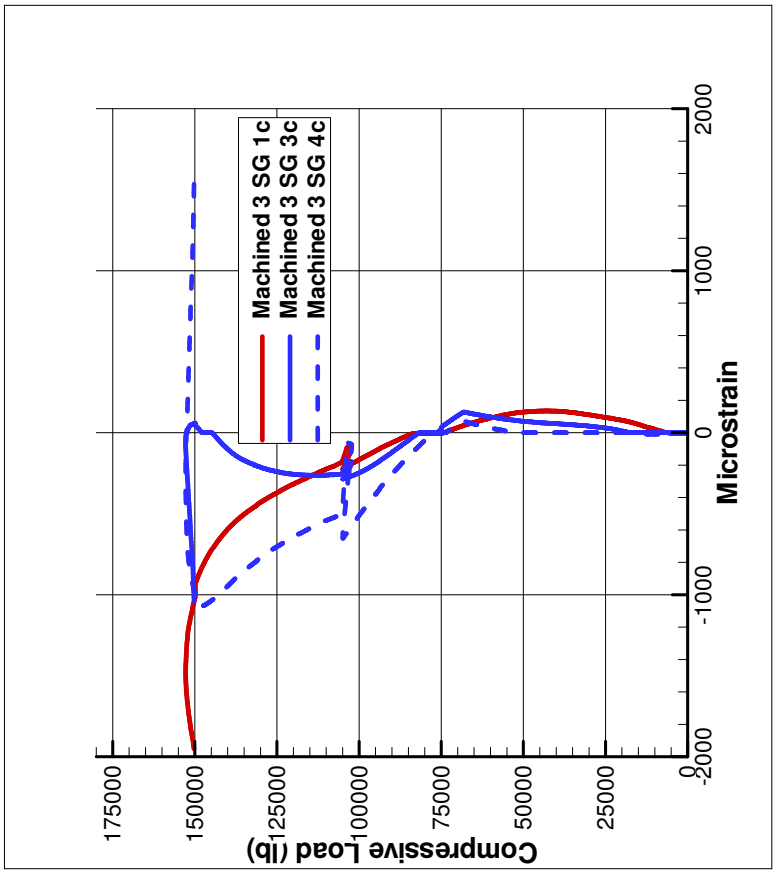

Figure B.1: Strain measured from Strain Gages 1c, 3c, and 4c for Machined Panel 3

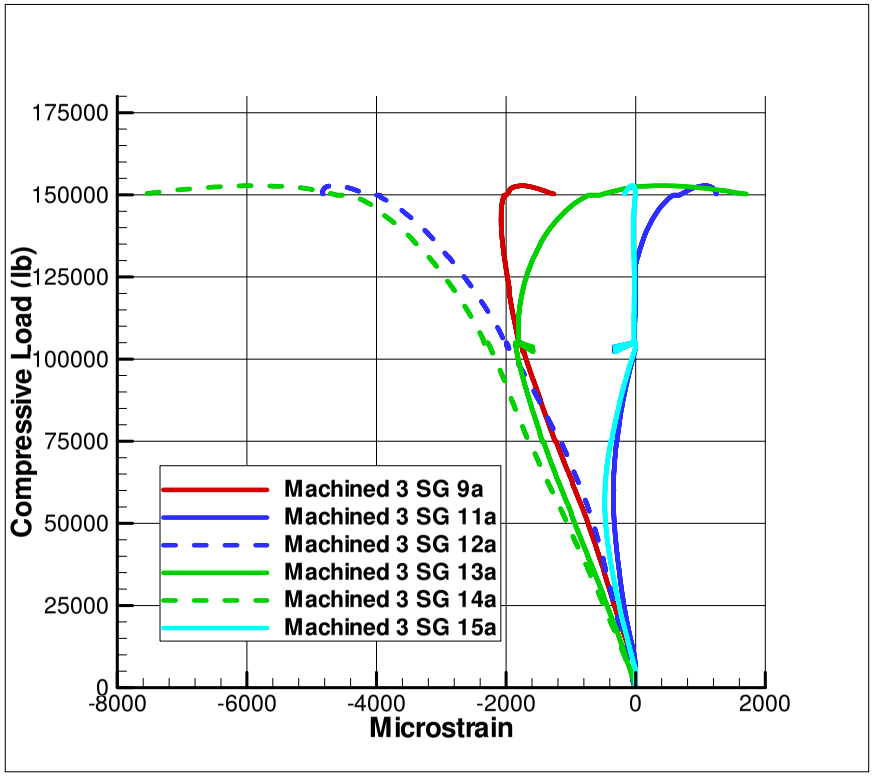

Figure B.2: Axial Strain measured from Strain Gages 9a and 11a-15a for Machined Panel 3

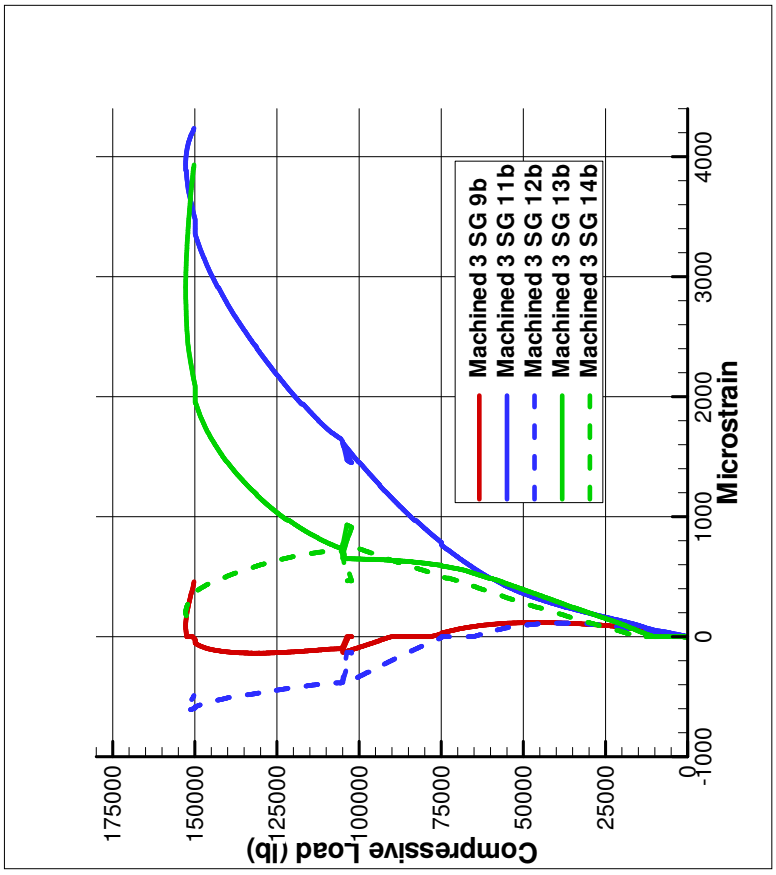

Figure B.3: Lateral Strain measured from Strain Gages 9b and 11b-15b for Machined Panel 3

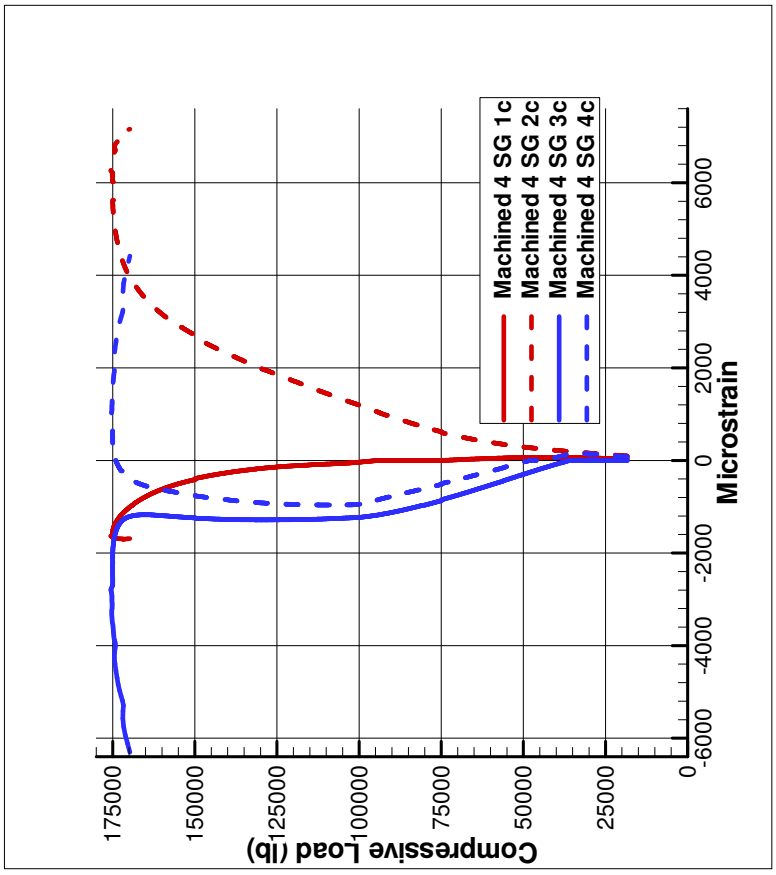

Figure B.4: Strain measured from Strain Gages 1c-4c for Machined Panel 4

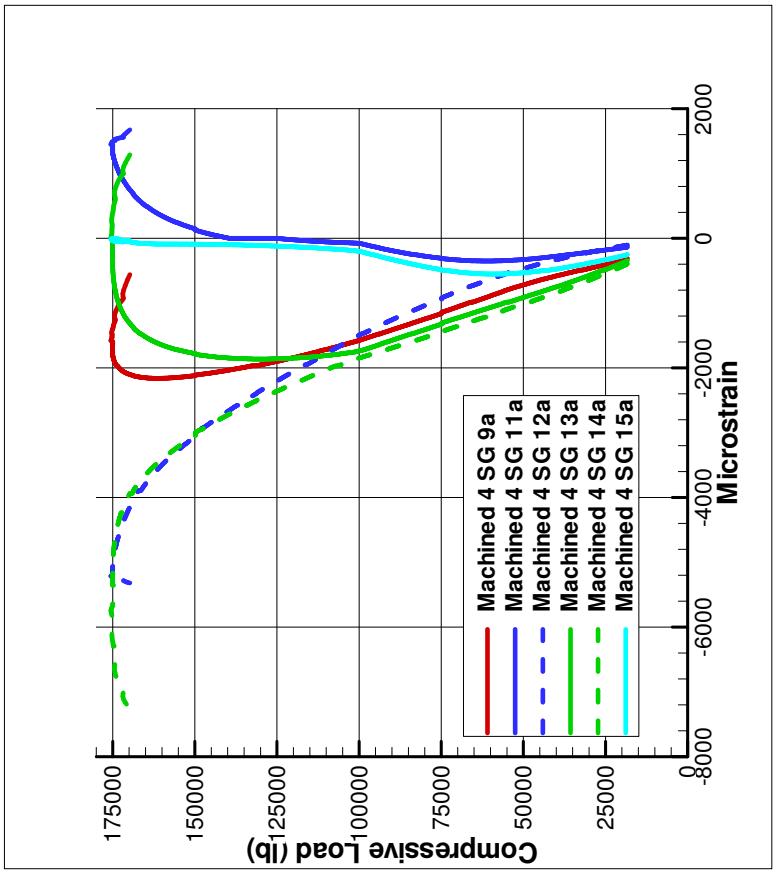

Figure B.5: Axial Strain measured from Strain Gages 9a and 11a-15a for Machined Panel 4

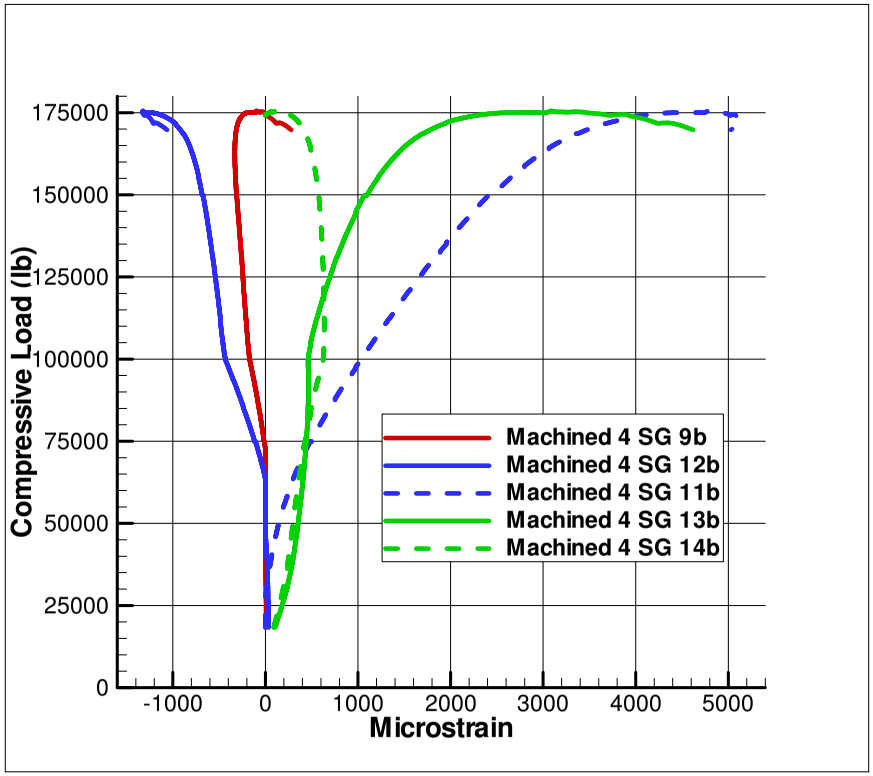

Figure B.6: Lateral Strain measured from Strain Gages 9b and 11b-15b for Machined Panel 4

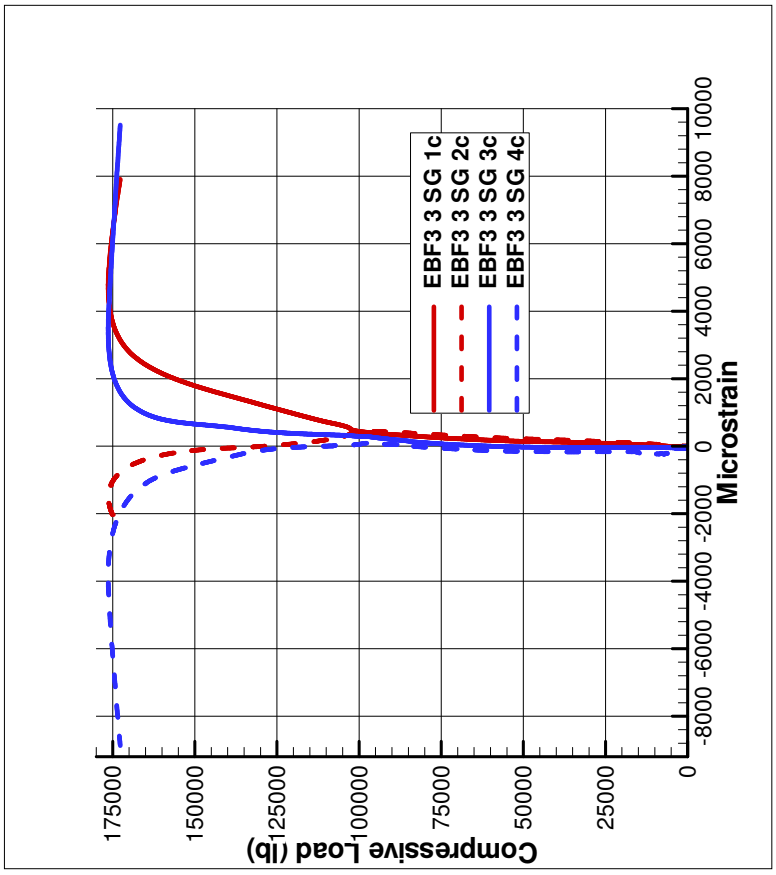

Figure B.7: Strain measured from Strain Gages 1c-4c for EBF3 Panel 3

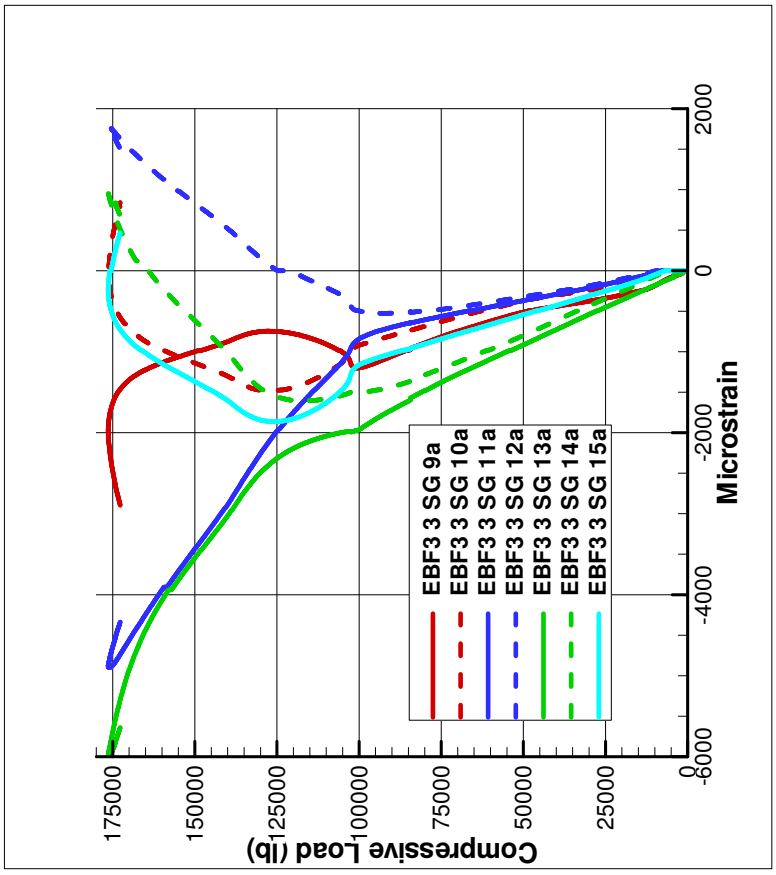

Figure B.8: Strain measured from Strain Gages 9a-15a for EBF3 Panel 3

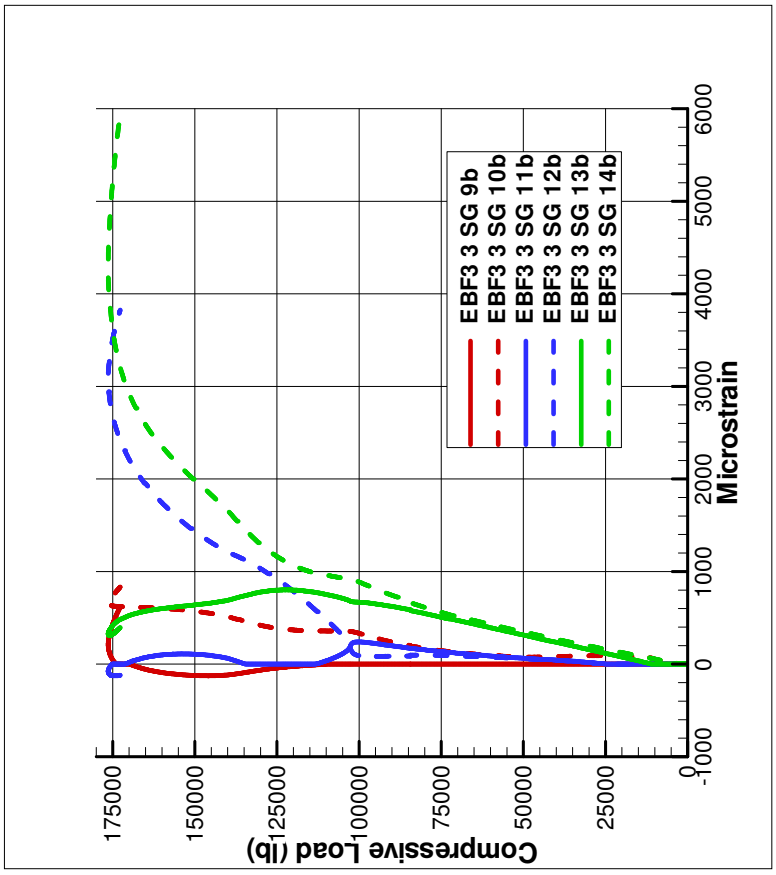

Figure B.9: Lateral Strain measured from Strain Gages 9b-14b for EBF3 Panel 3

Appendix C

Supplementary Linear Finite Element Analysis For Machined and EBF^3 Panel 1

This section contains all the remaining linear finite element analysis results not discussed for load case 1 graphed against Machined and EBF^3 Panel 1.

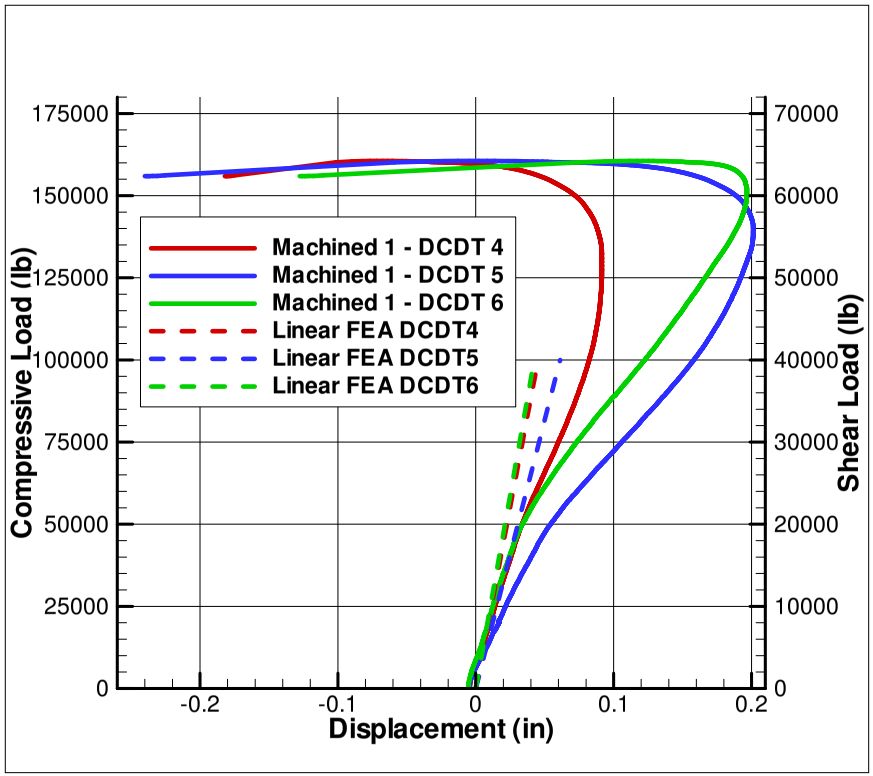

Figure C.1: Linear Finite Element Analysis Results and Experimental Results of DCDTs 4, 5, and 6 for Machined Panel 1

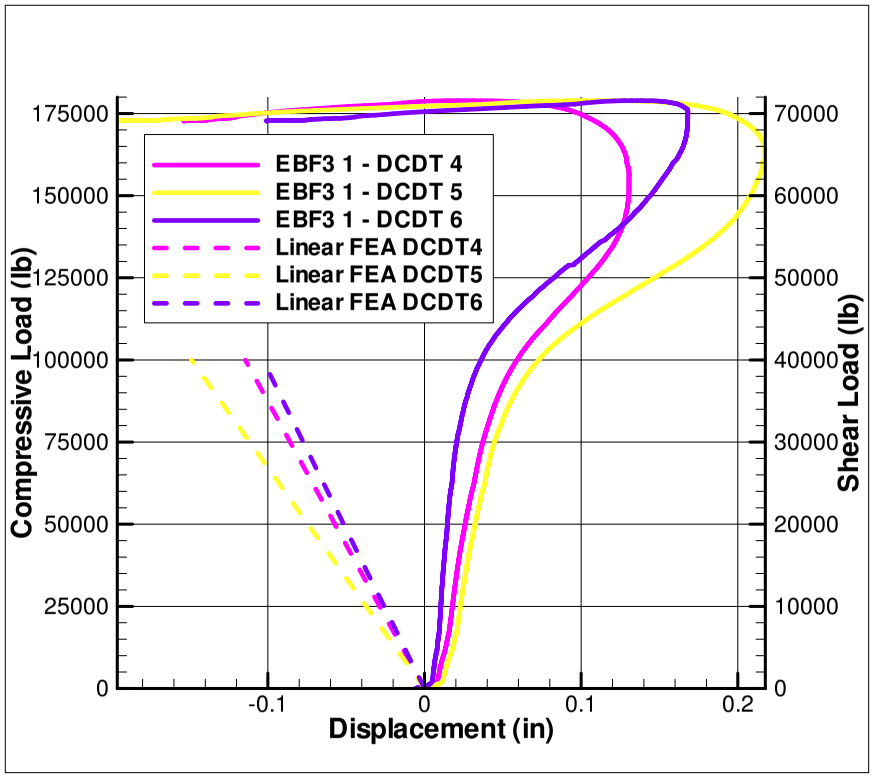

Figure C.2: Linear Finite Element Analysis Results and Experimental Results of DCDTs 5, 6, and 6 for EBF^3 Panel 1

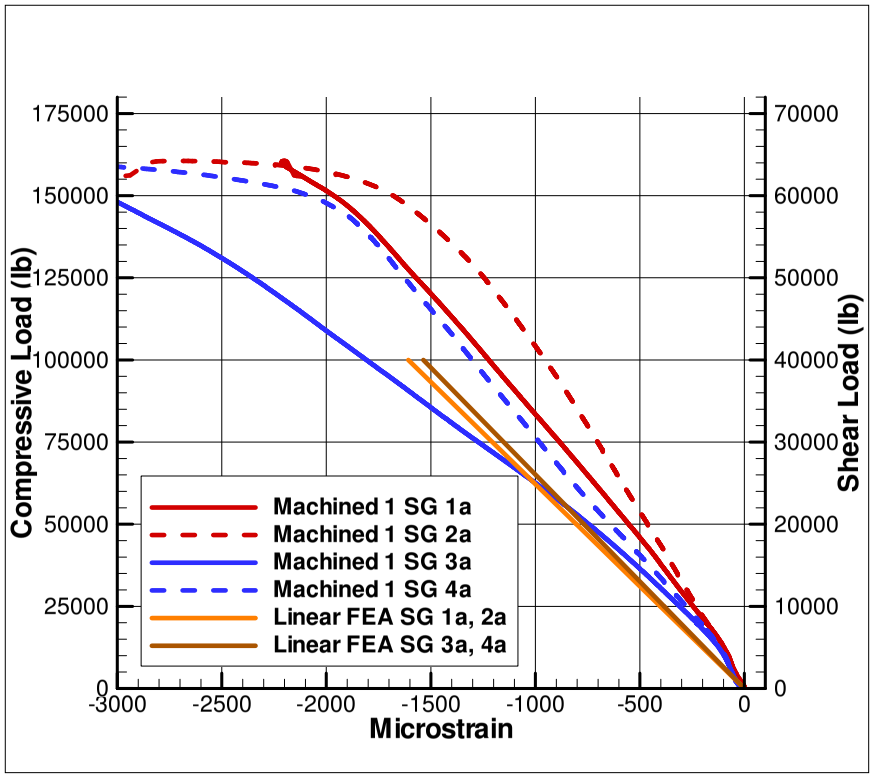

Figure C.3: Linear Finite Element Analysis Results and Experimental Results of Strain Gages 1a-4a for Machined Panel 1

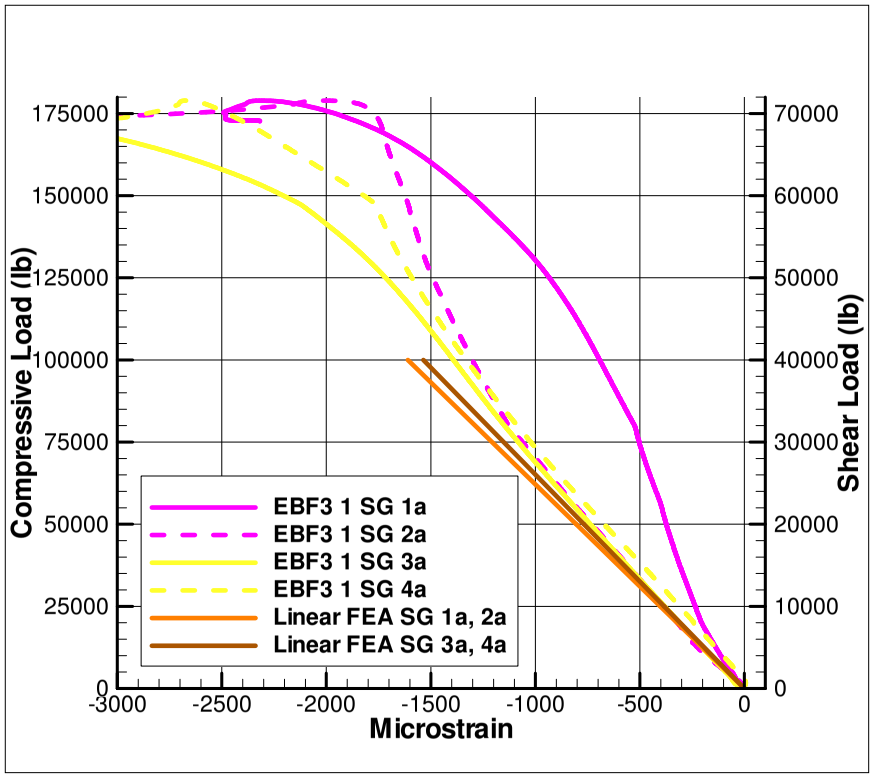

Figure C.4: Linear Finite Element Analysis Results and Experimental Results of Strain Gages 1a-4a for EBF^3 Panel 1

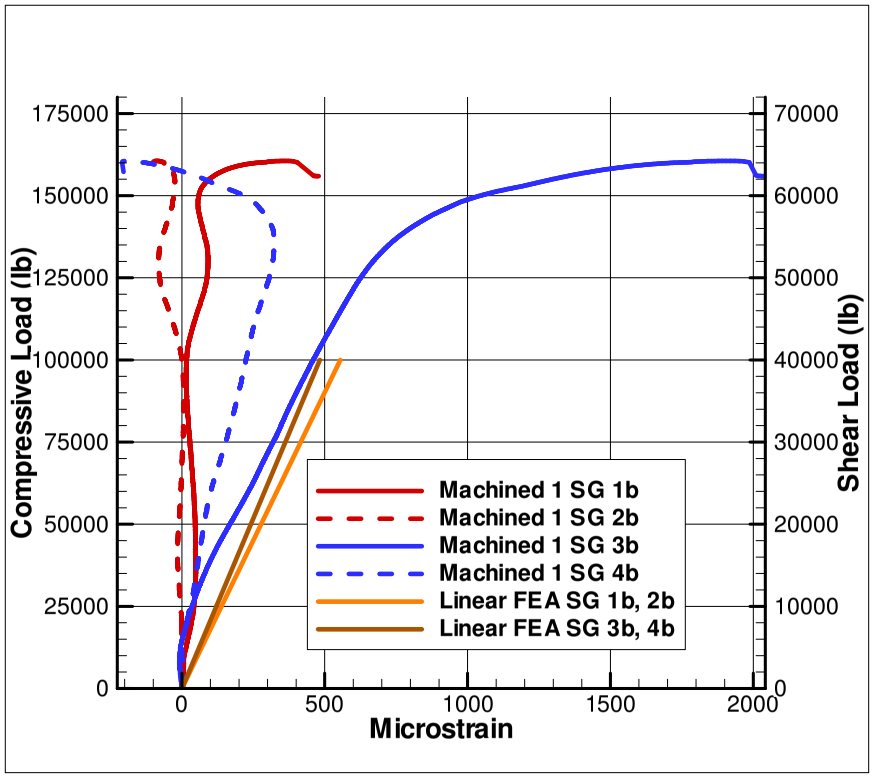

Figure C.5: Linear Finite Element Analysis Results and Experimental Results of Strain Gages 1b-4b for Machined Panel 1

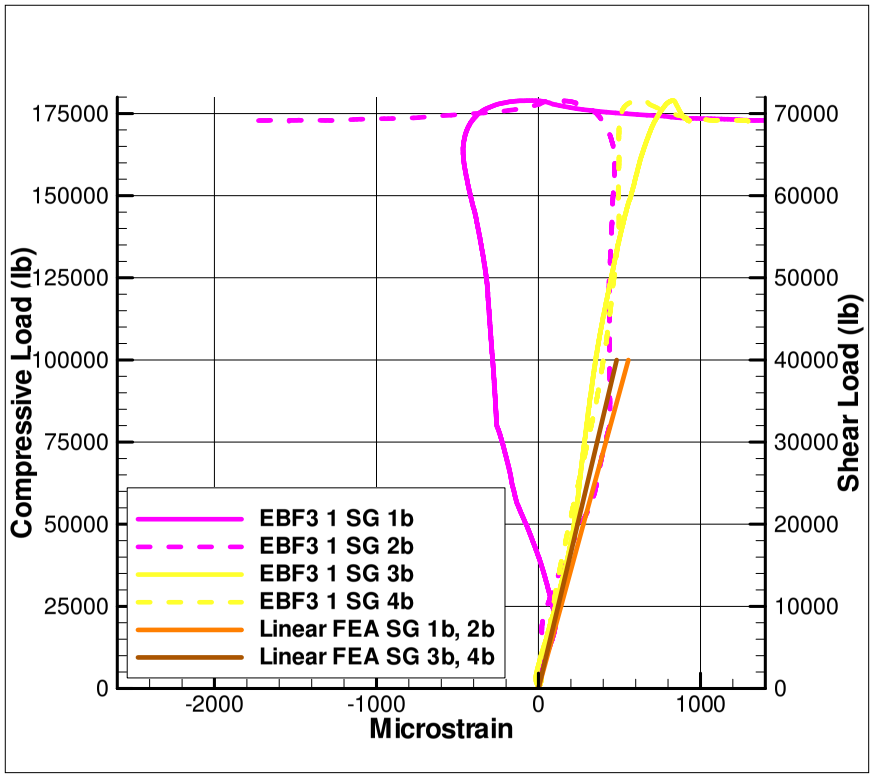

Figure C.6: Linear Finite Element Analysis Results and Experimental Results of Strain Gages 1b-4b for EBF^3 Panel 1

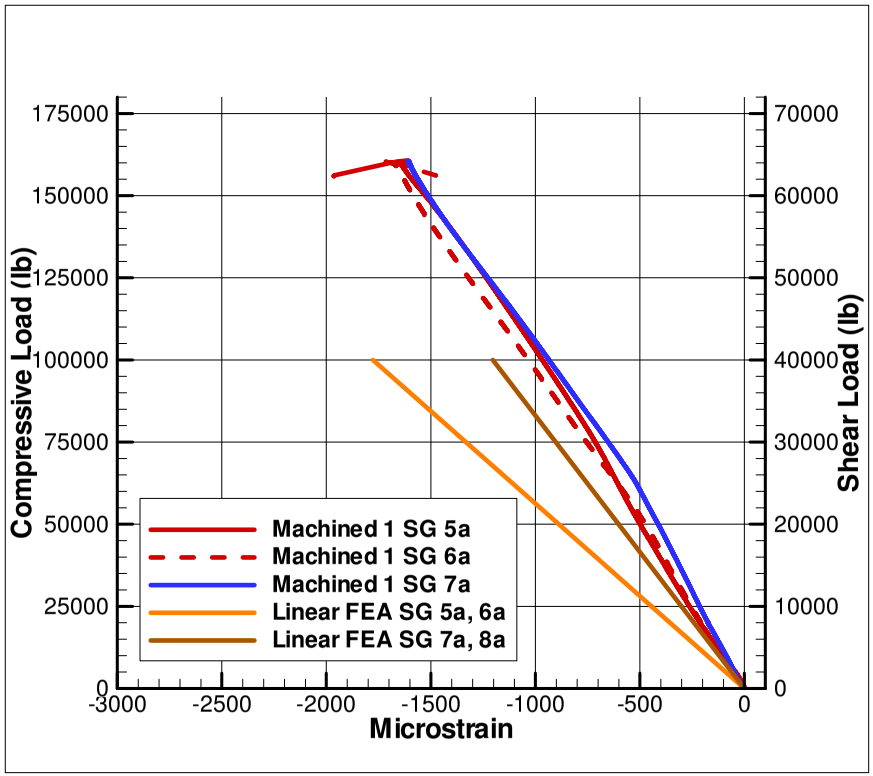

Figure C.7: Linear Finite Element Analysis Results and Experimental Results of Strain Gages 5a-8a for Machined Panel 1

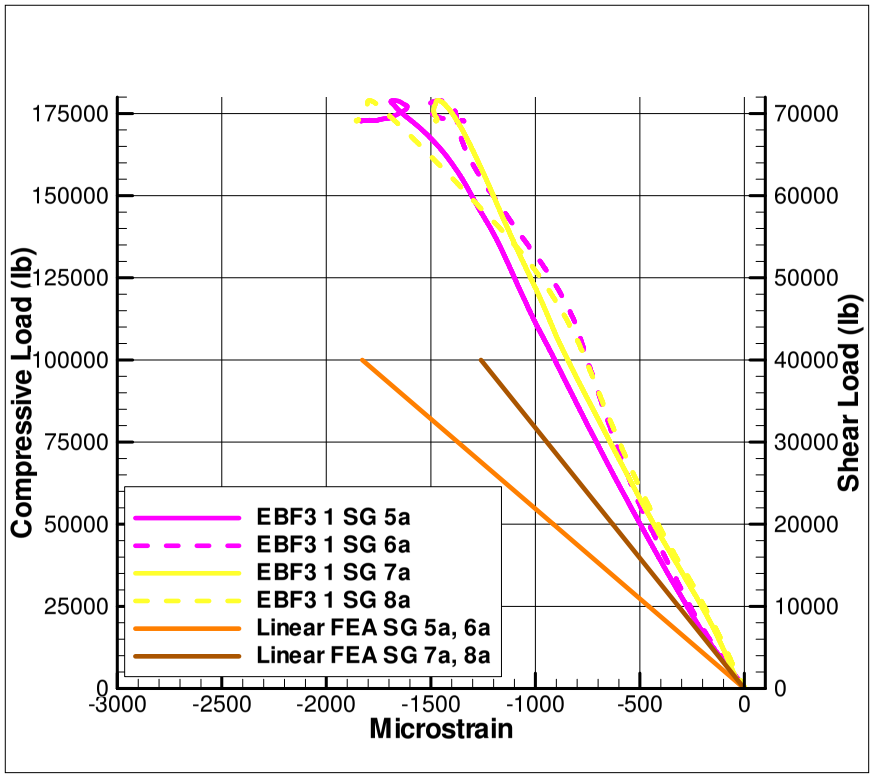

Figure C.8: Linear Finite Element Analysis Results and Experimental Results of Strain Gages 5a-8a for EBF^3 Panel 1

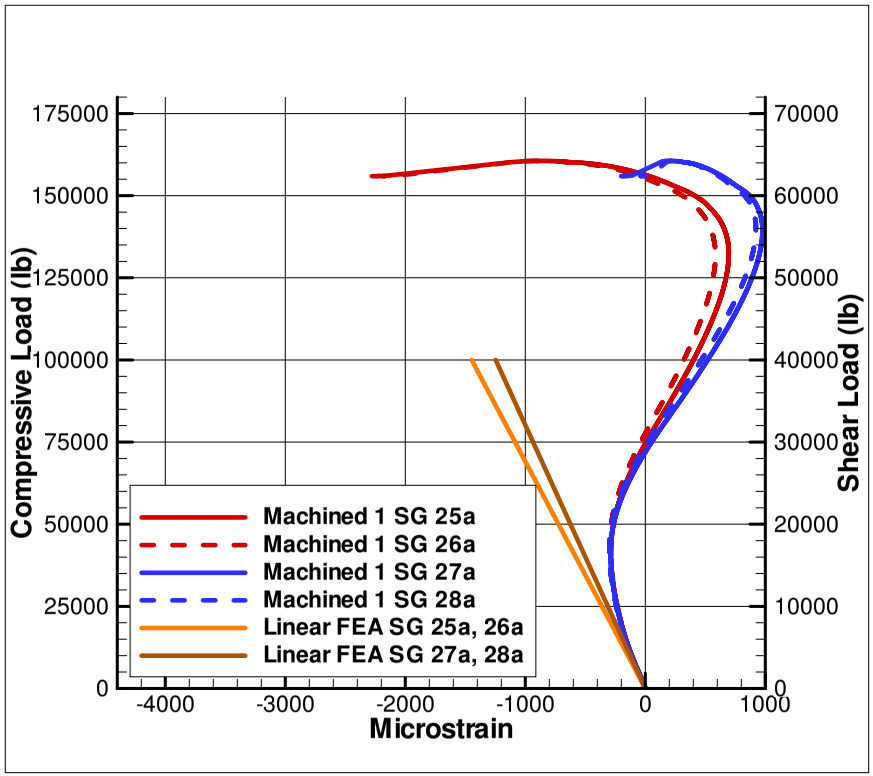

Figure C.9: Linear Finite Element Analysis Results and Experimental Results of Strain Gages 25a-28a for Machined Panel 1

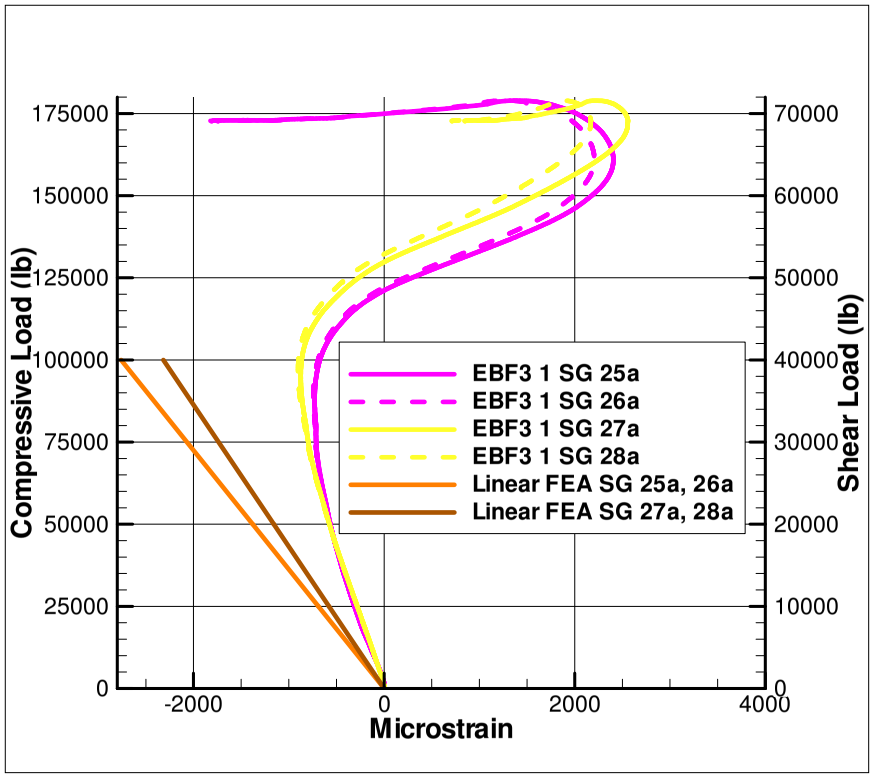

Figure C.10: Linear Finite Element Analysis Results and Experimental Results of Strain Gages 25a-28a for EBF^3 Panel 1

Appendix D

Supplementary Linear Finite Element Analysis For Machined and EBF^3 Panel 3

This section contains all the remaining linear finite element analysis results not discussed for load case 2 graphed against Machined and EBF^3 Panel 3.

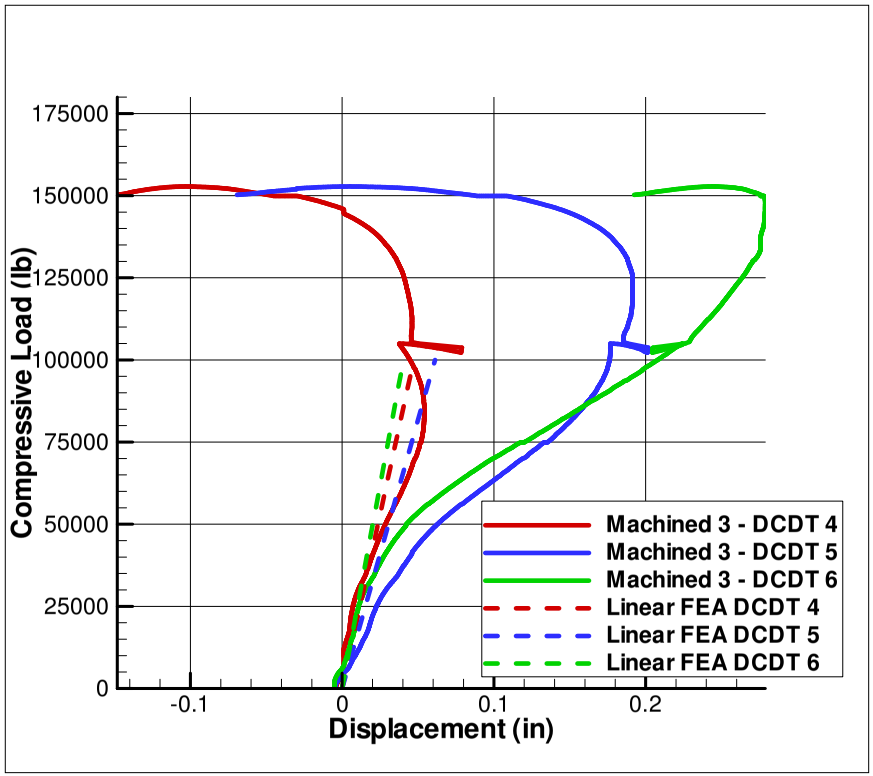

Figure D.1: Linear Finite Element Analysis Results and Experimental Results of DCDTs 4, 5, and 6 for Machined Panel 3

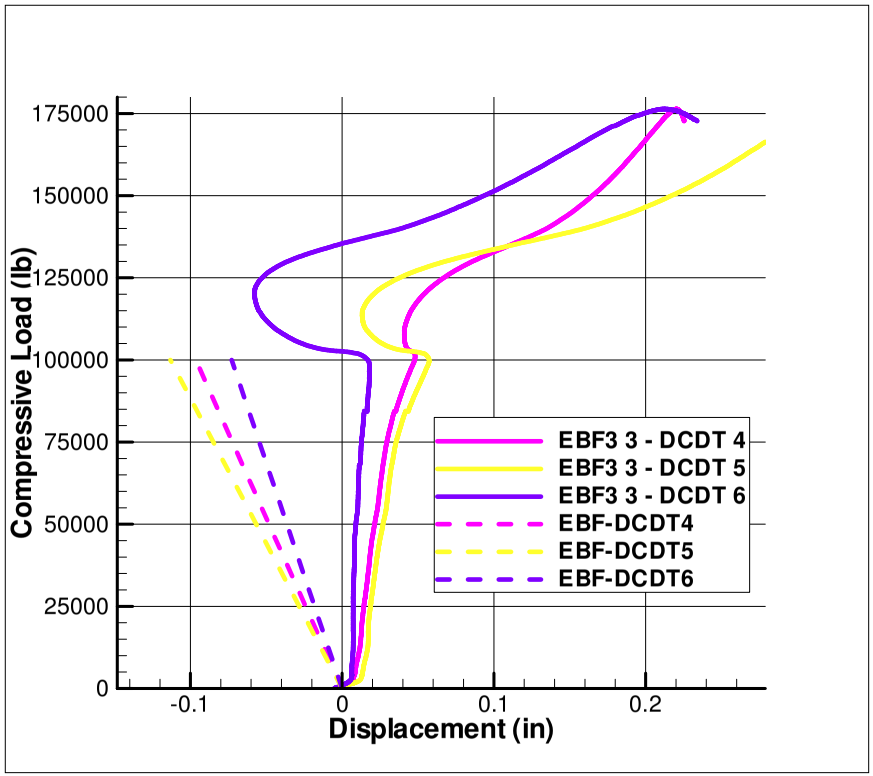

Figure D.2: Linear Finite Element Analysis Results and Experimental Results of DCDTs 4, 5, and 6 for EBF^3 Panel 3

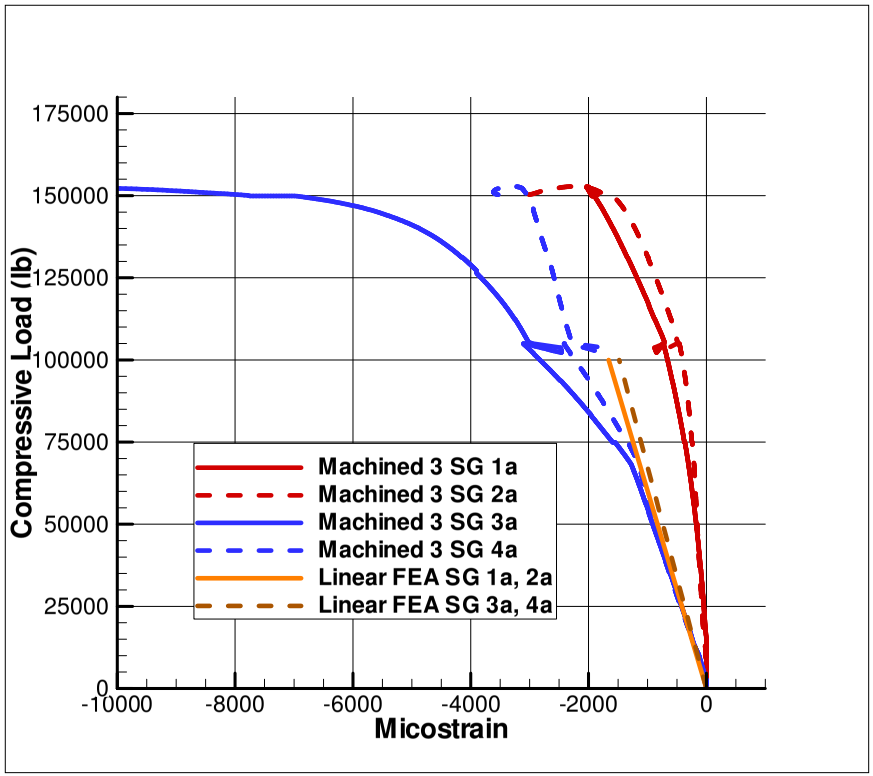

Figure D.3: Linear Finite Element Analysis Results and Experimental Results of Strain Gages 1a-4a for Machined Panel 3

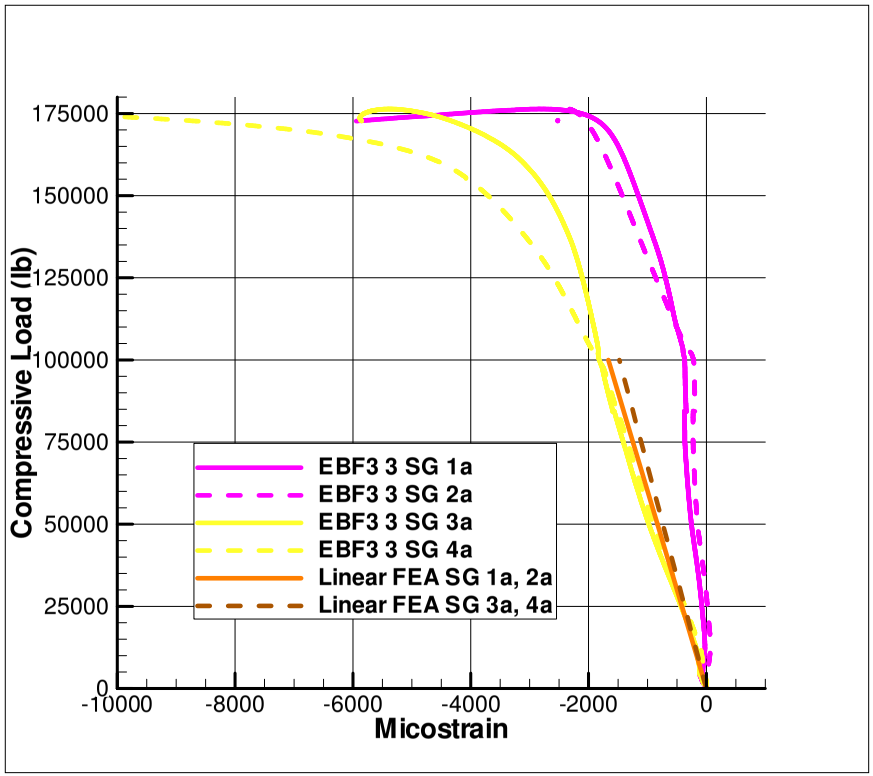

Figure D.4: Linear Finite Element Analysis Results and Experimental Results of Strain Gages 1a-4a for EBF^3 Panel 3

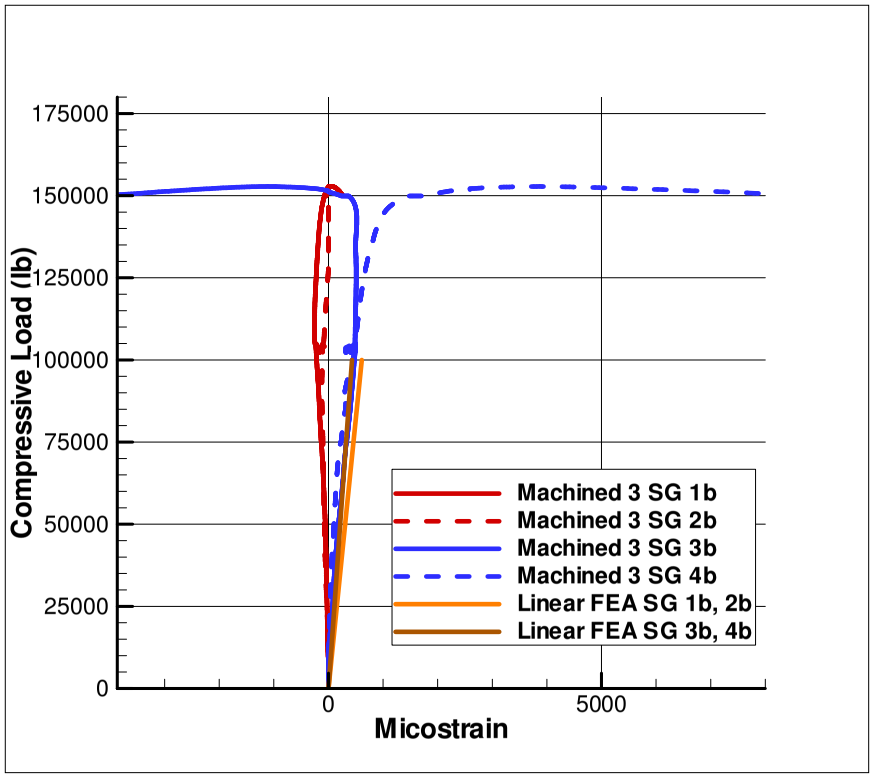

Figure D.5: Linear Finite Element Analysis Results and Experimental Results of Strain Gages 1b-4b for Machined Panel 3

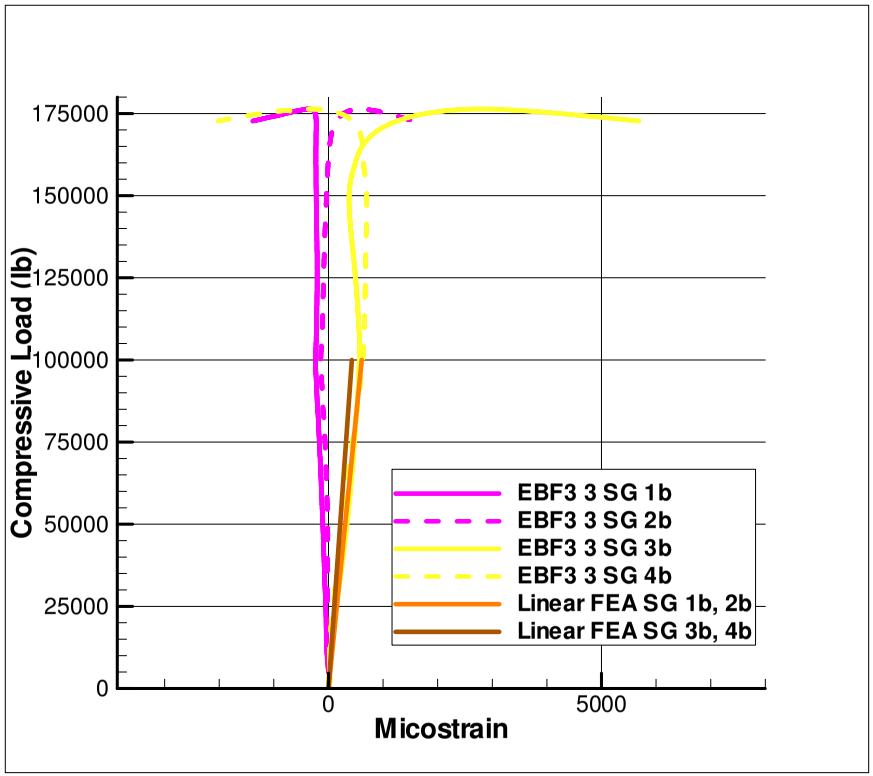

Figure D.6: Linear Finite Element Analysis Results and Experimental Results of Strain Gages 1b-4b for EBF^3 Panel 3

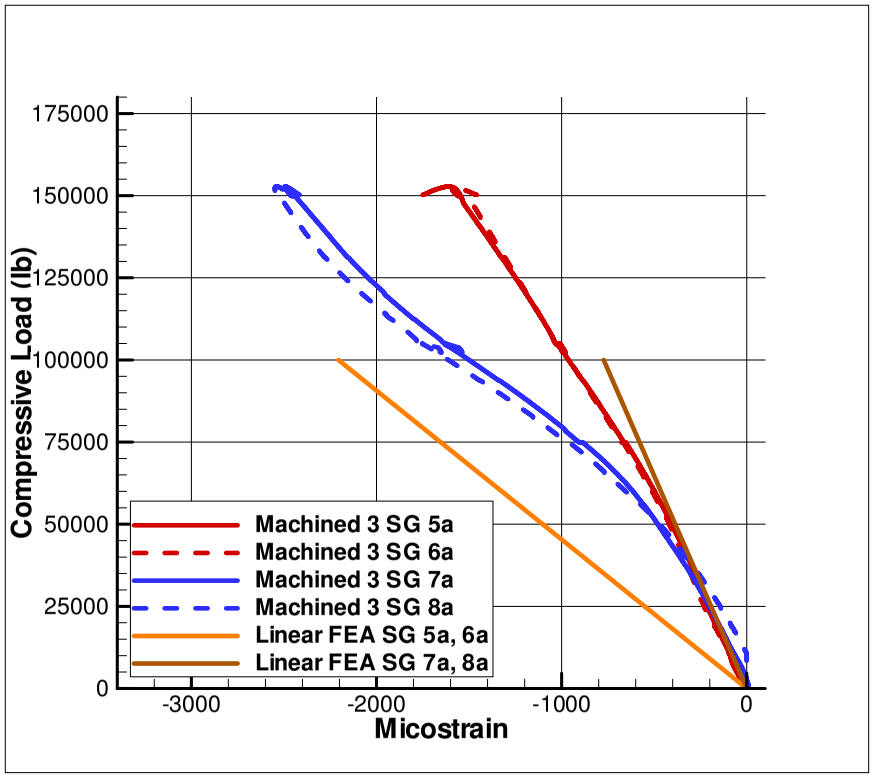

Figure D.7: Linear Finite Element Analysis Results and Experimental Results of Strain Gages 5a-8a for Machined Panel 3

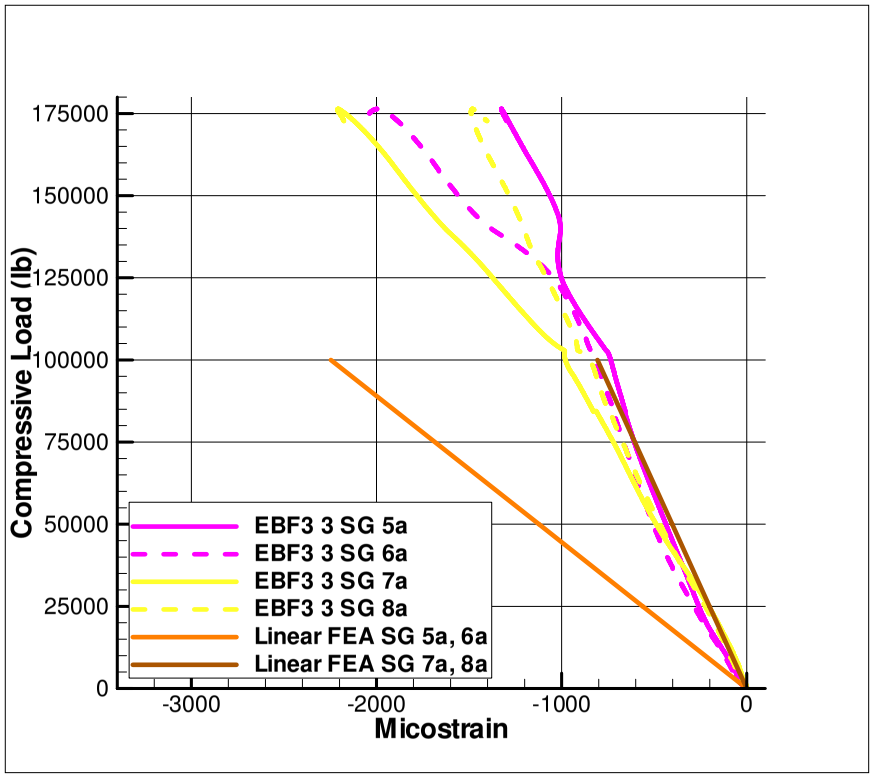

Figure D.8: Linear Finite Element Analysis Results and Experimental Results of Strain Gages 5a-8a for EBF^3 Panel 3

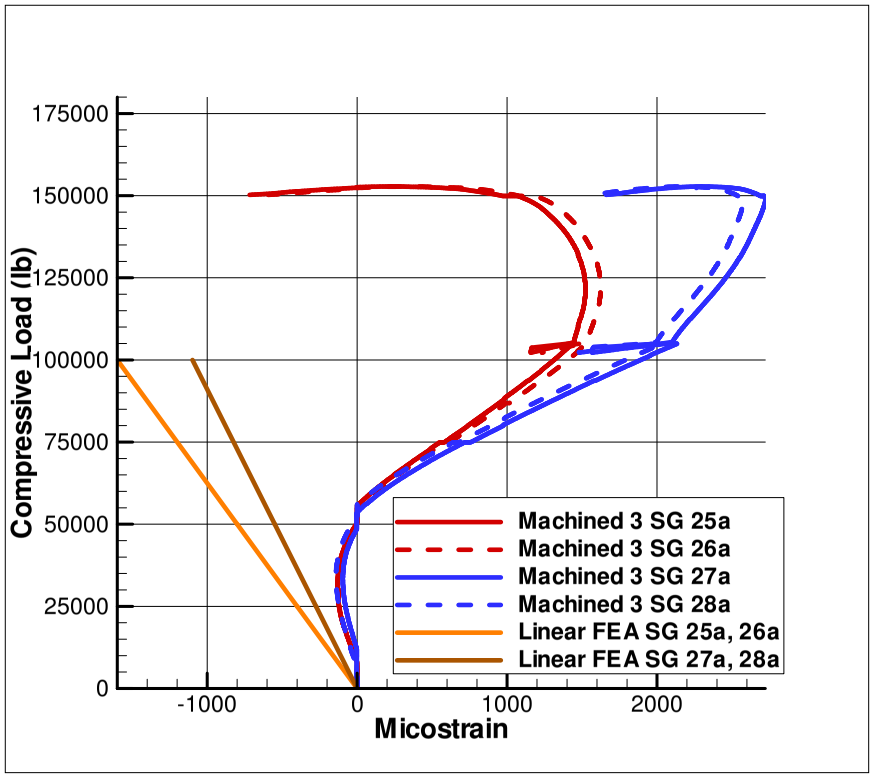

Figure D.9: Linear Finite Element Analysis Results and Experimental Results of Strain Gages 25a-28a for Machined Panel 3

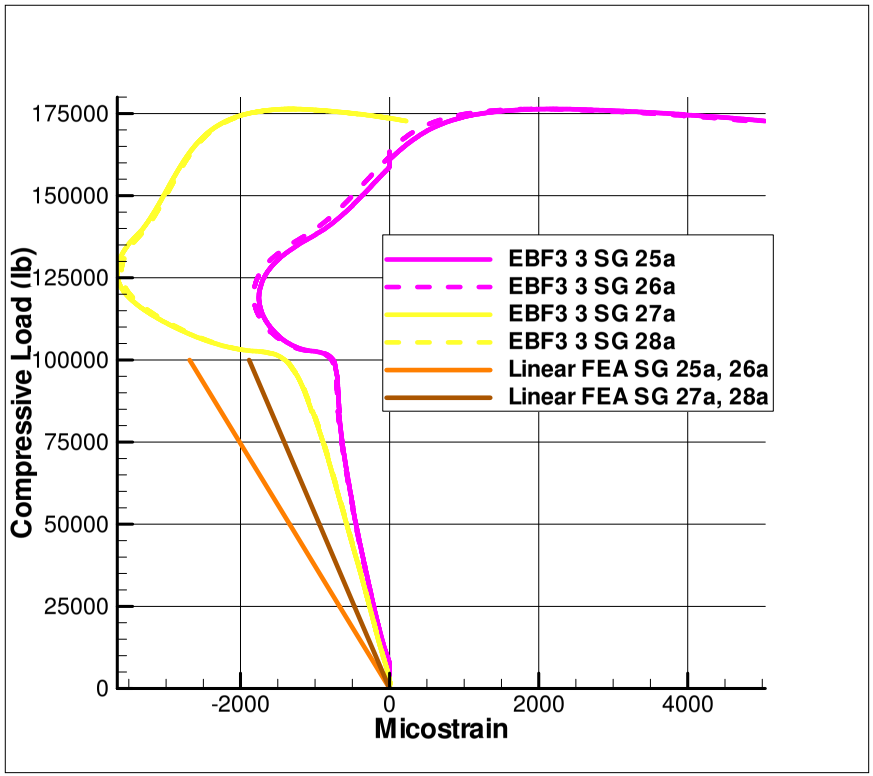

Figure D.10: Linear Finite Element Analysis Results and Experimental Results of Strain Gages 25a-28a for EBF^3 Panel 3

Appendix E

Additional Nonlinear Explanation

E.1 Material nonlinearity

Most engineering materials show nonlinear effects in a stress-strain curve after a certain load. For small strains Hooke's Law is valid. In Hooke's Law the modulus of elasticity (E), or Young's Modulus, and the shear modulus (G) are taken to be constant values and independent of the stress-strain level[23]. In this case the material is considered to be linear elastic. If the load remains small enough that the material remains linear for all strains and the material exhibits no yielding then the problem is considered linear elastic. [46]

However, it is not practical to use one set of equations to label a material for all range of conditions. There are many different conditions that require material nonlinear analysis. If strain levels exceed the linear range, nonlinear

elastic or plastic behavior can be seen. If the structure retains its original shape when unloaded, it is considered nonlinear elastic. Structures that deform permanently when unloaded are considered nonlinear plastic. Temperature effects cause thermal stresses on a material which could result in nonlinear thermo-elasticity and thermo-plasticity. The strain-rate could have effects on the material properties and visco-elastic or visco-plastic material nonlinearities should be considered, such as in creep[46]. Thermo and visco nonlinearities are not considered in this research.

The stress-strain relationship for a material is needed in order to solve material nonlinear problems. The exact relationship of the stress-strain curve in the nonlinear regime can be used if the data is available for the material, however, that is not always possible. If the exact relationship is not known, an approximation is made. Ramberg and Osgood developed an approximation to describe the nonlinear regime of certain materials in terms of three parameters: Elastic Modulus and two secant yield strengths[47].

In linear elastic finite element problems, the linear stiffness matrix (K) is calculated from a constitutive matrix (D), and the strain-displacement matrix (B). The constitutive matrix, also called the material matrix, is calculated by the values of Young's Modulus and Poisson's ratio (ν). The strain-displacement matrix describes the relationship between the strain and displacement. The stiffness matrix is normally calculated through numerical integration, where the values for the matrices used are found at each integration point. The equation for the linear stiffness matrix is:

$$K_{ij} = \int_V B_i^T D B_j \partial V \rightarrow K_{ij} = \sum_m [B_i]_m^T D_m [B_j]_m W_m \tag{E.1}$$

W_m is the Gauss-Legendre quadrature weight which is based on the mesh used. For every integration point m, $D_m = D$ if the material is elastic. If the material is nonlinear the linear elastic constitutive equations are no longer valid[22]. This results in the material matrix D having to be calculated at every point, with values of E, G, and ν which are dependent on the strain. The non-constant material matrix is calculated from the complex constitutive relations. The constitutive relations use the values of the material properties calculated from the nonlinear material model. Regardless of the nonlinear material model used, the nonlinear results are only as accurate as the constitutive model used[23].

Once the stiffness matrix is assembled the equilibrium equation is solved. The most basic equation of equilibrium for material nonlinearities is

$$[K]\{q\} = [P'] + \{Q(q)\} \tag{E.2}$$

Where [K] is the global stiffness matrix, $\{q\}$ is the column matrix of generalized displacements, $[P']$ is the generalized forces due to the applied loads, and $\{Q(q)\}$ is the column matrix of pseudo forces due to initial strains. Preferably equation E.2 is solved exactly. However, that is not always possible

and the equation is approximated within a certain tolerance[48]. Because of this, the equation is generally shown with an unbalanced force term, $\{f\}$:

$$\{f\} = -[K]\{q\} + [P'] + \{Q(q)\} \tag{E.3}$$

$\{f\}$ must be zero in order to solve the equation exactly. In order to have $\{f\}$ be zero or close to zero, an incremental/iterative approach can be used.

E.2 Geometric nonlinearity

Geometric nonlinearities refer to problems where there is large structural deformation. This can introduce complexities like follower forces due to large rotation, geometric stiffening due to initial stress, and large strain due to significant deformation. According to Kirchhoff and Love, the definition of large displacement in a plate is a deflection of more than 20% of the plate thickness or 2% of the small span length. However, geometric nonlinear effects are dependent on the boundary conditions and the dimension of the structures so there is no concrete limit where a problem must be considered "large displacements". Typically, it is up to the engineer to decide if the problem requires the extensive computer analysis required of geometric nonlinear analysis[46].

There are 3 kinds of geometric nonlinearities: large displacement/large rotation/small strain; large displacement/small rotation/small strain; or large

displacement/large rotation/large strain. [22]

The most widely used method for solving geometric nonlinear problems is using an incremental approach. An incremental approach is very slow and inefficient, but relatively easy to perform and gives accurate answers, accounting for its wide use[49].

When considering both geometric and material nonlinearities, an equilibrium equation similar to equation E.2 is used

$$[K]\{q\} = [P'] + \left\{Q^P\right\} + \left\{Q^{NL}\right\} \tag{E.4}$$

where [K], $\{q\}$, and $[P']$ are defined in equation E.2. $[Q^P]$ are the pseudo forces due to nonlinear material properties and $[Q^{NL}]$ are the pseudo forces due to geometric nonlinearities[48]. If the first derivative of equation E.4 with respect to the load parameter is taken, it can be written as

$$([K] - [\frac{\partial Q_i^{NL}}{\partial q_j}] - [\frac{\partial Q_i^P}{\partial q_j}])\{\dot{q}\} = \left\{\overline{P}\right\} \tag{E.5}$$

The matrices $[\frac{\partial Q_i^{NL}}{\partial q_j}]$ and $[\frac{\partial Q_i^P}{\partial q_j}]$ contribute to the stiffness matrix where

$$\left[K^{NL}\right] = -\left[\frac{\partial Q_i^{NL}}{\partial q_j}\right] \tag{E.6}$$

$$\left[K^P\right] = -\left[\frac{\partial Q_i^P}{\partial q_j}\right] \tag{E.7}$$

and $[K^{NL}]$ is the contribution from the geometric nonlinearities and $[K^P]$ is the contribution from the material nonlinearities to the stiffness matrix[48]. Once again there are several different methods to solve equation E.5 with an incremental/iterative approach like the Newton-Raphson method[50].

E.3 Solving Nonlinear Equations

Solving nonlinear problems by hand is impractical except for the most simple of problems. Several strategies have been developed for solving a set of nonlinear equations and nearly all have been adapted to finite element codes.

The equilibrium equations need to be developed first. Which equilibrium equation to be solved is dependent on the type of nonlinearities being considered as seen in equations E.2 and E.4. The equilibrium equation is also reliant on the boundary conditions, load conditions, and shape of the structure. The equilibrium equation can be graphically represented as the equilibrium path showing the load versus displacement of the structure[22].

The Newton-Raphson method is a simple yet fairly robust incremental/iterative approach to solving nonlinear equations. The Newton-Raphson technique increments the load at each step. At each load increment, the process calculates the tangent stiffness matrix. The tangent stiffness matrix is formulated based on the elastic and geometric stiffness matrices. The geometric stiffness matrix describes the stiffness of the structure from the geometric

shape, seen in equation E.6. The elastic stiffness matrix describes the stiffness of the structures from the material, seen in equation E.7. The tangent stiffness matrix describes the stiffness of the whole structure. The equilibrium equations calculate the displacement using the tangent stiffness matrix. For each load increment, the process iterates calculating a new tangent stiffness matrix and the displacement each time until the displacement converges to an answer. Once a solution for the displacement of the structure for a given load is found, the load increments. This entire process is repeated until the maximum load is reached or until a solution is not possible[25].

The Newton-Raphson method is not flawless. One of the biggest problems with the full Newton-Raphson approach is recalculating the tangent stiffness matrix at each iteration. This can be incredibly slow and taxing especially for large systems[25]. Also the Newton-Raphson scheme does not account for sudden nonlinearities such as cracks or gap closures. In addition, the Newton-Raphson approach typically has a constant load during each iteration. If the applied load is larger than the structure's limits, the solution will never converge. If the solution does not converge when iterating, then the process must be stopped or restarted with a smaller iteration[22].

A modified Newton-Raphson method exists that does not calculate the tangent stiffness matrix at each iteration but instead at each load or displacement increment. It uses the same tangent stiffness matrix for each iteration. This modification generally results in more iterations being required and a less stable process. However, the modified Newton-Raphson approach is not

as computationally demanding as the full method[25]. Figure E.1 illustrates the difference in convergence between the full and modified Newton-Raphson methods, where the slope of the line in the figure is based on the stiffness matrix. It can be seen that more iterations are needed in the modified Newton-Raphson method.

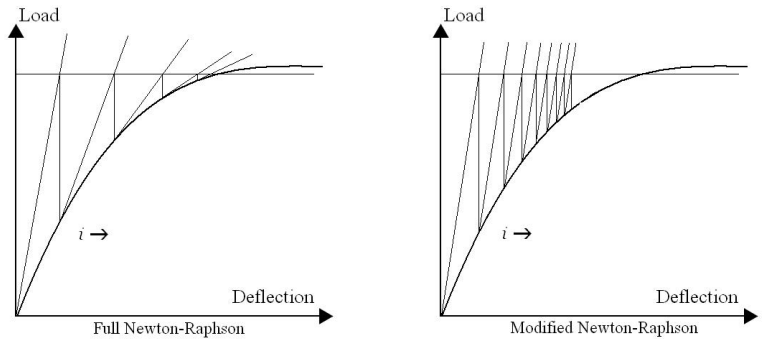

Figure E.1: Full Newton-Raphson versus Modified Newton-Raphson[25]

The Newton-Raphson technique demonstrates the basic steps for solving nonlinear problems. First, the method for advancing on the equilibrium path occurs. This is done by the load increment. The tangent stiffness matrix is calculated. This is either done when calculating the displacement at each iteration, at each load case, or some combination thereof. The displacement of the structure is calculated by solving the equilibrium equation. In other finite element programs the stress, strain, and other properties of the problem for a given load are also calculated[51]. Lastly the convergence criterion is decided upon and determines when the approximations for the equations for a load case are accurate enough.